Université du Québec
Institut National de la Recherche Scientifique
Centre Énergie, Matériaux et Télécommunications

LANTHANIDE DOPED NANOPARTICLES ENGINEERED FOR CANCER THERANOSTICS

Par

Miao Wang

Thèse présentée pour l'obtention du grade de
Philosophiæ doctor (Ph.D.)
en sciences de l'énergie et des matériaux

Jury d'évaluation

Président du jury et examinateur interne	Prof. Jinyang Liang INRS-EMT
Examinateur externe	Prof. Armand Soldera Department of Chemistry University of Sherbrooke
Examinateur externe	Prof. Gonzalo Cosa Department of Chemistry McGill University
Directeur de recherche	Prof. Fiorenzo Vetrone INRS-EMT
Codirecteur de recherche	Prof. Federico Rosei INRS-EMT

ACKNOWLEDGMENTS

It is my honour and privilege to express my deepest and sincere gratitude to Professor Fiorenzo Vetrone and Professor Federico Rosei, for giving me this wonderful opportunity to do my doctoral research under their supervision. I thank them for their enthusiasm, advice and effort, which make this thesis a reality. Their attitude towards academic research has greatly motivated me to be a good researcher. It has been a pleasure working with Professor Vetrone, who created a warm and stimulating research environment for us. The discussions with him at different stages of my research work largely contributed to the success of my research. I am forever and extremely grateful for his dedicated and sincere guidance, constant encouragements, his trust and understanding, the valuable freedom to think and work independently and at my own pace.

Beside my supervisors in INRS, I would like to express my sincere thanks to Professor Alex Chang, an oncologist of department of oncology, Johns Hopkins University, who was also my supervisor when I worked in Johns Hopkins international medical centre of Singapore. He continues to give me some invaluable advice and grant support for my PhD project. His endless effort in encouraging me to pursue my dreams makes me explore a fascinating scientific field. He has always been a strong supporter when I face difficulties throughout the duration of my PhD study.

I would like to acknowledge Professor Kishore Bhakoo, Singapore Bioimaging Consortium (SBIC), Agency for Science, Technology and Research (A*STAR) for allowing me to carry out the in vitro experiments and bioimaging (confocal microscopy, MRI and CT) characterizations at SBIC. I would be also grateful to Professor Xu Li, Institute of Materials Research and Engineering (IMRE), A*STAR, for collaboration of the development of theronostic nanocapsules. Their invaluable and suggestions and support have greatly improved the progress of my research project and the quality of the articles I wrote for publication. I would appreciate Professor Doingling Ma (INRS), Professor Jerome Claverie (University of Sherbrooke), Professor Sun, Shuhui (INRS), and Professor Gauthier, Marc Andre (INRS) for their invaluable help.

I would like to thank Dr. Yu Zhang (IMRE, Singapore), Dr. Ting Cheng (INRS, CA), and Artiom Skripka (INRS, CA), who have contributed to my research work by carrying out some experiments involved in my project and discussing with me about the experiments design, results and articles writing. Many thanks to Michael Ng (SBIC, Singapore) for his assistance with the MIR measurements and Dr. Way cherng Chen (Broker Singapore Pte. Ltd.) for his help with the experiments of CT imaging.

I am also grateful to Dr Eva Hemmer and Dr Marta Quintanilla Morales from our lab for their teaching me the experiment and data analysis skills. Thanks to Dr. Andrea Greschner for her assistance for the use of UV-VIS spectrophotometer.

I would like to express my sincere thanks to INRS-EMT administrative and technical staffs for their help. Special thanks to Ms. Hélène Sabourin, Mr. Christophe Chabanier and Ms. Tatiana Brahmi for their kind, efficient, and professional assistance whenever I need.

A massive thanks to all my friends both in Canada and Singapore, for the help, company and heartily support whenever I encountered the difficulties in my life. They are Yeh Ching Linn, Gaixia Zhang, Xin Jin, Jianming Zhang, Qian Yu, Yufeng Zhou, Yue Huang, Wei Huang, and Daling Cui and many others.

I am eternally grateful to my parents, who have been a constant source of love for me. I wish to thank to my husband and my dearest son, for your deep love and selfless support, and who have always been a part my life wherever I am.

Finally, I wish to acknowledge the following organizations for their financial support to my research: the Natural Sciences and Engineering Research Council (NSERC) of Canada, Canada Foundation for Innovation, Canada Research Chairs program, and the Fonds de recherche du Québec-Nature et technologies (FRQNT). I am also grateful to the Johns Hopkins Singapore Research Fund provided by Private limited Company for supporting their Santa Fe research programme and the support of A*STAR, Singapore.

RÉSUMÉ

Les nanodispositifs théranostiques jouent un rôle essentiel dans le traitement du cancer de par leur capacité à permettre le suivi temps réel de l'évolution de la maladie lors de traitements par thérapie photodynamique (PDT) et thérapie photothermique (PTT). Les nanoparticules dopées aux lanthanides (LnNPs) sont des matériaux émergents prometteurs pour des applications nanothéranostiques grâce à leur remarquable propriété de photoluminescence par conversion ascendante (UC, pour *upconversion*) ou descendante (DS, pour *downshifting*). En dépit des progrès récents, la transposition de ces nanoparticules théranostiques, du laboratoire au chevet des patients, est toujours entravée par des obstacles majeurs.

Dans cette thèse, nous traitons du développement de nanocapsules théranostiques (optimisation de la synthèse, modification de la surface des LnPs) dédiées à l'application en PDT et PTT assistées par imagerie et opérées par proche infrarouge (NIR, pour *near infrared*).

Dans la Partie I, nous proposons une stratégie ***de thermolyse en une étape*** pour la synthèse de nanoparticules de β-$NaGdF_4$ dopées à Er^{3+} et Yb^{3+}, à propriété de conversion ascendante (UCNPs), de morphologie et dispersité contrôlées. Nous avons établi que le choix de la température, lors de l'étape d'injection à chaud, était crucial pour le contrôle de la forme et de la taille des nanocristaux de β-NaGdF4 en formation. Grâce à cette subtilité, nous avons rapporté pour la toute première fois la synthèse directe de nanobâtonnets de β-$NaGdF_4$. L'étude poussée des mécanismes mis en jeu révèle que des températures distinctes s'accompagnent de concentrations différentes en condition sursaturée. Ceci influence sensiblement les processus de germination et de croissance de la phase α, ainsi que le mûrissement d'Ostwald ayant lieu lors de la transition de phase α → β.

Le contrôle de la morphologie s'avère important pour la maîtrise de l'UC et du contraste négatif en imagerie par résonance magnétique (IRM). Nous avons établi d'une part que l'intensité d'UC sous excitation à 980 nm diminuait avec l'augmentation du rapport aire-volume des UCNPs, et d'autre part qu'un rapport de forme proche de 1 maximisait le rapport des intensités verte-rouge émises. L'amélioration du contraste négatif en IRM pondéré en T_2 s'accroît avec la taille des LnNPs, à l'exception des nanobâtonnets qui démontrent les meilleurs performances malgré leur taille inférieure à celle des nanoplaques.

Dans la Partie II, nous co-encapsulons des nanoparticules de β-$NaGdF_4$ avec de la phtalocyanine de zinc (ZnPc, une molécule utilisée en PDT), au sein d'un même nanodispositif théranostique pouvant servir à la fois en IRM et en PDT opérée par NIR.

La modification de la surface est une étape nécessaire pour rendre les UCNPs et agents thérapeutiques dispersables dans l'eau et donc adaptés aux applications *in vivo*. Nous avons développé une stratégie inédite **d'encapsulation « tout-en-un »**, en milieu aqueux *quasi* neutre. Les UCNPs et la ZnPc sont initialement confinées au sein de micelles de poly(éthylène glycol)-*b*-poly(propylène glycol)-*b*-poly(éthylène glycol), un copolymère triblocs de formule PEG_{106}-PPG_{70}-PEG_{106}. Le scellage en lui-même est réalisé par formation d'une coquille de silice à l'interface décrite par les blocs de PPG et de PEG. **Les nanocapsules de silice structurées par micelles polymériques (NCs)** dispose d'un rayon hydrodynamique de 85 nm, d'un indice de polydispersité de 0.1 et d'une excellente stabilité colloïdale. De plus, la faible distance entre les charges co-encapsulées favorise les transferts d'énergie. Lorsqu'utilisées *in vitro*, les NCs font preuve d'une biocompatibilité adéquate, d'un contraste T_2 amélioré, et d'une efficacité exemplaire dans l'éradication des cellules cancéreuses BT474 sous irradiation NIR.

Dans la Section 2, nous appliquons une stratégie similaire pour l'encapsulation de la doxorubicine (DOX, une molécule chimiothérapeutique), mais en en fonctionnalisant cette fois la surface des NCs avec un agent de pénétration de l'enveloppe nucléaire (le peptide TAT) permettant l'administration active de principe actif dans des cellules cancéreuses. L'agrégation de la DOX au sein des NCs est évitée grâce à l'incorporation de triméthoxy(2-phényléthyl)silane (TMPES). Par cette stratégie, la DOX est administrée plus efficacement, car accumulée dans les noyaux cellulaires, comme démontré par imagerie de fluorescence et l'inhibition accrue de cellules cancéreuses habituellement résistantes à la DOX.

Enfin dans la Partie III, nous étendons l'usage des NCs théranostiques à la PTT opérée par NIR. Nous co-encapsulons à cet effet des nanoparticules de $LiLuF_4:Nd^{3+}@LiLuF_4$ à propriété de conversion descendante (DSNPs) et un « radiateur optique », le diimide N,N'-dicyclohexylaminopérylène-3,4,9,10-tétracarboxylique (sPDI). Les DSNPs, synthétisés par deux couches successives par thermolyse, jouent le rôle de nanothermomètres ratiométriques pour la mesure non-invasive de la température locale. Le dégagement de chaleur causé par sPDI peut ainsi être quantifié en temps réel et contrôlé pendant la thérapie. Les deux charges peuvent être excitées à 793 nm, dans la première fenêtre biologique, tandis que le nanothermomètre émet à 1060 nm, dans la seconde fenêtre biologique. De plus, le réseau hôte de $LiLuF_4$ constitue un émetteur efficace utilisé en tomodensitométrie des cellules MCF-7 du cancer du sein. Ces nanocapsules théranostiques sont photothermiquement stables et produisent un effet photothermique intense à l'encontre des cellules cancéreuses.

Mots-clés: théronostic, nanocapsules, nanoparticules dopées aux lanthanides, thermolyse, proche infrarouge, upcoversion, nanothermométrie, thérapie photodynamique, thérapie photothermique

ABSTRACT

Theranostic nanoplatforms play an essential role in cancer treatment as it is able to report on the status of the disease in real-time during treatments such as photodynamic therapy (PDT) and photothermal therapy (PTT). Lanthanide doped nanoparticles (LnNPs) have emerged as a promising material for use in nanotheranostics due to their remarkable upconversion (UC) or downshifting (DS) photo luminescence (PL) capabilities. Despite the recent advances, many obstacles still need to be overcome in order to translate these nanotheranostic NPs from "bench" to "bedside".

In this thesis, we mainly focus on the development of theranostic nanocapsules through optimizing the synthesis and surface modification strategies of LnNPs for use in image-guided NIR-regulated PDT and PTT.

In Part I, we report a ***one-step thermolysis*** approach for the morphology-controlled synthesis of monodispersed, uniform β-$NaGdF_4$ upconversion nanoparticles (UCNPs) doped with Er^{3+} and Yb^{3+} ions. We found that the modulation of temperature during the hot-injection step was an effective approach to control the size and shape of β-$NaGdF_4$ nanocrystals formed, and we used it to achieve the direct synthesis of β-$NaGdF_4$ nanorods, which has not been previously reported in literature. Further investigation into the mechanism revealed that different temperatures resulted in different supersaturation concentration, which changes the nucleation and growth of α-phase NPs, subsequently affecting the Ostwald ripening mode during the α→ β phase transition.

Careful control of the morphology is important because it affects both UC PL intensity and negative contrast enhancement in magnetic resonance imaging (MRI). We found that the UC PL intensity upon 980 nm NIR irradiation decreases with increasing surface-to-volume ratio of the UCNPs and a higher ratio of green to red emission was observed when the aspect ratio was close to 1. The negative contrast enhancement on T_2–weighted MRI increases with increasing size with the exception of nanorods that has the best performance as T_2 contrast agents despite being smaller compared to the nanoplates.

In Part II, we co-encapsulated the above synthesized β-$NaGdF_4$ UCNPs and a PDT drug, Zinc phthalocyanine (ZnPc), into a single theranostic nanocapsule that carried both MRI and NIR-regulated PDT functionalities.

Surface modification is a critical step to convert hydrophobic UCNPs and therapeutic agents into a water dispersible formulation for *in vivo* applications. We established an original ***one-pot encapsulation*** approach, with straightforward steps in near neutral pH aqueous environment. Both UCNPs and ZnPc are first co-encapsulated in triblock copolymer (Ethylene oxide)$_{106}$(Propylene oxide)$_{70}$(Ethylene oxide)$_{106}$ (PEO-PPO-PEO) micelles. Thereafter, a silica shell is grown between the PPO and PEO interface to increase its chemical and mechanical stability. The resultant ***polymeric micelle/silica nanocapsules (NCs)*** have an average hydrodynamic size of 85 nm, low polydispersity index of 0.1 and excellent colloidal stability. In addition, the close distance between the two co-encapsulated payloads allows for efficient energy transfer. *In vitro*, it demonstrates good biocompatibility, T_2 contrast enhancement and eradication of BT474 breast cancer cells following NIR irradiation.

In Section 2 of the same part, we employed the same strategy to encapsulate chemotherapy drug doxorubicin (DOX), and conjugated nuclear targeted agents (TAT peptides) onto the NCs surface for active drug delivery into cancer cells. In addition, we prevented the aggregation of DOX molecules inside NCs with the addition of trimethoxy (2-phenylethyl) silane (TMPES). With this delivery system, DOX is more efficiently delivered and accumulated in the nucleus, as demonstrated by enhanced fluorescence imaging and improved DOX resistant cancer cell growth inhibition.

Finally in Part III, we extended the one-pot encapsulation strategy to develop a ***theranostic NC*** for NIR-regulated PTT. We co-encapsulated $LiLuF_4$:Nd^{3+} @$LiLuF_4$ downshifting NPs (DSNPs) and an optical heater, dicyclohexylamino substituted perylene diimide (sPDI) into the NCs. The Nd^{3+}-doped DSNPs, synthesized *via* a two-step multilayer thermolysis, serves as a ratiometric nanothermometer for contactless detection of temperature, so that the heating caused by sPDI could be monitored in real-time and controlled during therapy. Both materials can be excited at 793 nm, in the first BWs, while the nanothermometer emission (1060 nm) is located within the second BWs. Moreover, the $LiLuF_4$ host matrix functions as an effective probe for computer tomography (CT) imaging as demonstrated by CT imaging of MCF-7 breast cancer cells. This theranostic NCs also demonstrate high photothermal-stability and strong PTT effects against cancer cells.

Keywords: theronostic, nanocapsules, lanthanide-doped nanoparticles, thermolysis, near-infrared, upcoversion, nanothermometry, photodynamic therapy, photothermal therapy

SOMMAIRE RÉCAPITULATIF

Nanoparticules dopées au lanthanide conçues pour la théranostic du cancer

1. Introduction

Nanomédecine du cancer : le cancer est l'une des principales causes de décès et l'un des obstacles les plus importants à l'augmentation de l'espérance de vie dans tous les pays du monde. [1] Selon le rapport annuel de la Société canadienne du cancer publié en 2019 (Statistiques canadiennes sur le cancer 2019. Toronto, ON: Société canadienne du cancer; 2019), il est estimé qu'environ 1 Canadien sur 2 développera un cancer au cours de sa vie et qu'environ 1 Canadien sur 4 en mourra. La chirurgie, la chimiothérapie, la radiothérapie (ou la combinaison de ces 3 techniques) constituent l'approche thérapeutique conventionnellement employée. Cependant, dans de nombreux cas cette stratégie demeure inefficace en raison de métastase ou rechute du cancer voire d'effets secondaires notoires. De nouvelles stratégies comme la thérapie moléculaire ciblée, l'immunothérapie, la thérapie génique ou la photothérapie ont été développées en vue d'améliorer l'efficacité des traitements.

La nanomédecine est une science émergente clé du XXI^{ème} siècle. Elle s'appuie sur l'utilisation de nanovecteurs spécifiquement élaborés, et est utilisée à des fins diagnostiques et thérapeutiques. [2, 3] En oncologie, la nanomédecine a été fréquemment associée à l'utilisation de nanoparticules (NPs) puisque la perméabilité des tissus tumoraux et leur capacité de rétention sont adaptées aux particules de taille nanométrique. [4] C'est ce que l'on appelle l'administration passive ciblée. Afin de favoriser l'accumulation d'un principe actif dans les tumeurs, l'administration active ciblée a été développée. Il s'agit de greffer à la surface des NPs des ligands interagissant spécifiquement avec la cible à traiter. [5-9] Il existe déjà un certain nombre de nanomédicaments disponibles sur le marché ou en cours d'essais cliniques [10] et qui permettent une administration mieux contrôlée des principes actifs, [4] des thérapies de haute précision, [11] ainsi que de meilleures performances en imagerie. [12]

Le progrès des nanotechnologies s'accompagne également de développements significatifs en photothérapie: thérapie photodynamique (PDT) et thérapie photothermique (PTT), conçues pour éliminer sélectivement les cellules cancéreuses par dommages oxydatifs photo-induits (PDT) ou dommages thermiques (PTT).La *théranostique* (contraction de « thérapeutique » et « diagnostique »), nanodispositif multifonctionnel capable de diagnostiques locaux et de thérapies ciblées, a le potentiel d'améliorer davantage le traitement du cancer. [14-17]. Lorsque

le principe actif et l'agent de contraste sont combinés dans une seule formulation, il est généralement supposé que leur biodistribution dans l'organisme et au sein de la tumeur du sujet soient similaires. Par conséquent, la nanothéranostique devrait aider les médecins à prendre des décisions éclairées sur la stratégie thérapeutique à considérer, les dosages à utiliser et le moment propice à la prise d'un traitement. Cette médecine personnalisée peut conduire à une efficacité des soins améliorée, à des effets secondaires atténués et à une augmentation sensible de la qualité de vie des patients. [6,13] Par exemple, la nanothéranostique optique s'accommode de la précision d'un faisceau laser pour offrir un outil de détection et d'éradication non invasif de maladies telles le cancer. [18] Il est envisagé que la nanothéranostique en photoluminescente permettra à terme l'irradiation et l'élimination locale d'une tumeur maligne grâce à un contrôle à distance qui minimisera les dommages occasionnés aux tissus sains. Bien que la nanothéranostique réponde à un besoin médical clair réel, la faisabilité reste encore à être démontrée et de nombreux verrous doivent au préalable être levés si l'on souhaite porter ces NPs du laboratoire directement au chevet du patient.

Au sein du large éventail de nanomatériaux examinés à des fins théranostiques, les nanoparticules dopées aux lanthanides (LnNPs) ont considérablement attiré l'attention du fait de caractéristiques intrinsèques particulièrement intéressantes lorsqu'utilisées comme fluorophore d'imagerie, nanothermomètres ou médiateurs dans le contrôle de la libération de principe actifs par la lumière. Ici, Nous présenterons brièvement l'état de l'art des LnNPs: propriétés, synthèse, passivation et modification de la surface ainsi que les applications en bioimagerie, photothérapie et nanothermométrie.

Propriétés des LnNPs: Les lanthanides ont des configurations électroniques similaires, de la forme [Xe] $4f^n 5d^{0-1} 6s^2$. [28] En s'ionisant, les électrons sont retirés des orbitales 6*s* et 5*d* de sorte que tous les cations Ln^{3+} suivent la configuration [Xe] $4f^n$. Les ions lanthanides les plus courants et les plus stables ont donc le nombre d'oxydation +III (Ln^{3+}). Les états d'énergie ($^{2S+1}L_J$) de la sous-couche 4*f* sont régis par le couplage spin-orbite entre S et L, où S est le moment angulaire intrinsèque, L le moment angulaire orbital et J est moment angulaire total. Les électrons 4*f* sont des électrons de cœur, indifférents aux ligands, ne prenant part à aucune liaison et donc faiblement affectés par le champ cristallin. Ainsi, l'état fondamental d'un ion Ln^{3+} quelconque est pratiquement indépendant de son environnement. Par conséquent, les ions Ln^{3+} présentent des bandes *f–f* d'absorption ou d'émission très étroites et des durées de vie longues pour les états excités intermédiaires, 2 caractéristiques cruciales qui conduisent à une émission stable dans l'UV-visible bien que l'excitation se fasse dans le NIR.

À l'exception de La^{3+} et Lu^{3+} tous les ions Ln^{3+} ont des électrons *f* non-appariés et sont donc paramagnétiques. Le nombre maximal d'électrons non appariés est de 7, pour Gd^{3+}, avec un moment magnétique de 7,94μ_B tandis que les moments magnétiques les plus importants atteignent 10,4 et 10,7μ_B pour Dy^{3+} et Ho^{3+}. Cependant, tous les électrons ont un spin parallèle dans le cas de Gd^{3+}, il dispose donc d'un temps de relaxation électron-spin relativement long ($\sim 10^{-9}$s) par rapport à d'autres ions paramagnétiques tel que Dy^{3+} ($\sim 10^{-13}$s), ce qui favorise la relaxation du spin nucléaire.

Une propriété remarquable des LnNPs est leur capacité de conversion ascendante (UC, pour *upconversion*) ou descendante (DS, pour *downshifting*) de photon. L'UC est un processus qui permet la conversion d'un rayonnement proche infrarouge incident en un rayonnement de plus autre énergie (UV, visible ou NIR) via un processus multiphotonique ($\lambda_{ex} > \lambda_{em}$). La DS quand a elle convertit un photon du proche infrarouge en un photon décalé davantage vers le rouge ($\lambda_{ex} < \lambda_{em}$). Le concept général de l'UC a été formulé indépendamment pour la première fois par Auzel, Ovsyankin et Feofilov au milieu des années 1960. [30, 31] Il s'agit d'un processus non linéaire caractérisé par l'absorption successive de deux ou plusieurs photons d'excitation par des niveaux d'énergie, successifs eux aussi, de longue durée de vie. Le dernier état atteint se relaxe via l'émission d'un photon de longueur plus courte que la longueur d'onde initiale d'excitation. Le mécanisme de la UC rencontrée avec les LnNPs est principalement divisé en 4 étapes: l'absorption à l'état excité (ESA, Figure 1.2), le transfert d'énergie par UC (ETU, Figure 1.3), la relaxation croisée (CR, Figure 1.4), et l'avalanche photonique (PA, Figure 1.5). [33, 35-37]

Les LnNPs sont généralement des systèmes hôtes-invités dilués, où les ions Ln^{3+} dopant sont dispersés dans un réseau diélectrique hôte adéquate. [37] Dans le cas de la photoluminescence par sensibilisateurs, l'ion dopant émet après avoir été excité par transfert d'énergie non radiatif en provenance d'un autre ion dopant. L'ion qui émet le rayonnement est appelé activateur, tandis que le donneur d'énergie est appelé le sensibilisateur. Bien que l'UC puisse en principe se manifester dans la plupart des réseaux cristallins dopés au Ln, une UC efficace ne se produit que dans le cas de couples hôte-dopant bien choisis. Les propriétés d'émission (c'est-à-dire la couleur et l'intensité) des LnNPs sont étroitement liées à la quantité et au type de dopants employé, à la morphologie et à la structure cristalline du réseau hôte, et cela est particulièrement important pour l'obtention d'une théranostique de haute performance. Pour toutes ces raisons, un cahier des charges précis a été mis en œuvre dans le développement de LnNPs: [33] i) sélection de matériaux hôtes; ii) ajustement du champ cristallin local; iii) rationalisation des phénomènes de

transfert d'énergie; iv) suppression des désactivations par la surface grâce au choix de l'architecture cœur-coquille.

Les réseaux hôtes doivent généralement avoir des caractéristiques géométriques favorables aux ions dopants ainsi que de faibles énergies de phonons pour obtenir une photoluminescence (PL) intense. Parmi les hôtes étudiés, les matrices fluorées ont une énergie de coupure pour les phonons plus faible (i.e. ~350 cm^{-1} pour l'hôte $NaYF_4$) ainsi qu'une stabilité chimique élevée. En outre, la composition et le type de phase cristalline des LnNPs hôtes régissent l'intensité du champ cristallin et la (dis)symétrie d'environnement perçue par les dopants. Une faible symétrie améliore le couplage électronique entre les niveaux d'énergie 4*f* et des niveaux supérieurs, augmentant dès lors la probabilité de transition *f–f* au sein des ions dopants. [39] Le choix de réseaux hôtes à faible champ cristallin est une voie prometteuse pour l'amélioration de l'UC des LnNPs. Par exemple, le réseau hexagonal des microcristaux de $NaYF_4$ dopés à Yb^{3+} et Er^{3+} présentent une luminescence visible par UC, 4,4 fois plus élevée que son équivalent formant un réseau cubique, [40]. Les NPs de $LiYF_4$ de structure tétragonale dopées à Yb^{3+} et Tm^{3+} émettent plus fortement dans l'UV et le bleu en raison du champ cristallin plus intense. [41] Cependant, il est impossible de modifier davantage l'environnement local autour des ions Ln^{3+} une fois que le réseau hôte fixé. Une autre voie prometteuse pour améliorer l'UC est *d'adapter l'environnement local autour des* Ln^{3+} par dopage avec des cations non émissifs. Ces cations non luminescents peuvent remplacer les cations déjà présents dans les nœuds du réseau ou occuper des sites interstitiels autour de ceux-ci, réduisant ainsi la symétrie locale autour des dopants Ln^{3+} et favorisant l'efficacité de l'UC. [42]

Le choix de la paire sensibilisateur/activateur est la clé régissant le transfert d'énergie entre les dopants. Concernant le processus d'ETU, le sensibilisateur doit posséder un coefficient d'extinction molaire élevée à la longueur d'onde d'excitation et des niveaux d'énergie coïncidant avec ceux de l'activateur. Un exemple classique d'émission procédant de l'UC dans les LnNPs est donné par le couple Yb^{3+}/Er^{3+} (sensibilisateur/activateur). L'ion Yb^{3+} possède une structure de niveaux d'énergie extrêmement simple avec un seul niveau 4*f* excité: $^2F_{5/2}$. La bande d'absorption $^2F_{5/2}$ de Yb^{3+} est située aux alentours de 980 nm et dispose d'un plus grand coefficient d'extinction molaire. De plus, les transitions $^2F_{7/2} \rightarrow {}^2F_{5/2}$ de Yb^{3+} et *f–f* de Er^{3+} sont résonantes: $^4I_{15/2} \rightarrow {}^4I_{11/2}$ (premier transition) et $^4I_{11/2} \rightarrow {}^4F_{7/2}$ (deuxième transition) ont des écarts énergétiques similaires (figure 1.6). [32] Sous irradiation à 980 nm, Yb^{3+} est excité le premier (depuis $^2F_{7/2}$ vers $^2F_{5/2}$) et puisque la transition $^4I_{15/2} \rightarrow {}^4I_{11/2}$ de Er^{3+} est en résonance avec la transition $^2F_{5/2} \rightarrow {}^2F_{7/2}$ de Yb^{3+} alors il en résulte un processus de transfert d'énergie efficace et l'ion Yb^{3+} retourne finalement à

son état fondamental ($^2F_{7/2}$).En raison de la coïncidence des niveaux d'énergie, Er^{3+} peut atteindre des états excités plus énergétiques encore ($^2F_{7/2}$, $^4F_{9/2}$) par simple réitération du transfert d'énergie résonant, depuis Yb^{3+} vers Er^{3+}, que l'on vient de décrire. Après relaxation multiphonon vers les états $^2H_{11/2}$ et $^4S_{3/2}$, des émissions vertes à 525 et 545 nm sont observées et attribuées respectivement au passage de ces états excités $^2H_{11/2}$ et $^4S_{3/2}$ vers l'état fondamental $^4I_{15/2}$. Par ailleurs, l'émission rouge à 655 nm provient de l'état excité $^4F_{9/2}$, dont le peuplement provient lui-même soit de la relaxation non radiative depuis l'état $^4S_{3/2}$ soit directement de Er^3 puisque l'état $^4F_{9/2}$ peut se peupler à partir de l'état $^2H_{13/2}$ via le transfert d'énergie permis depuis le niveau $^2F_{5/2}$ de Yb^{3+}.

La teneur en dopant peut affecter l'intensité de PL des LnNPs par extinction induite par une trop grande concentration. La relaxation non radiative survenue dans le processus de CR dépend de la distance ion-ion, qui est régie par la concentration de dopant dans les LnNPs. Quant au processus de CR dans les couples sensibilisateur/activateur de Yb^{3+}/Tm^{3+}, Yb^{3+}/Er^{3+} et Yb^{3+}/Ho^{3+}, la concentration optimale de l'activateur (Tm^{3+}, Er^{3+} ou Ho^{3+}) donnant une efficacité élevée au processus d'UC est évaluée comme étant généralement inférieur à 2%. [30] En ce qui concerne les LnNPs dopées au Nd^{+3}, le processus non radiatif de relaxation croisée $^4F_{3/2} + {}^4I_{9/2} \rightarrow 2{}^4I_{15/2}$ dépeuple le niveau excité $^4F_{3/2}$, défavorisant ainsi l'émission par DS par le phénomène d'extinction de PL induit par la concentration. Le rendement quantique le plus élevé jamais observé est d'environ 22% pour des LnNPs de $NaGdF_4$ dopées à 3% de Nd^{3+}. [34]

Les désactivations par la surface sont un autre facteur important limitant la PL des LnNPs. Celles-ci sont généralement causées par des défauts de surface, des contraintes dans le réseau, ou des ligands et solvants qui possèdent une énergie de phonons élevée. Ces processus se manifestent fortement dans les NPs en raison de leur rapport surface/volume élevé à l'échelle nanométrique. Les désactivations par la surface procèdent de 2 façons: i) les dopants photoexcités situés à la surface, ou à proximité, peuvent être désactivés directement par des sites d'extinction avoisinants; ii) l'énergie d'excitation des ions intérieurs peut aussi être transférée à la surface par l'intermédiaire d'ions dopants adjacents puis finalement dissipée par voie non radiative. La deuxième voie est la plus fréquente pour les UCNPs étant donné qu'une forte quantité de sensibilisateur Yb^{3+} (plus de 18%) est souvent introduite dans nanophosphores dopés au Yb^{3+}/Tm^{3+}, Yb^{3+}/Er^{3+} et Yb^{3+}/Ho^{3+} (afin d'atteindre une intensité de PL par UC élevée). [31] Le transport d'énergie à longue distance dans un sous-réseau de Yb^{3+} est favorisé par la structure unique à deux niveaux d'énergie de Yb^{3+} et la longue durée de vie de ses états excités. [54] Dès lors, la suppression de désactivation par la surface dans les LnNPs est particulièrement

importante pour atteindre des PL intenses par UC. Le moyen le plus efficace d'y parvenir est la conception d'une structure cœur/coquille dans laquelle le matériau hôte de l'enveloppe doit présenter une forte compatibilité de structure du réseau avec celui du noyau. Nous en discuterons en détails dans la section suivante.

Synthèse des LnNPs: Le contrôle de la morphologie des LnNPs est essentiel pour la bioimagerie et les applications thérapeutiques. En plus d'influencer sur les propriétés de PL des LnNPs [21], la taille, la forme, la structure cristalline (phase), la dispersité et l'uniformité peuvent régir des comportements clé tels que l'absorption puis le rejet cellulaire. [3, 19, 20] L'optimisation de la voie synthèse est essentielle pour obtenir des LnNPs avec une morphologie, une composition chimique et des propriétés optiques adéquates.

La décomposition thermique (thermolyse) est une stratégie de synthèse courante des LnNPs de haute qualité, uniformes et monodisperses. La thermolyse implique ici des composés organométalliques jouant le rôle de précurseurs qui se décomposent à haute température, en présence d'un tensioactif, dans un solvant à haut point d'ébullition. Les précurseurs couramment utilisés sont des sels de trifluoacétate métalliques; le solvant peut être le 1-octadécène (ODE); les tensioactifs peuvent être l'acide oléique (OA), l'oléylamine (OM) et/ou l'oxyde de trioctylphosphine (TOPO) qui disposent tous un groupe fonctionnel pouvant coordonner l'élément métallique d'intérêt et une longue chaîne hydrocarbonée empêchant l'agrégation des nanoparticules formées. La décomposition thermique a été développée pour la première fois en 2005 pour la synthèse de monocristaux monodisperses de LaF_3. [50] Cette approche s'est ensuite répandue comme une voie de synthèse commune pour l'obtention de nanocristaux de $NaYF_4$ de haute qualité en 2006. [51-53] F.Vetrone *et al.* ont davantage affiné cette stratégie en proposant une approche dite « *par injection à chaud* ». [52] Comme montré à la figure 1.7, le précurseur de trifluoroacétate, préalablement chauffé, est lentement injectés dans une solution chaude de tensioactif. Ils synthétisent ainsi avec succès des NPs hautement cristallines avec une distribution de taille remarquablement étroite et sans procédure de fractionnement par taille. Dans ce procédé, l'ajout lent des précurseurs à la solution est suivi du changement de la température du milieu et conduit à une séparation temporelle nette des phases de nucléation et de croissance cristalline. [52, 53] Ainsi, la haute sursaturation induite par l'injection à chaud permet une nucléation homogène et rapide, suivie d'une croissance cristalline contrôlée par diffusion. En choisissant soigneusement les paramètres expérimentaux, tels que la nature des solvants, la concentration de précurseurs, la température et la durée de la réaction, ainsi que la vitesse d'injection, la synthèse de NPs de morphologie contrôlée peut être réalisée. Dans cette thèse (*chapitre 4*), nous

avons modifié cette approche pour la synthèse contrôlée d'UCNPs de $NaGdF_4$ de diverses morphologies.

Ingénierie cœur/coquille : les protocoles de thermolyse peuvent être adaptés pour créer des nanostructures cœur/coquille, faire croître différentes coquilles fonctionnalisées sur des LnNPs préformant un cœur. Cette stratégie est utilisée pour manipuler la dynamique des transferts d'énergie dans les LnNPs, permettant ainsi d'augmenter l'intensité de l'émission, de faire varier sa couleur, de réduire les désactivations par la surface et d'introduire de nouvelles voies d'excitation ou d'émission. Dans de telles structures, les coquilles des LnNPs (ainsi que les cœurs dans certains cas) sont généralement classées comme actives ou inertes, indiquant respectivement si la coquille est dopée avec un ion Ln^{3+} optiquement actif et participe aux échanges d'énergie ou non. Une excellente démonstration a été faite par F. Vetrone *et al.* qui ont développé une stratégie synthétique pour obtenir une UCNPs composée d'un cœur actif de $NaGdF_4$:Yb^{3+}, Er^{3+} et d'une coquille active $NaGdF_4$:Yb^{3+} dans laquelle une concentration raisonnable de dopants Ln^{3+} (le sensibilisateur) est introduite. Cette architecture permet l'augmentation significative de l'intensité d'UC depuis le proche infrarouge vers le visible par rapport à leurs analogues à noyau actif/enveloppe inerte ou à noyau seul. Cela s'explique par: i) la séparation des activateurs Er^{3+} et des sources d'extinction externes, ii) la récolte rendue possible de davantage de photons du NIR. Cette étude montre également que l'énergie acquise par excitation peut être partagée entre les différentes couches de l'UCNP. [55] En modifiant cette approche, notre groupe a récemment développé une stratégie d'obtention en deux étapes des petites, mais très luminescentes, LnNPs cœur/coquilles à base de lithium. [56] Les cœurs sont initialement synthétisés par thermolyse puis stabilisés par un excès d'OA et d'ODE. Dans un second temps, les coquilles des LnNPs sont formées suivant la stratégie d'injection à chaud.

Modification de la surface des LnNPs: Les applications biomédicales en nanomédecine du cancer requièrent que les nanovecteurs possèdent les caractéristiques suivantes: i) être solubles ou dispersables dans l'eau, et biocompatibles; ii) pouvoir échapper au système réticulo-endothélial (demi-vie plus longue dans l'organisme) ; iii) améliorer le taux d'accumulation des agents à administrer au sein du tissu tumoral, par rapport aux tissus sains, par ciblage passif et/ou administration active ciblée. [13] À cette fin, les LnNPs devraient posséder des groupes fonctionnels de surface hydrophiles. Les LnNPs produites par thermolyse sont hydrophobes car elles sont fonctionnalisées par des ligands hydrophobes comme l'OA, l'OM, la trioctylphopshine (TOP) ou le TOPO. Ainsi, elles ne sont pas dispersables en solution aqueuse ou dans un tampon biologique et doivent donc être modifiés à la surface avant de pouvoir être employées dans des

applications biologiques. [32, 52] À ce jour, diverses stratégies de modification de surface telles que *l'échange de ligands, l'oxydation de ligands, l'élimination de ligands, l'encapsulation par des polymères amphiphiles, l'enrobage par la silice* ont été proposées pour adapter les LnNPs aux applications biomédicales. Chacune d'entre elles dispose de ses propres avantages et inconvénients. Par exemple, l'enrobage par silice, en particulier par la silice mésoporeuse ou des composites, a largement été employé dans la fabrication de nanodispositifs multifonctionnels car elle est très stable, biocompatible et optiquement transparente. De plus, les mésopores présents la coquille de silice offre un volume de stockage conséquent pour y placer des molécules d'intérêt ou des principes actifs. [61] Cependant, l'enrobage de nanoparticule par de la silice mésoporeuse implique typiquement un procédé multi-étape. Tout d'abord le revêtement de silice lui-même est formé autour des LnNPs. Dans un second temps, les pores sont formés dans la silice par élimination des micelles de tensioactif précédemment impliquées, soit par décomposition thermique soit par extraction par un solvant. Enfin, le stockage de molécules d'intérêt au sein des pores peut être envisagé. [62, 63] Le bromure de cétyltriméthylammonium (CTAB), le tensioactif couramment utilisé pour générer les mésopores, est hautement toxique. Par conséquent, toute élimination incomplète du CTAB peut contrevenir à l'utilisation des LnNPs en biomédecine. [64] La fuite de charges utiles (i.e. molécules d'intérêt stockées dans la silice mésoporeuse) lors du parcours du système sanguin est inévitable sans l'obstruction des pores. Dans de tels cas, l'accumulation de charge(s) utile(s) dans d'autres régions du corps ou en périphérie de la zone à traiter peut présenter une toxicité potentielle. À ce jour, l'un des grands défis précédent l'application des nanoparticules enrobées de silice est de réussir à réaliser une synthèse « tout-en-un » où les charges utiles se stockeraient dans des nanovecteurs au cours même de leur formation. [66] Pour résoudre les problèmes susmentionnés, un système hybride silice-polymère est proposé dans cette thèse. Nous avons développé une stratégie de synthèse inédite, en une étape, pour co-encapsuler des LnNPs hydrophobes et diverses molécules fonctionnelles grâce à l'approche par croissance promue par l'interface. Les détails sont discutés au *Chapitre 5*.

Applications en nanomédecine du cancer: les LnNPs possèdent certains avantages par rapport aux matériaux fluorescents conventionnels tels que les fluorophores organiques et les points quantiques de semi-conducteurs (QDs). [67-71] Typiquement: i) une autofluorescence nulle, offrant un meilleur rapport signal/bruit (SNR); ii) de grands déplacements anti-Stokes et Stokes, offrant une séparation commode entre les longueurs d'onde de PL et celles d'excitations; iii) des bandes d'émission étroites, facilitant l'imagerie multiplexée; iv) une photostabilité élevée, idéale pour supporter l'imagerie à répétition ou à long terme. Plus important encore, la pénétration dans tissus profonds est permise uniquement dans le cas d'excitation et/ou d'émission prenant

place dans la fenêtre biologique du proche infrarouge, car c'est dans cette région que le sang et les tissus sont les plus transparents aux rayonnements (Figure. 1.8). [43] Cette zone limite par ailleurs la phototoxicité vis-à-vis des tissus biologiques. [31, 67-73] Une LnNP possède plusieurs émissions d'UC: par exemple, lorsque dopée au Tm^{3+}, des rayonnements dans l'UV, le bleu, le rouge et le NIR observées. Cela permet le développement d'un nanodispositif multifonctionnel où le rayonnement UV/bleu est exploité pour activer une autre fonctionnalité, telle qu'un principe actif de PDT (UC-PDT), tandis que le rayonnement NIR peut être exploité *in situ* pour l'imagerie optique de la tumeur. De plus, l'incorporation de certains ions Ln^{3+}, comme Gd^{3+} ou Lu^{3+}, dans le réseau hôte, procure des propriétés supplémentaires: les LnNPs deviennent des agents de contraste en imagerie par résonance magnétique (IRM) et/ou en tomodensitométrie (CT). [74, 75] La possession de multiples propriétés rendent les LnNPs très attrayantes pour une utilisation dans une large gamme d'applications biomédicales, telles que la bioimagerie, la photothérapie, la nanothermométrie ainsi que la nanothéranostique. [76-87]

Imagerie : En 1999, les UCNPs ($Y_2O_2S:Er^{3+}$, Yb^{3+} et $Y_2O_2S:Tm^{3+}$, Yb^{3+}) ont été exploités pour la première fois dans des applications biomédicales. [90] Cette étude a montré que les UCNPs ont à la fois une sensibilité et une stabilité de fluorescence considérables pour la détection d'antigènes dans les membranes cellulaires et les tissus. Les UCNPs utilisés, de taille inférieure au micron (0,2 – 0,4 µm), ont été fonctionnalisés en surface par des anticorps capables de se lier spécifiquement à des antigènes présents sur des cellules et des tissus, selon une approche similaire à celle de l'immunohistochimie (IHC). Depuis lors, de substantielles contributions ont été apportées à la bioimagerie par le biais des UCNPs, que ce soit *in vitro* ou *in vivo*. [91-94] Par exemple, l'imagerie intracellulaire de cellules cancéreuses HeLa vivantes a été rendue possible pour la première fois par l'utilisation d'UCNPs de $NaYF_4:Yb^{3+}$, Er^{3+}. [93] L'imagerie intracellulaire montre clairement la redistribution des UCNPs au sein de la cellule au cours de l'incubation, démontrant ainsi un certain potentiel pour vis-à-vis de l'imagerie en temps réel et de l'étude de la dynamique cellulaire.

Avec l'objectif de pénétrer profondément dans les tissus tout en présentant une phototoxicité minimale, de nombreux efforts ont été portés sur l'ajustement de la longueur d'onde d'excitation, mais aussi d'émission, des LnNPs dans les fenêtres biologiques. [81-85]. Depuis que le processus du transfert d'énergie ($Nd^{3+} \rightarrow Yb^{3+} \rightarrow Er^{3+}/Tm^{3+}$), au sein duquel Nd^{3+} joue le rôle de sensibilisateur 800 nm et Yb^{3+} celui d'intermédiaire dans le transfert, a été reporté, [95] les UCNPs dopés au Nd^{3+} disposant d'une nanostructure optimisée ont été utilisés *in vitro* et *in vivo.* Elles ont montré une profondeur de pénétration plus élevée et une élévation de température locale

beaucoup plus faible en comparaison aux UCNPs sensibilisées à Yb^{3+} et donc excitées à 980 nm. [48, 96, 97] Cependant, elles présentent l'inconvénient mineur que l'émission se situe principalement dans la région visible du spectre. Pour dépasser cette limitation, une stratégie très prometteuse a été développée: favoriser l'émission DS des LnNPs. Les LnNPs fonctionnant du NIR vers le NIR par DS sont clairement préférables à celles procédant par UC. [98]

Outre l'imagerie utilisant les phénomènes d'UC ou de DS, les LnNPs peuvent également être utilisées comme agent de contraste en l'IRM (typiquement, Gd^{3+}) et en CT (typiquement, Lu^{3+}) et fournir ainsi une solution d'imagerie multimodale. Par exemple, les NPs à base de Gd^{3+} sont généralement utilisées comme agents de contraste T_1 pour augmenter la densité de signal en IRM pondérée en T_1 (images lumineuses). [99] Des études antérieures ont rapporté que les LnNPs à base de Gd^{3+} permettaient obtenir un contraste positif élevé dans les images pondérées en T_1 uniquement lorsque la taille des nanoparticules était inférieure à 10 nm, [100, 101] car ce sont les ions Gd^{3+} à la surface des LnNPs qui contribuent le plus à la relaxivité T_1. [101-103] Ainsi des LnNPs ont été conçues, disposant d'une fine coquille de $NaGdF_4$ déposée sur un cœur de $NaYF_4$:Er^{3+}, Yb^{3+} (exempt de Gd^{3+}), spécifiquement pour utilisation bimodal en IRM pondéré en T_1 et l'imagerie de fluorescence par UC (relaxivité T_1 (r_1) = 6,18 $mM^{-1}s^{-1}$). [104] Les NPs cœur-coquille de $NaLuF_4$:Yb^{3+}, Tm^{3+} (cœur) et SiO_2 (coquille), fonctionnalisées par le ligand Gd-DTPA, ont été conçues pour utilisation trimodale en imagerie de fluorescence NIR-NIR par UC, IRM et CT. [105] En plus de la possibilité de raccourcir le temps de relaxation T_1, les LnNPs de Gd_2O_2S:Eu^{3+} font preuve d'une forte relaxivité transversale (r_2) et d'une forte absorption des rayons X, ce qui permet leur utilisation comme agent de contraste pour IRM pondérée en T_2 et CT. [106] En effet, la relaxivité T_2 (r_2) des LnNPs paramagnétiques augmente avec le champ magnétique alors que le r_2 des agents de contraste T_2 conventionnels (particules à base d'oxyde de fer) plafonne à des intensités de champ magnétique > 1 T. [107] Dans cette thèse, nous avons également étudié au C*hapitre 4* les valeurs de relaxivité T_1 et T_2 prises par des UCNPs de β-$NaGdF_4$ de diverses morphologies, sous des haut champs magnétiques (3T, 7T et 9.4T), ainsi que la propriété d'atténuation des rayon X et capacité de contraste en CT des DSNPs de $LiLuF_4$ au *chapitre 6*.

Photothérapie: La photothérapie permet l'utilisation de lumière, stimulus non invasif et contrôlable dans l'espace et le temps, pour obtenir des résultats spécifiques et réduire les effets secondaires. La possibilité de contrôler des paramètres tels que la longueur d'onde, l'intensité et la durée d'exposition, offre un degré de contrôle supplémentaire. À cette fin, les photothérapies telles que la PDT, la PTT, l'administration photo-contrôlée de principes actifs et les thérapies

combinées, synergisant deux ou plusieurs des techniques précédentes, ont été mises en avant. En plus des avantages énumérés ci-dessus, la PDT est capable de surmonter la résistance aux médicaments multiples causée par la chimiothérapie, ainsi que de déclencher une réponse immunitaire antitumorale par activation du système immunitaire inné et/ou adaptatif, réduisant ainsi le taux de mortalité des patients. [46, 47] La PTT est également capable d'améliorer la susceptibilité des cellules cancéreuses à d'autres traitements, [48] comme la chimiothérapie, [49] la radiothérapie [50] et l'immunothérapie. [51-55]

La PDT a été largement prescrite pour le traitement du cancer, incluant les cancers de la peau, de la prostate, de la tête et du cou, du pancréas, du sein et du poumon. [109-112] Elle utilise des photosensibilisateurs (PS) en guise de médicaments photoactivables par irradiation à longueur d'onde appropriée pour traiter localement des tissus cibles. Les PS photoexcités interagissent avec les molécules d'oxygène environnantes pour générer espèces réactives de l'oxygène (ROS), incluant l'oxygène singulet ($^1O_2$), qui occasionne des dommages oxydatifs aux substrats biologiques et aboutit *in fine* à la mort des cellules, comme présenté à la figure 1.9 [113] Toutefois, les longueurs d'onde typiques d'excitation des photosensibilisateurs se situent dans le visible et pénètrent peu en profondeur dans les tissus. Pour cette raison, la PDT est généralement utilisée pour traiter des tumeurs extérieures ou situées juste sous la peau, sur des muqueuses d'organes internes ou des cavités, d'où une limitation des cas pouvant être traités par cette technique. [116] Afin d'atteindre des tumeurs profondes, le rayonnement NIR situé dans les fenêtres biologique pourrait être mis à profit. [33, 43] Cependant, les photosensibilisateurs les plus performants ne sont pas directement excitables par du rayonnement NIR. Pour surmonter cet obstacle majeur, la combinaison synergique d'entités à propriétés d'UC et de photosensibilisateurs de PDT a été proposée et étudiée ces dernières années. [62, 80, 117-121]

Jusqu'à présent, de nombreuses études ont réussi à combiner des UCNPs et des photosensibilisateurs, utilisant pour la plupart $NaYF_4:Er^{3+}$, Yb^{3+} ou $NaYF_4:Tm^{3+}$, Yb^{3+} comme matériau présentant des propriétés d'UC et utilisant différentes modifications de surface pour créer un système UC-PDT avec un ou plusieurs photosensibilisateurs, tels que la phtalocyanine de zinc (ZnPc), la mérocyanine 540 (MC 540), la chlorine e6 (Ce6), pour lesquelles les bandes d'absorptions coïncident avec les différentes émissions d'UC des UCNPs. [121] Les premiers travaux combinant $NaYF_4:Er^{3+}$, Yb^{3+} UCNPs et MC540 a démontré la viabilité du concept de l'UC-PDT sur des cellules de cancer du sein. [117] Les progrès rapides de l'UC-PDT ainsi que les résultats prometteurs *in vitro* ont motivé d'avantage d'études, *in vivo* cette fois, utilisant ces UCNPs. [118] Des nanodispositifs multifonctionnels remplissant des missions théranostiques ont

également vu le jour. Par exemple, un nanodispositif composé d'une UCNP enrobée de silice mésoporeuse convertit le rayonnement NIR en visible (absorption puis émission), le rayonnement visible étant ensuite absorbé par le MC540 et le ZnPc. Des études *in* vivo ultérieures montrent une inhibition significative de la croissance tumorale chez des souris ayant reçues par injection intraveineuse le nanodispositif susmentionné (figure 2.0). [80] Bien que les UCNPs enrobées de silice mésoporeuses soient considérées comme l'approche courante de l'UC-PDT, [80, 120, 122, 123] certaines difficultés doivent encore être résolues (voir le paragraphe intitulé M*odification de surface de LnNPs*). Dans le système UC-PDT, le $^1O_2$ cytotoxique est généré par le photosensibilisateur, activé *via* un transfert d'énergie depuis les UCNPs elles-mêmes excitées par rayonnement NIR. Le transfert d'énergie peut être radiatif [82, 117, 120, 124, 125] ou non radiatif [118, 126-129] et son efficacité affectée par la distance entre l'UCNP donneur et le photosensibilisateur accepteur. Ici, nous traitons de NCs co-encapsulant à la fois des UCNPs hydrophobes de $NaGdF_4:Er^{3+}$ (2 mol%), Yb^{3+} (20 mol%) et de la ZnPc, ce qui a l'avantage de minimiser la distance entre ces deux charges utiles en comparaison d'une incorporation conventionnelle au sein d'une coquille de silice mésoporeuse (C*hapitre 5*).

La PTT est une stratégie thérapeutique reposant sur un dégagement thermique résultant de l'absorption des photons d'un rayon laser: l'élévation de la température produit des dommages thermiques aux substrats biologiques (i.e. dénaturation des protéines, altération de l'ARN/ADN) aboutissant à leur mort des cellules (Figure 2.1). [131-135] La thermothérapie est basée sur l'augmentation de la température de la tumeur, par action externe, jusqu'à des niveaux cytotoxiques (43-45°C). Pour s'assurer que la température souhaitée est atteinte, mais pas dépassée, la température de la zone traitée doit être surveillée au cours du traitement. [135, 170, 171] Ainsi, il est crucial que l'apport de chaleur à la cible se fasse de manière contrôlée et efficiente en terme de conversion photothermique des agents PTT. La précision de la PTT requiert une accumulation adéquate d'agents de PTT dans la zone d'intérêt, un guidage par imagerie et une lecture *in situ* de la température locale. [168, 169] Cependant, les équipements et les solutions actuellement disponibles pour effectuer ce type de PTT de précision présentent encore quelques limitations et nécessitent des davantage d'améliorations.

Le progrès de la nanotechnologie et ses applications potentielles en PTT améliorent sensiblement l'efficacité et la sélectivité des traitements. Par ailleurs, les nanodispositifs hybrides concentrent au sein d'un même objet des fonctions multiples permettant notamment les thérapies combinées (PTT avec chimiothérapie ou radiothérapie ou immunothérapie), l'imagerie et la lecture de température en temps réel. Cela réduit la complexité du traitement tout en offrant une meilleure

efficacité thérapeutique. Plus récemment, des nanodispositifs hybrides ont été proposées, ajoutant une fonctionnalité thermométrique aux agents de PTT. [172-175] Bien que ces approches fournissent des preuves de concept intéressantes, dans la plupart des études la détermination de la température procède de la PL visible plutôt que de l'émission dans le NIR. De plus, la taille des nanoobjets en question excédant les 200 nm, ils ne peuvent être utilisés dans des applications *in vivo*. Nous rapportons dans cette thèse une NC théranostique fonctionnant entièrement dans le proche infrarouge et dédiée à la fois à la PPT assistée par imagerie et à la détermination *in situ* de la temperature locale. Les détails sont discutés au *Chapitre 6.*

Nanothermométrie : La nanothermométrie par PL s'appuie sur la relation liant la température et les propriétés de PL pour proposer une mesure de la temperature à partir l'analyse spatiale et spectrale du rayonnement généré par l'objet à imager. Les nanothermomètres ratiométriques, dont le spectre de PL consiste en de multiples raies ou bandes dont les intensités relatives dépendent fortement de la température, représentent une solution simple pour la mesure exacte de température de la température. [184] Ceux disposant d'un unique centre doivent disposer de nombreux états d'énergie, y compris de paires d'états couplés vibrationnellement et dont les populations suivent une distribution de Boltzmann. [185] La dépendance du rapport des intensités de PL en température (LIR) entre de tels niveaux d'énergie est déterminée par l'équation ci-dessous. [186]

$$LIR = A \times exp\left(-\frac{\Delta E}{k_B T}\right)$$

Où *A* est une constante, *E* est l'écart énergétique entre les deux états excités, k_b est la constante de Boltzmann et T est la température absolue (en kelvin). À partir du rapport d'intensité mesuré expérimentalement, une détermination de température peut être faite. Dans ce cas-ci, la dépendance en température est très reproductible car la plupart des paramètres affectant la PL des états thermalisés n'affectent pas la distribution des populations entre ceux-ci. Une sensibilité thermique appréciable n'est atteinte que si la séparation d'énergie entre les états émissifs est faible, de sorte que de petits changements de température puissent induire des redistributions importantes de la population électronique. Les nanothermomètres basés sur la PL ont leur performance caractérisée par leur sensibilité thermique relative, leur incertitude thermique et la répétabilité de leur mesure.

Les nanothermomètres à base de Ln^{3+}, comme Er^{3+}, Tm^{3+}, Ho^{3+} ou Nd^{3+}, et leurs applications biomédicales ont été étudiées au cours des dernières années.[82, 184, 187-189] En ce qui concerne la nanothermométrie ratiométrique par un centre émissif unique, l'ion Er^{3+} est probablement le plus largement utilisé. En effet, il émet intensément dans le vert, grâce à deux bandes de PL à 520 et 540 nm dont les intensités relatives varient fortement avec la température. [186, 187, 190-194] Ces deux bandes peuvent être facilement peuplées par UC à l'aide d'ions sensibilisateurs tels que Yb^{3+}. [195] La figure 2.2 (A) montre les mécanismes de la mesure optique de la température par transfert d'énergie entre Er^{3+}/Yb^{3+} sous une excitation dans le NIR, à 980 nm. [196] La nanothermométrie basée sur ces phénomènes a été utilisée dans des applications biomédicales. [187, 197-199] La première nanothermométrie intracellulaire utilisant des UCNPs a été réalisée par F. Vetrone en 2010. [187] Dans ce travail pionnier, les propriétés nanothermométriques de $NaYF_4$:Er^{3+}, Yb^{3+} ont été caractérisées puis mises à profit dans la surveillance de l'apoptose de cellules de cancer HeLa causée par une source de chaleur externe. L'objectif de microscope utilisé pour focaliser le faisceau d'un laser de longueur d'onde 920 nm (excitation) a aussi permis de récolter les photons émis par les UCNPs. L'analyse spectrale qui s'en suit a permis de déterminer de manière non invasive la température au cœur de la cellule (figure 2.3). En prévision d'essais *in vivo*, beaucoup d'efforts ont été menés pour porter les longueurs d'onde d'excitation et d'émission des nanothermomètres dans une fenêtre biologique. Au cours des dernières années, les DSNPs dopés au Nd^{3+} ont acquis une reconnaissance croissante en tant que nanothermomètres ratiométriques fonctionnant entièrement dans le NIR, en raison de la dépendance en température de la population des sous-niveaux Stark couplés vibrationnellement au sein l'état excité $^4F_{3/2}$ de Nd^{3+}. [202-205] Les bandes d'émission caractéristiques de Nd^{3+} (aux alentours de 880, 1060 et 1340 nm) se situent toutes dans une fenêtre biologique Par ailleurs, les bandes d'émission de Nd^{3+} situées dans la seconde fenêtre biologique sont significativement moins affectées par les tissus (autofluorescence, absorption et diffusion par ceux-ci), permettant ainsi une profondeur d'imagerie accrue et le maintien d'une résolution spatiale élevée. [82, 206-209] Le passage de la nanothermométrie basée sur l'UC à la nanothermométrie basée sur le NIR est donc fortement souhaitable pour les applications *in vivo*.

2. Objectifs et plan

Dans cette thèse nous nous proposons le développement d'un outil inédit à visée théranostique: des NCs co-encapsulant à la fois des LnNPs et des agents thérapeutiques moléculaires compatibles avec et la photothérapie par rayonnement NIR. Ici, les LnNPs peuvent être des UCNPs ou des DSNPs multifonctionnelles, et les agents thérapeutiques peuvent être des

principes actifs de PDT, des PTT ou chimiothérapeutiques. Pour atteindre cet objectif, nous nous concentrons spécifiquement sur trois axes.

Un contrôle minutieux de la morphologie est important car elle régit à la fois l'intensité de la PL par UC, ainsi que le gain en contraste des LnNPs en IRM. Dans la partie I, nous rapportons une stratégie de thermolyse en une étape permettant le contrôle de la morphologie d'UCNPs β-$NaGdF_4$:Er^{3+}, Yb^{3+} uniformes et monodisperses. Alors que les UCNPs de $NaGdF_4$ sphériques ou plats peuvent être synthétisés par thermolyse suivant une injection à chaud, la synthèse directe de nanobâtonnet n'avait pas été rapportée auparavant dans la littérature. Nous avons constaté que la modulation de la température au cours de l'étape d'injection à chaud permettait le contrôle de la taille et la forme des nanocristaux de β-$NaGdF_4$ formés, et permettait ainsi la synthèse de nanobâtonnets de β-$NaGdF_4$. Une étude plus approfondie du mécanisme a révélé que différentes températures entraînaient une concentration de sursaturation différente, ce qui modifie le processus de nucléation et de croissance de la phase α des nanoparticules, affectant par la suite le processus de mûrissement d'Ostwald lors de la transition de phase α → β.

La modification de la surface est une étape critique dans la conversion des UCNPs hydrophobes et des agents thérapeutiques en des entités dispersables dans l'eau, favorables aux applications *in vivo*. À la suite de la partie II, nous avons proposé une approche originale d'encapsulation en une étape dans un milieu aqueux à pH *quasi*-neutre. Nous avons co-encapsulé des UCNPs de NaGdF4 et un agent de PDT, le ZnPc, dans une nanocapsule. Le Gd^{3+} présent dans les UCNPs agit comme agent de contraste T_2, tandis que le transfert d'énergie des UCNPs aux molécules de ZnPc sous irradiation dans le NIR induit la génération d'oxygène singulet ($^1O_2$) conformément à l'effet cytotoxique recherché en PDT. Dans la section 2 de la même partie, nous avons utilisé la même stratégie développée ci-dessus pour encapsuler la doxorubicine (DOX) (médicament chimiothérapeutique) et modifier la surface des NCs par conjugaison avec des agents de pénétration de l'enveloppe nucléaire (peptides TAT) pour l'administration active de médicaments dans les cellules cancéreuses. De plus, l'agrégation de molécules organiques à l'intérieur des NCs peut-être prévenue grâce à l'incorporation de triméthoxy(2-phényléthyl)silane (TMPES).

Enfin, dans la partie III, nous avons amélioré la stratégie d'encapsulation en une étape pour co-encapsuler les DSNPs de $LiLuF_4$:Nd^{3+}@$LiLuF_4$ (de type cœur@coquille) en incluant un « radiateur optique », le sPDI, pour PTT contrôlé par NIR permettant la mesure *in situ* de la température. Les DSNPs dopés à Nd^{3+}, synthétisés par une thermolyse en deux étapes, jouent le rôle de nanothermomètre ratiométrique pour la lecture non-invasive et en temps réel de la température de sorte à pouvoir surveiller la chauffe induite par le sPDI au cours de la thérapie.

Les deux entités peuvent être excitées à la même longueur d'onde de 793 nm, dans la première fenêtre biologique, tandis que l'émission du nanothermomètre est située dans la seconde fenêtre biologique. Par ailleurs, nous avons choisi $LiLuF_4$ en guise réseau hôte en raison de la forte atténuation des rayons X offerte par Lu^{3+}, permettant ainsi l'obtention d'un fluorophore efficace pour la tomodensitométrie.

3. Résultats et conclusions

Les trois chapitres suivants correspondent à des articles publiés ou soumis.

Chapitre 4: thermolyse en une étape

Contrôle de la morphologie des nanocristaux de $NaGdF_4$ dopés au lanthanide *via* une thermolyse en une étape.

Miao Wang, Yu Zhang, Qiaofeng Yao, Michael Ng, Ming Lin, Xu Li, Kishore Kumar Bhakoo, Alex Y. Chang, Federico Rosei et Fiorenzo Vetrone.

Chem. Mater. 2019, 31, 14, 5160-5171. [82] – **Article de couverture**

Dans cet article, des UCNPs monodisperses et uniformes de β-$NaGdF_4$:Er^{3+} (2%mol), Yb^{3+} (20%mol) possédant diverses morphologies sont fabriquées par thermolyse de précurseurs trifluoroacétates dans le 1-octadécène et l'acide oléique via une stratégie révisée d'injection à chaud. Nous démontrons pour la première fois que la modulation de la température au cours de l'étape d'injection à chaud est une approche efficace pour contrôler la taille et la forme des UCNPs résultantes (20~65 nm), permettant même la synthèse directe de nanobâtonnets. Les différents taux de sursaturation atteints aux différentes températures ont permis contrôler directement la nucléation et la croissance de la phase α au sein des UCNPs avant la transition de phase α → ß, influençant ainsi le mûrissement d'Ostwald ayant lieu pendant cette transition α → ß et permettant ainsi l'accès à de nombreuses morphologie (nanobâtonnets, nanosphères, nanoprismes, nanoplaques et nanodisques) et à de grandes uniformités et monodispersités. Par ailleurs, nous avons montré que l'amélioration du contraste négatif sur les images pondérées en T_2, permise par les UCNPs synthétisées, augmentait davantage avec la taille des nanoparticules (à l'exception des nanobâtonnets qui sont les plus performants comme agents de contraste en T_2 malgré leur taille inférieure aux nanoplaques). En résumé, cette étude fondamentale offre une meilleure compréhension de la stratégie synthétique des UCNPs de β-$NaGdF_4$ dopés au lanthanide, en particulier en ce qui concerne le contrôle de leur morphologie. Il fournit également un support scientifique solide pour la conception de nanodispositifs théranostiques pour de futures applications biomédicales.

Chapitre 5: encapsulation en une étape

5.1 Synthèse en une étape de nanocapsules théranostiques contenant des nanoparticules dopées au lanthanide

M. Wang, Y. Zhang, M. Ng, A. Skripka, T. Cheng, L. Xu, K. K Bhakoo, AY Chang, F. Rosei et F. Vetrone.

Chem. Sci., 2020, 11, 6653-6661. [106] – **Article de couverture**

Dans cet article, nous rapportons une stratégie inédite de synthèse en une étape pour co-encapsuler des UCNPs de NaGdF4:Er^{3+}(2 mol%), Yb^{3+}(20 mol%) et du ZnPc dans des NCs en suivant l'approche par croissance promue par l'interface L'encapsulation procède d'un mécanisme de microémulsion, en milieu aqueux (pH *quasi*-neutre) dû à la présence d'un copolymère triblocs (F127), le PEG-PPG-PEG, jouant le rôle de précurseur de structure et de protecteur. Il permet d'abord d'encapsuler les UCNPs dans des micelles PEG-PPG-PEG, puis de faire croître la coquille de silice au sein du cœur de la micelle micellaire (bloc PPG) jusqu'à l'interface définie par les blocs de PEG. Avec ce protocole, nous avons co-encapsulé en une seule étape les UCNPs (sans en modifier la surface, maintenant ainsi leurs propriétés optiques d'origine) et le ZnPc, minimisant de la sorte la distance entre les deux charges utiles en vue de faciliter leurs transferts d'énergie. Les NCs démontrent d'excellentes propriétés: stabilité colloïdale, biocompatibilité, faible probabilité de fuite de la ZnPc, ainsi qu'un contraste négatif amélioré en imagerie pondérée en T_2 et en thérapie photodynamique. Cette dernière utilisation résulte de l'excitation indirecte de la ZnPc par les UCNPs, entraînant la génération d'oxygène singulet et l'éradication *in vitro* des cellules cancéreuses du sein BT474. Globalement, la stratégie présentée d'encapsulation « tout-en-un » marque le franchissement d'un cap dans le domaine de l'ingénierie de surface des systèmes d'UCNPs et d'UC-PDT. Cette approche pourrait être augmentée pour inclure divers agents thérapeutiques, diagnostiques ou de ciblage, élargissant ainsi l'éventail de fonctionnalités théranostiques et favorisant l'accès à une médecine personnalisée.

5.2 Micelles de copolymère à blocs réticulées par silice/organosilane à fluorescence amplifiée pour l'administration de principe actif ciblée au noyau cellulaire

Yu Zhang,* **Miao Wang**,* Grace HB Ng,***** Mingyan Tan, Cathleen Teh, Alex Yuang-chi Chang, Federico Rosei, Fiorenzo Vetrone, Xu Li et John Wang.

En préparation.

***,** Les auteurs ont contribué équitablement à la publication.

Pour démontrer davantage la capacité des NCs à l'administration active ciblée, nous avons conjugué un agent de pénétration de l'enveloppe nucléaire (peptide TAT) à la couronne polymérique (PEO) des NCs. La doxorubicine (DOX), un médicament chimiothérapeutique conventionnel, est choisie comme principe actif modèle dans cette étude. La DOX agit en partie par interférence avec le fonctionnement normal de l'ADN. La multirésistance des cellules cancéreuses aux médicaments causée par une administration inadéquate de principe actif est l'un des obstacles majeurs au traitement efficace du cancer. Les systèmes d'administration aux noyaux cellulaires sont autorisés pour améliorer la distribution de la DOX au sein du noyau et réduire les effets secondaires systématiques. Par ailleurs, la DOX peut jouer le rôle de marqueur fluorescent en raison de ses propriétés de photoluminescence intrinsèques, permettant de la localiser facilement dans les cellules sans avoir à introduire de fluorophore supplémentaire. Cependant, nous avons remarqué que la fluorescence de la DOX encapsulée subissait une extinction en raison de l'agrégation des molécules, elle-même provoquée par des concentrations locales élevées. À cette fin, nous avons développé un protocole dans lequel un composé organosilicié tel que le TMPES est introduit à l'interface interne de la coquille de silice pour limiter l'agrégation des molécules encapsulées. Cet organosilane interagit notamment avec la DOX encapsulée par empilement hydrophobe et/ou π-π, inhibant ainsi l'auto-agrégation de la DOX. Cette approche se montre relativement versatile et peut s'appliquer pour limiter l'extinction de la fluorescence par agrégation d'autres fluorophores aromatiques planaires, comme la coumarine et la rhodamine. Plus généralement, cette stratégie s'avère prometteuse pour des applications biomédicales où une charge utile élevée et une fluorescence intense sont simultanément requises luminosité de fluorescence. Nous rapportons une NC conjuguée à des peptides TAT pouvant limiter l'auto-agrégation des charges utiles encapsulée. Avec un tel système, la DOX est délivrée de manière plus adéquate *i.e.* accumulée dans le noyau, comme établi à la fois par imagerie de fluorescence et par l'inhibition de la croissance des cellules cancéreuses, en particulier celles résistant habituellement à la DOX. Cette étude démontre que les NCs développées peuvent être agrémentées d'autres fonctionnalités en vue d'améliorer le diagnostic et l'administration médicamenteuse.

Chapitre 6 : Nanocapsules théranostiques

Nanocapsules (NCs) théranostiques conçues pour la thermothérapie, l'imagerie et la thermométrie

Miao Wang, Artiom Skripka, Yu Zhang, Ting Cheng, Michael Ng, Xuan Sun, Xu Li, Kishore Kumar Bhakoo, Alex Y. Chang, Federico Rose, Fiorenzo Vetrone*

Prêt à être soumis.

Dans cet article, nous avons appliqué la stratégie d'encapsulation en une étape à la synthèse de NCs théranostiques, de taille hydrodynamique inférieure à 200 nm, fonctionnelles dans le proche infrarouge (NIR) pour la thérapie photothermique (PTT) assistée par imagerie et permettant la mesure en temps réelle de la température locale. Nous avons co-encapsulé simultanément des molécules organiques, le diimide N,N'-dicyclohexylaminopérylène-3,4,9,10-tétracarboxylique (sPDI) substitué sur les régions de type « baie » en guise d'antenne photothermique performante, avec des NPs de structure « cœur-coquille » (LiLuF4:10 mol% Nd^{3+}@LiLuF4) à propriété de conversion descendante (DSNPs) servant de nanothermomètres et de fluorophore d'imagerie. Les ions Lu^{3+} présents dans la matrice hôte servent d'agent de contraste en tomodensitométrie pour faciliter la localisation de la cible d'intérêt. Les deux matériaux peuvent être excités à 793 nm, longueur d'onde connue pour être inoffensive et athermique vis-à-vis des tissus. L'émission du nanothermomètre (à 1060 nm) est située dans la deuxième fenêtre biologique et permet la lecture de la température à des profondeurs accrues dans les tissus. Les molécules de sPDI s'auto-assemblent une fois confinées dans les NCs, entraînant un décalage vers le rouge de l'absorption vers des régions plus favorables du NIR. Sous irradiation, les agrégats de sPDI produisent de la chaleur par relaxation vibrationnelle (non radiative), conduisant à une augmentation locale de la température et à l'éradication complète des cellules MCF-7 du cancer du sein. Le sPDI démontre ici une stabilité photothermique remarquable. Par ailleurs, la vitesse de chauffage peut être ajustée via la quantité de SPDI encapsulées dans les NCs lors de l'étape de synthèse. D'autre part, la température est précisément évaluée *in situ* grâce à la manifestation de la transition Nd^{3+} $^4F_{3/2} \rightarrow {}^4I1_{1/2}$ des DSNPs. Utilisés comme nanothermomètres, les DSNPs disposent d'une sensibilité thermique relative de l'ordre de 0.35%°C^{-1} et une incertitude thermique absolue d'environ 0.15°C autour de la température ambiante. Une amélioration du contraste positif est également observée sur les images de CT des cellules cancéreuses, témoignant d'un potentiel certain pour une application en PTT assistée par imagerie. En résumé, les NCs combinent avec succès les exigences relatives à la photothermie (chauffage), à l'imagerie, à l'acquisition de la température et démontrent ainsi un fort potentiel pour des avancées en théranostique.

4. Perspectives

Nous avons conçu un nanodispositif théranostique basée sur les LnNPs et d'autres modalités thérapeutiques pour la PDT et la PTT assistée par imagerie. Bien qu'elle semble démontrer un fort potentiel pour des applications biologiques, le nanodispositif en est encore à un stade prématuré. Davantage de recherche est nécessaire pour envisager les applications *in vivo* à venir.

Optimisation des matériaux photoluminescents: dans le chapitre 5, nous nous concentrions sur le développement de l'encapsulation en une étape en vue d'optimiser la modification de la surface des LnNPs et ainsi créer un nanodispositif théranostique pour la PDT par conversion ascendante. Nous sélectionnions des UCNPs de $NaGdF_4$ dopées au Yb^{3+}/Er^{3+} en tant que médiateur énergétique et agent de contraste en IRM, en association du ZnPc (un photosensibilisateur utilisé en PDT). Pour améliorer davantage encore les bénéfices thérapeutiques de ce système, plusieurs options sont envisageables dans de futures études. i) l'architecture cœur-coquille des UCNPs peut être utilisée pour améliorer l'efficacité de la conversion ascendante. Les ions Nd^{3+} pourraient également être co-dopés avec du Yb^{3+} dans la coquille pour faciliter le transfert d'énergie selon l'ordre $Nd^{3+} \rightarrow Yb^{3+} \rightarrow Er^{3+}$, puisque Nd^{3+} peut être excité par la longueur d'onde idéale de 793 nm, pénétrant plus profondément dans les tissus que 980 nm. Afin d'éviter les désactivations par la surface, la croissance d'une coquille supplémentaire, inerte chimiquement, pourrait être envisagée. ii) les photosensibilisateurs de PDT (dont la bande d'absorption chevauche l'émission verte de Er^{3+}) tels que le Rose Bengale (RB) peuvent être co-encapsulés avec le ZnPc (absorbant l'émission rouge de Er^{3+}) dans les NC. Par ce biais ci, les émissions visibles sont absorbées à la fois par le RB (~540 nm) et la ZnPc (~680 nm). La production d'oxygène singulet ($^1O_2$) qui en résulte améliore les dommages photooxydatifs contre les cellules cancéreuses.

Développement de nanocapsules théranostiques pour la thérapie combinée: Dans le Chapitre 6, nous avions démontré l'efficacité théranostique de NCs pour la PTT. L'évaluation *in vitro* de ces NCs montre des résultats prometteurs en termes d'efficacité en PTT, d'amélioration de contraste en CT et de lecture en temps réel de la température locale. La sensibilité thermique de ces thermomètres peut cependant encore être améliorée en ajustant la concentration du dopant Nd^{3+}, car notre groupe a récemment démontré que le dopage à hauteur de 5% de Nd^{3+} dans l'hôte $LiLuF_4$ permet d'obtenir la sensibilité thermique la plus élevée combinée à l'incertitude la plus faible. Afin de cibler de futures applications *in vivo*, nous envisageons d'étendre ce système pour y intégrer davantage de fonctionnalités. i) Conjuguer des anticorps spécifiques aux NC, permettant l'administration active de principe actif. Le trastuzumab, un anticorps monoclonal dirigé contre le récepteur HER2, est largement utilisé pour le traitement des patientes atteintes

d'un cancer du sein HER2 positif, à un stade précoce, localement avancé ou à l'état métastatique. [212] Par conséquent, le trastuzumab peut être utilisé à la fois pour le traitement et l'administration médicamenteuse dans le cas d'un cancer du sein HER2 positif s'il est conjugué aux chaînes de PEO des NCs (en utilisant l'EDC et le NHS comme catalyseurs. Cette approche de conjugaison est décrite à la *section 5.2*). ii) Le paclitaxel, une substance chimiothérapeutique, peut-être co-encapsulé dans les NCs. L'association du trastuzumab et du paclitaxel est supposée produire synergie thérapeutique surmontant les limites de la chimiothérapie conventionnelle. De plus, la libération de paclitaxel pourrait s'accroître avec l'augmentation locale de la température locale engendrée par le sPDI encapsulé. iii) Les performances des NCs développées combinées à la thérapie moléculaire ciblée, à la chimiothérapie et à la PTT, peuvent d' abord être évaluées *in vitro* dans des lignes de cellules de cancer du sein, avec divers degrés d'expression de HER2 (BT-474, MDA-MB-468 et MCF-7), et de cellules mammaires saines (HMEC). Les performances *in vivo* peuvent être évaluées à l'aide du modèle murin de xénogreffe pour HER2 positif.

Évaluation *in vivo*: dans cette thèse, nous nous concentrons sur la préparation et la caractérisation des NCs théranostique. Leurs performances ont également été évaluées au niveau cellulaire. Cependant, l'expérimentation *in vivo* est indispensable pour faire progresser la nanomédecine. Plus spécifiquement, des études sur la toxicité (y compris la cytotoxicité pour les tissus normaux), la biodistribution des LnNPs, le métabolisme, la pharmacocinétique et la pharmacodynamique sur des animaux modèles sont nécessaires; De plus, la PDT, la PTT et la bioimagerie multifonctionnelle basée sur les LnNPs mentionnés précédemment pourraient être expérimentées sur animaux modèles.

LIST OF CHEMICAL COMPOUNDS, ABBREVIATIONS AND SYMBOLS

Chemical compounds

ABDA 9,	10-Anthracenediyl-bis(methylene)dimalonic acid
CCK-8,	Cell counting kit-8
CF_3COOH,	Triflouroacetic acid
CF_3COONa,	Sodium trifluoroacetate
CF_3COOLi,	Lithium trifluoroacetate
DMEM,	Dulbecco's modified Eagle medium
EDTA,	Ethylenediaminetetraacetic acid
DOX,	Doxorubicin
Ln_2O_3,	Lanthanide oxides
$(CF_3COO)_3Ln$,	Lanthanide triflouroacetate
FBS,	Fetal bovine serum
H_2O,	Water
OA,	Oleic acid
ODE,	Octadecene
OM,	Oleylamine
SiO_2,	Silicon dioxide
ZnPc,	Zinc phthalocyanine
PBS,	Phosphate buffered saline
PDI,	Perylene diimide
sPDI,	Dicyclohexylamino substituted PDI
PEO-PPO-PEO,	$(\text{Ethylene oxide})_{106}(\text{Propylene oxide})_{70}(\text{Ethylene oxide})_{106}$
THF,	Tetrahydrofuran
TMOS,	Tetramethoxysilane

TMPES, Trimethoxy (2-phenylethyl) silane

TOPO, Trioctylphosphine oxide

Abbreviations

CMC, Critical micelle concentration

CR, Cross-relaxation

CT, Computed tomography

DS, Downshifting

DSNP(s), Downshifting nanoparticle(s)

DI, Deionized

DLS, Dynamic light scattering

ESA, Excited state absorption

ET, Electron tomography

ETU, Energy transfer upconversion

EPR, Enhanced permeability and retention effect

FN, First Nuclei

FTIR, Fourier transform infrared

GSA, Ground state absorption

ICP-AES, Inductively coupled plasma – atomic emission spectroscopy

LIR, luminescence intensity ratios

Ln, Lanthanide

LnNP(s), Lanthanide doped nanoparticle(s)

MRI, Magnetic resonance imaging

NC(s), Polymeric micelle/silica nanocapsule(s)

NIR, Near-infrared

PA, Photon avalanche

PDT, Photodynamic therapy

PL,	Photoluminescence
PS,	Photosensitizers
PTT,	Photothermal therapy
QDs,	Quantum dots
ROS,	Reactive oxygen species
SNR,	Signal-to-noise ratio
TEM,	Transmission electron microscopy
TPL,	Two-photo luminescence
UC,	Upconversion (or upconverting)
UCNPs,	Upconverting nanoparticles
UC-PDT,	Upconversion based photodynamic therapy
UV,	Ultraviolet
VIS,	Visible
XRD,	X-ray diffraction

LIST OF FIGURES

LIST OF TABLES

TABLE OF CONTENTS

1 INTRODUCTION

1.1 Cancer nanomedicine

Cancer ranks as a leading cause of death and an important barrier to increasing life expectancy in every country of the world.[1] According to the Canadian Cancer Society's Annual report released in 2019 (Canadian Cancer Statistics 2019. Toronto, ON: Canadian Cancer Society; 2019), it is estimated that about 1 in 2 Canadians will develop cancer in their lifetime, and about 1 in 4 Canadians will die of cancer. In 2019 alone, it is estimated that 220,400 Canadians were diagnosed with cancer and 82,100 will die from the disease. Surgery, chemotherapy, radiotherapy or their combinations is the first line conventional treatment regimen. However, in many cases, they are not effective due to the cancer metastasis and relapse, or the notorious side effects. New treatment modalities including molecular targeted therapy, immunotherapy, gene therapy, and phototherapy, have been investigating for the improvement of treatment outcome.

Nanomedicine is an emerging key technology of the 21st century. Taking advantage of using engineered carriers, it is being exploited for diagnostic and therapeutic applications.[2, 3] From the beginning, nanomedicine has been frequently associated with the use of nanoparticles (NPs) in oncology as the enhanced permeability and retention (EPR) effect of tumor tissues is validated for particles at the nanoscale.[4] Namely, NPs preferentially accumulate in tumors

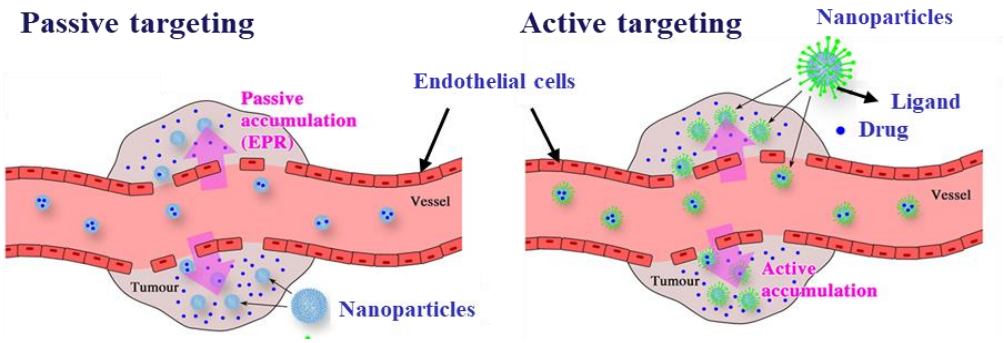

Figure 1.1 Schematic illustration of NP delivery to tumor tissue.

(A) Passive targeting relies on the leaky vasculature that is exhibited by tumors, allowing nanoparticles to travel through the fenestrations and reach tumors. (B) Active targeting can be used when nanoparticles have ligands on their surface that can recognize and bind receptors that are overexpressed on tumor cells. Reproduced with permission from [8].

through the EPR effect, leading to higher intra-tumorous drug concentrations. NPs (≥8 nm) are unable to penetrate normal vasculatures including capillaries, thus leading to lower drug concentration in normal tissues compared with their small molecule counterparts delivered without NPs. This is the so-called passive targeting delivery. To further increase drug accumulation in tumors, active targeting delivery is investigated by grafting ligands at the

surface of the NPs for specific binding to the target of interest (Figure 1.1).[5-9] In fact, there are already a number of nanomedicines available on the market, or undergoing clinical trial,[10] which offer better drug delivery,[4] high-precision therapy,[11] and enhanced imaging.[12]

Although clinically approved nanodrugs such as Doxil/Caelyx (PEGylated liposomal doxorubicin) and Abraxane (Albumin-bound paclitaxel nanoparticles) have consistently shown value in reducing drug toxicity, their use has not always translated into improved clinical outcomes.[13] The so-called *theranostics* (*thera*peutics + diag*nostics*), a multifunctional nanoplatform, which are capable of targeted diagnosis and therapy, have the potential to further improve the cancer treatment. [14-17] When therapeutic and imaging contrast agents are combined into a single formulation, they are usually assumed to have similar bio-distribution and tumor localization in living subjects. As a result, nanotheranostics are expected to help physicians make informed decisions about timing, dosage, drug choice, and treatment strategies. Such "personalized medicine" can lead to improved efficacy, lower off target toxicity, and an overall increase in quality of life and patient outcome[6, 13].

In addition to the conventional cancer therapy, the breakthrough of nanotechnology also makes a significant step forward in phototherapy including photodynamic therapy (PDT) and photothermal therapy (PTT), which is designed to selectively kill cancer cells through light induced oxidative damage (PDT) or thermal damage (PTT). In particular, optical nanotheranostics offer laser-point-accuracy in non-invasive disease (i.e. cancer) detection and eradication.[18] It is envisioned that photoluminescent nanotheranostics will be able to illuminate the malignancy and treat it locally under remote control with reduced damage to healthy tissues. Although the development of nanotheranostics shed light on both necessity and feasibility, many obstacles are yet to be overcome in order to translate these NPs from the "bench" to the "bedside" for the betterment of human health.

Among the broad spectrum of nanomaterials being investigated for cancer nanomedicine, lanthanide (Ln) doped nanoparticles (LnNPs) have attracted significant attention due to their intrinsic upconversion (UC) or downshifting (DS) luminescence capabilities. UC is a process that can convert near-infrared (NIR) light to the higher energy regions spanning the ultraviolet-visible-NIR (UV-VIS-NIR) through a multiphoton process while DS results when the NIR excitation light is further red shifted.

1.2 Basics of LnNPs

1.2.1 Ln^{3+}

Lanthanides refer to the series of metallic chemical elements with atomic numbers 57 through 71 located at the sixth period and IIIB group in the periodic table, ranging from lanthanum to

lutetium.[19, 20] They are called lanthanides because the elements in the series are chemically similar to lanthanum. These lanthanide elements, along with the other chemically similar elements scandium and yttrium, are also known as the rare earth elements.[21, 22] The lanthanides were first discovered in 1787 when a black mineral (named gadolinite in 1800) was found in a town called Ytterby in Sweden. Johann Gadolin then obtained yttria (an impure form of yttrium oxide) in 1794 from gadolinite. Over one hundred years, the 15 lanthanide elements were gradually separated from different minerals.[23,24] Subsequently, with the development of lanthanide chemistry, these elements have been applied in different fields including the chemical, optoelectronics, automotive, agriculture, and biomedical industries.[25-27]

Table 1.1 Ground state electronic configurations of the lanthanide elements. [28]

Z	Name	Symbol	Electronic outside the Ln	Configuration [Xe] core Ln^{3+}	Metallic radius (pm)	Ionic radius Ln^{3+} (pm)	Colour of Ln^{3+}
57	Lanthanum	La	5d16s2	-	187	106	Colourless
58	Cerium	Ce	4f15d16s2	4f1	183	103	Colourless
59	Praseodymium	Pr	4f36s2	4f2	182	101	Green
60	Neodymium	Nd	4f46s2	4f3	181	100	Lilac
61	Promethium	Pm	4f56s2	4f4	-	98	Yellow
62	Samarium	Sm	4f66s2	4f5	179	96	Yellow
63	Europium	Eu	4f76s2	4f6	204	95	Pale pink
64	Gadolinium	Gd	4f75d16s2	4f7	180	94	Colourless
65	Terbium	Tb	4f96s2	4f8	178	92	Pale pink
66	Dysprosium	Dy	4f106s2	4f9	177	91	Yellow
67	Holmium	Ho	4f116s2	4f10	176	89	Yellow
68	Erbium	Er	4f126s2	4f11	175	88	Rose pink
69	Thulium	Tm	4f136s2	4f12	174	87	Pale green
70	Ytterbium	Yb	4f146s2	4f13	194	86	Colourless
71	Lutetium	Lu	4f145d16s2	4f14	174	85	Colourless

Electronic configuration: The lanthanides have similarities in their electronic configuration, (Table 1.1).[28] The electronic configuration of lanthanide atoms are [Xe] $4f^n$ $5d^{0\text{-}1}$ $6s^2$. In forming the ions, electrons are removed first from the 6*s* and 5*d* orbitals so that all the Ln^{3+} ions have [Xe] $4f^n$ arrangement. Some of the lanthanides, such as Yb^{2+}, Tb^{4+} and Ce^{4+}, may exist in the 2+, 4+ oxidation states, owing to the fact that the *f* orbital is fully, half occupied or empty, while the most common and stable lanthanide ions (Ln^{3+}) are in the 3+ oxidation state. This is because the 3+ oxidation state leaves the ions in the 4*f* sub-shell and the ionization energy of the *f* electrons is large. There is a decrease in radius of the Ln^{3+} ions crossing the series from La to Lu, due to the contraction of 4*f* orbitals (known as lanthanide contraction). As the atomic number increases from La^{3+} to Lu^{3+}, 5*s* and 5*p* orbitals penetrate the 4*f* sub-shells and are not shielded from the increasing nuclear charge, hence they are drawn closer towards the nucleus with the increasing effective nuclear charge, resulting in the decreased ionic radius. Ln^{3+} ions with smaller radius (heavy in mass) are more difficult to lose electrons than that of larger ones (light in mass).[28] This intrinsic property has a direct impact on the chemistry of the formation of LnNPs. For example, in the controlled growth of $AREF_4$

nanocrystals (A =Li to K, RE = La to Lu, and Y), $LiREF_4$ was only formed from the heavier lanthanides, from Tb to Lu and Y, while $KREF_4$ was only formed from lighter lanthanides, from La to Gd and Y.[29]

Spectroscopic and magnetic properties:[28] The spectroscopic and magnetic properties of Ln^{3+} may be accounted for using the Russell–Saunders coupling (also known as LS coupling) scheme, in which the electron spins are coupled together (S) separately from the coupling of the orbital angular momenta (L) of the electrons. The energy states in the 4*f* sub-shell of Ln^{3+} ($^{2S+1}L_J$) are defined by the spin-orbital coupling between S and L, where $S = \sum m_s ; L = \sum m_l ; J = (S+L), (S+L)-1, (S+L)-2, \ldots\ldots (S-L)$. The ground state can be determined using Hund's rules. The 4*f* electrons are 'inside' the 5*s* and 5*p* orbitals, being shielded from the ligands, taking no part in bonding, and thus the crystal field splitting is weak. Therefore, the ground state for a given Ln^{3+} ion is largely independent of surrounding environment. As a result, the Ln^{3+} ions exhibit very narrow *f-f* absorption and emission bands and long lifetimes of intermediate excited states, leading to an extremely photo stable emission. These optical characteristics are significant advantages for use as optical probes. All the Ln^{3+} ions, except La^{3+} and Lu^{3+}, have unpaired *f* electrons and are paramagnetic. Their magnetic properties are mainly determined by the ground state of Ln^{3+} ions, and their magnetic moment is generally given by the equation below.

$\mu_{eff} = g_J \sqrt{J(J+1)}$, where g_J is the Landé g-factor, which is defined as

$g_J = 3/2 + [S(S+1) - L(L+1)]/2J(J+1).$

The maximum number of unpaired electrons is 7, in Gd^{3+}, with a magnetic moment of 7.94 μ_B, but the largest magnetic moments, at 10.4–10.7 μ_B, are exhibited by Dy^{3+} and Ho^{3+}. However, in Gd^{3+} all the electrons have parallel spin and it has a relatively long electron-spin relaxation time (~10^{-9} s) compared to other paramagnetic ions such as Dy^{3+} (~10^{-13} s), which makes it more favourable for nuclear spin relaxation.

To date, much attention has been devoted to lanthanide photoluminescence (PL) when doped in inorganic hosts, particularly when the host has particle sizes in the nanoscale regime. Typically, this occurs upon direct excitation of the Ln^{3+} ion into an excited state followed by radiative emission and return to the ground state again. A suitable excitation source, whose wavelength is resonant with the energy gap separating the ground and a specific excited state, is required.

1.2.2 Upconversion (UC) processes

One of the remarkable properties of the lanthanide ions is their ability to convert low energy NIR excitation wavelengths to higher energies spanning UV-VIS-NIR, through a process known as UC. The general concept of UC was first revealed and formulated independently by Auzel, Ovsyankin, and Feofilov in the mid-1960s. It refers to a nonlinear process characterized by the successive absorption of two or more excitation photons *via* intermediate long-lived energy states followed by the emission of light at a shorter wavelength than the excitation wavelength. The intermediate excited states possess long lifetimes typically in the μs to ms range, which allows for the sequential and step-wise absorption of photons to achieve excitation of the final energy state followed by the generation of a higher energy photon.[30, 31] Compare with two-photon luminescence (TPL) processes, UC can be induced by a low power (1-10^3 W cm^{-2}), continuous wave laser. In the case of TPL, absorption of the photons occurs simultaneously, therefore it requires excitation with costly, high intensity (10^6-10^9 W cm^{-2}) ultrafast (femtosecond) pulsed lasers.[32] The mechanism of upconversion processes explored in upconversion nanoparticles (UCNPs) up to now, is mainly divided into four basic classes:[33] excited state absorption (ESA), energy transfer upconversion (ETU), cross-relaxation (CR), and photon avalanche (PA). They are briefly highlighted below.

Excited state absorption (ESA): In the case of ESA, there is only a single ion involved in the sequential absorption of two pump photons. As shown in the Figure 1.2, if an incoming photon

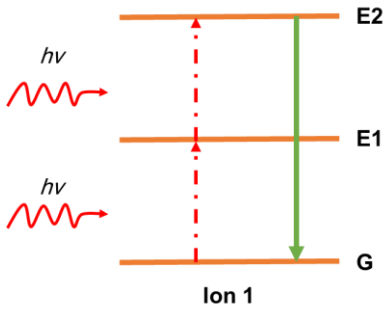

Figure 1.2 Schematic illustration of the ESA process.

of a wavelength resonant with the transition energy from ground state G to excited state E1 is absorbed, it will populate the ion to the intermediate excited state (E1) from the ground state (G). Subsequently, a second photon promotes it to the higher-lying state (E2) due to the long lifetime of E1, before its decay to the ground state. Consequently, UC emission will occur from the E2 level. The efficiency in an ESA process is independent of the dopant concentration due to its single ion characteristic. To achieve highly efficient ESA, a ladder-like arrangement of the energy states of lanthanide is required.

Energy transfer upconversion (ETU): ETU involves two neighbouring ions in close proximity where one ion acts as a sensitizer, while the second acts as an activator (Figure 1.3). In an ETU process, ion 1 is first excited from the ground state to its intermediate state E1 by absorbing a pump photon, then sensitizer ions transfer their harvested energy to ion 2 through a non-radiative energy transfer and promotes the activator to its intermediate state E1. A second transfer subsequently occurs and promotes the activator ions to the upper emitting state E2, while sensitizer ion 1 relaxes back to ground state G twice. The UC efficiency of an ETU process is sensitive to the average distance between the neighbouring sensitizer-activator, which is determined by the concentrations of dopants. It has been widely used to offer highly efficient UC (two orders of magnitude higher than ESA) over the past decade.[31]

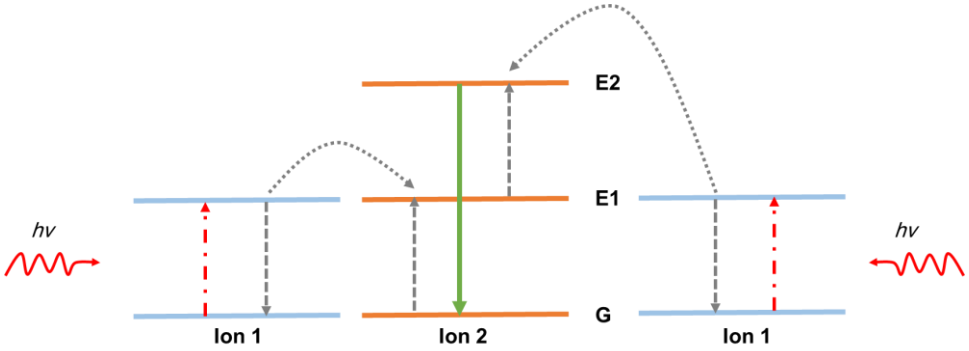

Figure 1.3 Schematic illustration of the ETU process.

Cross-relaxation (CR): CR is an energy transfer process, resulting from ion−ion interaction in which ion 1 transfers part of its excited energy to ion 2 (Fig. 1.4), through a process of E2 (ion 1) + G (ion 2) → E1 (ion 1) + E1 (ion 2). Ion 1 and ion 2 can be either identical or different, and ion 2 can also be in its excited state in some cases. The efficiency of CR is in close relation with the dopant concentration. CR is the main reason for the well-known "concentration quenching mechanism" of emission. As to the CR in the sensitizer/activator systems of Yb^{3+}/Tm^{3+}, Yb^{3+}/Er^{3+} and Yb^{3+}/Ho^{3+}, an optimum concentration of the activator (Tm^{3+}, Er^{3+}, and

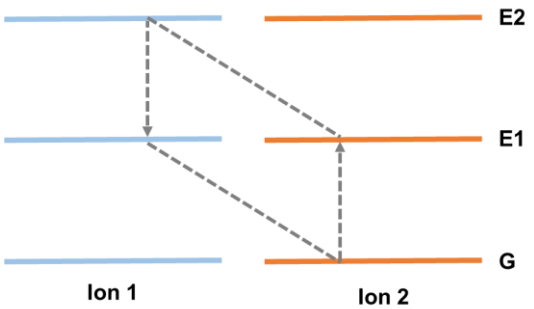

Figure 1.4 Schematic illustration of the CR process.

Ho^{3+}) is determined to be generally below 2 mol% to yield high UC efficiency.[30] With respect to Nd^{3+}-doped LnNPs, the CR process of $^4F_{3/2} + {}^4I_{9/2} \rightarrow 2{}^4I_{15/2}$ non-radiatively depopulates the excited $^4F_{3/2}$ level, which adversely affects the DS luminescence intensity by concentration

quenching. The highest quantum yield is about 22%, observed in the $NaGdF_4:Nd^{3+}$ (3 mol%) LnNPs. [34]

Photon avalanche (PA): The phenomenon of PA was first discovered by Chivian and co-workers in Pr^{3+}-based infrared quantum counters.[35] PA-induced UC features an unusual pump mechanism that requires a pump intensity above a certain threshold value. As shown in Fig. 1.5, the PA process may lead to strong UC emission from level E2 without any resonant ground state absorption (GSA). The pump wavelength is only resonant between a metastable state E1 and a higher energy level E2. After the metastable level population is established, cross-relaxation energy transfer occurs between the excited ion (ion 1) and a neighbouring ground state ion (ion 2), resulting in both ions occupying the intermediate level E1. Two ions are now available for further ESA absorption of the pump light. After which, by the same feeding process, four ions will be further available in this metastable state and so on, producing strong UC emission as an avalanche process. In the PA process, the pump photons need to be resonant with only one transition, so that only one pump beam is necessary. Moreover, the Ln^{3+} concentration should be high enough for the ion-ion interactions to cause efficient CR ET, which populates the metastable state and induces the ESA. Thus, as with ETU, PA is expected to be an efficient pumping process for UC lasers with sufficiently high Ln^{3+} concentration.[36, 37]

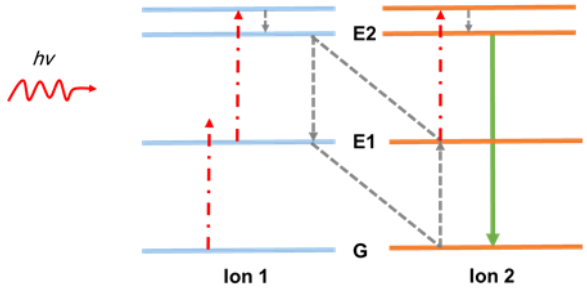

Figure 1.5 Schematic illustration of the PA process.

1.2.3 LnNPs

LnNPs are generally dilute guest-host systems, where doped Ln^{3+} ion emitters are dispersed as guests in an appropriate dielectric host lattice[38]. The dopants are usually in the form of localized luminescent centres, in which the distance between Ln^{3+} ions should be below ~10 Å to allow energy transfer, which constitutes the most efficient mechanism of UC.[33] In the case of sensitized luminescence, the dopant ion radiates upon its excitation to a higher energetic state obtained from the non-radiative transfer of energy from another dopant ion. The ion that emits the radiation is called an activator, while the donor of the energy is the sensitizer. Although UC can be expected in principle from most Ln^{3+}-doped crystalline host materials, efficient UC only occurs using a small number of well selected dopant - host combinations.

The amount and type of dopants, morphology and crystal structure of host NPs can be tuned to achieve multiple emissions over a wide spectral range.[32]

Host materials**:** The host materials generally require close lattice matches to dopant ions and low phonon energies for achieving intense PL. Among investigated hosts, fluoride materials have lower phonon cut off energy (*e.g.*, ~350 cm^{-1} for the $NaYF_4$ host lattice) and high chemical stability. In addition, the crystal field of a host material has a profound effect on the UC PL of Ln^{3+} emitters. Low symmetry hosts typically exert a crystal-field containing more uneven components around the dopant ions compared to high symmetry counterparts. The uneven components enhance the electronic coupling between the 4*f* energy levels and higher electronic configuration and subsequently increase *f* – *f* transition probabilities of the dopant ions.[39] Selection of certain host lattices with low crystal field and high crystal strength is a promising way to enhance the UC PL of LnNPs. For example, hexagonal phase $NaYF_4$:Yb^{3+}, Er^{3+} microcrystals exhibit visible UC PL, which is 4.4 times higher than its cubic phase counterparts,[40] tetragonal $LiYF_4$:Yb^{3+}, Tm^{3+} NPs emit more intense UV/blue light due to the high crystal field strength of $LiYF_4$ host.[41] However, it is unable to further modify the local environment around the Ln^{3+} once the host lattice is fixed. Another promising route to enhance the UC emission is to tailor the local environment around the Ln^{3+} through an intentional doping of non-luminescent cationic ions. The non-luminescent ions can replace the cationic ions in the lattice points or occupy the interstitial sites around the Ln^{3+}, thus lowering the local symmetry around the Ln dopants and favouring the UC process. For example, Li et al. demonstrated that up to 10-fold enhancement of UC PL in singly Er^{3+}-doped $YAlO_3$ phosphor by exchanging about 40% of Y^{3+} to larger Gd^{3+} (1.159 vs 1.193 Å) due to the expansion of the host lattice and the distortion of the local symmetry.[42]

Sensitizers**:** Regarding the ETU process, the sensitizer should possess a high absorption cross-section for the excitation wavelength and energy levels matching those of the activator. Yb^{3+} possesses an extremely simple energy level scheme with only one excited 4*f* level, $^2F_{5/2}$. The $^2F_{5/2}$ absorption band of Yb^{3+} is located around 980 nm and has a larger absorption cross-section than that of other Ln^{3+} ions around the same wavelength. Additionally, the $^2F_{7/2}$ - $^2F_{5/2}$ transition of Yb^{3+} is well resonant with many *f* - *f* transitions of typical UC Ln^{3+} (Er^{3+}, Tm^{3+}, and Ho^{3+}), thus facilitating efficient energy transfer from Yb^{3+} to these other ions (Figure 1.6). These optical characteristics make Yb^{3+} the most commonly applied co-dopant and particularly suitable for use as a UC sensitizer[32]. Over the last few years, Nd^{3+} has been gaining growing recognition as a sensitizer due to its large absorption cross-section and quantum yield.[43] The absorption cross section of Nd^{3+} (~10^{-19} cm^2 at ~800 nm) is relatively higher compared to that of Yb^{3+} (~10^{-20} cm^2 at ~ 980 nm).[44] Thus the replacement of the Yb^{3+} sensitizer ion by Nd^{3+} allows for excitation with light in the range of 800 nm rather than 980

nm. In fact, the choice of the excitation wavelength is vital for biomedical application, when aiming for an enhancement of the tissue penetration and minimization of potential photothermal damage to the biological tissue.[45, 46] It has been shown that a 60% weaker energy attenuation of the 800 nm light when compared to 980 nm after passing through water.[47] The minimum heating effect on the biological tissues upon 800 nm laser irradiation, is also demonstrated in the cellular level as well as the mouse animal models.[48]

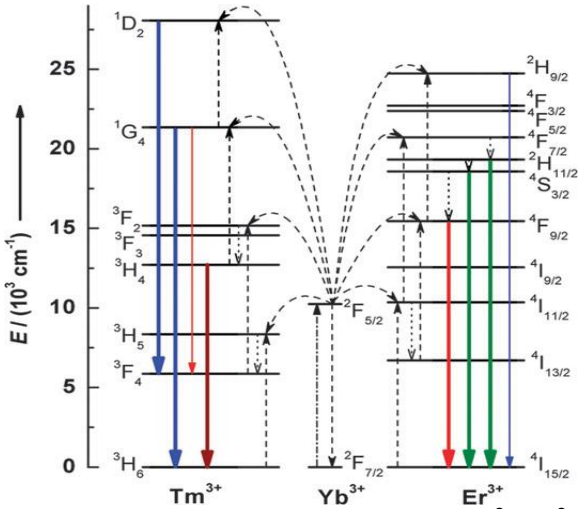

Figure 1.6 Energy transfer diagram showing the UC processes in Er^{3+}, Yb^{3+} and Tm^{3+}, Yb^{3+} co-doped UCNPs under 980 nm excitation.

The dashed-dotted, dashed, dotted, and full arrows represent photon excitation, energy transfer, multiphonon relaxation, and emission processes, respectively. [32]

Activators**:** Based on the ETU process, the activators should be characterized by energy levels homogeneously distributed, with an energy separation between them equivalent to the sensitizer emission. Once sensitizers are excited, activators are likely to extract energy from nearby excited sensitizers to promote transitions to higher energy states. In this regards, Er^{3+}, Tm^{3+} and Ho^{3+} are ideal ETU activators owing to the unique ladder-like arrangement of their energy levels.[33] Another important factor, which dictates the efficiency of the UC process, is the non-radiative multiphonon relaxation rate between energy levels. The multiphonon relaxation rate constant k_{nr} for 4*f* levels of Ln^{3+} is described as[49]

$$k_{nr} \propto exp\left(-\beta \frac{\Delta E}{hw_{max}}\right)$$

Where β is an empirical constant of the host, ΔE is the energy gap between the populated level and the next lower-lying energy level of Ln^{3+}, and hw_{max} is the highest energy vibrational mode of the host lattice. The energy gap law implies that the multiphonon relaxation rate constant decreases exponentially with increasing energy gap. Er^{3+} and Tm^{3+} have relatively large energy gaps and thus low probabilities of non-radiative transitions among various excited levels of the ions. In agreement with the energy gap law, the most efficient UCNPs known to date are obtained with Er^{3+} and Tm^{3+} as the activators.

Er^{3+} exhibits the highest upconversion efficiency amongst the commonly used activators. It mainly attributes to the similar energy gaps from $^4I_{15/2}$ to $^4I_{11/2}$ (first transition) and $^4I_{11/2}$ to $^4F_{7/2}$ (second transition). For example, in Yb^{3+}, Er^{3+} co-doped UCNPs, the green and red emissions are most commonly observed under 980 nm laser irradiation. As displayed in Figure 1.6, the green and red emissions emanate from the $^2H_{11/2}$, $^4S_{3/2} \rightarrow {}^4I_{15/2}$ and $^4F_{9/2} \rightarrow {}^4I_{15/2}$ transitions, respectively. Upon laser irradiation, Yb^{3+} is first excited from $^2F_{7/2}$ to $^2F_{5/2}$ and since the $^4I_{15/2} \rightarrow {}^4I_{11/2}$ transition of Er^{3+} is resonant with the $^2F_{5/2} \rightarrow {}^2F_{7/2}$ transition of Yb^{3+}, this subsequently results in a very efficient energy transfer process. The Yb^{3+} ion then drops back to its $^2F_{7/2}$ ground state. Due to the energy level match, the Er^{3+} can be populated to the higher excited state ($^2F_{7/2}$, $^4F_{9/2}$) through similar resonant energy transfer from the Yb^{3+}. After non-radiative multiphonon relaxation to the $^2H_{11/2}$ and $^4S_{3/2}$ states, green emissions at 525 and 545 nm are observed and attributed to radiative decay from the $^2H_{11/2}$ and $^4S_{3/2}$ excited states to the $^4I_{15/2}$ ground state, respectively. Alternatively, the red emission at 655 nm arises from the $^4F_{9/2}$ state, which is populated from either non-radiative decay from the higher $^4S_{3/2}$ state or directly exciting Er^{3+} from the $^2H_{13/2}$ state to the $^4F_{9/2}$ state *via* energy transferring from the $^2F_{5/2}$ of Yb^{3+}.

All of the above, the emission property (*e.g.* colour, intensity) of LnNPs are strongly related to their composition, morphology and crystal structure and this is critical for extended bioimaging and therapeutic applications. Moreover, the morphology, monodispersity and uniformity of LnNPs also can dictate key behavior such as cellular uptake and their removal from the cell.[3] For this reason, some general strategies have been employed in the development of LnNPs:[33] i) selection of host materials; ii) tailoring the local crystal field; iii) engineering energy transfers; iv) suppression of surface related deactivations through core/shell engineering.

1.3 Synthesis of LnNPs

There have been different chemical methods investigated for the successful synthesis of LnNPs. Co-precipitation, hydro(solvo)thermal, and thermal decomposition (or thermolysis) are widely used to synthesize high quality LnNPs for biomedical applications.[32, 33] Optimization of the synthesis procedure is critical to obtain LnNPs with tailored morphology, chemical composition, and optical properties.

1.3.1 Thermal decomposition (Thermolysis)

Thermal decomposition (thermolysis) has been recognized as a common route to fabricate high quality monodispersed uniform LnNPs with a narrow size distribution. The thermolysis strategy generally employs organometallic compounds as precursors, which decompose in a high boiling point organic solvent with the assistance of surfactants at an elevated temperature. The commonly used precursors are metallic trifluoacetate salts; the solvent can be 1-

octadecene (ODE); the surfactants can be oleic acid (OA), oleylamine (OM) and/or trioctylphosphine oxide (TOPO), which typically contain a functional capping group to coordinate the metallic elements and the long hydrocarbon chain to prevent NPs aggregation. Thermolysis was first developed for synthesis of single-crystalline and monodisperse LaF_3 in 2005.[50] This approach was later extended as a common route to the synthesis of high quality $NaYF_4$ nanocrystals in 2006.[51-53] For example, during the synthesis of $NaYF_4$ UCNPs co-doped with Yb^{3+}/Er^{3+} or Yb^{3+}/Tm^{3+} *via* the thermal decomposition of metal trifluoroacetate precursors in the presence of OA and ODE, the non-coordinating ODE was used as the primary solvent due to its high boiling point (315 ^oC). OA was chosen not only as a solvent but also as a coordinating ligand. In this synthesis, the reaction solution containing precursors, surfactants as well as solvents at room temperature is simultaneously heated to high temperature for thermal decomposition. This is so called the "***heating-up***" thermolysis strategy.[51,52] This technique was further refined and a "***hot-injection***" approach was established.[53] As shown in Figure 1.7, the pre-heated trifluoroacetate precursors are slowly

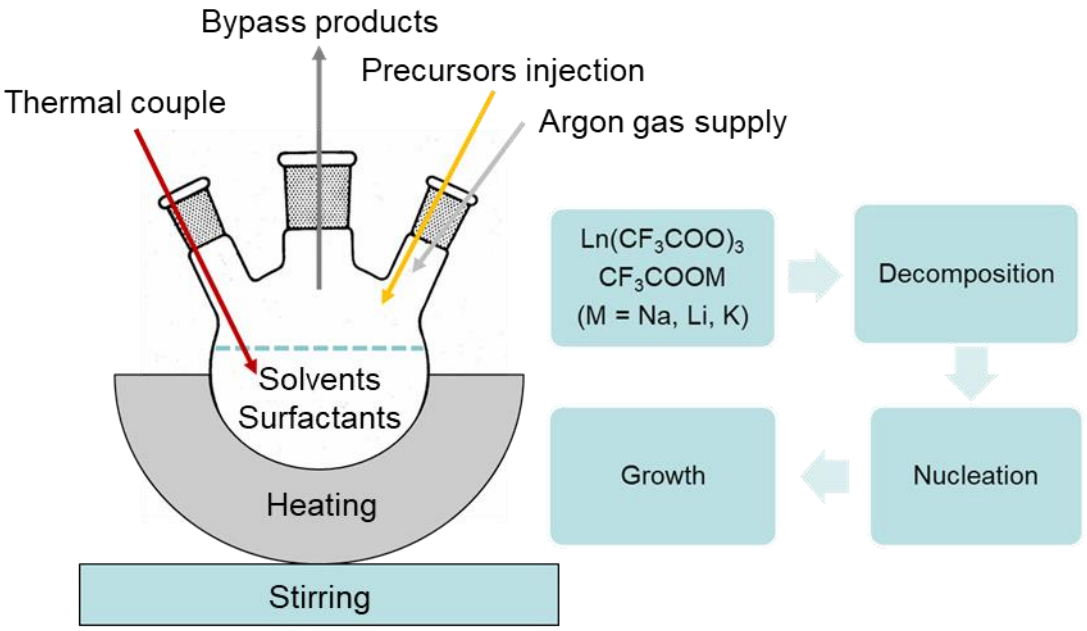

Figure 1.7 Scheme illustrations of one-step thermolysis of trifluoroacetate precursors by the hot-injection strategy.

injected into a hot surfactant solution, and successfully synthesized high crystalline NPs with a remarkably narrow size distribution without the need for size-selective fractionation. In this process, the slow addition of the precursors to the solution and subsequent manipulation of the temperature, lead to a temporal separation of nucleation and crystal growth.[53] Thus, the high supersaturation induced by the hot-injection causes a rapid homogeneous nucleation that followed by a diffusion controlled crystal growth. By carefully tailoring the experimental variables, such as the nature of solvents, the concentration of precursors, and the reaction temperature and time, as well as the injection rate for the hot-injection strategy, morphology

controlled synthesis of good crystalline LnNPs can be realized. In this thesis, we further modified the hot-injection strategy to synthsize uniform, monodispersed $NaGdF_4$ UCNPs with diverse morphologies (details will be discussed in *chapter 4*).

1.3.2 Core/shell engineering

LnNP synthesis protocols can be tailored to create core/shell nanostructures, growing different functional shells on pre-formed LnNP cores, in which the host material of the shell should exhibit a low lattice mismatch with the core materials. This strategy is used to manipulate energy transfer dynamics in LnNPs in order to increase emission intensity, vary colour, reduce surface-related deactivations, and introduce novel excitation or emission pathways. LnNP shells (as well as cores in certain cases) are typically classified as active and inert, which respectively signifies if the particular shell is doped with optically active Ln^{3+} and participates in energy exchange or not. For example, a high sensitizer concentration of Yb^{3+} (more than 18%) is often introduced into UCNPs, doped with Yb^{3+}/Tm^{3+}, Yb^{3+}/Er^{3+} and Yb^{3+}/Ho^{3+}, to achieve high UC PL. In this case, photo-excited dopants located on or around the surface can be deactivated directly by neighbouring quenching centers (surface defects, lattice strains, as well as ligands and solvents that possess high phonon energy), and excitation energy of the interior Yb^{3+} ions can also be transferred to the surface through adjacent dopant ions and eventually dissipated non-radiatively.[31, 54] The introduction of a crystalline shell around each doped UCNPs provides an effective way to improve the UC efficiency. An excellent demonstration was made by F. Vetrone et al, who established an active core/active shell strategy to obtain $NaGdF_4:Yb^{3+}$, Er^{3+} active-core@$NaGdF_4:Yb^{3+}$ active shell UCNPs, in which a reasonable concentration of Ln^{3+} dopants (generally the sensitizer) is introduced to the shell layer. It displayed a significant increase in the intensity of NIR-to-Vis UC when compared to their active-core@inert shell analogs and the core-only UCNPs by: i) shielding Er^{3+} activators from external quenchers, and ii) by harvesting more of incoming NIR photons. This study also showed that excitation energy can be shared among different layers of UCNPs.[55] By modifying this approach, our group recently established a two-step strategy to obtain small yet bright lithium-based LnNPs.[56] First nuclei (FN) formation and stabilization were involved for core synthesis. FN was synthesized by the heating-up thermolysis by controlling the relative amount of coordinating ligands, namely OM and OA. Core LnNPs were then formed by the stabilization of FN with excess of OA and ODE. Second, a shell with controlled thickness was grown on these stabilized cores of LnNPs by the hot-injection strategy.

1.4 Surface modification of LnNPs

Biomedical applications in cancer nanomedicine require the nanocarriers to own the following characteristics: i) water-dispersible and biocompatible; ii) successfully escaping from the reticuloendothelial system to result in longer circulation half-lives; iii) increasing the ratio of the accumulation of delivered agents in tumor tissue respective to healthy tissue through passive targeting or/and active targeting delivery[13]. To this end, the LnNPs should possess hydrophilic surface functional groups. Whereas some fabrication processes (*e.g.*, hydro(solve)thermal) produce LnNPs already coated with a hydrophilic ligand, other methods, *e.g.*, thermal decomposition (often chosen to produce high quality LnNPs with narrow size distribution), produce LnNPs that are hydrophobic as they are capped by the hydrophobic ligands such as OA, OM, TOP, or TOPO. Thus they are not dispersible in an aqueous solution or biological buffer and need to be surface-modified before they can be used in biological applications.[32, 52]. To date, a variety of surface modification strategies such as *ligand exchange, ligand oxidation, ligand removal, amphiphilic polymer encapsulation, and silica coating* have been utilized to make LnNPs more suitable for biomedical applications. Most of the surface-modified LnNPs are stable in aqueous dispersion, but they often suffer from a poor colloidal stability under physiological conditions, some of which are only stable for a few hours in physiological buffers (phosphate, tris, and borate buffers). Salts presented in buffers show high affinity toward Ln^{3+} on the surface of LnNPs, thus detach the ligand, which produced from either the ligand oxidation or the ligand exchange procedure. The ligand-stripped LnNPs might become aggregated in physiological buffers due to the reaction of salts ions with exposed Ln^{3+} on the LnNPs surface.[33]

1.4.1 Amphiphilic polymer encapsulation

Amphiphilic polymer encapsulation is used to convert the hydrophobic LnNPs to hydrophilic ones. This approach involves the van der Waals interaction between the hydrophobic part of the amphiphilic polymer and the original hydrophobic ligand capped on the LnNPs surface to immobilize the amphiphilic polymer onto the nanoparticle surface. The outer hydrophilic part of the amphiphilic polymer coated on LnNPs leads to aqueous dispersion and further bio-application. However, the polymeric micelles formed by amphiphilic polymer usually spontaneously dissociate when they are diluted below the critical micelle concentration (CMC), and this is of particular concern during *in vivo* applications when they will be diluted up to several orders of magnitude upon intravenous delivery.[57] As a result, the micelles could disintegrate and precipitate out their content.

1.4.2 Silica coating

Silica coating is an inorganic surface treatment strategy to make LnNPs water-dispersible and biocompatible. Silica is well known to be highly stable, biocompatible, and optically transparent. There are two types of related chemistry to coat silica onto the LnNPs, depending on the polar nature of the capping ligands on the NP surface. One is the Stöber method, which can be utilized to coat silica on hydrophilic LnNPs. The other one is the reverse microemulsion (water in oil) strategy, which is better suited for OA or OM capped LnNPs and gives core/shell particles coated with a uniform layer of silica (SiO_2).[58] Igepal CO-520 as a surfactant is widely used because it forms adequately stable reverse microemulsions for polymerization of precursors such as tetraethyl orthosilicate (TEOS). Ammonia is added as a catalyst. The hydrolysis and condensation take place in confined hydrophilic cavity (reactor space) generated by a homogeneous mixture of ammonia, cyclohexane (solvent), surfactant Igepal CO-520, and TEOS.[59] Another advantage of silica coating is that a mesoporous organically modified silica shell can be easily obtained by replacing a part of TEOS with (3-aminopropyl) triethoxysilane (APTES)[60] or in combination with the use of TEOS with cetyltrimethylammonium bromide (CTAB).[61] The mesoporous silica, with open mesopores, is immobilized on NPs and offers many sites for the accommodation of functional biomolecules and drugs onto the surface of LnNPs, as well as protects them from being degraded by the physiological buffers.[61] To this end, silica coating, especially mesoporous silica and their composites with LnNPs have been widely selected for the usage of multifunctional nanoplatforms. However, a typical mesoporous silica coating requires a multi-step process as described above, and additional surface modification of the silica shell may be required to prevent silica coated LnNPs from aggregating.[62, 63] The surfactant CTAB is highly toxic, therefore, any incomplete removal of CTAB can impede the LnNPs' use in biomedicine.[64] The leakage of payloads during the circulation in blood circulatory system is inevitable without capping the pores, otherwise this leads to potential whole-body toxicity and inadequate accumulation of payloads in the targeted tissue.[65]

1.4.3 Polymeric micelle/silica encapsulation

To solve the aforementioned issues, a silica-polymer hybrid system was applied in this thesis. In fact, it is a big challenge to achieve one-pot synthesis whereby the payloads is loaded into the nanocarriers as they are being synthetized.[66] Here, we established an original one-pot synthesis strategy to co-encapsulate hydrophobic LnNPs and other functional moieties *via* the interfacial templating condensation approach. The basic idea of this one-pot encapsulation is to confine the hydrolysis and condensation of the silica precursors to the core/corona interface of an amphiphilic triblock copolymer micelles. This forms a nanocapsule where the polymeric

micelle is stabilised by silica cross linking to prevent its disintegration. The free dangling PEO blocks of triblock copolymers, $(ethylene\ oxide)_{106}(propylene\ oxide)_{70}(ethylene\ oxide)_{106}$ (PEO-PPO-PEO), can also prevent unwanted aggregation of the silica shells. In addition, the silica cross linking provides more effective diffusion channel for water in and out of the silica shell without the need for making pores. The encapsulation takes place in an aqueous environment of a near neutral pH, and the resultant *polymeric micelle/silica nanocapsules* (*NCs*) exhibited excellent colloidal stability and biocompatibility for cancer theranostics (Details will be discussed in *Chapter 5*).

1.5 LnNPs in cancer nanomedicine

As described above, LnNPs possess some advantages over conventional fluorescent materials such as organic dyes and semiconductor quantum dots (QDs):[67-71] i) zero autofluorescence background to improve signal-to-noise ratio (SNR); ii) large anti-Stokes and Stokes shifts allowing for the efficient separation of the PL from the excitation wavelength; iii) narrow emission bandwidths allowing ease of multiplexed imaging; iv) high photostability making it suitable for long-term repetitive imaging. More important, deep tissue penetration are caused by the excitation and/or emission being in the NIR region that is within the biological windows (BWs), in which blood and tissue are maximally transparent (Figure. 1.8),[43] minimizing the phototoxicity to biological tissues.[67-73]

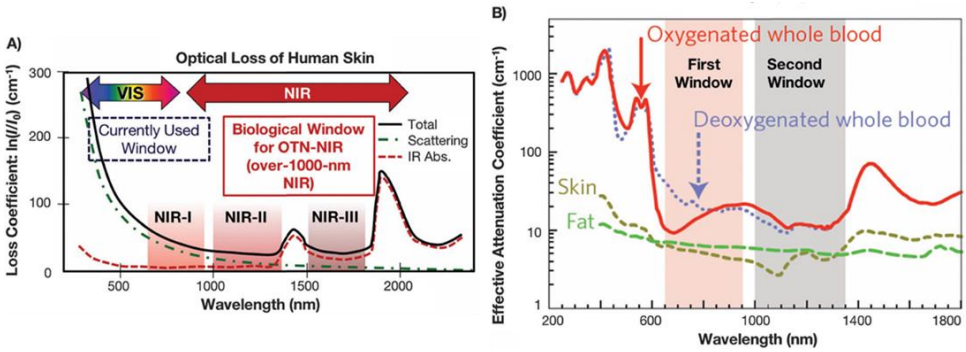

Figure 1.8 Biological windows in human skin, fat and blood.

(A) Absorption spectrum of human skin showing the first (NIR-I: 700-950 nm), second (NIR-II: 1000-1350 nm) and third (NIR-III: 1550-1870 nm) BWs. (B) Zoom-in of the two first optical windows in some biological tissues and fluids. These plots of effective attenuation coefficient (on a log scale) versus wavelength show the quantitative relevance of different body substances (oxygenated blood, deoxygenated blood, skin and fatty tissue) when aiming for deep sub-skin. [43]

A single LnNP has multiple UC emissions, for example, when doped with Tm^{3+}, UV, blue, red, and NIR emissions are observed. This allows for the development of a multifunctional nanoplatform where the UV/blue light is harnessed to trigger another light-activated modality, such as a PDT drug functionalized to their surface known as UC-PDT, while the NIR light can be used for in situ optical imaging of the tumor. Moreover, when some Ln^{3+} ions, such as Gd^{3+} or Lu^{3+} are incorporated into the matrix, further multifunctionality is attained as they can act as

contrast agents for magnetic resonance imaging (MRI) and/or for computed tomography (CT), respectively.[74, 75] These properties render LnNPs highly desirable, possessing multiple functionalities for use in a range of biomedical applications, such as cell and tissue tracking, imaging, fluorescence assays, nanothermometry, light controlled release of therapeutic moieties, as well as drug delivery.[76-78] Furthermore, they have also been considered as excellent candidates used for the development of nanotheranostics.[79-87]

1.5.1 Imaging

Medical imaging techniques are used for different types of cancer detection and diagnosis, including X-ray radiography, CT, MRI, ultrasound (US), positron emission tomography (PET), single photon emission computed tomography (SPECT), and optical imaging. They all have their own intrinsic advantages and limitations. However, the sensitivity of these current modalities does not satisfy the most sought after criteria, detecting small numbers of cancer cells.[88] NPs as new imaging contrast agents for the aforementioned imaging modalities, are becoming potentially transformative tools for the early detection of cancer. To improve lesion detection, imaging probes with more than one detection modalities, are especially desired.[89]

In 1999, UCNPs ($Y_2O_2S:Er^{3+}$, Yb^{3+} and $Y_2O_2S:Tm^{3+}$, Yb^{3+}) were first exploited for biomedical applications.[90] This study proved that UCNPs had considerable sensitivity and fluorescence stability in the detection of antigens in cell membranes and tissue sections. It consists of submicron size UCNPs (0.2-0.4 μm), which were surface-labelled with antibodies capable of binding specifically to the antigens on intact cells and tissue sections using immunohistochemistry (IHC) staining. Since then, there has been a substantial contribution to the bioimaging relying on the use of UCNPs.[91] For example, polyethylenimine (PEI) coated $NaYF_4:Yb^{3+}$, Er^{3+} UCNPs were first reported for their success in *in vitro* imaging tracking,[92] as well as the intracellular imaging of HeLa cancer cells.[93] The intracellular imaging clearly shows redistribution of UCNPs inside the cell as the incubation time increases, demonstrating the promising applications for real time imaging of cellular dynamics. The first *in vivo* imaging was demonstrated in the digestive system of live nematode C. Elegans in 2006.[76] It proved that $Y_2O_3:Yb^{3+}$, Er^{3+} UCNPs in the size range of 50-150 nm can be inoculated into the worms without notable defects during feeding. Upon excitation at 980 nm, the statistical distribution of the UCNPs in the intestines of the worms can be clearly visualized. An intriguing development was later demonstrated for *in vivo* imaging in anesthetized Wistar rats by using 50 nm $NaYF_4:Yb^{3+}$, Er^{3+} UCNPs.[92] The rats were injected with the UCNPs under the skin in the groin and upper leg regions. Using a combination of simple optical techniques and a 980 nm NIR laser, the UCNPs could be detected up to 10 mm beneath the skin, far deeper than depths managed through use of QDs. This method holds promise for providing a new

technique for imaging tissue structures at different depths and for performing minimally invasive detection. To allow imaging tissues with further deeper penetration, NIR to NIR UCNPs (both the excitation wavelength and UC emission are in the NIR range) were investigated. For example, 20-30 nm sized $NaYF_4$: Tm^{3+}, Yb^{3+} UCNPs, which have an emission around 800 nm upon 980 nm excitation, were successfully applied for *in vivo* imaging in a BALB-c mouse model.[94] Recently, more attention have been paid to 800 nm excited UCNPs based on the big absorption cross-section of Nd^{3+} around 800 nm. Since the concept of energy transfer (Nd^{3+} → Yb^{3+} → Er^{3+}/Tm^{3+}) was illustrated,[95] Nd^{3+}-doped UCNPs with optimized nanostructure have been evaluated *in vitro* and *in vivo*, and showed a higher penetration depth and a much lower undesirable overheating compared to 980 nm excited Yb^{3+} sensitized UCNPs.[48, 96, 97] However, it has the partial drawback that the emission light is mostly in the visible range of the spectrum. To overcome this limitation, a very promising strategy has been developed to exploit LnNPs for DS emission. A preference for NIR-to-NIR DSNPs with respect to NIR-to-NIR UCNPs for *in vivo* imaging has been evidenced,[98] including a higher PL quantum yield, a larger penetration depth and the possible use of light sources with a relatively low density, and a lower possibility of biological damages.

Besides the imaging utilizing the UC and DS emission, LnNPs also can be used as contrast agents for both MRI (*e.g.*, Gd^{3+}) and CT scans (*e.g.*, Lu^{3+}) to provide a multimodal imaging platform. For example, Gd^{3+}-based NPs are generally developed for the usage of T_1 contrast agents, which increase signal density in T_1-weighted MR imaging (bright images).[99] Previous studies reported that Gd^{3+}-based LnNPs could achieve high positive contrast in T_1-weighted images only when the particle size was less than 10 nm,[100, 101] because Gd^{3+} ions on the surface of the LnNPs make up the major contributions to T_1 relaxivity enhancement.[101-103] In this regard, LnNPs were designed with a thin $NaGdF_4$ layer deposited on Gd^{3+}-free $NaYF_4$:Er^{3+}, Yb^{3+} cores for bimodal T_1-weighted MR imaging and UC fluorescent imaging, achieving a T_1 relaxivity (r_1) value of 6.18 $mM^{-1}s^{-1}$.[104] $NaLuF_4$:Yb^{3+}, Tm^{3+} core@SiO_2 shell NPs, complemented with the complex Gd-DTPA as the surface ligand, have been also designed for trimodal NIR-to-NIR UC, MRI and CT imaging.[105] Beside the ability to shorten T_1 relaxation, Gd_2O_2S:Eu^{3+} LnNPs show a strong transverse relaxivity (r_2) and a strong X-ray absorption, allowing for their use as contrast agents for T_2-weighted MRI and CT.[106] In fact, the T_2 relaxivity (r_2) of paramagnetic LnNPs increases with the magnetic field whereas the r_2 of conventional T_2 contrast agents (iron oxide based particles) gets saturated at magnetic field strengths >1T.[107] In this thesis, we also investigated the T_1/T_2 relaxivities of β-$NaGdF_4$:Er^{3+}, Yb^{3+} UCNPs with various morphologies at high magnetic field (3T, 7T, and 9.4T). All of these studied UCNPs demonstrate promising T_2 relaxivity and significant negative contrast enhancement in T_2-weighted MRI (Details will be discussed in *Chapter 4*).[108]

1.5.2 Phototherapy

Phototherapy allows the use of light; a non-invasive, spatially, and temporally controllable stimulus, to achieve specific outcomes and reduce side effects. In addition, the ability to control parameters such as wavelength, intensity, and duration of exposure, provide an added degree of control. To this end, phototherapies such as PDT, PTT, photo-controlled release of drugs, and combination therapies involving the synergistic use of two or more of the previous techniques have come to the fore. The applications of LnNPs for phototherapy are introduced as below.

Upconversion induced Photodynamic Therapy (UC-PDT): PDT has been widely administrated for cancer treatment including skin, prostate, head and neck, pancreas, breast, and lung cancers.[109-112] It utilizes photosensitizers (PS) as light-sensitive drugs to treat the target tissue locally upon the irradiation of light with appropriate wavelengths. The excited PS interacts with surrounding oxygen molecules to generate reactive oxygen species (ROS), including singlet oxygen ($^1O_2$), which cause oxidative damage to biological substrates and ultimately cell death. As shown in Figure 1.9, the PS initially absorbs a photon that excites it to the first excited singlet state and can then relax to the more long lived triplet state. This triplet PS can interact with molecular oxygen in two pathways, type 1 and type 2, leading to the formation of ROS.[113] In addition to having less systemic side effects and cumulative cytotoxicity, PDT is able to overcome the multi-drug resistance caused by chemotherapy. Moreover, unlike chemotherapeutic drugs and radiotherapy that tend to be immunosuppressive, PDT is capable of triggering an antitumor immune response by activation of the innate and/or adaptive immune system, subsequently prolonging survival of patients.[114, 115] However, the typical PS excitation wavelengths in the visible spectral range have limited tissue penetration depth. For this reason, PDT is usually used to treat tumors on or just under the skin, or on the lining of internal organs or cavities, thus being less effective in treating large and deep seated tumors.[116] In order to reach deep-seated tumors, NIR light within the BWs could be used;[43,33] yet, most efficient PS cannot be excited with NIR light directly. To overcome

this crucial challenge, the synergistic combination of UCNPs and PS has been proposed and explored in recent years.[80, 117-121]

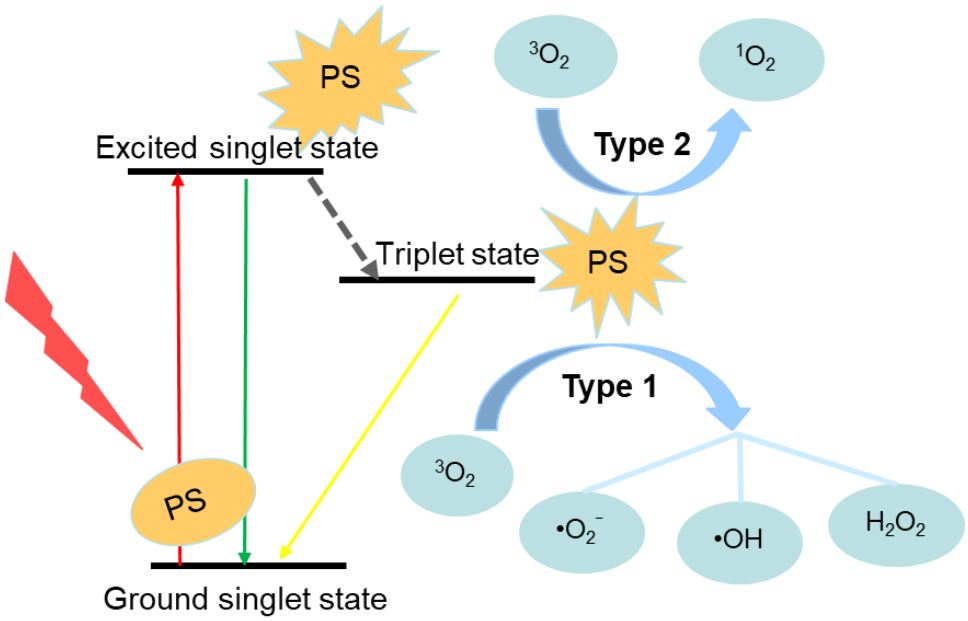

Figure 1.9 Schematic illustration of photodynamic therapy.

Many studies have successfully combined UCNPs and PS for UC-PDT, with most of them using $NaYF_4$: Er^{3+}, Yb^{3+} or $NaYF_4$:Tm^{3+}, Yb^{3+} as the UC material and different surface modifications to create a UC-PDT system, with either one PS, such as ZnPc, Merocyanine 540 (MC 540), Chlorine 6 (Ce6), or more, in which case their absorption bands match different UC emissions of the UCNPs.[121] The first work combining UCNPs and PS was published in 2007.[117] In this study, $NaYF_4$:Er^{3+}, Yb^{3+} was used in the core to generate intense visible emission at ~540 nm, exciting the MC540 incorporated in the outer silica shell. The results demonstrate the ability of such a concept of UC-PDT in breast cancer cells. However, the limited spectral overlap between the donor and acceptor restricts the $^1O_2$ production yield. An improvement in energy transfer between the UCNP and the PS can be achieved using additional Ln^{3+} as dopants. Following this idea, a core/shell $NaYF_4$ UCNPs was prepared with Tm^{3+}, Yb^{3+} in the core (mainly emitting blue light) and Er^{3+}, Yb^{3+} in the shell (mainly emitting green light). The emitted light was used to activate monomalonic fullerene (C60MA) with a broad absorption band, and the *in vitro* experiments on cancer cells verified the efficient PDT effects of the nanoplatform.[119] The rapid progress of UC-PDT as well as successful *in vitro* results has motivated further *in vivo* evaluation of these UCNPs. The first *in vivo* UC-PDT study was shown in 2012.[118] The researchers loaded Ce6 onto $NaYF_4$ with polyethylene glycol (PEG), forming a supramolecular UCNP-Ce6 complex, which was used for NIR light-induced PDT treatment of tumors in an animal model. Engineered multifunctional nanoplatforms have also emerged to realize the twin-objective of accurate diagnosis with imaging followed by the therapy. For example, a nanocomplex was developed using mesoporous-silica-coated

UCNPs as an energy transducer to convert deeper penetrating NIR light to Vis light, which is then absorbed by both MC540 and ZnPc. The close proximity between the two moieties encased in the mesoporous silica shell and the UC core allows for efficient energy transfer from the core to the PS. Subsequent *in vivo* studies show significant tumor growth inhibition in PDT-treated melanoma tumor-bearing mice by intravenous injection of the studied nanocomplex (Figure 1.10).[80]

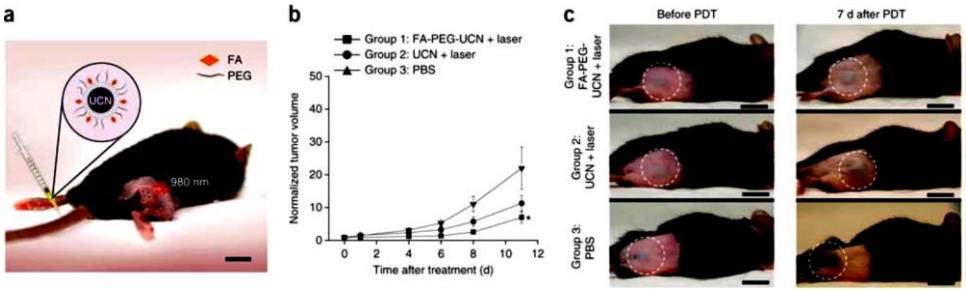

Figure 1.10 Schematic diagram showing UCNPs-based targeted PDT in a mouse model of melanoma intravenously injected with UCNPs. [80]

To date, even though mesoporous silica and their composites with UCNPs are considered as a common method applied for UC-PDT[80, 120, 122, 123], many problems as described in *section 1.4*, still need to be solved. Furthermore, in the UC-PDT system, cytotoxic $^1O_2$ is generated by PS that are activated *via* an ET from the NIR excited UCNPs. The ET can be either radiative[82, 117, 120, 124, 125] or non-radiative[118, 126-129], and its efficiency is affected by the distance between the UCNPs (energy donors) and PS (energy acceptors). In this thesis, we developed a theranostic NC for use as image-guided UC-PDT. $NaGdF_4$:Er^{3+}, Yb^{3+} UCNPs and ZnPc were simultaneously co-encapsulated into the NCs, advantageously minimizing the distance between the two, as compared to the conventional loading of PS in the mesoporous silica coating. The encapsulated $NaGdF_4$ UCNPs also act as a negative contrast agent used for MRI (Details will be discussed in *chapter 5*).[130]

Photothermal therapy (PTT): PTT is a treatment strategy based on the use of laser light induced thermal treatment where the high temperatures produced through optical absorption can cause thermal damage to biological structures (*e.g.*, denaturation of proteins, impairment of RNA/DNA) and ultimately cell death (Figure 1.11).[131-135] For example, cancer hyperthermia (or thermal therapy) is based on externally inducing an increment in the tumors' temperature up to cytotoxic levels (43-45 °C).[136] PTT is attracting considerable attention because of the possibility of controlling the incorporation of light-activated heating NPs into disease tissues (*e.g.* tumors), allowing for high heat deposition in the tumor area at low laser light intensities and thus minimizing the damage in the surrounding healthy tissue.[137] Further reduction of non-desired light absorption by healthy tissues can be achieved by using specific laser wavelengths lying in the so-called BWs.[138, 139] In addition to the advantages of localized

treatment, minimal invasiveness, less systemic side effects and cumulative cytotoxicity, PTT is also able to enhance the susceptibility of cancer cells to other treatment,[140] such as chemotherapy,[141] radiotherapy,[142] and immunotherapy.[143-147]

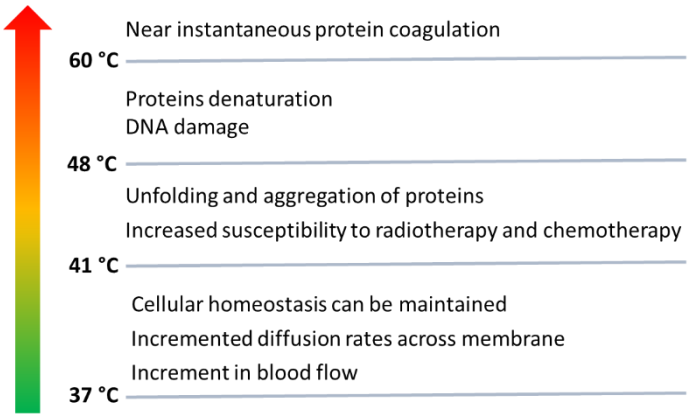

Figure 1.11 Schematic diagram of the variety of effects caused by the different thermal treatments as classified by the corresponding operating temperature. [132]

Different types of nanomaterials (inorganic and organic) have been explored for cancer PTT, including metal-based nanostructures (*e.g.*, gold, silver, and copper), carbon-based NPs, QDs, organic molecules and polymers.[132, 148-151] To date, gold-based nanostructures are the most investigated for PTT. For example, gold-silica nanoshells (GSN) have been approved in a clinical trial to focally ablate low-intermediate-grade tumours within the prostate.[152] This trial shows that GSN directed laser ablation is a safe and technically feasible procedure for the targeted destruction of prostate tumours. However, its therapeutic efficacy has not been fully established. Compared with the inorganic nanomaterials, small organic dyes have good biodegradability, the ease of renal clearance, and moreover their photothermal features are flexible based on the modification of their chemical structures. [153-160] For example, indocyanine green (ICG, cyanine-based dyes), which is approved by the US food and drug administration (FDA) as an optical imaging agent, has also been investigated as a PTT agent for cancer treatment in the past decades. Nevertheless, the photothermal conversion efficiency of most studied cyanine dyes is overshadowed by their NIR fluorescence.[153-156] Most recently, perylene diimide (PDI) derivatives, a class of pigments, have gained a research attention as NIR photoacoustic[161-164] and PTT[165, 166] agents, due to their exceptional chemical, thermal, and optical stabilities in air and water.[167]

Precise PTT requires selective accumulation of PTT agents in the region of interest and image-guided treatment with in situ temperature monitoring.[168, 169] To ensure that the desired temperature is reached, but not exceeded, the temperature of the treated area should be monitored throughout the treatment.[135, 170, 171] However, the equipment and techniques currently available to perform such types of PTT present some limitations and need further improvements. The breakthrough of nanotechnology and its potential application in PTT

enhances the efficiency and selectivity of treatment. In addition, hybrid nanostructures allows combination therapies (PTT combined with chemotherapy, radiotherapy or immunotherapy), imaging and real-time thermal information feedback during PTT, to be accomplished in a single NP. This reduces treatment complexity and provides better therapeutic efficacy. Indeed, the combination of heating, temperature monitoring as well as imaging-based tracking of NPs, is an ambitious goal that aims to extend and facilitate the application of PTT. Recently, hybrid nanostructures have been proposed, by adding a thermometric capability to the PTT probes.[172-175] Though these approaches constitute interesting proof-of-concept experiments, in most of the studies temperature sensing was based on the thermal coupled VIS luminescence rather than NIR wavelength, and the size of hybrid nanostructures in some studies are too large (much more than 200 nm) for in vivo applications. In this thesis, we report an original theranostic NCs working entirely in the NIR for image-guided PTT while recording temperature *in situ* (Details will be discussed in *Chapter 6)*.

Photo-triggered Drug Release: The majority of the existing photo-responsive drug carriers usually require UV or short VIS wavelength excitation, which would seriously hinder their application in living systems. Hence, NIR-to-UV/VIS UCNPs have promising potential in the design of photo controlled drug delivery at a desired location and specific time. Recently, UCNPs have been combined with photo-responsive drug carriers to induce drug release using NIR light. Upon excitation with a NIR laser, the UCNPs convert the incident light to UV or VIS that releases the drugs in two different ways:[77, 79, 176-182] i) the first one involves an additional component that absorbs the UC light and exerts an effect on the neighbouring environment (*e.g.*, causing changes in pH, or temperature) to result in the drug release. ii) The second approach initiates a photoreaction in a photo-responsive compound (*e.g.*, photo-cleavage, or photo-isomerization) engineered on the surface of UCNPs, to cause drug release directly using the UC light. For example, G. Jalani, et al. demonstrates the NIR-triggered delivery of macromolecules from UCNPs coated with a photo-cleavable hydrogel.[77] $LiYF_4$:Yb^{3+}, Tm^{3+}@SiO_2 are individually coated with a layer of chitosan (CH) hydrogel cross-linked with a photo-cleavable cross-linker (PhL). Fluorescent bovine serum albumin (FITC-BSA) were also encapsulated inside the gel as a model macromolecule drug. Under 980 nm excitation, the UC UV emission cleaved the PhL cross-links and instantaneously liberates the FITC-BSA. The release was immediately arrested if the excitation source was switched off, and the dose and rate of drug release could be tuned by changing the laser power and irradiation time.

1.5.3 Luminescence Nanothermometry

Temperature is one of the most important parameters influencing the dynamic and viability of biological systems ranging from the simplest cell to the most sophisticated organism.[133-135]

Since temperature is strongly linked to cellular functions, intracellular temperature can actually be used as an indicator of cellular activity.[183] In addition, a local temperature increase in the cellular environment is the basis of hyperthermia therapies as described in *section 1.5.2*. In order to measure temperature during the PTT, remote (non-invasive) thermal sensing within the tissue, and not the surface, is preferred. In the current clinical practice of monitoring temperature in the deep-seated tumors, a thin plastic catheter with thermal probes is implanted either under CT guidance percutaneously or intraoperatively at the time of explorative surgery (*e.g.* incisional biopsy).[170] This thermometry approach is invasive to patients and has some disadvantages including pain, risk of infections, and a limited number of measuring points. The emergence of NPs exhibiting temperature dependent luminescence is of particular interest as they can be incorporated into living specimens to provide remote-sensing *via* excitation and measurement of emitted light traveling through the sample. Research in luminescence nanothermometry is rapidly growing to exploit remote thermal sensing for intracellular temperature detection as well as monitoring and control of laser induced thermal treatment (*i.e.* hyperthermia).

Ratiometric nanothermometers: Luminescence nanothermometry exploits the relationship between temperature and luminescence properties to achieve thermal sensing from the spatial and spectral analysis of the light generated from the object to be thermally imaged. The grouping of luminescence nanothermometry into different classes is based on the particular parameter of luminescence, which is analyzed (*e.g.* intensity, band shape and width, or lifetime), and from which the thermal reading is ultimately extracted. Among these, ratiometric nanothermometers (whose luminescence spectra consist of several lines/bands with a relative intensity that is strongly dependent on temperature) represent a significant advancement over intensity-based nanothermometers since the temperature reading is not affected by fluctuations in the concentration of luminescent centres, thus achieving more accurate thermal reading. Moreover, unlike lifetime-based nanothermometry, which need a specific experimental set-up to perform time-resolved spectroscopy, ratiometric nanothermometry requires a simpler experimental set-up. The mechanism behind ratiometric nanothermometry depends on whether the luminescence lines under analysis are generated by a single type of Ln^{3+} or by a combination of different Ln^{3+}. For luminescence lines/bands generated by different emitting centres, temperature induced variation in band-shape is due to either different thermal quenching of each centre or thermally induced changes in energy transfer rates among these centres. On the other hand, for luminescence spectra generated by a unique centre, changes to the band-shape is instead due to thermally induced population re-distribution among the different energy levels of the emitting centre.[184]

Ln^{3+} used for ratiometric nanothermometers with single emitting centre must have abundant energy states including different pairs of thermal coupled states whose populations follow the Boltzmann distribution.[185] To be in a thermal coupled energy state, the upper and lower electronic energy levels must be very close to each other, but the population at the lower electronic energy level must not reach the upper energy levels by absorbing heat. Empirically, the energy gap between thermal coupled energy states ranges from 200 to 2000 cm^{-1}, which guarantees that the two emission bands are spectrally separated for respective characterization. The temperature dependent luminescence intensity ratio (LIR) between this two energy levels, is determined by the equation as below. [186]

$$LIR = A \times exp\left(-\frac{\Delta E}{k_B T}\right)$$

where *A* is a constant, Δ*E* is the energy gap between the two excited states, k_B is the Boltzmann constant and *T* is the temperature in kelvin. From the experimentally determined intensity ratio, a temperature reading can thus be reached. In this case, the thermal dependence is very stable as most parameters affecting the luminescence of the thermalized states do not affect the population balance between them. Appreciable thermal sensitivity would only be achieved if the energy separation between emitting levels is small, so that small temperature changes can induce large population re-distributions.

Characterization of nanothermometers: PL nanothermometers are nominally characterized by their relative thermal sensitivity, S_r, thermal uncertainty, δT, and measurement repeatability, *R*. The thermal sensitivity defines the rate of change of thermometric parameter, Δ, relative to temperature, *T*. In order to directly compare different nanothermometers, regardless of their working principle, composition, or experimental setup, the thermal sensitivity is normalized to the value of Δ, giving rise to the relative thermal sensitivity. *Sr* is typically expressed in $\%\cdot K^{-1}$ or $\%\cdot {}^{\circ}C^{-1}$:

$$S_r = \frac{1}{\Delta}\left|\frac{\partial \Delta}{\partial T}\right|$$

The temperature uncertainty (or temperature resolution), δT, is the smallest temperature that can be resolved with a given nanothermometer. δT can be determined experimentally by evaluating the fluctuation in time of the measured temperature given by a thermometric parameter, Δ. From the cumulative of these measurements, standard deviation from the actual set temperature represents the uncertainty δT. Alternatively, δT can be estimated as:

$$\delta T = \frac{1}{S_r}\frac{\delta \Delta}{\Delta}$$

Here, $\delta\Delta/\Delta$ is the relative uncertainty of Δ, which depends on the measurement setup and is estimated from Δ error. For intensity based nanothermometers, this value depends on the SNR of the emission spectrum, and can be improved by using longer signal acquisition times and/or averaging of consecutive measurements.

The repeatability characteristic, *R*, describes how well a nanothermometer provides accurate temperature measured repeatedly under the same circumstances, and is given as:

$$R = 1 - \frac{max|\Delta c - \Delta i|}{\Delta c}$$

Δ*c* is thermometric parameter extracted from a calibration curve at a given temperature and Δ*i* represents the thermometric parameter at that temperature of repeated measurements *i*. **LnNPs used for nanothermometers:** Ln^{3+} (such as Er^{3+}, Tm^{3+}, Ho^{3+} or Nd^{3+}) -based nanothermometers are promising candidates used for biomedical applications.[82, 184, 187-189] As for the single-centre ratiometric nanothermometry, Er^{3+} is probably most widely used as it typically shows a very intense green emission that consists of two luminescence bands centred at 525 and 545 nm, whose relative intensity is strongly temperature dependent.[186, 187, 190-194] These two bands can be easily populated through multiphoton absorption of NIR radiation (UC) with the assistance of sensitizer ions such as Yb^{3+}.[195] Figure 1.12 (A)

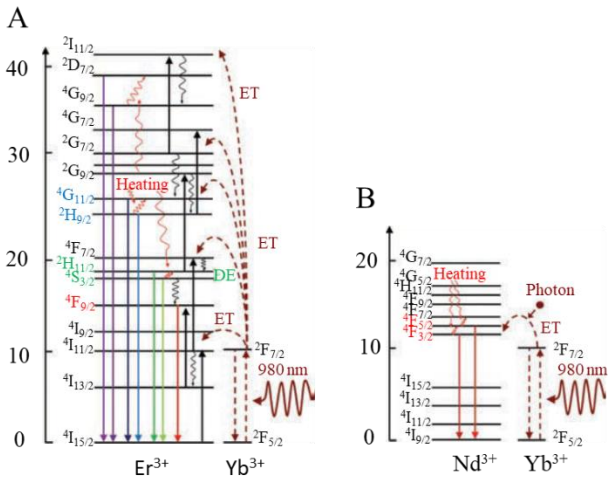

Figure 1.12 Schematic diagram of optical thermal sensing through (A) Er^{3+}/Yb^{3+}, (B) Nd^{3+}/Yb^{3+} energy transfer under 980 nm NIR excitation.[196]

demonstrates the mechanisms of optical thermal sensing through Er^{3+}/Yb^{3+} energy transfer under 980 nm NIR excitation.[196] Consequently, nanothermometry based on this effect was used for biomedical applications.[187,197-199] The first intracellular nanothermometry using UCNPs was realized by F. Vetrone in 2010.[187] In this pioneering work, the UC emission of $NaYF_4$:Er^{3+}, Yb^{3+} UCNPs obtained at two different temperatures is shown in Figure 1.13. The presence of two thermally coupled levels is evidenced by the temperature induced change in ratio of the 525 and 545 nm luminescence bands. The temperature variation of the LIR follows

an almost linear relationship up to 40 °C allowing for the straight forward determination of temperature. Once the $NaYF_4:Er^{3+}$, Yb^{3+} nanothermometers were calibrated, they were introduced to HeLa cancer cells to monitor cell apoptosis caused by an external heating source. A 920 nm laser beam was focused inside the cell so that the Er^{3+} luminescence was induced through a two-photon absorption process involving the excited states of Yb^{3+} and was collected by the same microscope objective lens that was used for focusing the excitation laser beam inside the cell. A subsequent spectral analysis of the intracellular luminescence non-invasively and accurately determined the intracellular temperature.

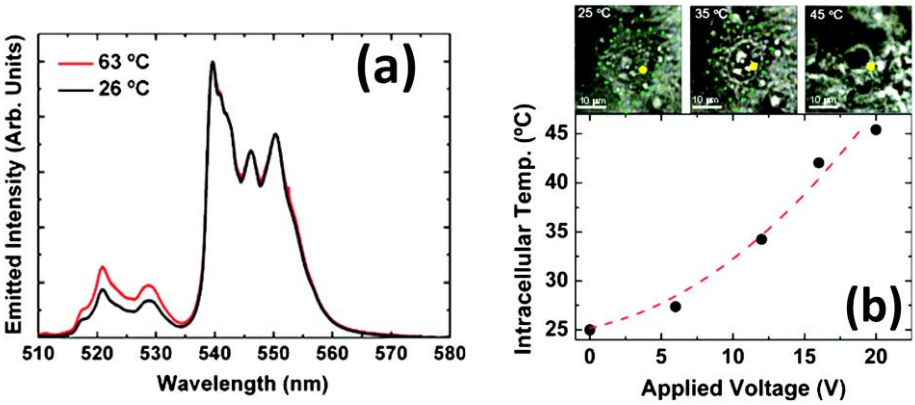

Figure 1.13 Intracellular temperature determined by the $NaYF_4:Er^{3+}$, Yb^{3+} nanothermometers.

(a) Luminescence emission spectra generated from $NaYF_4:Er^{3+}$, Yb^{3+} UCNPs under 920 nm excitation as obtained at two different temperatures. (b) Intracellular temperature (as obtained from the spectral analysis of the intracellular Er^{3+} luminescence) as a function of the applied voltage to a resistance attached to the micro-chamber containing the cell. The optical transmission images of the cell at different applied voltages are also shown. [187]

For the sake of *in vivo* practice, much effort has been made to bring both the excitation and emission wavelengths used for nanothermometry into the BWs. In the case of Nd^{3+}/Yb^{3+} co-doped LnNPs under 980 nm illumination, as depicted in Figure 1.12 (B), the population of the Nd^{3+} excited levels does not follow an upconversion mechanism but a phonon-assisted energy transfer process from the $^5F_{5/2}$ excited level of Yb^{3+} to the $^4F_{3/2}$ excited level of Nd^{3+} caused by the energy mismatch between the electronic levels involved. Subsequently, radiative relaxation can take place from the NIR emitting levels of Nd^{3+}. In fact, it is this emission of NIR light that triggered an increasing interest in Nd^{3+}-doped LnNPs when seeking optical probes for biomedical applications, and ultimately opens new avenues for the use of optical probes in the biomedical field. Moreover, as seen in Figure 1.12 (B), the energy gaps between the $^4F_{3/2}$, $^4F_{5/2}$, and $^4F_{7/2}$ levels are relatively small, so that the $^4F_{5/2}$ and $^4F_{7/2}$ states can be thermally populated from their lower energy levels. This makes it suitable for thermal sensing. For instance, a previous study revealed the temperature dependence of the NIR emissions originating from the $^4F_{7/2}/^4S_{3/2} \rightarrow {}^4I_{9/2}$ (~750 nm), $^4F_{5/2}/^2H_{9/2} \rightarrow {}^4I_{9/2}$ (~803 nm), and $^4F_{3/2} \rightarrow {}^4I_{9/2}$

(~863 nm) transitions of Nd^{3+} ions in Nd^{3+}/Yb^{3+} co-doped oxyfluoride glass ceramic[200] and in CaWO4 powder[201] under 980 nm laser excitation. In another study,[202] upon the direct excitation of Nd^{3+} ions in heavily Nd^{3+}-doped $NaYF_4$ nanoparticles using a 830 nm laser, thermal sensing was achieved by monitoring the absolute NIR luminescence intensity or by measuring the intensity ratio from the emission of the two Stark sub-levels of the $^4F_{3/2}$ multiplet in the Nd^{3+} ions. Therefore the temperature dependent population of thermally coupled Stark sub-levels in Nd^{3+}-doped DSNPs has been demonstrated to be suitable for ratiometric nanothermometry (Figure 1.14).[188]

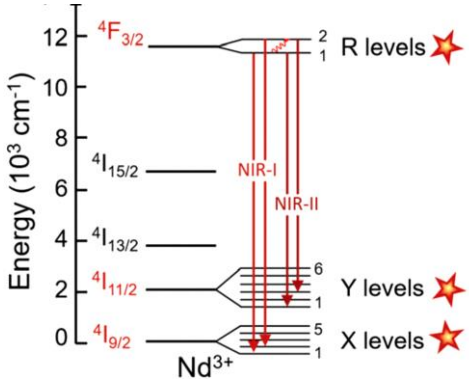

Figure 1.14 Stark sub-levels of Nd^{3+} levels $^4F_{3/2}$, $^4I_{11/2}$ and $^4I_{9/2}$. [188]

The fine Stark structure of the bands in the $^4F_{3/2} \rightarrow {}^4I_{9/2}$ transition around 880 or 940 nm are usually employed in temperature sensing, where temperature is correlated to the PL intensity ratio of the two emission bands, respectively originating from the thermally coupled $^4F_{3/2}$ (R_1) and $^4F_{3/2}$ (R_2) energy levels.[202-205] The most intense PL around 1060 nm, stemming from the $^4F_{3/2} \rightarrow {}^4I_{11/2}$ transition, has recently been used for PL nanothermometry.[82, 174, 206-208] More recently the possibility of using Nd^{3+}-doped $LiLuF_4$ core/shell DSNPs as single-band NIR nanothermometers was explored.[208] In this study, the thermometric parameter defined for the most intense Nd^{3+} emission around 1060 nm, shows higher temperature sensitivity (~0.49% $°C^{-1}$), and lower temperature uncertainty (0.3 °C) as compared to the thermometric parameters defined for the 880 and 1320 nm Nd^{3+} emissions, and represents a significant improvement for Nd^{3+}-based single-band PL nanothermometry, demonstrating its potential for integration within more sophisticated multifunctional theranostic nanostructures.

Since the first report of Ln^{3+}-based nanothermometry in 2002[209] the field of optical nanothermometry has clearly seen significant advancements through the development of novel dopant/host combinations for improved sensitivity in practically relevant temperature ranges. A future shift from upconversion-based to NIR light-based nanothermometry for *in vivo* applications is also greatly desired.

In this thesis, we developed an original theranostic NC co-encapsulating LnNPs and small organic therapeutic agents in one-pot, allowing for image-guided, NIR regulated phototherapy. LnNPs could be UCNPs or DSNPs equipped with multifunctional modalities. Therapeutic agents could be PDT drugs, PTT agents, or chemotherapeutic drugs. These hybrid NCs demonstrate excellent theranostic capability and high potential for future *in vivo* applications.

2 AIM AND OUTLINE

2.1 Objectives

The overall objective of this thesis is to develop theranostic NCs, co-encapsulating multifunctional LnNPs and therapeutic agents, allowing for image-guided, NIR-regulated phototherapy. In order to realize the overall objective, we specifically aim for the following.

2.1.1 One-step thermolysis for morphology controlled synthesis of UCNPs

- To synthesize β-$NaGdF_4$:Er^{3+}, Yb^{3+} UCNPs with diverse morphologies by optimized one-step thermolysis approach
- To investigate the mechanism underlying the formation of nanorods
- To characterize the optical and magnetic relaxivity of the synthesized UCNPs with respect to their morphologies

2.1.2 One-pot encapsulation for the synthesis of theranostic NCs

- To establish an original one-pot polymeric micelle/silica encapsulation approach possible for passive and active targeted drug delivery
- To develop theronostic NCs (UCNPs-ZnPc@NCs) for MRI-guided UC-PDT: co-encapsulating $NaGdF_4$:Er^{3+}, Yb^{3+} UCNPs and ZnPc by the one-pot strategy
- To *in vitro* evaluate the UC-PDT efficacy and negative MRI contrast enhancement induced by UCNPs-ZnPc@NCs
- To further modify the one-pot encapsulation approach for enhanced fluorescence and nuclear-targeted drug delivery

2.1.3 Theranostic NCs engineered for imaging, heating, and thermal sensing

- To synthesize $LiLuF_4$:Nd^{3+}@$LiLuF_4$ DSNPs *via* a two-step multilayer thermolysis approach
- To establishing theranostic NCs, co-encapsulate $LiLuF_4$:Nd^{3+}@$LiLuF_4$ DSNPs and dicyclohexylamino substituted PDI (sPDI) (DSNPs+sPDI@NCs) for CT-guided NIR-regulated PTT
- To characterize the thermal sensitivity and photothermal stability of DSNPs+sPDI@NCs
- To *in vitro* evaluate the PTT efficacy and positive CT contrast enhancement induced by DSNPs+sPDI@NCs

2.2 Thesis organization

This thesis is divided into seven chapters and organized as follows:

Chapter 1 Introduction: brief overview of the background concepts involved;

Chapter 2 Aim of the thesis: outline of the main goals of this thesis;

Chapter 3 Experiments and characterization: description of experimental details and main characterization techniques;

Chapter 4 One-step thermalysis, and publication related to this chapter is

Miao Wang, Yu Zhang, Qiaofeng Yao, Michael Ng, Ming Lin, Xu Li, Kishore Kumar Bhakoo, Alex Y. Chang, Federico Rosei, and Fiorenzo Vetrone. Morphology Control of Lanthanide Doped $NaGdF_4$ Nanocrystals *via* One-Step Thermolysis. ***Chem. Mater.*** 2019, 31, 14, 5160–5171.

Chapter 5: One-pot encapsulation, and publication related to this chapter is

5.1 M. Wang, Y. Zhang, M. Ng, A. Skripka, T. Cheng, L. Xu, K. K. Bhakoo, A. Y. Chang, F. Rosei and F. Vetrone. One-pot synthesis of theranostic nanocapsules with lanthanide doped nanoparticles. ***Chem. Sci.***, 2020, 11, 6653–6661.

5.2 Yu Zhang,‖ **Miao Wang**,‖ Grace H. B. Ng,‖ Mingyan Tan, Cathleen Teh, Alex Yuang-chi Chang, Federico Rosei, John Wang, Fiorenzo Vetrone, Xu Li. Silica shell stabilized nanocapsules for Fluorescence-Enhanced and Nuclear-Targeted Drug Delivery. (In preparation)

‖, the authors have the same contribution to the manuscript.

Chapter 6: Theranostic NCs, and publication related to this chapter is

Miao Wang, Artiom Skripka, Yu Zhang, Ting Cheng, Michael Ng, Xuan Sun, Xu Li, Kishore Kumar Bhakoo, Alex Y. Chang, Federico Rose, Fiorenzo Vetrone. Theranostic Nanocapsules engineered for heating, imaging and thermal sensing. (Ready for submission to ACS NANO)

Chapter 7 General conclusions and perspectives: summary of the main results and discussion on potential directions for future work.

I performed most of work in this thesis, however, some parts were conducted through collaboration with our group members. More specifically, DSNPs used in chapter 5 were synthesized by Dr. Ting Cheng. Nanothermometry experiments were conducted by Artiom Skripka, who also assisted with the PL measurements. I wrote the first drafts of the manuscripts for publication and subsequently made any necessary revisions.

3 EXPERIMENTS AND CHARACTERIZATION

In this chapter, the experimental details and characterization of LnNPs (UCNPs and DSNPs), theranostic NCs, and the *in vitro* evaluations are described. In the first section, we mainly focus on the synthesis of $NaGdF_4$:Er^{3+} (2 mol%), Yb^{3+} (20 mol%) UCNPs with diverse morphologies (nanorods, nanospheres, nanoprisms, nanoplates, and nanodiscs) in a modified single-step thermolyisis approach (*Chapter 4*). We also synthesized $LiLuF_4$:Nd^{3+}@$LiLuF_4$ DSNPs by a two-step multilayer thermolysis approach (*Chapter 6*). In the second section, we focus on the development of NCs with LnNPs for biomedical applications. First we developed an original one-pot synthesis method to co-encapsulate $NaGdF_4$:Er^{3+} (2 mol%), Yb^{3+} (20 mol%) UCNPs and ZnPc for UC-PDT, and then we further modified this approach to achieve enhanced fluorescence and nuclear-targeted delivery of their payloads (*Chapter 5*). Finally in *Chapter 6,* we successfully extended the one-pot encapsulation approach to synthesize theranostic NCs, co-encapsulating $LiLuF_4$:Nd^{3+}@$LiLuF_4$ DSNPs and sPDI for precise PTT. In the last section, we mainly describe the characterization and evaluation of the developed LnNPs and theranostic NCs for biomedical applications.

3.1 Synthesis of LnNPs

All the LnNPs studied in this thesis are synthesized using modified thermolysis approach, which allowed direct decomposition of the metal trifluoroacetate precursors.

Materials: Gadolinium oxide (Gd_2O_3, 99.99%), erbium oxide (Er_2O_3, 99.99%), ytterbium oxide (Yb_2O_3, 99.99%), lutetium oxide (Lu_2O_3, 99.99%), neodymium oxide (Nd_2O_3 99.999%), oleic acid (OA, technical grade, 90%), 1-octadecene (ODE, technical grade, 90%) are purchased from Alfa Aesar (USA). Trifluoroacetic acid (CF_3COOH, 99%), sodium trifluoroacetate (CF_3COONa, 98%), lithium trifluoroacetate (CF_3COOLi, 98%), and oleylamine (OM, 70%) are purchased from Sigma-Aldrich (USA). All chemicals are used without further purification.

Preparation of precursors: First, the metal trifluoroacetate precursors were prepared *via* addition of a 10 mL mixture of distilled water/trifluoroacetic acid (1:1) to a 50 mL round-bottom flask containing the designated amount of Ln_2O_3 based on the composition of the proposed LnNPs. The solution was heated at 80 °C with stirring in excess of 6 h until it became clear and then the temperature was decreased to 60 °C to evaporate the residual liquid.

3.1.1 Synthesis of UCNPs

β-$NaGdF_4$:Er^{3+} (2%), Yb^{3+} (20%) UCNPs were synthesized by ***one-step thermolysis***. 12.5 mL of OA and 12.5 mL of ODE were added to a 100 mL 3-neck round-bottom flask (Solution

A). Approximately 2.50 × 10^{-3} mol of CF3COONa was added to the dried precursor solids along with 7.5 mL of OA and 7.5 mL of ODE (Solution B). The resulting solutions were degassed with stirring at the designated temperature (150 °C for Solution A and 125 °C for Solution B) for 30 min to remove residual water and oxygen. Subsequently, Solution A was heated to 315 °C under a gentle flow of argon gas for 30 min and adjusted to the designated temperature (310 °C − 320 °C) before addition of Solution B using a mechanical pump system at a rate of 1.5 mL/min (Harvard Apparatus 11 Elite, USA). The system temperature was immediately tuned to 315 °C as soon as the injection was terminated and was left to stir vigorously for an additional 1-3 h. At various time points after termination of the injection, 2 mL of the solution was removed from the reaction system. After the reaction was completed, the solution was allowed to cool to room temperature, and the synthesized UCNPs were precipitated using absolute ethanol and centrifuged at 6500 rpm for 15 min. The solids were then washed with a mixture of hexane/ethanol (1:4) twice to remove any impurities.

3.1.2 Synthesis of DSNPs

$LiLuF_4:Nd^{3+}$ (10 mol%)@$LiLuF_4$ DSNPs were prepared by two-step multilayer thermolysis (core/shell engineering). First nuclei (FN) formation and stabilization were involved for core synthesis.

FN formation: Dried Ln (Lu and Nd) trifluoroacetate precursors were mixed with 1.0 mmol lithium trifluoroacetate, 5 mL OA, 5mL OM and 10 mL ODE. Solution was degassed at 110 ºC under vacuum for 30 min. After degassing, the solution was back-filled with argon, the temperature was raised to 330 ºC. After 1 h reaction, the solution was then cooled to room temperature (RT). Magnetic stirring was maintained during the process. A small portion (0.5 mL) of FN was sampled for characterization.

Stabilization: Core DSNPs were formed by the stabilization of FN with excess of OA and ODE. FN (0.5 mmol, ~ 10 mL of stock solution) was mixed with 15 mL each of OA and ODE in a 100 ml three-neck round bottom flask. Similarly, the solution was degassed at 110 ºC under vacuum for 30 min first, followed by 1 h reaction at 330 ºC in argon environment. A small portion (0.5 mL) of core RENPs was sampled for characterization after cooling.

Core shelling: Shelling of the core material was achieved *via* the hot-injection approach. Two solutions were prepared. Solution A was prepared by adding equal parts of OA and ODE into 0.1 mmol of stabilized DSNPs core in 100 mL three-neck round bottom flask. The total volume of solution A was 20 mL. Solution B was a mixture of 0.2 mmol Ln shelling precursors, 0.2 mmol lithium trifluoroacetate, and 10 mL each of OA and ODE. Both solutions were degassed under vacuum at 110 ºC for 30 min. After degassing, temperature of Solution A was raised to

315 ºC under argon. Solution B was then injected into Solution A using a syringe and pump system (Harvard Apparatus Pump 11 Elite, USA). The injection rate was 1.5 mL/min. Solution cooled to RT after 1 h reaction. Resultant core/shell DSNPs were precipitated with ethanol, and washed sequentially with hexane/ethanol, toluene/acetone and hexane/ethanol (1/4 v/v in each case) *via* centrifugation (5400 RCF).

3.2 Synthesis of polymeric micelle/silica nanocapsules (NCs)

NCs with various payloads were prepared by modifying the interfacial templating condensation approach (***one-pot encapsulation*****)**

Materials: Pluronic F127 ((ethylene oxide)106(propylene oxide)70(ethylene oxide)106, PEO-PPO-PEO, MW = 12,600 g mol-1), tetramethoxysilane (TMOS, 98%), tetrahydrofuran (THF, 99.9%) and zinc phthalocyanine (ZnPc, 97%) were all purchased from Sigma-Aldrich. ZnPc was dissolved in THF at a concentration of 2 mg mL^{-1} (stock solution). Dicyclohexylamino substituted PDI (sPDI) are obtained from our collaborator, Department of Chemistry, Shandong University, China.

3.2.1 Synthesis of NCs for UC-PDT

Synthesis parameters of NCs are listed in table 1.2.

Table 1.2 Synthesis parameters of the NCs studied for UC-PDT

NCs	**UCNPs (mg)**	**ZnPC (mg)**	**THF (µL)**	**F127 (mg)**	**TMOS (µL)**	**DI water (mL)**
ZnPc@NCs	×	0.3	900 (+300)	37.5	55	10
S-UCNPs@NCs	6.4	×	900 (+300)	15	30	10
M-UCNPS@NCs	9.5	×	900 (+300)	15	30	10
UCNPs+ZnPc@NCs	6.4	0.3	900 (+300)	15	30	10

NCs encapsulated with small organic molecules ZnPc only (ZnPc@NCs)**:** F127 (37.5 mg) was dissolved in THF (750 µL) and mixed with ZnPc (150 µL). After stirring at room temperature for 3 h, TMOS (55 µL) was added to the solution and sonicated for 1 min. The solution was injected into stirred deionized (DI) water (10 mL) at a rate of 60-90 µL min^{-1}. Stirring was continued for another 4 days for THF evaporation as well as TMOS hydrolysis and condensation. Afterwards, the solution was dialyzed against DI water for 24 h using a dialysis membrane (MWCO of 10,000 g mol^{-1}, Spectra/Por regenerated cellulose). Finally, the solution was centrifuged for 10 min at 10,000 rpm, the supernatant was further passed through a 0.2 µm filter to remove large aggregates.

NCs encapsulated with UCNPs only (S-UCNPs@NCs and M-UCNPs@NCs)**:** The numbers of UCNPs (N) inside of the NCs can be tuned by the amount of UCNPs added, namely S-UCNPs@NCs (n < 3) and M-UCNPs@NCs (n > 3). Designated amounts of UCNPs stock solution was firstly air dried to remove hexane. Then, the dried UCNPs were re-dispersed in THF and mixed with F127, namely Solution A1 (6.4 mg UCNPs, 15 mg F127, and 900 µL THF), Solution A2 (9.5 mg UCNPs, 15 mg F127, and 900 µL THF), respectively. After stirring at room temperature for 3 h and sonicating for 10 min, each of the solutions were individually injected into DI water (10 mL) at a rate of 60-90 µL min^{-1} while being stirred, to obtain respective Solutions B1 and B2. Stirring was continued for 2 more days to evaporate THF. Afterwards, 30 µL of TMOS was dissolved in THF (300 µL) and injected at a rate of 60-90 µL min-1 into each of the solutions B1 and B2. It was stirred at room temperature for another 2 days for hydrolysis and condensation of TMOS. The solution was then subjected to centrifugation (6,000 rpm for 30 min), discarding the supernatant containing empty (i.e., UCNP-free) nanocapsules and re-dispersing the precipitates in DI water. The dispersion was further passed through a 0.2 µm filter to remove large aggregates.

NCs co-encapsulated with UCNPs and ZnPc (UCNPs-ZnPc@NCs)**:** Designated amounts of UCNPs stock solution was firstly air dried to remove hexane. Then, the dried UCNPs were re-dispersed in THF and mixed with F127, and then mixed with ZnPc. The mixture was stirred for 3 h and then sonicated for 10 min to obtain a transparent solution. The following steps are the same as the protocol for encapsulation of UCNPs only.

Synthesis of hydrocarbon-modified TAT-conjugated NCs: the details are described in the supporting information of *chapter 5.2.*

3.2.2 Synthesis of NCs for PTT

Utilizing the one-pot encapsulation approach described above (*section 3.2.1*), three groups of NCs are synthesized, and the synthesis parameters are listed in table 1.3. NCs with DSNPs

Table 1.3 Synthesis parameters of the NCs studied for PTT

NCs	DSNPs (mg)	sPDI (mg)	THF (µL)	F127 (mg)	TMOS (µL)	DI water (mL)
sPDI@NCs	×	0.6	900 (+300)	37.5	55	10
DSNPs@NCs	6.4	×	900 (+300)	15	30	10
DSNPs+sPDI_L@NCs	6.4	0.3	900 (+300)	15	30	10
DSNPs+sPDI_M@NCs	6.4	0.6	900 (+300)	15	30	10
DSNPs+sPDI_H@NCs	6.4	1.2	901 (+300)	15	30	10

only (DSNPs@NCs), NCs with sPDI only (sPDI@NCs), and NCs co-encapsulated with both DSNPs and various amounts of sPDI, including DSNPs+sPDI_L@NCs (sPDI = 0.3 mg), DSNPs+sPDI_M@NCs (sPDI = 0.6 mg), and DSNPs+sPDI_H@NCs (sPDI =1.2 mg).

3.3 Characterizations

3.3.1 Characterization of LnNPs

Powder X-ray Diffraction (XRD) Analysis: XRD is a method used for determining the atomic and molecular structure of a crystal, in which the crystalline atoms cause a beam of X-rays to diffract into many specific directions. Incident X-rays are scattered by a crystalline sample according to Bragg's law: $n\lambda = 2d\sin\theta$, where λ is the wavelength of the X-ray beam, θ is the incident angle, and d is the distance between crystal planes. The value of d is dependent on the Miller indices h, k and l. In this thesis, the measurements of powdered samples were analyzed by XRD (Bruker D8 Advanced Diffractometer, Cu Kα radiation), Cu Kα radiation (λ = 1.5406 Å, power of the generator: 40 kV and 40 mA). The scan range was set from 20 to 80° 2θ with a step size of 0.04° and a count time of 1 s.

Transmission Electron Microscopy (TEM): TEM is a major analysis tool for directly observing the morphology and size of nanostructures by using a beam of electrons to transmit through a specimen to form an image. TEM and high resolution TEM (HRTEM) measurements of the various LnNPs in colloidal dispersion were performed with a JEOL JEM-2010F microscope operating at 200 kV. A drop of the resulting solution was evaporated on a Formvar/carbon film supported on a 300 mesh copper grid (3 mm in diameter). ImageJ software was used to analyze the particle size distributions and the *d*-spacing between the lattice planes from the TEM and HRTEM data, respectively.

Electron Tomography (ET): ET is an extension of traditional TEM for obtaining detailed 3-dimensional space (3D) structures of objects. The morphological and structural analysis of the obtained UCNPs were performed on an FEI Titan 80/300 Scanning/Transmission Electron Microscope (80 kV). A total of 75 HAADF-STEM images were collected for electron tomography over a tilt range of −74° to 74° with a 2° tilt step. The acquisition time for one 1024 × 1024 sized image was 30 s. The magnification was 215 000 corresponding to a resolution of 0.61 nm per pixel. The final tilt series was aligned using a cross-correlation method and reconstructed by the simultaneous iterative reconstruction technique (SIRT, 50 iterations) using Inspect3D, and the reconstructed 3D volume was visualized with Amira 4.1.

Inductively Coupled Plasma−Atomic Emission Spectroscopy (ICP-AES): ICP-AES is a method of emission spectroscopy that excites atoms and ions with a plasma, causing it to emit electromagnetic radiation at wavelengths characteristic of a particular element. In this thesis,

ICP-AES was used to determine the content of Ln^{3+} (*e.g.* Gd^{3+}, Yb^{3+}, Er^{3+}, Nd^{3+}, and Lu^{3+}). The samples were prepared by an acid digestion procedure. Briefly, the synthesized LnNPs or LnNPs are encapsulated in the NCs were digested in 70% HNO_3 under sonication at 65 °C for 1 h and kept at room temperature for 2 days, then diluted to below 5% HNO_3 before conducting ICP-AES measurements.

Luminescence Spectroscopy: The upconverting and NIR PL spectra of LnNPs were acquired under continuous laser excitation of 980 and 793 nm, respectively. The upconverting emission signal focused by a lens in 90^o configuration was collected by an Avaspec − 2048L − USB2A spectrometer (Avantes) through an optical fiber. By keeping the same optical path configuration, the NIR emission spectra was detected by a Shamrock 500i monochromator (Andor) equipped with an iDus InGaAs 1.7 NIR detector (Andor).

Relaxivity Measurements and MRI: T_1 and T_2 relaxation measurements and phantom images were obtained by using a 3-T Mediso nanoScan, 7-T Bruker Clinscan, and 9.4-T Bruker BioSpec MRI system, respectively. Prior to imaging, a phantom was prepared by dissolving the UCNPs or NCs in a 0.5% agarose solution. T_1 relaxation times were determined by an inversion recovery experiment using the following sequence: repetition time (TR) = 7.7 ms; echo time (TE) = 5000 ms; and inversion recovery times 41, 100, 200, 400, 800, 1600, 2400, 3200, and 4800 ms. T_2 relaxation times were determined from a multi-echo spin−echo sequence: TR = 4000 ms; TE: 6.7−250.6 ms. The longitudinal (r_1) and transverse (r_2) relaxivities were calculated from the slope of $1/T_1$ or $1/T_2$ versus molar [Gd^{3+}] concentration plots. The relevant acquisition parameters were optimized to generate T_1 and T_2-weighted images, being TR/TE = 610/7.8 ms and TR/TE = 3000/61 ms, respectively.

CT imaging: Phantoms of DSNPs are prepare and scanned using a high performance in vivo micro-CT scanner for preclinical research (SkyScan 1176, Bruker Biospin, Germany**)**. Imaging parameters are as follows: image pixel size, 35 µm; voltage, 40 KV; current, 600 µA; rotation steps, 0.7 degrees; exposure time 37 ms.

3.3.2 Characterization of the NCs

Dynamic light scattering (DLS): DLS is a technique used to determine small particle size distribution profile in suspension or polymers in solution by measuring the random changes in the intensity of light scattered from the suspension or solution. In this thesis, DLS was performed with Malvern Zetasizer Nano-S using a HeNe laser (633 nm) to measure the hydrodynamic size and size distribution of different NCs. All measurements were conducted using DI water as the dispersant in a glass cuvette.

Fourier-transform infrared (FTIR) spectroscopy: FTIR spectroscopy is an effective analytical method for detecting functional groups through characteristic IR absorption of chemical bonds in organic molecules. In this thesis, an FTIR spectrophotometer (Varian 3100 Excalibur) was used to characterize the chemical composition of the synthesised NCs. For FTIR sample preparation, the aqueous suspensions of NCs were freeze-dried and dispersed in KBr pellets (KBr is used as a reference).

Absorption spectroscopy: The absorption spectra of all samples were measured by a UV-VIS-NIR spectrophotometer (Varian Cary 5000) with scan speed of 600 nm min^{-1}. All experiments were performed in a transmission mode on NCs solutions filled in a quartz cuvette.

Nanothermometry measurements:

Temperature Sensitivity of DSNPs: The thermal response of the theranostic NCs in water was measured in the 20–45 °C temperature range at 5 °C increments. The temperature was changed using a temperature controlled cuvette holder (qpod 2e by Quantum Northwest, Washington, USA). 10 min intervals were maintained between the measurements in order to assure the stabilization of set temperature across the sample.

PL of different DSNPs was recorded under 793 nm laser diode excitation (CNI, China; 710 mW, ~3 mm diameter excitation spot size $\asymp$ 10 W/cm2) with a Shamrock 500i monochromator (Andor, Ireland) equipped with an iDus InGaAs 1.7 NIR detector (Andor, Ireland). 4 s integration time per spectrum was used for calibration and heating measurements. Each heating experiment was done in a triplicate. In order to remove any stray light from the excitation source long pass (LP) 830 nm filter (Semrock, Inc., USA) was used.

Nanothermometer characterizing parameters were calculated following the guidelines set by Brites et al.[210] PL intensity ratio (Δ) was estimated taking the ratio between the integrated intensities I_1 (1050.7-1055.5 nm) and I_2 (1055.9-1057.2 nm) at each temperature value:

$$\Delta = \frac{I_1}{I_2}$$

The relative thermal sensitivity (Sr) of the DSNPs was calculated as

$$S_r = \frac{1}{\Delta}\frac{\partial \Delta}{\partial T}$$

And the temperature uncertainty (δT) was given by

$$\delta T = \frac{1}{S_r}\frac{\delta \Delta}{\Delta}$$

The $\delta\Delta/\Delta$ was estimated by

$$\frac{\delta\Delta}{\Delta} = \sqrt{\left(\frac{\delta I_1}{I_1}\right)^2 + \left(\frac{\delta I_2}{I_2}\right)^2}$$

Here, δI_i and I_i were calculated by integrating, equivalent in range, baseline variation (noise, out of signal range), and the emission band (signal), respectively, thus obtaining the signal-to-noise ratio. (note, the above 4 equations also appear in P24)

Singlet oxygen ($^1O_2$) production: $^1O_2$ production was detected by 9, 10-anthracenediyl-bis(methylene) dimalonic acid (ABDA) (Sigma-Aldrich). In this method, the ABDA fluorescence emission is bleached due to reaction with the $^1O_2$. Briefly, ABDA was dissolved in dimethyl sulfoxide (DMSO) (Sigma Aldrich, USA) and diluted in water to a final concentration of 20 µM. UCNPs-ZnPc@NCs, UCNPs@NCs, or ZnPc@NCs alone were mixed with ABDA and irradiated by a 980 nm CW laser (1.5 W cm^{-2}) for 0, 20, 40, and 60 min, respectively. Magnetic stirring and constant temperature (24 °C) were kept during the irradiation experiments. The fluorescence emission of ABDA at 431 nm (excited at 380 nm) was measured using a microplate fluorescence spectrophotometer (Cytation/5 imaging reader, BioTek).

3.3.3 Evaluation of the NCs for biomedical applications

Cell culture and cytotoxicity assay: The breast cancer cell lines BT474 and MCF-7 (American Type Culture Collection) were cultured in Dulbecco's modified Eagle medium (DMEM) (high glucose [4.5 g L^{-1}], with sodium pyruvate and L-glutamine), containing 10% fatal bovine serum (Invitrogen), 1% antibiotic with 100 UI mL^{-1} penicillin, and 100 mg mL^{-1} streptomycin (Invitrogen). Cell incubation was maintained at 37 ^oC, and 5% CO_2. The culture medium was changed two to three times a week and cells were passaged serially using 0.25% trypsin/EDTA (Invitrogen). The cytotoxicity of synthesized theranostic NCs was evaluated by determining the viability of breast cancer cells using Cell Counting Kit-8 (CCK-8) (Sigma-Aldrich), of which highly water-soluble tetrazolium salt is reduced by dehydrogenases in cells to give an orange colour product (formazan). The amount of the formazan dye generated is directly proportional to the number of living cells. Briefly, breast cancer cells were seeded into 96 well plates at a designated density per well and incubated for 24 h. Different groups of the NCs were added to the cultured cells. After incubation with NCs for 24 h or 72 h, CCK-8 solution was added into cultured cells and incubated for another 2 h. The absorbance at 450 nm of the mixture was measured using a Benchmark Plus microplate spectrophotometer (Bio-Rad). The absorbance values obtained were recalculated as percentage values of viability. Viability (%) = 100 x (AT-AB)/(AC-AB) where AT, is the absorption values of wells containing NCs, AC is the absorption values of control wells, and AB is the absorption values of a blank

solution. Data were expressed as mean ± standard deviation (SD). Statistical significance of differences observed between groups was calculated using a two-tail paired Student's t-Test at the 95% confidence level. Significance was represented as p-value < 0.05.

In vitro therapeutic efficacy of UC-PDT: To determine the therapeutic effect of UCNPs-ZnPc@NCs, we evaluated the growth inhibition and apoptosis of breast cancer BT474 cells after 980 nm irradiation (1.5 W cm^{-2}). The sequential irradiation was done as follows: 40 min of irradiation, 40 min rest, 40 min of irradiation. The total irradiation period was 80 min. Cell growth inhibition by UCNPs-ZnPc@NCs, UCNPs@NCs, and ZnPc@NCs was tested using CCK-8 cell proliferation assay as described in the previous section. The apoptosis induction was evaluated using Caspase-3/7 green detection reagent (Invitrogen), a fluorescence probe that presents green emission upon 488 nm excitation if reacted with the Caspase-3/7, released by the apoptotic cells. Briefly, 30,000 cells were seeded in eight-chambered cover glass plate (LAB-TEK, Chambered Cover glass System), and incubated with the above 3 groups of NCs containing 100 µM UCNPs and / or 3.5 µM ZnPc for 24 h before the sequential irradiation treatment. After another 24 h of incubation, the Caspase-3/7 green detection reagent was added and incubated with the cells for 6 h to allow the accumulation of the reagent into the cells. Live cell imaging was performed using a confocal laser scanning microscope (Nikon). 20×/0.5 NA dry objective (Nikon) was selected for imaging acquisition. The fluorescence image was acquired at λ_{ex} = 488 nm and λ_{em} = 530 nm.

In vitro therapeutic efficacy of PTT: To determine the therapeutic effect of DSNPs+sPDI@NCs, we evaluated the growth inhibition and apoptosis of breast cancer MCF-7 cells after 20 min of 793 nm laser irradiation (10 W cm^{-2}). Cell growth inhibition by DSNPs+sPDI@NCs, DSNPs@NCs, and sPDI@NCs was tested using CCK-8 cell proliferation assay, and the apoptosis induction was evaluated using Caspase-3/7 green detection reagent (Invitrogen) following the methods described above.

In vitro MRI and CT imaging: Breast cancer cells were seeded in 6-well plates and incubated for 24 h. The NCs with the designated concentrations of LnNPs and therapeutic agents were added into 3 of the 6 wells and kept the other 3 untreated wells as control. After 24 h incubation, the cells were washed with 1×PBS 3 times, and then detached and collected the cell pellets in 0.2 ml PCR tubes. The cell pellets (both treated and untreated) were imaged by MRI or CT scan following the instructions described in *section 3.3.1.*

The following three chapters each correspond to articles which are published, submitted and in preparation. In ***Chapter 4***, we illustrate the morphology controlled synthesis of β-$NaGdF_4$:Er^{3+} (2%), Yb^{3+} (20%) UCNPs with diverse morphologies *via* a single-step thermolysis approach, investigate the mechanism underlying the formation of different morphologies,

especially nanorods, and demonstrate the morphology effects on their PL and paramagnetic relaxivity. In ***Chapter 5***, we demonstrate the synthesized UCNPs as both imaging probes and energy transducer for MRI-guided UC-PDT. First, we develop an original one-pot synthesis approach to simultaneously co-encapsulate UCNPs and ZnPc into NCs. Subsequently we investigate the *in vitro* MRI (diagnostic) and UC-PDT (therapeutic) effects of the synthesized NCs. In the second part of the same chapter, we further modify this encapsulation approach by introducing hydrocarbon group into the silica shell in order to prevent the aggregation of loaded doxorubicin (DOX), therefore enhance the fluorescence intensity of DOX. We also successfully demonstrate the NCs can be functionalized for nuclear targeted drug delivery. To achieve deeper tissue penetration and lower possibility of tissue damage, in ***Chapter 6***, we synthesize $LiLuF_4:Nd^{3+}@LiLuF_4$ DSNPs by a two-step multilayer thermolysis approach. Both their excitation and emission wavelengths lie within the biological windows. This multifunctional DSNPs can be used for CT imaging and nanothermometry. Inspired by the promising one-pot encapsulation approach, we co-encapsulate the DSNPs and sPDI for CT-guided NIR-regulated PTT with real-time monitor and control of the temperature by nanothermometers. The *in vitro* therapeutic efficacy is also studied in breast cancer cells.

4 ONE-STEP THERMOLYSIS

Morphology Control of Lanthanide Doped NaGdF4 Nanocrystals via One-Step Thermolysis

Contrôle de la morphologie des nanocristaux de NaGdF4 dopés au lanthanide via une thermolyse en une étape.

Miao Wang[†, ¦], Yu Zhang[‡], Qiaofeng Yao[⊥], Michael Ng[#], Ming Lin[‡], Xu Li[‡, ⁑, †], Kishore Kumar Bhakoo[#], Alex Y. Chang[§, ¦], Federico Rosei[†], Fiorenzo Vetrone[*†]

[†] Institut National de la Recherche Scientifique (INRS), Centre Énergie, Matériaux et Télécommunications, Université du Québec, Varennes (QC), Canada

[‡] Institute of Materials Research and Engineering (IMRE), Agency for Science, Technology and Research (A*STAR), Singapore

[⊥] Department of Chemical and Biomolecular Engineering, National University of Singapore, Singapore

[#] Singapore Bioimaging Consortium (SBIC), Agency for Science, Technology and Research (A*STAR), Singapore

[§] Department of Oncology, Johns Hopkins University, Baltimore, Maryland, USA

[¦] Johns Hopkins Singapore, Singapore

[⁑] Department of Chemistry, National University of Singapore, Singapore

Chem. Mater. 2019, 31, 14, 5160–5171. – **Cover Article**

DOI: 10.1021/acs.chemmater.9b01155

Received: March 26, 2019; Revised: June 3, 2019; Published: June 3, 2019

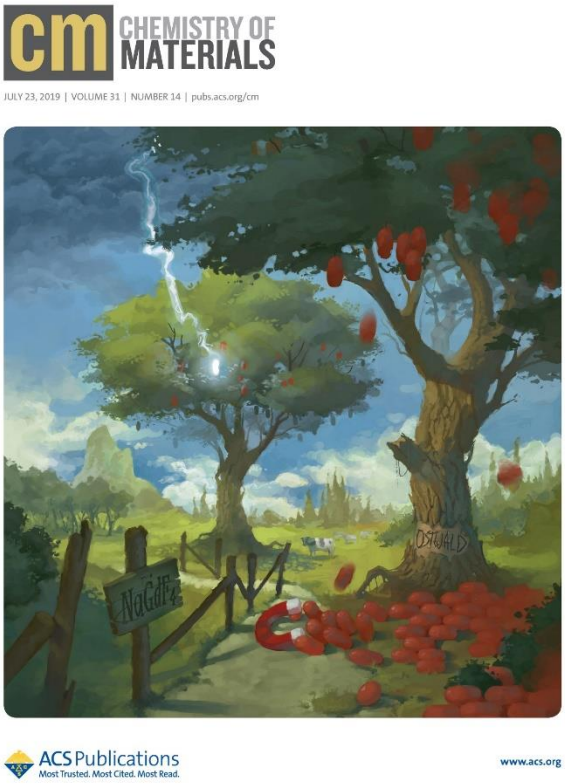

As introduced in chapter 1, UCNPs have gained in popularity in recent years especially in the context of multi-functional nanostructures for biomedical applications due to their inherent ability to convert biologically friendly NIR excitation light to higher energies, spanning the UV, VIS, and NIR spectral regions through a multiphoton process known as UC. At the forefront of this field are fluoride based nanoparticles (*e.g.* $NaYF_4$ or $LiYF_4$) as hosts for the lanthanide dopants due to the low phonon (or vibrational) cut-off energies of their crystal lattices, which results in intense UC PL. To render further functionality to these fluoride based UCNPs, typically Gd^{3+} can be added to the host matrix (replacing Y^{3+}) since Gd^{3+} can be used as a contrast agent for both MRI and CT due to its paramagnetism and high X-ray attenuation, respectively. Hexagonal phase $NaGdF_4$ (β-$NaGdF_4$) UCNPs have received considerable attention in this regard and previous studies have proved that their size, crystallinity, crystal structure (phase), as well as surface properties will affect their UC PL as well as their paramagnetic relaxivity. Moreover, for both *in vitro* and *in vivo* experiments, the morphology, monodispersity and uniformity of the UCNPs can dictate key behavior such as cellular uptake and their removal from the cell. Thus, it is clear that developing β-$NaGdF_4$ UCNPs with the morphology favorable for biomedical applications is of paramount importance.

In this chapter, monodispersed uniform β-$NaGdF_4$:Er^{3+} (2 mol%), Yb^{3+} (20 mol%) UCNPs possessing diverse morphologies are fabricated from the thermolysis of trifluoroacetate precursors in 1-octadecene and oleic acid by modifying the hot-injection strategy. *We demonstrate, for the first time, that modulation of the injection temperature during the hot-injection step was an effective approach to control the size and shape of the prepared UCNPs (20 ~ 65 nm) and allowed for the direct synthesis of nanorods.* The different supersaturation caused by the different temperatures could directly manipulate the nucleation and growth of α-phase UCNPs before the α → β phase transition, subsequently influences the Ostwald ripening mode during the α → β phase transition, and consequently affects their morphology (*i.e.*, nanorods, nanospheres, nanoprisms, nanoplates, and nanodisks), uniformity, and

monodispersity. Also, we revealed that the negative contrast enhancement on T_2–weighted images caused by the prepared UCNPs are increased with increasing size with the exception of the nanorods, which performed the best as T_2 contrast agents despite being smaller compared to the nanoplates. In a nutshell, this fundamental study provide a more profound understanding of Ln^{3+}-doped β-$NaGdF_4$ UCNP synthesis strategies, particularly with regards to controlling their morphologies. It also provides strong scientific support for the design of theranostic nanoplatforms for future biomedical applications.

CHEMISTRY OF MATERIALS
Cite This: Chem. Mater. XXXX, XXX, XXX−XXX
Article
pubs.acs.org/cm

Morphology Control of Lanthanide Doped $NaGdF_4$ Nanocrystals via One-Step Thermolysis

Miao Wang,[†,⊥] Yu Zhang,[‡] Qiaofeng Yao,[∥] Michael Ng,[#] Ming Lin,[‡] Xu Li,[‡,¶,†] Kishore Kumar Bhakoo,[#] Alex Y. Chang,[§,⊥] Federico Rosei,[†] and Fiorenzo Vetrone*[,†]

[†]Institut National de la Recherche Scientifique (INRS), Centre Énergie, Matériaux et Télécommunications, Université du Québec, Varennes, J3X 1S2 Québec, Canada

[‡]Institute of Materials Research and Engineering (IMRE) and [#]Singapore Bioimaging Consortium (SBIC), Agency for Science, Technology and Research (A*STAR), 138632 Singapore

[∥]Department of Chemical and Biomolecular Engineering and [¶]Department of Chemistry, National University of Singapore, 119077 Singapore

[§]Department of Oncology, Johns Hopkins University, Baltimore, Maryland 21218, United States

[⊥]Johns Hopkins Singapore, 308433 Singapore

Supporting Information

ABSTRACT: β-phase $NaGdF_4$ nanocrystals doped with Er^{3+} and Yb^{3+} possessing diverse morphologies were synthesized from the thermolysis of trifluoroacetate precursors in 1-octadecene and oleic acid by modifying the hot-injection strategy. Modulation of the injection temperature during the hot-injection step was an effective approach to control the size and shape of the prepared nanocrystals and allowed for the direct synthesis of nanorods. Here, we report for the first time the fabrication of monodispersed uniform nanorods through a one-step thermolysis approach. The different supersaturation caused by the different temperatures could directly manipulate the nucleation and growth of α-phase nanoparticles before the $\alpha \rightarrow \beta$ phase transition, subsequently influences the Ostwald ripening mode during the $\alpha \rightarrow \beta$ phase transition, and consequently affects their morphology (i.e., nanorods, nanospheres, nanoprisms, nanoplates, and nanodisks), uniformity, and monodispersity. The upconversion luminescence intensity decreased with increase of the surface to volume ratio of the upconverting nanocrystals, and a higher ratio of green to red emission was observed when the aspect ratio was close to 1. The negative contrast enhancement on T_2-weighted magnetic resonance images caused by the upconverting nanocrystals was increased with increasing size with the exception of the nanorods, which performed the best as T_2 contrast agents despite being smaller compared to the nanoplates. Our work provided strong evidence for the use of morphology controlled synthesis in $NaGdF_4$ based upconverting nanocrystals and their implementation in multifunctional nanoplatforms for future biomedical applications.

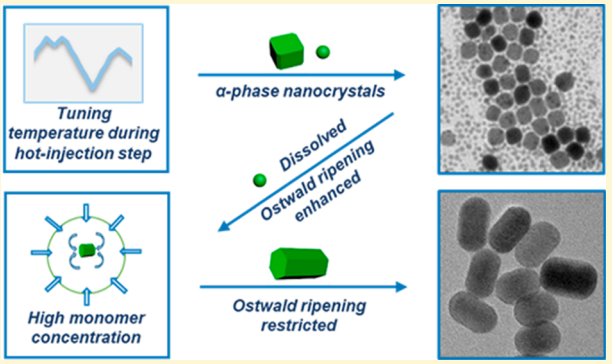

1. INTRODUCTION

Lanthanide (Ln) based upconverting nanoparticles (UCNPs) have unique photophysical properties, which allow them to convert near-infrared (NIR) radiation to higher energies spanning the UV−visible−NIR regions through a multiphoton process known as upconversion.[1] UCNPs possess some distinct advantages compared to traditional fluorophores, such as large anti-Stokes shifts and high photostability as well as the ability to be excited with NIR light. The latter leads to lack of background autofluorescence, as well as the ability to deeply penetrate tissues.[2−6] These properties render UCNPs (e.g., Y_2O_3, Y_2O_2S, $NaYF_4$, $NaGdF_4$, $LiYF_4$, et al.) highly desirable, possessing multiple functionalities for use in a range of biomedical applications, such as cell and tissue tracking, imaging, fluorescence assays, nanothermometry, and visualizing controlled release of therapeutic moieties, as well as photodynamic/photothermal therapies.[7−14] Hexagonal phase $NaGdF_4$(β-$NaGdF_4$) UCNPs have gained in popularity in recent years especially in the context of multifunctional nanostructures. This is not only attributed to the low phonon cutoff energy of the crystal lattice, but also because Gd^{3+} can be used as a contrast agent for both magnetic resonance (MR) imaging due to its paramagnetism, as well as computed tomography (CT) because of its high X-ray attenuation.[15−17] Thus, β-$NaGdF_4$ UCNPs are considered as an excellent starting point for the development of smart, multimodal

Received: March 26, 2019
Revised: June 3, 2019
Published: June 3, 2019

DOI: 10.1021/acs.chemmater.9b01155
Chem. Mater. XXXX, XXX, XXX−XXX

nanoplatforms, which can combine two or more functionalities; for example, in vivo MR imaging, CT, and fluorescence imaging with simultaneous therapeutic functionality.[18]

For biomedical applications, both in vitro or in vivo, the morphology, monodispersity, and uniformity of nanoparticles are of critical importance as they can dictate key behavior such as cellular uptake and their removal from the cell.[19] For example, nanoparticles with a rod shape (diameter: 5−10 nm, length: 100−300 nm) were more favorable for intranuclear accumulation by passive diffusion compared to spherical nanoparticles with a diameter of 20 nm. Since the nuclear pore size is 9−12 nm for human cells, spherical nanoparticles with diameters larger than 12 nm had a difficult time entering the nucleus. However, rod-like nanoparticles with large volumes have higher potential for intranuclear accumulation compared to other morphologies as long as the diameter is less than 12 nm.[20] Moreover, size, crystallinity, crystal structure (phase), and surface properties will also affect their upconversion luminescence[21] as well as their paramagnetic properties. This includes magnetic relaxivity, which is used to characterize the MR imaging contrast agents, indicating the degree to which contrast agents can enhance the longitudinal or transverse water relaxation rate constant (r_1 or r_2) normalized to concentration of the contrast agents. The relaxivity of paramagnetic nanoparticles is strongly related to their magnetization, as well as the number of magnetic ions with high magnetic moments on the surface of the nanoparticles.[22−25] In this regard, optimization of the synthesis procedure is critical to obtain UCNPs with tailored crystal structures and morphologies for future multimodal biomedical applications.

Thermal decomposition or thermolysis is one of the most successful approaches to obtain lanthanide doped $NaGdF_4$ UCNPs (as well as the more studied $NaYF_4$).[26,27] Previously, a "heating-up" or "one-pot" strategy was used to obtain β-$NaGdF_4$ UCNPs by thermal decomposition of trifluoroacetate precursors (CF_3COOLn and CF_3COONa) in an oleic acid (OA)/1-octadecene (ODE) system, in which the reaction solution at room temperature was heated to high temperature. However, to date a procedure to synthesize uniform β-$NaGdF_4$ nanorods in a single step has not been reported. Previous reports have demonstrated that such nanorods could only be fabricated through a two-step thermolysis growth route: first the growth of cubic phase $NaGdF_4$ (α-$NaGdF_4$) nanoparticles followed by their use as seeds to form β-$NaGdF_4$ nanorods through the α-to-β phase transition. Single step growth was not possible using the one-pot strategy due to the difficulty in controlling the growth rate during crystallization.[28] Subsequently, a hot-injection approach was devised, in which the preheated trifluoroacetate precursors were injected into a hot surfactant solution and successfully synthesized highly crystalline, monodispersed β-$NaGdF_4$ UCNPs.[29] This synthetic procedure led to significant advances in the synthesis of high quality $NaGdF_4$ based nanoparticles with controlled size; however, only nanospheres and nanoplates were reported. Therefore, refinement of this strategy is still required to obtain β-$NaGdF_4$ based UCNPs with different well-defined morphologies such as nanorods.

Most investigations on the morphology controlled synthesis of $NaLnF_4$ UCNPs via the hot-injection approach so far have focused on tuning the synthesis parameters including reaction temperature and time, injection rate, ratio of Na^+/Ln^{3+}, and composition of the solvent.[30−33] The process of injection is of great importance for the hot-injection strategy where the slow addition of the precursors to the solvent and subsequent manipulation of the temperature lead to a temporal separation of nucleation and crystal growth.[33] The high supersaturation induced by the hot injection causes a rapid homogeneous nucleation that is followed by a diffusion controlled crystal growth, resulting in the formation of monodispersed UCNPs. On this basis, we hypothesize that changing of temperature during the hot-injection step would induce different nucleation processes, which further determines the growth of nanocrystals by influencing their thermodynamics and kinetics. Thus, in the quest to find a synthesis procedure to prepare β-$NaGdF_4$ UCNP nanorods in a single step, we investigated tuning of the temperature during the hot-injection step. As such, we have elucidated a new one-step approach for the synthesis of β-$NaGdF_4$ UCNPs codoped with Er^{3+} (2%), Yb^{3+} (20%) with diverse morphologies (nanorods, nanoprisms, nanospheres, nanoplates, and nanodisks) with sizes ranging from approximately 20−65 nm. To the best of our knowledge, this is the first report of the synthesis of monodispersed uniform β-$NaGdF_4$ nanorods through direct thermolysis of trifluoroacetate precursors as well as the reported mechanism underlying the formation of nanorods. Meanwhile, we also investigated the anisotropic growth and shape evolution of the synthesized β-$NaGdF_4$ nanocrystals to study the mechanism of diverse morphology formation. Moreover, the nanorods, nanoplates, and nanoprisms obtained by this strategy have constant composition fraction of metal ions (Na^+, Gd^{3+}, Yb^{3+}, Er^{3+}) and coating ligands (OA), which is particularly crucial for further studying of the morphology effect on their optical and magnetic properties.

The different morphologies (including nanorods) of the synthesized upconverting β-$NaGdF_4$ nanocrystals influenced both the upconversion luminescence and magnetic relaxivities. With regards to the latter, Gd^{3+} based contrast agents shorten both the longitudinal and the transverse relaxation times (T_1 and T_2) of nearby water protons.[34] Generally, Gd^{3+} based nanoparticles are developed for the usage of T_1 contrast agents, which increase signal density in T_1-weighted MR imaging (bright images).[35] Previous studies indicated that $NaGdF_4$ nanoparticles could achieve high positive contrast in T_1-weighted images only when the particle size was less than 10 nm.[24,36] Here, we elucidated the morphology effect of $NaGdF_4$ nanocrystals with sizes from 20 to 65 nm on their T_1/T_2 relaxivities at high magnetic field (3 T, 7 T, and 9.4 T). Though all of these upconverting β-$NaGdF_4$ nanocrystals achieved promising T_2 relaxivity and significant negative contrast enhancement in T_2-weighted MR imaging (dark images) due to their high magnetization at high magnetic field, the nanorods performed best as T_2 contrast agents.

Our work provides strong evidence for morphology controlled synthesis of β-$NaGdF_4$ nanocrystals for the design of multifunctional nanoplatforms in biomedical applications.

2. EXPERIMENTAL SECTION

2.1. Upconverting Nanocrystal Synthesis. Gadolinium oxide (Gd_2O_3, 99.99%), erbium oxide (Er_2O_3, 99.99%), ytterbium oxide (Yb_2O_3, 99.99%), trifluoroacetic acid (CF_3COOH, 99%), sodium trifluoroacetate (CF_3COONa, 98%), oleic acid (technical grade, 90%), and 1-octadecene (technical grade, 90%) were all purchased from Sigma-Aldrich and used without further purification. All β-$NaGdF_4$:Er^{3+} (2%), Yb^{3+} (20%) nanocrystals were synthesized using a single-step hot-injection thermolysis approach,[9,18,29] which allowed direct decomposition of the metal trifluoroacetate precursors. The

DOI: 10.1021/acs.chemmater.9b01155
Chem. Mater. XXXX, XXX, XXX−XXX

individual parameters of all the studied nanocrystals are listed in Table S1.

First, the metal trifluoroacetate precursors were prepared via addition of a 10 mL mixture of distilled water/trifluoroacetic acid (1:1) to a 50 mL round-bottom flask containing 2.50×10^{-5} mol of Er_2O_3 (0.00956 g, 2 mol % Er^{3+}), 2.50×10^{-4} mol of Yb_2O_3 (0.0985 g, 20 mol % Yb^{3+}), and 9.75×10^{-4} mol of Gd_2O_3 (0.3534 g). The solution was heated at 80 °C with stirring in excess of 6 h until it became clear. The solution was then heated to dryness at 60 °C overnight to evaporate any excess water/trifluoroacetic acid.

Second, 12.5 mL of oleic acid and 12.5 mL of 1-octadecene were added to a 100 mL 3-neck round-bottom flask (Solution A). Approximately 2.50×10^{-3} mol of CF_3COONa was added to the dried precursor solids along with 7.5 mL of oleic acid and 7.5 mL of 1-octadecene (Solution B). The resulting solutions were degassed with stirring at the designated temperature (150 °C for Solution A and 125 °C for Solution B) for 30 min to remove residual water and oxygen. Subsequently, Solution A was heated to 315 °C under a gentle flow of argon gas for 30 min and adjusted to the designated temperature (310 °C–320 °C) before addition of Solution B using a mechanical pump system at a rate of 1.5 mL/min (Harvard Apparatus Econoflow). The system temperature was immediately tuned to 315 °C as soon as the injection was terminated and was left to stir vigorously for an additional 1–3 h. At various time points after termination of the injection, 2 mL of the solution was removed from the reaction system. After the reaction was completed, the solution was allowed to cool to room temperature, and the synthesized upconverting nanocrystals were precipitated using absolute ethanol and centrifuged at 6500 rpm for 15 min. The solids were then washed with a mixture of hexane/ethanol (1:4) twice to remove any impurities.

2.2. Powder X-ray Diffraction (XRD) Analysis. XRD patterns were measured using a Bruker D8 Advanced Diffractometer, Cu Kα radiation (λ = 1.5406 Å, power of the generator: 40 kV and 40 mA). The scan range was set from 20 to 80° 2θ with a step size of 0.04° and a count time of 1 s.

2.3. Transmission Electron Microscopy (TEM). TEM and high resolution TEM (HRTEM) measurements of the various upconverting nanocrystals in colloidal dispersion were performed with a JEOL JEM-2010F microscope operating at 200 kV. A minute amount of sample was dispersed in an appropriate amount of hexane to yield an approximate 0.1 wt % solution. A drop of the resulting solution was evaporated on a Formvar/carbon film supported on a 300 mesh copper grid (3 mm in diameter). ImageJ software was used to analyze the particle size distributions and the *d*-spacing between the lattice planes from the TEM and HRTEM data, respectively.

2.4. Electron Tomography. The morphological and structural analysis of the obtained nanocrystals were performed on an FEI Titan 80/300 Scanning/Transmission Electron Microscope (80 kV). A total of 75 HAADF-STEM images were collected for electron tomography over a tilt range of −74° to 74° with a 2° tilt step. The acquisition time for one 1024 × 1024 sized image was 30 s. The magnification was 215 000 corresponding to a resolution of 0.61 nm per pixel. The final tilt series was aligned using a cross-correlation method and reconstructed by the simultaneous iterative reconstruction technique (SIRT, 50 iterations) using Inspect3D, and the reconstructed 3D volume was visualized with Amira 4.1.

2.5. Inductively Coupled Plasma–Atomic Emission Spectroscopy (ICP-AES). ICP-AES was used to determine the content of Na^+, Gd^{3+}, Yb^{3+}, and Er^{3+}. The samples were prepared by an acid digestion procedure. Briefly, the synthesized upconverting nanocrystals were digested in 70% HNO_3 under sonication at 65 °C for 1 h and kept at room temperature for 2 days before sending for ICP-AES measurement.

2.6. Upconversion Luminescence Spectroscopy. Luminescent measurements were carried out under excitation with 980 nm using an unfocused fiber-coupled diode laser (Thorlabs Inc., U.S.A.) with a maximum power of 330 mW. The laser illuminated the sample using a lens to obtain a Gaussian beam with a 0.4 mm diameter. Laser power density was tuned to 120 W/cm^2 for all the measurements. The emission light was collected by a lens in a 90° configuration and then transferred to a spectrophotometer (Avaspec − 2048L − USB2) using an optical fiber.

2.7. Relaxivity Measurements and MR Imaging. T_1 and T_2 relaxation measurements and phantom images were obtained by using a 3-T Mediso nanoScan, 7-T Bruker Clinscan, and 9.4-T Bruker BioSpec MRI system, respectively. Prior to imaging, a phantom was prepared by dissolving the nanocrystals in a 0.5% agarose solution. T_1 relaxation times were determined by an inversion recovery experiment using the following sequence: repetition time (TR) = 7.7 ms; echo time (TE) = 5000 ms; and inversion recovery times 41, 100, 200, 400, 800, 1600, 2400, 3200, and 4800 ms. T_2 relaxation times were determined from a multiecho spin–echo sequence: TR = 4000 ms; TE: 6.7–250.6 ms. The longitudinal (r_1) and transverse (r_2) relaxivities were calculated from the slope of $1/T_1$ or $1/T_2$ versus molar [Gd^{3+}] concentration plots. The relevant acquisition parameters were optimized to generate T_1 and T_2-weighted images, being TR/TE = 610/7.8 ms and TR/TE = 3000/61 ms, respectively.

2.8. Statistical Consideration. The correlation coefficient (r) was calculated by the Pearson product–moment correlation coefficient, and statistical significance (p-value) was analyzed from (r).

3. RESULTS AND DISCUSSION

3.1. Characteristics of β-$NaGdF_4$:Er^{3+} (2%), Yb^{3+} (20%) Nanocrystals with Various Morphologies. The TEM (Figure 1a–e) images showed that all synthesized upconverting nanocrystals were uniform and monodispersed with narrow size distributions (Table S1). To clearly identify the upconverting nanocrystals studied here, we defined the various morphologies as follows: nanospheres—nanocrystals with spherical shape; nanoprisms—hexagonal prisms with an AR close to 1; nanorods—rod-like hexagonal prisms with an AR less than 1; nanoplates—hexagonal prisms with an AR more than 1.5; nanodisks—nanoplates with disk-like bases. From the HRTEM images (Figure 1f–j), the lattice fringes corresponding to the specific lattice planes revealed their specific shapes. Specifically, the TEM images demonstrated uniform nanorods including Rods-D20 (Figure 1a), Rods-D23, Rods-D17, and Rods-D16 (Figure S1A and Table S1). The rod shape was further confirmed by HRTEM and electron tomography analysis. The HRTEM images showed a preferred growth direction along the *c*-axis for the rod-like nanocrystals as well as the hexagonal cross-section (Figure 1f, Figure S1b,c, and Figure 3C-90 min). The nanorods were either surrounded by the family of {100} and {001} or {100} and {101} lattice planes. The electron tomography results (Figure 2) complemented and confirmed the deduction from the HRTEM, allowing the rod shape structure to be determined more conclusively and with greater rigor. The (100) and (111) lattice planes demonstrated in the different individual nanocrystals (Figure 1g) revealed the spherical structure of the nanospheres (Spheres-D21, Figure 1b). Figure 1c showed the hexagonal nanoprisms (Prisms-D19) standing on the TEM grids on either the side faces or the bottom faces. From the HRTEM images (Figure 1h for top view and Figure 1i for side view), both the nanoprisms and nanoplates (Plates-D40, Figure 1d, and Plates-D63, Figure S4A) were enclosed by {100} and {001} facets as the hexagonal nanoprisms can be considered as the nanoplates with the AR close to 1. Most of the nanodisks (Disks-D63, Figure 1e) sat on their bottom faces, and the HRTEM images (Figure 1j and Figure S5) revealed that the rounded bottom faces were {001} facets. The (110) and (101) lattice planes (Figure S5) indicated the side faces of Disks-D63.

The XRD patterns (Figure S2A) revealed the β-phase of $NaGdF_4$:Er^{3+} (2%), Yb^{3+} (20%) upconverting nanocrystals,

DOI: 10.1021/acs.chemmater.9b01155
Chem. Mater. XXXX, XXX, XXX–XXX

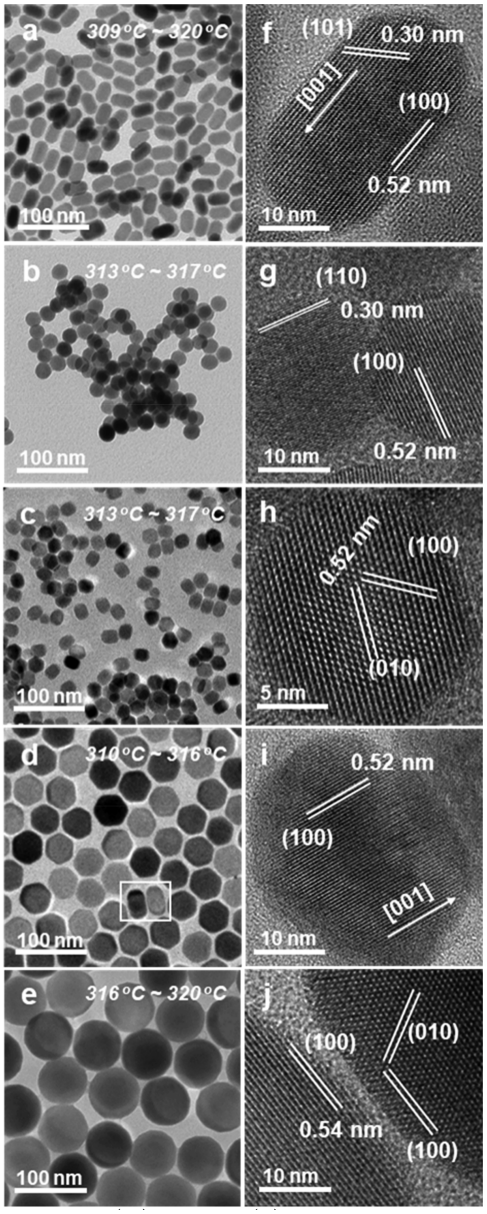

Figure 1. TEM (a–e) and HRTEM (f–j) images demonstrating the diverse morphologies of β-$NaGdF_4$:Er^{3+} (2%), Yb^{3+} (20%) upconverting nanocrystals: Rods-D20 (a and f), Spheres-D21 (b and g), Prisms-D19 (c and h), Plates-D40 (d and i), and Disks-D63 (e and j). (i) shows the side view of nanoplates enclosed in the white box of (d). The temperature labeled in a–e demonstrated the range of temperature changes during the hot-injection step in the formation of the upconverting nanocrystals, respectively.

and all the diffraction peaks indicated a pure hexagonal phase (space group: $P\bar{6}$ or $P6_3/m$), in excellent agreement with the reference data (JCPDS 27-699). The diffraction intensity of the crystal lattice as a function of 2θ reveals a correlation between the AR of the diverse architectures and their crystal lattice planes (Figure S2B). The rods exhibit enhanced (100) and (110) as well as diminished (002) diffractions, whereas the reversed trend is observed in the case of the plates and disks. This indicates that the majority of the rods are lying with a preference for the [001] direction (the side faces), with the *c*-axis parallel to the glass substrate used for the XRD measurements. In comparison to the rods, a smaller portion of nanoprisms are lying on their side faces while more

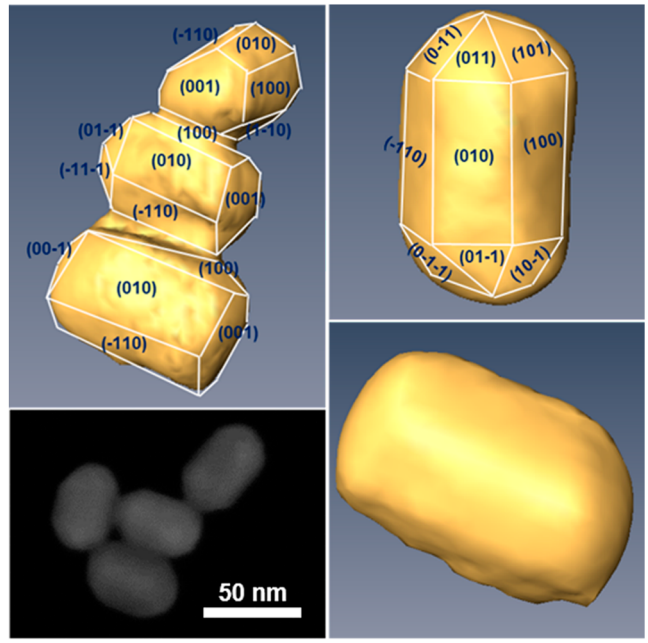

Figure 2. Electron tomography images demonstrating the shape structure of β-$NaGdF_4$:Er^{3+} (2%), Yb^{3+} (20%) nanorods. Please refer to the Supporting Information for the electron tomography video of the nanorod.

nanocrystals are standing on their bottom faces with the *c*-axis perpendicular to the substrates. The majority of the plates, disks with large AR, are generally sitting on their bottom faces, respectively. This finding is useful to predict the morphology of β-phase nanocrystals based on the XRD analysis.

3.2. Mechanisms Underlying the Formation of Monodispersed β-$NaGdF_4$:Er^{3+} (2%), Yb^{3+} (20%) with Various Morphologies. The temperature determines the phase selection. β-$NaGdF_4$ nanocrystals are the thermodynamically stable crystalline form compared with the α-phase, and relatively high energy is needed to overcome the energy barrier of the $\alpha \rightarrow \beta$ phase transition. In this work, 315 °C can supply sufficient energy to obtain monodispersed β-phase nanocrystals. To better understand the process of the $\alpha \rightarrow \beta$ phase transition and the growth kinetics, an aliquot was removed from the solution during reaction at various time points after the hot injection was terminated and characterized by TEM, HRTEM imaging, and XRD analysis. Table S1 summarizes the experimental parameters of the upconverting nanocrystals, and Table S3 describes the evolution of their crystal structures and morphologies.

Since the fabrication of $NaGdF_4$ nanoplates has been well-established (see, for example, ref 18), we set it as a control to study the formation of nanorods. Both nanorods and nanoplates exhibited typical α-phase (JCPDS 27-698) at 20 min post-hot injection; however, with extension of the reaction time, the α-phase particles were transferred to the β-phase (Figure S3), indicating that both the rods and plates were formed via a delayed α to β-phase transition pathway. According to a previous study,[37,38] a diffusion controlled kinetic model was proposed for the $\alpha \rightarrow \beta$ phase transition behavior of $NaLnF_4$ in the thermolysis of trifluoroacetate approach. It is classified into two modes: an enhanced or restricted Ostwald ripening process. The selection of enhanced or restricted Ostwald ripening is dependent on the

DOI: 10.1021/acs.chemmater.9b01155
Chem. Mater. XXXX, XXX, XXX–XXX

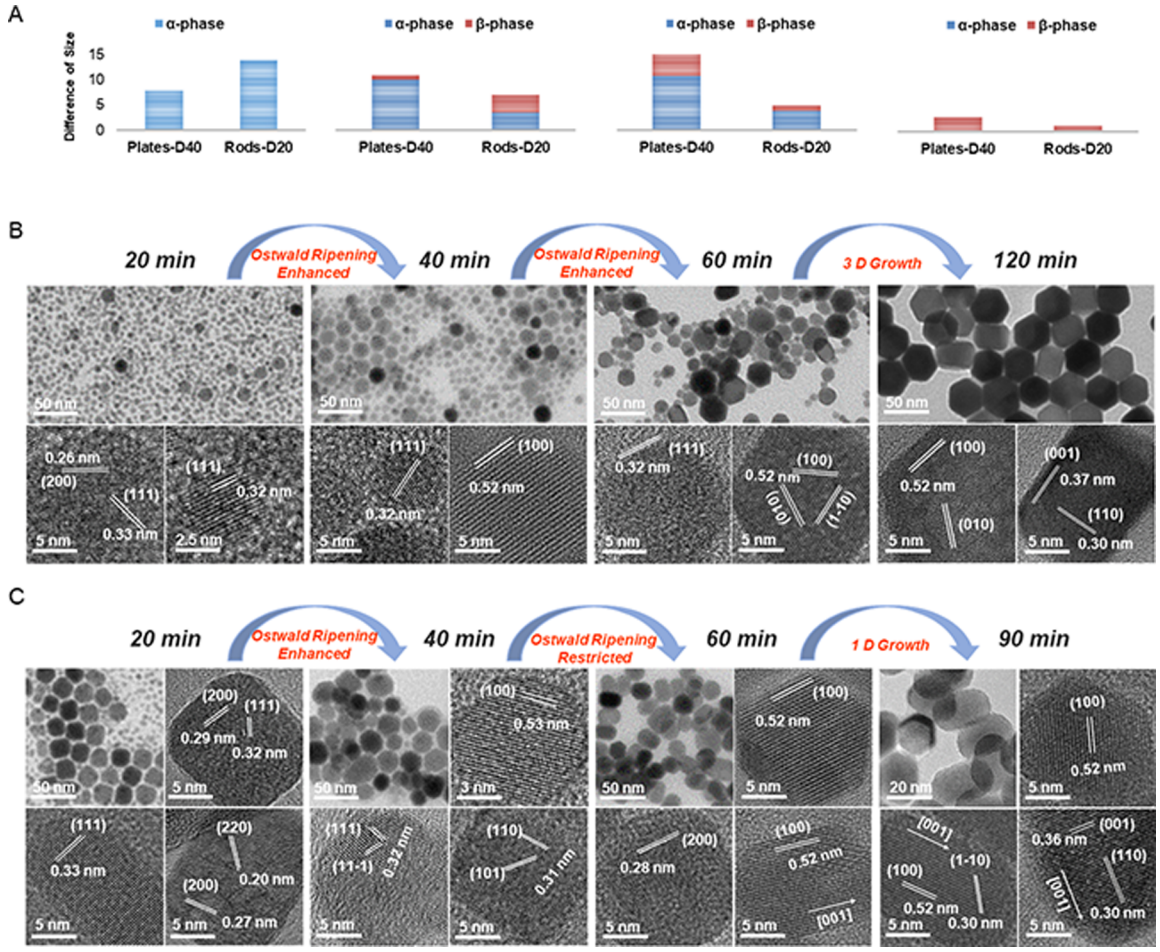

Figure 3. TEM and HRTEM images illustrating the mechanism of the formation of β-$NaGdF_4$:Er^{3+} (2%), Yb^{3+} (20%) nanocrystals with nanoplate and nanorod morphology. (A) Comparison of size evolution of nanocrystals between the formation of nanoplates and nanorods. (B, C) TEM and HRTEM images showed the phase transition and shape evolution at different time points post-hot injection during the formation of the nanoplates (B) and nanorods (C), respectively. Nanoplates were formed via the diffusion controlled enhanced Ostwald ripening during the $\alpha \rightarrow \beta$ phase transition.

concentration of monomers (NaF and LnF_3), which are decomposed from the metal trifluoroacetate precursors. A high monomer concentration will favor the restricted Ostwald ripening, while on the contrary, enhanced Ostwald ripening will occur if the monomer concentration is low enough. The high supersaturation is the main driving force for the anisotropic growth of inorganic nanostructures, and shape-controlled nanocrystals could be generated by the diffusion controlled growth process.[39,40] Briefly, 1-dimensional (1D) growth would be promoted if the monomer concentration in the bulk solution (the area away from the crystal surface) was much higher than that in the stagnant solution (the area right next to the crystal surface). On the other hand, 3D growth would be preferred if the monomer concentration in the bulk solution was lower than that for 1D growth, yet still higher than that in the stagnant solution. Intraparticle diffusion would occur if the chemical potential in the bulk solution was approximately equal to the average chemical potential of the entire surface atoms of a nanocrystal. In this work, a diffusion controlled kinetic model was also proposed to elucidate the phase transition and shape evolution of the synthesized nanocrystals.

For the formation of the nanoplates (Figure 3B), we observed a mixture containing a large portion of small size α-polyhedral particles (~5 nm) as well as some large spheres (~13 nm) at 20 min post-hot injection. Their α-phase structure was confirmed by the HRTEM images, namely, the observation of the (111) lattice fringes for the small polyhedrons and the (200) lattice fringes for the large spheres, respectively. At 40 min post-hot injection, two observations were made. The spheres grew bigger with a larger particle size distribution (6−16 nm) and particles with hexagonal surface (~21 nm) were observed. The spherical particles showed lattice fringes, (111), that were indicative of the α-phase structure, and the β-phase structure of the hexagonal cross sections was revealed by the (100) lattice fringes. It indicated that the small α-phase particles redissolved, and NaF and GdF_3 were released into the solution and then combined with the larger α-phase particles to form the β-phase nanocrystals.[30,37,38,41] With extension of the reaction time, more β-phase nanoplates with hexagon morphology were confirmed by the HRTEM images and gradually increased in size from approximately 26 × 19 nm (60 min) to 40 × 26 nm (120 min). The large size difference of α-phase nanocrystals (Figure 3A) was indicative of the enhanced Ostwald ripening due to the redissolution of the small α-phase nanocrystals. The 3D growth was also proved by the size evolution of β-phase nanocrystals. Therefore, monodispersed, uniform β-$NaGdF_4$:Er^{3+} (2%), Yb^{3+}

DOI: 10.1021/acs.chemmater.9b01155
Chem. Mater. XXXX, XXX, XXX−XXX

(20%) nanoplates were formed via diffusion controlled enhanced Ostwald ripening during the $\alpha \rightarrow \beta$ phase transition.

Figure 3C shows the formation of $NaGdF_4$ nanocrystals with nanorod morphology. In comparison with the formation of nanoplates, there were more uniform large particles (~18 nm) and fewer uniform small α-polyhedrons (~4 nm) at 20 min post-hot injection. The lattice fringes displayed on the large uniform particles revealed their α-phase nature. The less uniform small α-phase particles are easier to redissolve based on the Gibbs−Thomson relations (Ostwald−Freundlich equation).[42] The wider size distribution indicated that the Ostwald ripening occurred vigorously. When extending the reaction time to 40 min, a mixture of α-phase spheres and β-phase nanocrystals with hexagonal morphology were observed, which had similar size (~18 nm). At 60 min post-hot injection, β-phase nanorods were observed (~17 × 24 nm) mixed with spheres (~20 nm). Specifically, the lattice fringes associated with the (111) and (200) planes revealed the α-phase structure of the spheres (Figure 3C-40 min and Figure 3-60 min, bottom left), and the lattice fringes of the (100), (110), and (101) planes confirmed the β-phase structure of the nanocrystals with hexagonal morphology (Figure 3C-40 min and Figure 3C-60 min, right). The lattice fringes corresponding to the (001) lattice plane appeared along the nanorods (Figure 3C-60 min, bottom right), indicating the growth of the nanorods along the [001] direction parallel to the c-axis. The reduced size difference between the α-phase and β-phase nanocrystals revealed that the small α-phase particles redissolved rapidly and caused the high supersaturation in the solution and, thereby, the restricted Ostwald ripening. The monodispersed uniform nanorods ~17 × 28 nm (AR = 0.61) were observed at 90 min after the hot injection. The length of the nanorods was significantly elongated from 60 to 90 min. Taken together, this proves the 1D growth of the nanorods. With extension of the aging time to 180 min, the monomers in the solution gradually reduced. As a result, a 3D growth was demonstrated and the size of the nanorods increased to ~20 × 31 nm with similar AR (Figure S1B). Our results revealed that the β-$NaGdF_4$:Er^{3+} (2%), Yb^{3+} (20%) nanorods underwent a two-stage phase transition: Ostwald ripening was dominant at the beginning of the $\alpha \rightarrow \beta$ transition due to the broad size distribution of the α-phase particles (Figure 3A-20 min). Subsequently, when the monomer concentration increased high enough in the reaction system, the Ostwald ripening process was restricted, resulting in the narrow size difference between α- and β-phase nanocrystals (Figure 3A-40 min). Therefore, the high monomer concentration accelerated the growth rate and promoted the growth of nanocrystals along the c-axis (1D growth). The pure β-phase nanorods were finally formed via diffusion controlled restricted Ostwald ripening. In addition, the preference of the bonding of the oleate ligands to the side facets of hexagonal $NaLnF_4$ also promoted the 1D growth of nanorods.[32,43,44]

In addition, the small sized nanoprisms were formed through diffusion controlled restricted Ostwald ripening (Figure S4B). Specifically, the faster growth of the small α-phase nanocrystals (from 5.2 to 6.4 nm) compared with the larger ones (from 14.1 to 14.7 nm) demonstrated the high monomer concentration in the solution since the smaller nanocrystals grow faster than the larger ones when the monomer concentration is high enough in the solution (Figure S4B-0 min, Figure S4B-10 min).[30] Furthermore, the very narrow size distributions (Figure S4B-20 min) indicated the restricted Ostwald ripening, which promoted the very rapid transformation of α-phase nanocrystals simultaneously to the β-phase, was favored. The critical size for the $\alpha \rightarrow \beta$ transition was determined to be approximately 14.7 nm. The size evolution of the β-phase nanocrystals after phase transition revealed the 3D growth of nanoprisms.

With extension of the reaction time, the nanoprisms and nanoplates transferred to nanospheres and nanodisks, respectively (Figure 4). This can be explained by the

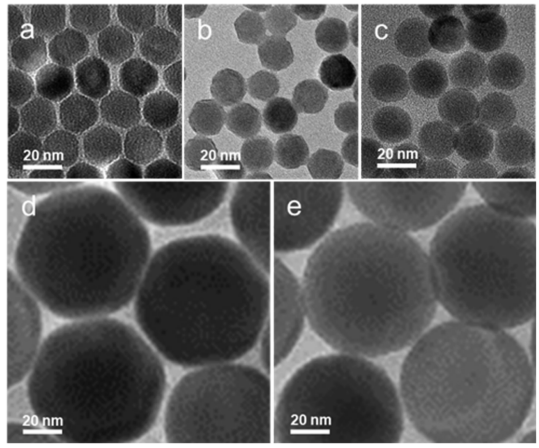

Figure 4. TEM images illustrating the shape evolution of nanoprisms → nanospheres (a, b, and c) and nanoplates → nanodisks (d and e) with extension of the reaction time.

intraparticle diffusion model: with the concentration of the monomers decreasing to the critical level, the ions located at the corners and tips, which were energetically less stable, redissolved and diffused to other facets.[39,40] Theoretically, in the intraparticle diffusion process, the nanodisks may eventually evolve to a spherical shape in order to minimize the surface energy if given enough time. In fact, the shape-evolution process, from rods to spheres via intraparticle diffusion, has been reported by previous research.[40] In our work, Disks-D63 (62.9 × 29.8 nm) in Figure 4e were obtained at 3 h post-hot injection, which had similar size as that of the Plates-D63 (62.6 × 29.2 nm), shown in Figure 4d, obtained at 2 h post-hot injection. The TEM and HRTEM analysis of Disks-D63 (Figure S5) indicated that the sharp corners, which were formed by two adjacent side faces, disappeared while the curved surface was observed. The ratios of Na^+/Gd^{3+} in nanospheres and nanodisks were increased to 1.6 and 3.4, respectively (Table S2), indicating more Na^+ occupied the vacancies of β-crystal lattice with extension of reaction time to 180 min.

Comparing the XRD analysis at 40 min post-hot injection (Figure S6A), a different percentage of β-phase nanocrystals was observed in the formation of Prisms-D19 (100%), Rods-D20 (53.5%), and Plates-D40 (16.2%), respectively. Pure β-phase nanocrystals were observed in the formation of Prisms-D19 while a mixture of α-phase and β-phase nanocrystals was demonstrated in the formation of Rods-D20 as well as Plates-D40. There were more β-phase nanocrystals formed for the nanorods than that of the nanoplates. This proved that high supersaturation is a prerequisite for the $\alpha \rightarrow \beta$ phase transition and the higher transition rate is related to the restricted Ostwald ripening.

In conclusion, the growth of β-phase nanocrystals occurred simultaneously with the phase transition resulting in uniform,

DOI: 10.1021/acs.chemmater.9b01155
Chem. Mater. XXXX, XXX, XXX−XXX

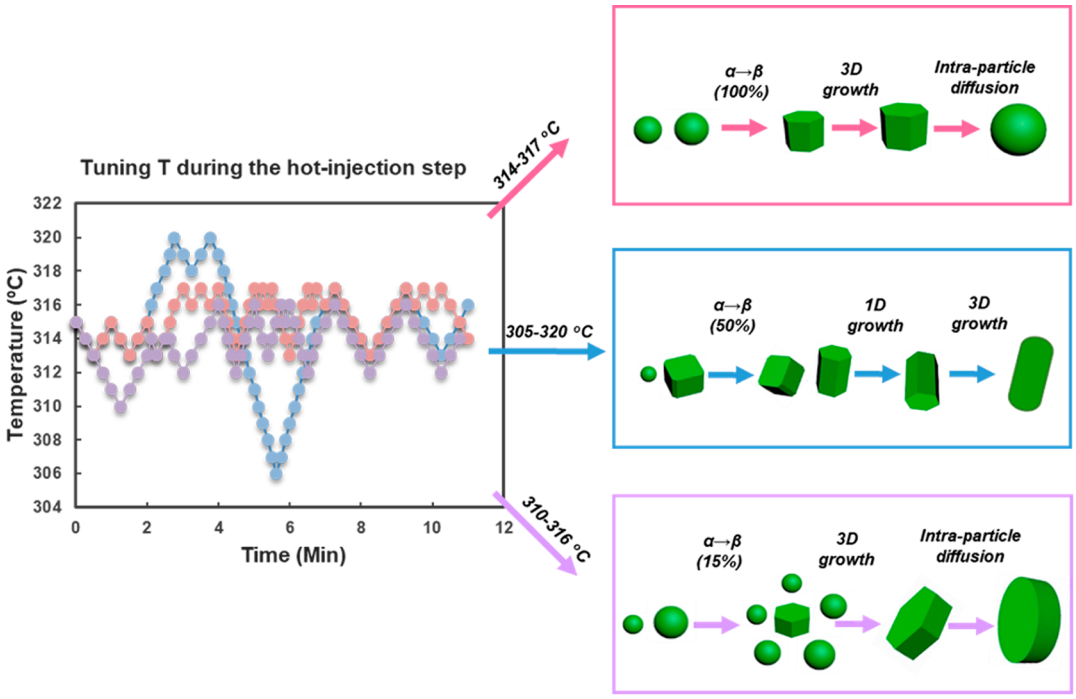

Figure 5. Scheme of the influence on shape evolution of upconverting nanocrystals by tuning injecting temperature during the hot-injection step.

monodispersed nanocrystals once the termination of the phase transition occurred. Thus, the monodispersity of the obtained nanocrystals would not change with further extension of the reaction time. The nucleation and growth of α-phase nanocrystals before the phase transition plays a vital role in the formation of various morphologies and subsequently influences the $\alpha \rightarrow \beta$ phase transition pathway.

3.3. Effects of Reaction Temperature on the Morphology of β-NaGdF$_4$:Er^{3+} (2%), Yb^{3+}(20%) Nanocrystals. According to the classical nucleation theory,[45] supersaturation is the driving force in crystallization. There are two critical factors that dominate the phase transition:[28,30,37,38,41] (1) the concentration of NaF decides the formation of β-NaGdF$_4$; (2) it is necessary to accumulate enough α-NaGdF$_4$ to reach the critical size for phase transition, which was also confirmed by our results above. According to the HRTEM results (Figure 3 and Figure S4) and Table S3, we estimated the critical sizes to be ∼14.7 nm (Prisms-D19), ∼15.1 nm (Plates-D63), ∼18.1 nm (Plates-D40), and ∼18.2 nm (Rods-D20), respectively. The reaction temperature could directly affect the rate of nucleation and growth and, subsequently, affect the morphology of the nanocrystals. Since the nucleation rate is more sensitive to the temperature variation in the process of hot injection than in that of the one-pot approach,[31] tuning the reaction temperature could be an effective approach to control the particle morphology. All experimental variables were kept constant during the hot-injection step except the temperature. Post-hot injection, the temperature was kept at 315 °C and maintained constant until the termination of the reaction resulting in uniform monodispersed nanorods and nanoplates (Table S1). With our heating system, tuning the injection temperature between 310 and 320 °C (see Figure 5, pink and purple), uniform nanoprisms and nanoplates were synthesized, respectively. On the other hand, tuning the temperature between 305 and 320 °C (see Figure 5, blue) during the injection, uniform nanorods were obtained. This demonstrated that the injecting temperature was directly related to the nucleation and growth of the NaGdF$_4$:Er^{3+}(2%), Yb^{3+} (20%) nanocrystals. Here, we elucidated the influence on shape evolution of the upconverting nanocrystals by tuning injecting temperature during the hot-injection step (Figure 5).

In more detail, a turbid solution was observed during the injection in all the experiments, indicating the nucleation of the α-phase nanocrystals. Comparing with the growth of nanoplates, the wide fluctuation (309−320 °C) during the hot-injection step used for the formation of Rods-D20 provided dynamic control of the nucleation and growth of α-phase nanocrystals. When the injection temperature reached 320 °C, a large amount of white gas vigorously escaped from the solution, indicating a burst of decomposition of precursors due to the higher temperature. When lowering the injection temperature to 309 °C, the solution appeared turbid, revealing a sudden nucleation of α-phase particles as a result of supersaturation of monomers. Then, the injection temperature was tuned back to 315 °C and maintained constant until the end of the injection. The obvious difference between the large and small α-phase nanocrystals observed at 20 min post-hot injection as shown in Figure 3C proved that some α-phase nanocrystals grew fast and became more uniform in some regions of the solution due to the temporary modulation of the temperature and subsequent manipulation of the supersaturation during the hot injection. With this condition, they were able to first reach the critical size for phase transition,[41] and the small α-phase nanocrystals completely redissolved because they were thermally unstable with the extension of time, therefore resulting in the high monomer concentration favorable for the 1D growth. On the other hand, the constant temperature during injection (314−317 °C) was important to form the small hexagonal shaped nanoprisms since the constant temperature leads to the constant driving force for the growth of α-phase nanocrystals, resulting in their narrow

DOI: 10.1021/acs.chemmater.9b01155
Chem. Mater. XXXX, XXX, XXX−XXX

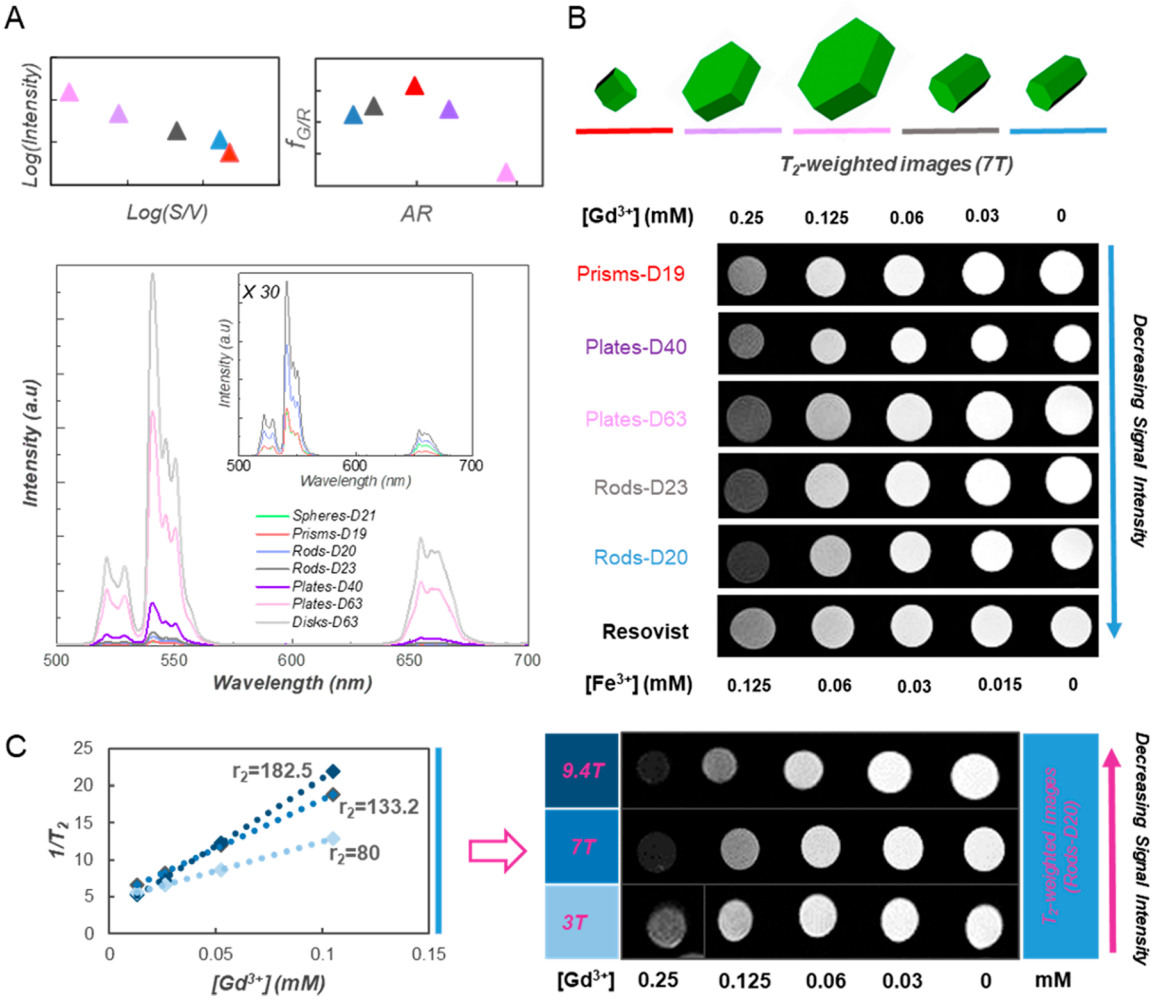

Figure 6. Upconversion luminescence spectra and MR imaging of the upconverting nanocrystals with various morphologies studied in this work. (A) The upconversion luminescence spectra, the upconversion luminescence intensity as a function of the S/V of upconverting nanocrystals in a logarithmic scale, and the $f_{G/R}$ as a function of the AR of the upconverting nanocrystals. (B) The negative contrast demonstrated on T_2-weighted images at 7 T. (C) The T_2-weighted MR images of Rods-D20 vs various Gd^{3+} concentrations in 0.5% agarose at 3 T, 7 T, and 9.4 T magnetic fields, respectively, and plot of $1/T_2$ versus Gd^{3+} concentration. The slope indicates the corresponding specific relaxivities r_2.

size distribution (6.4 ± 0.98 nm) at the onset of their $\alpha \rightarrow \beta$ phase transition compared (13.1 ± 6.25 nm) with that of the formation of large nanoplates (Figure S4A). There were no α-phase nanocrystals redissolved in the solution, and all of them simultaneously transferred to the β-phase via the diffusion controlled restricted Ostwald ripening. By tuning the temperature during the hot-injection we were able to manipulate the nucleation and growth of α-phase nanocrystals before the phase transition, which would subsequently decide the $\alpha \rightarrow \beta$ phase transition pathway as described in the previous section.

With increasing the injecting temperature to 320 °C and tuning back it to 315 °C after the hot injection, monodispersed 63 × 29 nm large nanoplates (Plates-D63) were formed (Figure S4A). Interestingly, the smaller nanoplates (Plates-D53, 53 × 29 nm) were obtained when the temperature was kept at 320 °C during the reaction. Only a slight increase of the particle size was observed when the reaction temperature was further increased to 330 °C (Figure S7). According to the classic theory of nucleation,[42] there are three main factors that govern the rate of nucleation: for nucleation to occur, it must overcome an energy barrier (ΔG) to form a nucleus stable enough to grow. Additionally, there is also a barrier ($\Delta G'$) for an atom to cross the interface separating the nucleus and the matrix, which addresses the effect of the viscosity of the solution. The nucleation rate (N) is described as the following equation:[42]

$$N = \exp[-16\pi\gamma^3 v^2/3k^3T^3(\ln S)^2 + \Delta G'/kT]$$

where T is the temperature, S is the supersaturation, γ is the surface energy, and v is the molecular volume. The size of a critical nucleus increases with temperature while the nucleation rate usually follows an exponential curve as the supersaturation is increased. However, in the process of hot-injection thermolysis, metal trifluoroacetate precursors are first decomposed followed by nucleation and further growth. The rate of decomposition of the precursors increases with temperature. When the temperature increases the equilibrium saturation of the solution (C^*) will increase accordingly, meanwhile the solution concentration (C) also increases with the temperature due to the increasing rate of thermal decomposition. Therefore, the supersaturation, $S = C/C^*$, would vary with temperature, and the nucleation rate will be decided by the temperature, the supersaturation, and the surface energy, as well as the viscosity of the solution. This will explain the

DOI: 10.1021/acs.chemmater.9b01155
Chem. Mater. XXXX, XXX, XXX−XXX

difficulty in increasing the particle size when increasing the temperature from 320 to 330 °C. When the temperature was tuned back to 315 °C from 320 °C after the hot injection, the sudden increase of the supersaturation will promote the growth of α-phase nanocrystals in some region of the solution to reach the critical size necessary for phase transition. When extending the reaction time, the large nanoplates were formed through the enhanced Ostwald ripening. This finding provides an effective way to increase the particle size by simply lowering the reaction temperature after the hot injection.

3.4. Morphology Effects on Upconversion Luminescence. In all cases, identical concentrations of upconverting nanocrystals were used to obtain the luminescence spectra. Figure 6A showed the corresponding upconversion luminescence spectra of the diverse β-$NaGdF_4$:Er^{3+}, Yb^{3+} nanocrystals following 980 nm laser excitation. In all cases, green emission was observed between ca. 510−570 nm ascribed to transitions from the $^2H_{11/2}$ and $^4S_{3/2}$ excited states to the $^4I_{15/2}$ ground state (centered at 525 and 550 nm, respectively) while red emission was observed between 638 and 680 nm from the $^4F_{9/2}$ excited state to the ground state (centered at 655 nm). As a general observation, the emission intensity of the lanthanide doped UCNPs is size-dependent since surface quenching effects play a pivotal role in increasing nonradiative decay. As such, smaller nanocrystals tend to have increased surface quenching sites and thus suppressed upconversion luminescence.[30,46−49] It is well-known that the surface to volume ratio (S/V) is the main factor related to surface quenching. It would be more accurate to elucidate the size effect on the upconversion intensity using the S/V value rather than the diameter of the UCNPs. Based on the results obtained from ICP-MS, the composition fractions of Er^{3+}, Yb^{3+}, Gd^{3+}, and Na^+ proved to be consistent in the synthesized upconverting nanocrystals except for nanospheres and nanodisks (Table S3). Therefore, it is reasonable to study the correlation between luminescence intensity and the ratio of S/V among the nanoprisms, nanorods, and nanoplates. By integrating the green and red emission intensities, we observed that the emission intensity was inversely proportional to the S/V in the logarithmic scale (Figure 6A). The amount of Er^{3+} on or near the surface in the individual nanocrystals would increase with the increased S/V, thus resulting in decreased upconversion emission since those luminescent ions do not contribute to the overall intensity. We also observed that the ratio of green to red emission ($f_{G/R}$) was correlated with the AR of the upconverting nanocrystals (Figure 6A). When the AR was close to 1, a higher ratio of green to red emission was observed. The red UC emission at 650 nm arises from the $^4F_{9/2}$ state, which can be populated by either nonradiative decay from the $^2H_{11/2}$/$^4S_{3/2}$ states or by directly exciting the Er^{3+} ions from the $^4I_{13/2}$ state to the $^4F_{9/2}$ state through energy transfer from Yb^{3+} ions. For the direct population of the $^4F_{9/2}$ state to occur, the excited Er^{3+} ions would have to non-radiatively decay to the $^4I_{13/2}$ state. In smaller UCNPs, a larger fraction of Er^{3+} ions would be on or near the surface. Hence, they would be exposed to the large vibrational energies of the capping ligand, solvent, etc. This makes multiphonon decay from the $^4I_{11/2}$ excited state to the lower $^4I_{13/2}$ state, and ultimately to the $^4I_{15/2}$ ground state, more probable. Thus, the smaller particles usually show higher $f_{G/R}$ compared with the larger one. Our results revealed that the particle size tended to become smaller when the AR was close to 1. In this regard, the size effect is one reasonable factor causing the correlation between the $f_{G/R}$ and the ARs.

3.5. Morphology Effect on r_1 and r_2 and MR Imaging. To study the effect of the morphologies of the diverse upconverting nanocrystals on the MR properties, we investigated their MR relaxivity at 3 T, 7 T, and 9.4 T to observe their effects at high magnetic fields, respectively. Figure 6C displayed the concentration-dependent negative contrast gradient produced by Rods-D20, indicating the consequence of high r_2 values. With the increase of magnetic fields, the r_2 relaxivity significantly increased, resulting in an enhanced negative contrast in T_2-weighted images. For example, we calculated the % of signal density at 0.125 mM of [Gd^{3+}] normalized to water at three different magnetic fields. They are 77% (3 T), 64% (7 T), and 53% (9.4 T), respectively. Similarly, the other upconverting nanocrystals also demonstrated promising r_2 relaxivity, extremely high r_2/r_1 ratio, and enhanced negative contrast at the three magnetic fields, which increased with magnetic fields (9.4 T > 7 T > 3 T) (Tables S4 and S5). We also found that the r_2 value varied based on their morphology such as size and shape. The nanorods showed higher r_2 and consequently displayed better contrast in T_2-weighted images comparing with other upconverting nanocrystals (Figure 6B, Figure S8). Theoretically, relaxation of bulk water arises from exchange of water molecules associated with Gd^{3+} ions. At high magnetic field (1.5 T and above), T_1 relaxivity typically decreases while T_2 relaxivity increases resulting in an increasing r_2/r_1 with increasing field strength.[50] In addition, the dramatically enhanced T_2 relaxivity is also attributed to the high magnetization of Gd^{3+} in the nanocrystals, which arises from the average alignment of Gd^{3+} magnetic moments along the applied field[51] and increases with the field strength.[52] r_1 decreased with increasing the size of the upconverting nanocrystals because relatively less Gd^{3+} on the surface of larger nanocrystals reduced its interaction with water molecules.[36] The size effect on r_2 could be explained by "spin-canting effects", with the decrease in nanocrystal size, the surface to volume ratio increasing, and curvature of the nanocrystals becoming more pronounced. As a result, spins located near the surface tend to be slightly tilted (i.e., canted spins) and result in a low magnetization value for small nanocrystals compared to that for big ones, hence, low T_2 relaxation.[53] From our results, r_2 depended on not only the size but also the shape of the nanocrystals. Even though the nanorods were smaller than the nanoplates, they had a higher r_2 and, therefore, better negative contrast enhancement in T_2-weighted images, and it was comparable to the commercial T_2 contrast agents (Resovist). One of the possible reasons is that the greater S/V of nanorods resulted in a greater number of hydrogen nuclei of water in proximity; therefore, a greater number of neighboring nuclei interacted with the magnetic field generated by the nanocrystals, resulting in faster relaxation.[54] In a nutshell, it suggests the high potential of these upconverting nanocrystal (20−60 nm) effective T_2 contrast agents at high magnetic fields. In addition, they have much higher upconversion photoluminescence intensity when compared to the smaller sized one (<10 nm) used for T_1 contrast agents.

4. CONCLUSIONS AND PERSPECTIVES

Our work has demonstrated that modulation of the hot-injection temperature and reaction time could be an effective

DOI: 10.1021/acs.chemmater.9b01155
Chem. Mater. XXXX, XXX, XXX−XXX

approach to control the morphology of β-$NaGdF_4$:Er^{3+}, Yb^{3+} upconverting nanocrystals. The different supersaturation at the different temperatures could directly manipulate the nucleation and growth of α-phase nanocrystals before the $\alpha \rightarrow \beta$ phase transition, subsequently influences the Ostwald ripening mode, and consequently affects the morphology, uniformity, and monodispersity of the upconverting nanocrystals. During the formation of nanorods, the high supersaturation caused by the sudden redissolution of α-phase nanocrystals (Ostwald ripening enhanced) at the onset of the phase transition inversely restricted the Ostwald ripening in the following reaction, and monodispersed uniform nanorods were finally formed through diffusion controlled restricted Ostwald ripening. The upconversion luminescence intensity decreased with increase of the S/V ratio of the upconverting nanocrystals and a higher ratio of green to red emission was observed when the AR was close to 1. The T_2 relaxivity, the r_2/r_1, and negative contrast enhancement of the upconverting nanocrystals are increased with increase of size except for the nanorods, which performed the best as a T_2 contrast agents even though they are smaller compared to the nanoplates. In a nutshell, our findings provided strong evidence for morphology controlled synthesis of $NaGdF_4$ UCNPs for the design of multifunctional platforms for biomedical applications.

■ ASSOCIATED CONTENT

Supporting Information

The Supporting Information is available free of charge on the ACS Publications website at DOI: 10.1021/acs.chemmater.9b01155.

Synthesis parameters, crystal structure (phase), and morphology of all upconverting nanocrystals studied (Table S1), monodispersed, uniform nanorods demonstrated by TEM analysis (Figure S1), elemental composition of studied upconverting nanocrystals (Table S2), summary of phase and size evolution of studied upconverting nanocrystals post-hot injection (Table S3), crystal structure of upconverting nanocrystals with various morphologies analyzed by XRD (Figure S2), phase transition during the formation of nanoplates and nanorods analyzed by XRD (Figure S3), phase transition and shape evolution during the formation of nanoprisms and large nanoplates (Figure S4), discotic morphology of nanodisks demonstrated by TEM and HRTEM analysis (Figure S5), comparison of the phase transition processes during formation of nanoprisms, nanorods, and nanoplates by XRD analysis and TEM images (Figure S6), influence on the size of nanoplates by tuning the temperature post-hot injection (Figure S7), r_1 and r_2 relaxivity and MR imaging of studied upconverting nanoparticles (Table S4), and negative contrast enhancement in T_2-weighted images by the upconverting nanocrystals studied (Table S5 and Figure S8) (PDF)

Video of synthesized nanorods (Rods-D20) analyzed by electronic tomography (MPG)

■ AUTHOR INFORMATION

Corresponding Author

*(F.V.) E-mail: vetrone@emt.inrs.ca.

ORCID

Miao Wang: 0000-0003-0625-3351

Yu Zhang: 0000-0002-2672-8943

Qiaofeng Yao: 0000-0002-5129-9343

Xu Li: 0000-0001-5589-2905

Federico Rosei: 0000-0001-8479-6955

Fiorenzo Vetrone: 0000-0002-3222-3052

Author Contributions

The manuscript was written through contributions of all authors. All authors have given approval to the final version of the manuscript

Notes

The authors declare no competing financial interest.

■ ACKNOWLEDGMENTS

F.V. acknowledges funding from the Natural Sciences and Engineering Research Council (NSERC) of Canada through the Discovery Grants program and the Discovery Accelerator Supplement (DAS) award, the Canada Foundation for Innovation for infrastructure and its operation, and the Fonds de Recherche du Québec Nature et technologies (FRQNT). F.R. acknowledges NSERC for a Discovery Grant and the Canada Research Chairs program for funding and partial salary support. M.W. and A.Y.C. are grateful to the Johns Hopkins Singapore Research Fund provided by Private limited Company for supporting their Santa Fe research programme. X.L., M.N., and K.K.B. acknowledge the support of A*STAR, Singapore.

■ REFERENCES

(1) Haase, M.; Schäfer, H. Upconverting Nanoparticles. *Angew. Chem., Int. Ed.* **2011**, *50* (26), 5808−5829.

(2) Auzel, F. Upconversion and Anti-Stokes Processes with f and d Ions in Solids. *Chem. Rev.* **2004**, *104* (1), 139−174.

(3) Bunzli, J.-C. G. Lanthanide Luminescence for Biomedical Analyses and Imaging. *Chem. Rev.* **2010**, *110* (5), 2729−2755.

(4) Park, Y. I.; Kim, J. H.; Lee, K. T.; Jeon, K.-S.; Na, H. B.; Yu, J. H.; Kim, H. M.; Lee, N.; Choi, S. H.; Baik, S.-I.; Kim, H.; Park, S. P.; Park, B.-J.; Kim, Y. W.; Lee, S. H.; Yoon, S.-Y.; Song, I. C.; Moon, W. K.; Suh, Y. D.; Hyeon, T. Nonblinking and Nonbleaching Upconverting Nanoparticles as an Optical Imaging Nanoprobe and T_1 Magnetic Resonance Imaging Contrast Agent. *Adv. Mater.* **2009**, *21* (44), 4467−4471.

(5) Yan, C.; Zhao, H.; Perepichka, D. F.; Rosei, F. Lanthanide Ion Doped Upconverting Nanoparticles: Synthesis, Structure and Properties. *Small* **2016**, *12* (29), 3888−3907.

(6) König, K. Multiphoton Microscopy in Life Sciences. *J. Microsc.* **2000**, *200* (2), 83−104.

(7) van de Rijke, F.; Zijlmans, H.; Li, S.; Vail, T.; Raap, A. K.; Niedbala, R. S.; Tanke, H. J. Up-Converting Phosphor Reporters for Nucleic Acid Microarrays. *Nat. Biotechnol.* **2001**, *19* (3), 273−276.

(8) Lim, S. F.; Riehn, R.; Ryu, W. S.; Khanarian, N.; Tung, C.-k.; Tank, D.; Austin, R. H. In Vivo and Scanning Electron Microscopy Imaging of Upconverting Nanophosphors in Caenorhabditis Elegans. *Nano Lett.* **2006**, *6* (2), 169−174.

(9) Boyer, J.-C.; Vetrone, F.; Cuccia, L. A.; Capobianco, J. A. Synthesis of Colloidal Upconverting $NaYF_4$ Nanocrystals Doped with Er^{3+}, Yb^{3+} and Tm^{3+}, Yb^{3+} via Thermal Decomposition of Lanthanide Trifluoroacetate Precursors. *J. Am. Chem. Soc.* **2006**, *128* (23), 7444−7445.

(10) Jalani, G.; Naccache, R.; Rosenzweig, D. H.; Haglund, L.; Vetrone, F.; Cerruti, M. Photocleavable Hydrogel-Coated Upconverting Nanoparticles: A Multifunctional Theranostic Platform for NIR Imaging and On-Demand Macromolecular Delivery. *J. Am. Chem. Soc.* **2016**, *138* (3), 1078−1083.

(11) Idris, N. M.; Gnanasammandhan, M. K.; Zhang, J.; Ho, P. C.; Mahendran, R.; Zhang, Y. In Vivo Photodynamic Therapy using

DOI: 10.1021/acs.chemmater.9b01155
Chem. Mater. XXXX, XXX, XXX−XXX

Upconversion Nanoparticles as Remote-controlled Nanotransducers. *Nat. Med.* **2012**, *18*, 1580−1585.
(12) Kumar, R.; Nyk, M.; Ohulchanskyy, T. Y.; Flask, C. A.; Prasad, P. N. Combined Optical and MR Bioimaging Using Rare Earth Ion Doped $NaYF_4$ Nanocrystals. *Adv. Funct. Mater.* **2009**, *19*, 853−859.
(13) Huang, Y.; Skripka, A.; Labrador-Páez, L.; Sanz-Rodríguez, F.; Haro-González, P.; Jaque, D.; Rosei, F.; Vetrone, F. Upconverting Nanocomposites with Combined Photothermal and Photodynamic Effects. *Nanoscale* **2018**, *10*, 791−799.
(14) Skripka, A.; Karabanovas, V.; Jarockyte, G.; Marin, R.; Tam, V.; Cerruti, M.; Rotomskis, R.; Vetrone, F. Decoupling Theranostics with Rare Earth Doped Nanoparticles. *Adv. Funct. Mater.* **2019**, *29*, 1807105.
(15) Zhou, B.; Shi, B.; Jin, D.; Liu, X. Controlling Upconversion Nanocrystals for Emerging Applications. *Nat. Nanotechnol.* **2015**, *10*, 924−936.
(16) Zeng, S.; Xiao, J.; Yang, Q.; Hao, J. Bi-Functional $NaLuF_4$: $Gd^{3+}/Yb^{3+}/Tm^{3+}$ Nanocrystals: Structure Controlled Synthesis, Near-Infrared Upconversion Emission and Tunable Magnetic Properties. *J. Mater. Chem.* **2012**, *22* (19), 9870−9874.
(17) Chen, G.; Qiu, H.; Prasad, P. N.; Chen, X. Upconversion Nanoparticles: Design, Nanochemistry, and Applications in Theranostics. *Chem. Rev.* **2014**, *114* (10), 5161−5214.
(18) Vetrone, F.; Naccache, R.; Mahalingam, V.; Morgan, C. G.; Capobianco, J. A. The Active-Core/Active-Shell Approach: A Strategy to Enhance the Upconversion Luminescence in Lanthanide-Doped Nanoparticles. *Adv. Funct. Mater.* **2009**, *19* (18), 2924−2929.
(19) Ho, D.; Sun, X.; Sun, S. Monodisperse Magnetic Nanoparticles for Theranostic Applications. *Acc. Chem. Res.* **2011**, *44* (10), 875−882.
(20) Hinde, E.; Thammasiraphop, K.; Duong, H. T. T.; Yeow, J.; Karagoz, B.; Boyer, C.; Gooding, J. J.; Gaus, K. Pair Correlation Microscopy Reveals the Role of Nanoparticle Shape in Intracellular Transport and Site of Drug Release. *Nat. Nanotechnol.* **2017**, *12*, 81−89.
(21) Gnach, A.; Bednarkiewicz, A. Lanthanide-Doped Up-Converting Nanoparticles: Merits and Challenges. *Nano Today* **2012**, *7* (6), 532−563.
(22) Na, H. B.; Hyeon, T. Nanostructured T_1 MRI Contrast Agents. *J. Mater. Chem.* **2009**, *19* (35), 6267−6273.
(23) Park, J.; Lee, E.; Hwang, N.-M.; Kang, M.; Kim, S. C.; Hwang, Y.; Park, J.-G.; Noh, H.-J.; Kim, J.-Y.; Park, J.-H.; Hyeon, T. One-Nanometer-Scale Size-Controlled Synthesis of Monodisperse Magnetic Iron Oxide Nanoparticles. *Angew. Chem., Int. Ed.* **2005**, *44* (19), 2872−2877.
(24) Johnson, N. J. J.; Oakden, W.; Stanisz, G. J.; Scott Prosser, R.; van Veggel, F. C. J. M. Size-Tunable, Ultrasmall $NaGdF_4$ Nanoparticles: Insights into Their T_1 MRI Contrast Enhancement. *Chem. Mater.* **2011**, *23* (16), 3714−3722.
(25) Jun, Y.-w.; Huh, Y.-M.; Choi, J.-s.; Lee, J.-H.; Song, H.-T.; Yoon, S.; Kim, K.-S.; Shin, J.-S.; Suh, J.-S.; Cheon, J.; Kim, K.-S. Nanoscale Size Effect of Magnetic Nanocrystals and Their Utilization for Cancer Diagnosis via Magnetic Resonance Imaging. *J. Am. Chem. Soc.* **2005**, *127* (16), 5732−5733.
(26) Wang, G.; Peng, Q.; Li, Y. Lanthanide-Doped Nanocrystals: Synthesis, Optical-Magnetic Properties, and Applications. *Acc. Chem. Res.* **2011**, *44* (5), 322−332.
(27) Wang, F.; Liu, X. Recent Advances in the Chemistry of Lanthanide-Doped Upconversion Nanocrystals. *Chem. Soc. Rev.* **2009**, *38* (4), 976−989.
(28) Mai, H.-X.; Zhang, Y.-W.; Si, R.; Yan, Z.-G.; Sun, L.-d.; You, L.-P.; Yan, C.-H. High-Quality Sodium Rare-Earth Fluoride Nanocrystals: Controlled Synthesis and Optical Properties. *J. Am. Chem. Soc.* **2006**, *128* (19), 6426−6436.
(29) Naccache, R.; Vetrone, F.; Mahalingam, V.; Cuccia, L. A.; Capobianco, J. A. Controlled Synthesis and Water Dispersibility of Hexagonal Phase $NaGdF_4$:Ho^{3+}/Yb^{3+} Nanoparticles. *Chem. Mater.* **2009**, *21* (4), 717−723.
(30) Shan, J.; Ju, Y. A Single-Step Synthesis and the Kinetic Mechanism for Monodisperse and Hexagonal-Phase $NaYF_4$:Yb, Er Upconversion Nanophosphors. *Nanotechnology* **2009**, *20* (27), 275603.
(31) Tian, Q.; Tao, K.; Li, W.; Sun, K. Hot-Injection Approach for Two-Stage Formed Hexagonal $NaYF_4$:Yb, Er Nanocrystals. *J. Phys. Chem. C* **2011**, *115* (46), 22886−22892.
(32) Fischer, S.; Swabeck, J. K.; Alivisatos, A. P. Controlled Isotropic and Anisotropic Shell Growth in β-$NaLnF_4$ Nanocrystals Induced by Precursor Injection Rate. *J. Am. Chem. Soc.* **2017**, *139* (35), 12325−12332.
(33) Boyer, J.-C.; Cuccia, L. A.; Capobianco, J. A. Synthesis of Colloidal Upconverting $NaYF_4$: Er^{3+}/Yb^{3+} and Tm^{3+}/Yb^{3+} Monodisperse Nanocrystals. *Nano Lett.* **2007**, *7* (3), 847−852.
(34) Viswanathan, S.; Kovacs, Z.; Green, K. N.; Ratnakar, S. J.; Sherry, A. D. Alternatives to Gadolinium-Based Metal Chelates for Magnetic Resonance Imaging. *Chem. Rev.* **2010**, *110* (5), 2960−3018.
(35) Na, H. B.; Song, I. C.; Hyeon, T. Inorganic Nanoparticles for MRI Contrast Agents. *Adv. Mater.* **2009**, *21* (21), 2133−2148.
(36) Naccache, R.; Chevallier, P.; Lagueux, J.; Gossuin, Y.; Laurent, S.; Vander Elst, L.; Chilian, C.; Capobianco, J. A.; Fortin, M.-A. High Relaxivities and Strong Vascular Signal Enhancement for $NaGdF_4$ Nanoparticles Designed for Dual MR/Optical Imaging. *Adv. Healthcare Mater.* **2013**, *2* (11), 1478−1488.
(37) Mai, H.-X.; Zhang, Y.-W.; Sun, L.-D.; Yan, C.-H. Size-and Phase-Controlled Synthesis of Monodisperse $NaYF_4$:Yb, Er Nanocrystals from a Unique Delayed Nucleation Pathway Monitored with Upconversion Spectroscopy. *J. Phys. Chem. C* **2007**, *111* (37), 13730−13739.
(38) Dühnen, S.; Rinkel, T.; Haase, M. Size Control of Nearly Monodisperse β-$NaGdF_4$ Particles Prepared from Small α-$NaGdF_4$ Nanocrystals. *Chem. Mater.* **2015**, *27*, 4033−4039.
(39) Peng, Z. A.; Peng, X. Mechanisms of the Shape Evolution of CdSe Nanocrystals. *J. Am. Chem. Soc.* **2001**, *123* (7), 1389−1395.
(40) Peng, X.; Manna, L.; Yang, W.; Wickham, J.; Scher, E.; Kadavanich, A.; Alivisatos, A. P. Shape Control of CdSe Nanocrystals. *Nature* **2000**, *404* (6773), 59−61.
(41) May, P. B.; Suter, J. D.; May, P. S.; Berry, M. T. The Dynamics of Nanoparticle Growth and Phase Change during Synthesis of β-$NaYF_4$. *J. Phys. Chem. C* **2016**, *120* (17), 9482−9489.
(42) Mullin, J. W. *Crystallization*; Butterworth-Heinemann: 2001.
(43) Wang, L.; Li, Y. Controlled Synthesis and Luminescence of Lanthanide Doped $NaYF_4$ Nanocrystals. *Chem. Mater.* **2007**, *19* (4), 727−734.
(44) Liu, C.; Wang, H.; Zhang, X.; Chen, D. Morphology- and Phase-Controlled Synthesis of Monodisperse Lanthanide-Doped $NaGdF_4$ Nanocrystals with Multicolor Photoluminescence. *J. Mater. Chem.* **2009**, *19* (4), 489−496.
(45) Cushing, B. L.; Kolesnichenko, V. L.; O'Connor, C. J. Recent Advances in the Liquid-Phase Syntheses of Inorganic Nanoparticles. *Chem. Rev.* **2004**, *104* (9), 3893−3946.
(46) Bai, X.; Song, H.; Pan, G.; Lei, Y.; Wang, T.; Ren, X.; Lu, S.; Dong, B.; Dai, Q.; Fan, L. Size-Dependent Upconversion Luminescence in Er^{3+}/Yb^{3+}-Codoped Nanocrystalline Yttria: Saturation and Thermal Effects. *J. Phys. Chem. C* **2007**, *111* (36), 13611−13617.
(47) Boyer, J.-C.; van Veggel, F. C. J. M. Absolute Quantum Yield Measurements of Colloidal $NaYF_4$: Er^{3+}, Yb^{3+} Upconverting Nanoparticles. *Nanoscale* **2010**, *2* (8), 1417−1419.
(48) Würth, C.; Fischer, S.; Grauel, B.; Alivisatos, A. P.; Resch-Genger, U. Quantum Yields, Surface Quenching, and Passivation Efficiency for Ultrasmall Core/Shell Upconverting Nanoparticles. *J. Am. Chem. Soc.* **2018**, *140* (14), 4922−4928.
(49) Martínez, E. D.; Brites, C. D. S.; Carlos, L. D.; García-Flores, A. F.; Urbano, R. R.; Rettori, C. Electrochromic Switch Devices Mixing Small- and Large-Sized Upconverting Nanocrystals. *Adv. Funct. Mater.* **2019**, *29* (8), 1807758.
(50) Caravan, P.; Farrar, C. T.; Frullano, L.; Uppal, R. Influence of Molecular Parameters and Increasing Magnetic Field Strength on

DOI: 10.1021/acs.chemmater.9b01155
Chem. Mater. XXXX, XXX, XXX−XXX

Relaxivity of Gadolinium- and Manganese-Based T_1 Contrast Agents. *Contrast Media Mol. Imaging* **2009**, *4* (2), 89−100.
(51) Das, G. K.; Johnson, N. J. J.; Cramen, J.; Blasiak, B.; Latta, P.; Tomanek, B.; van Veggel, F. C. J. M. $NaDyF_4$ Nanoparticles as T_2 Contrast Agents for Ultrahigh Field Magnetic Resonance Imaging. *J. Phys. Chem. Lett.* **2012**, *3* (4), 524−529.
(52) Boxerman, J. L.; Hamberg, L. M.; Rosen, B. R.; Weisskoff, R. M. MR Contrast due to Intravascular Magnetic Susceptibility Perturbations. *Magn. Reson. Med.* **1995**, *34* (4), 555−566.
(53) Jun, Y.-w.; Lee, J.-H.; Cheon, J. Chemical Design of Nanoparticle Probes for High-Performance Magnetic Resonance Imaging. *Angew. Chem., Int. Ed.* **2008**, *47* (28), 5122−5135.
(54) Joshi, H. M.; Lin, Y. P.; Aslam, M.; Prasad, P. V.; Schultz-Sikma, E. A.; Edelman, R.; Meade, T.; Dravid, V. P. Effects of Shape and Size of Cobalt Ferrite Nanostructures on Their MRI Contrast and Thermal Activation. *J. Phys. Chem. C* **2009**, *113* (41), 17761−17767.

DOI: 10.1021/acs.chemmater.9b01155
Chem. Mater. XXXX, XXX, XXX−XXX

Morphology Control of Lanthanide Doped $NaGdF_4$ Nanocrystals *via* One-Step Thermolysis

Miao Wang[†,⁞], Yu Zhang[‡], Qiaofeng Yao[□], Michael Ng[#], Ming Lin[‡], Xu Li[‡,⁑,†], Kishore Kumar Bhakoo[#], Alex Y. Chang[§,⁞], Federico Rosei[†], Fiorenzo Vetrone[*†]

[†] Institut National de la Recherche Scientifique (INRS), Centre Énergie, Matériaux et Télécommunications, Université du Québec, Varennes (QC), Canada

[‡] Institute of Materials Research and Engineering (IMRE), Agency for Science, Technology and Research (A*STAR), Singapore

[□] Department of Chemical and Biomolecular Engineering, National University of Singapore, Singapore

[#] Singapore Bioimaging Consortium (SBIC), Agency for Science, Technology and Research (A*STAR), Singapore

[§] Department of Oncology, Johns Hopkins University, Baltimore, Maryland, USA

[⁞] Johns Hopkins Singapore, Singapore

[⁑] Department of Chemistry, National University of Singapore, Singapore

*Email: vetrone@emt.inrs.ca

Table of Contents

Synthesis parameters, crystal structure (phase), and morphology of upconverting nanocrystals studied

Table S1. Synthesis parameters, phase, and size of β-$NaGdF_4$:Er^{3+} (2%), Yb^{3+} (20%) upconverting nanocrystals

T (°C) during hot-injection	T (°C) post hot-injection	t (min) post hot-injection	Phase	Morphology	Size (nm) (Diameter x Height)	AR (Diameter/Height)
306-320	315	120	β	Rods-D23 (Fig. S1A-a)	23.15±1.33 x 27.93±1.34	0.82
309-320	315	180	β	Rods-D20 (Fig. 1a)	19.74 ±1.43 x 31.39 ±1.92	0.63
307-320	315	180	β	Rods-D17 (Fig. S1A-b)	16.50±2.34 x 29.13±2.05	0.57
305-320	315	180	β	Rods-D 16 (Fig. S1A-c)	16.03±2.04 x 28.90±1.85	0.56
313-317	315	40	β	Prisms-D19 (Fig. 1c)	19.15±1.30 x 15.18±0.93	1.27
313-317	315	180	β	Spheres-D21 (Fig. 1b)	21.23±1.09	
310-316	315	120	β	Plates-D40 (Fig. 1d)	40.1±2.8 x 25.80±1.40	1.55
312-317	315	120	β	Plates-D44	43.51±2.50 x 24.72±1.62	1.76
316-320	315	90	β	Plates-D63 (Fig. S4B)	62.6±3.30 x 29.2±1.80	2.14
316-320	315	180	β	Disks-D63 (Fig. 1e)	62.91±3.10	2.14
316-320	320	60	β	Plates-D53 (Fig. S5b)	52.5±2.1 x 28.80±1.70	1.82
326-330	330	60	β	Plates-D54 (Fig. S5c)	54.1±2.8 x 29.11±1.52	1.86

Monodispersed, uniform β-$NaGdF_4$:Er^{3+} (2%), Yb^{3+} (20%) nanorods demonstrated by TEM analysis

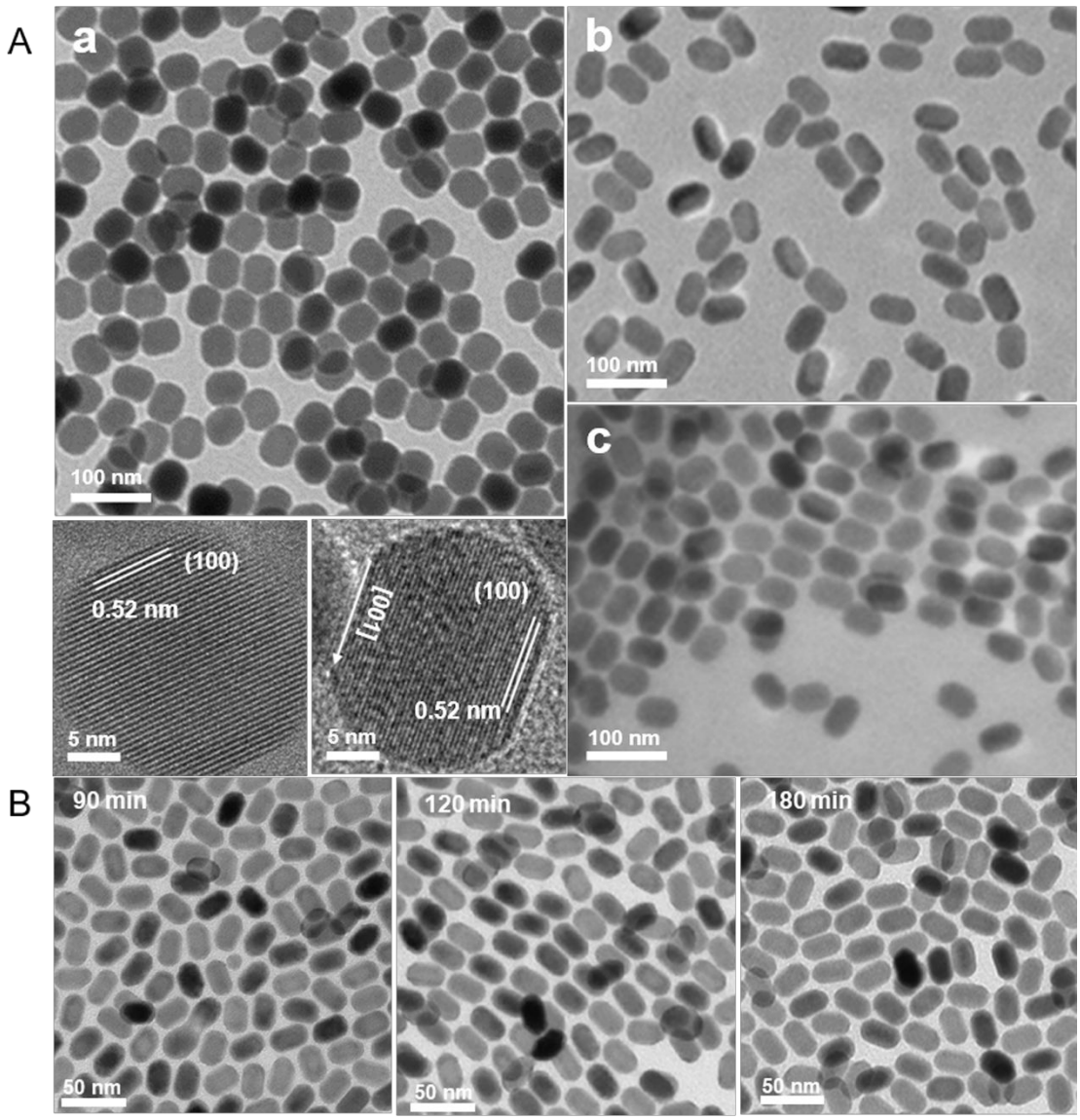

Figure S1. TEM and HRTEM images demonstrating the nanorods: (A) Rods-D23 (a), Rods-D17 (b); Rods-D16 (c). (B) 3D growth of Rods-D20 observed from 90, 120, and 180 min post hot-injection. The size increased from 17 x 28 to 20 x 31 nm.

Elemental composition of upconverting nanocrystals studied

Table S2. Elemental composition of β-$NaGdF_4$:Er^{3+} (2%), Yb^{3+} (20%) upconverting nanocrystals by ICP

Upconverting Nanocrystals	mM (mmoL/L)				Ratio		
	$[Gd^{3+}]$	$[Na^{+}]$	$[Yb^{3+}]$	$[Er^{3+}]$	$[Na^{+}]/[Gd^{3+}]$	$[Yb^{3+}]/[Gd^{3+}]$	$[Yb^{3+}]/[Er^{3+}]$
Prisms-D19	10.11	10.22	2.57	0.24	1.01	0.25	10.74
Spheres-D21	3.41	5.45	0.65	0.08	1.60	0.19	8.62
Rods-D17	54.06	51.81	13.77	1.15	1.05	0.25	11.98
Rods-D19	30.99	32.51	8.01	0.76	1.05	0.26	10.60
Rods-D23	21.14	22.87	5.42	0.55	1.08	0.26	9.79
Plates-D40	36.48	38.28	9.40	0.99	1.05	0.26	9.47
Plates-D63	13.43	14.35	3.41	0.34	1.07	0.25	9.96
Disks-D63	1.30	4.38	0.33	0.04	3.37	0.25	8.70

Summary of phase and size evolution of the upconverting nanocrystals studied at the designated time points post the hot-injection based on the TEM analysis

Table S3. Summary of phase and size of $NaGdF_4$:Er^{3+} (2%), Yb^{3+} (20%) upconverting nanocrystals post the hot-injection

Time of post hot-injection	Phase	Dimension Mean ± SD (nm)		Nanoprisms-D19	Nanospheres-D21	Nanorods-D20	Nanoplates-D40	Nanoplates-D63	Nanodisks-D63
0 min	α	Diameter	Small	5.19 ± 0.67	5.19 ± 0.67	NA	NA	NA	NA
			Large	14.09 ± 0.77	14.09 ± 0.77				
		Height	Small	NA	NA				
			Large						
	β	Diameter	Small	NIL	NIL				
			Large						
		Height	Small						
			Large						
10 min	α	Diameter	Small	6.38 ± 0.98	6.38 ± 0.98				
			Large	14.75 ± 0.99	14.75 ± 0.99				
		Height	Small	NA	NA				
			Large						
	β	Diameter	Small	NIL	NIL				
			Large						
		Height	Small						
			Large						
20 min	α	Diameter	Small	Small amount based on XRD	Small amount based on XRD	3.74 ± 1.12	4.75 ± 0.80	5.7 ± 0.88	5.7 ± 0.88
			Large			17.59 ± 1.44	12.62 ± 1.71	13.32 ± 0.85	13.32 ± 0.85
		Height	Small						
			Large						
	β	Diameter		18.62 ± 1.09	18.62 ± 1.09	NIL	NIL	NIL	NIL
		Length		12.75 ± 0.98	12.75 ± 0.98				
40 min	α	Diameter	Small	NIL	NIL	17.84 ± 3.57	5.82 ± 0.95	6.66 ± 1.05	6.66 ± 1.05
			Large				15.82 ± 0.94	15.17 ± 1.87	15.17 ± 1.87
		Height	Small						
			Large						
	β	Diameter	Small	19.15 ± 1.30	19.15 ± 1.30	18.18 ± 3.44	20.79 ± 0.87	15.05 ± 1.09	15.05 ± 1.09
			Large					26.71 ± 1.39	26.71 ± 1.39
		Height	Small	15.18 ± 0.93	15.18 ± 0.93				
			Large						
60 min	α	Diameter	Small	NIL	NIL	19.60 ± 3.85	8.59 ± 1.38	14.28 ± 1.99	14.28 ± 1.99
			Large				19.30 ± 1.74		
		Height	Small						
			Large						

Time of post hot-injection	Phase	Dimension Mean ± SD (nm)	Nanoprisms-D19	Nanospheres-D21	Nanorods-D20	Nanoplates-D40	Nanoplates-D63	Nanodisks-D63
	β	**Diameter**	19.43 ± 1.12	19.43 ± 1.12	16.55 ± 1.03	26.16 ± 5.90	62.6 ± 1.78	62.6 ± 1.78
		Height	15.32 ± 1.21	15.32 ± 1.21	24.30 ± 1.44	18.58 ± 1.98	NA	NA
120 min	α	**Diameter**	NIL	NIL	NIL	NIL	NIL	NIL
		Height						
	β	**Diameter**	19.74 ± 1.06	19.74 ± 1.06	18.03 ± 1.23	40.1 ± 2.80	62.6 ± 3.30	62.6 ± 3.30
		Height	NA	NA	28.85 ± 1.04	25.8 ± 1.40	29.2 ± 1.80	29.2 ± 1.80
180 min	α	**Diameter**	NIL	NIL	NIL	NIL	NIL	NIL
		Height						
	β	**Diameter**		21.23 ± 1.10	19.74 ± 1.43			62.91 ± 3.10
		Height		NA	31.39 ± 1.92			29.8 ± 1.50

Crystal structure (phase) of upconverting nanocrystals with various morphologies analyzes by XRD

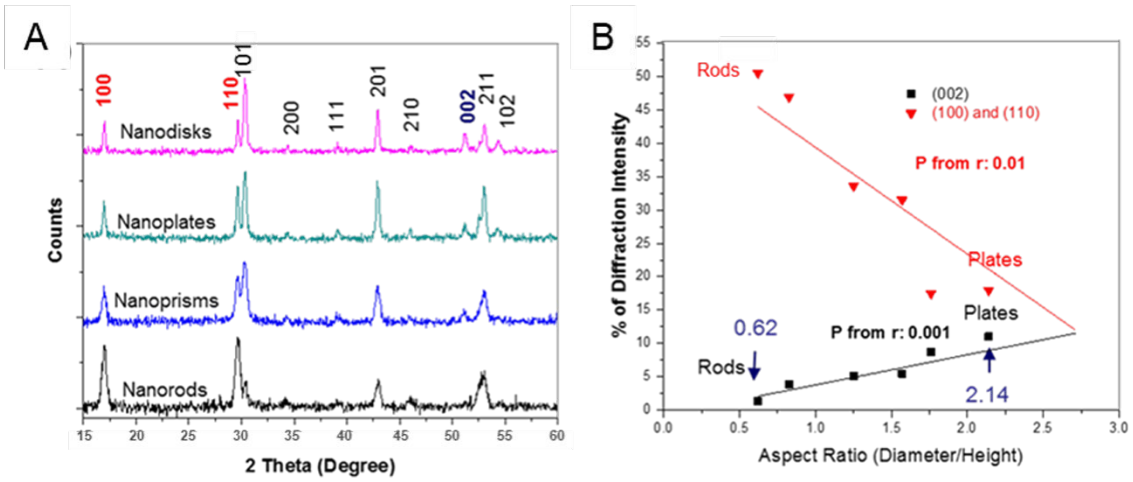

Figure S2. (A) XRD analysis of $NaGdF_4$:Er^{3+} (2%), Yb^{3+} (20%) nanocrystals with various morphologies. (B) Plots of % of diffraction intensity of lattice planes as a function of the AR of the nanocrystals. The aspect ratio, AR, is defined as the diameter from corner to corner/height. From nanorods to nanoplates (rods-prisms-plates) whose AR varies from 0.59 to 2.14, the evolution of the XRD patterns showed a linear trend (Pearson's r: 0.96 (black line), -0.89 (red line)) of the gradually decreased composition fraction of (100) and/or (110) planes (50.5%~18%) and increased composition fraction of (002) planes (1.3%~11%). The % indicates the fraction of the mathematic area of individual plane, which is calculated using the software's built-in integration feature (OriginPro 2016). The p value from Pearson's r proved that the correlation was statistically significant.

Phase transition during the formation of nanoplates and nanorods analysed by XRD

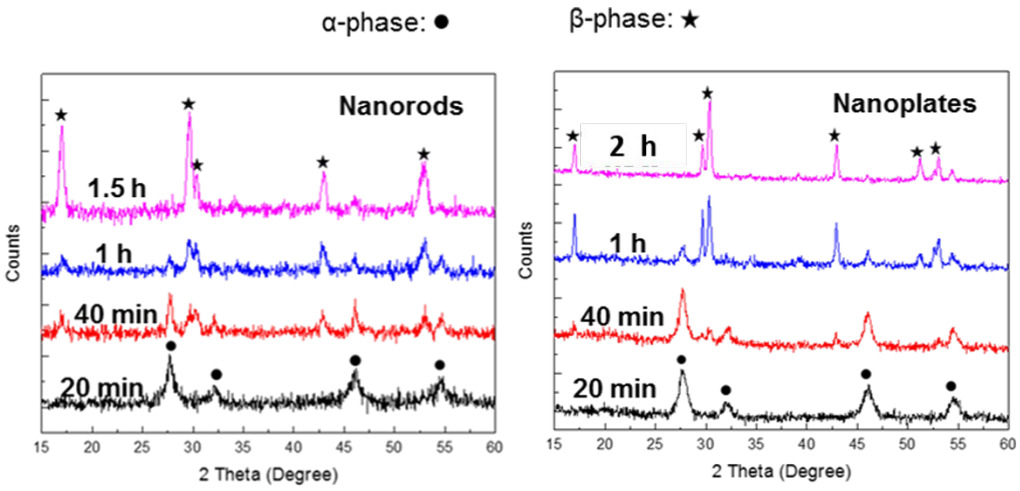

Figure S3. XRD analysis during the formation of nanoplates (Plates-D40) and nanorods (Rods-D20), respectively. The diffraction intensity as a function of the degrees 2 theta was demonstrated at designated time points after the hot-injection.

Phase transition and shape evolution during the formation of nanoprisms and large nanoplates

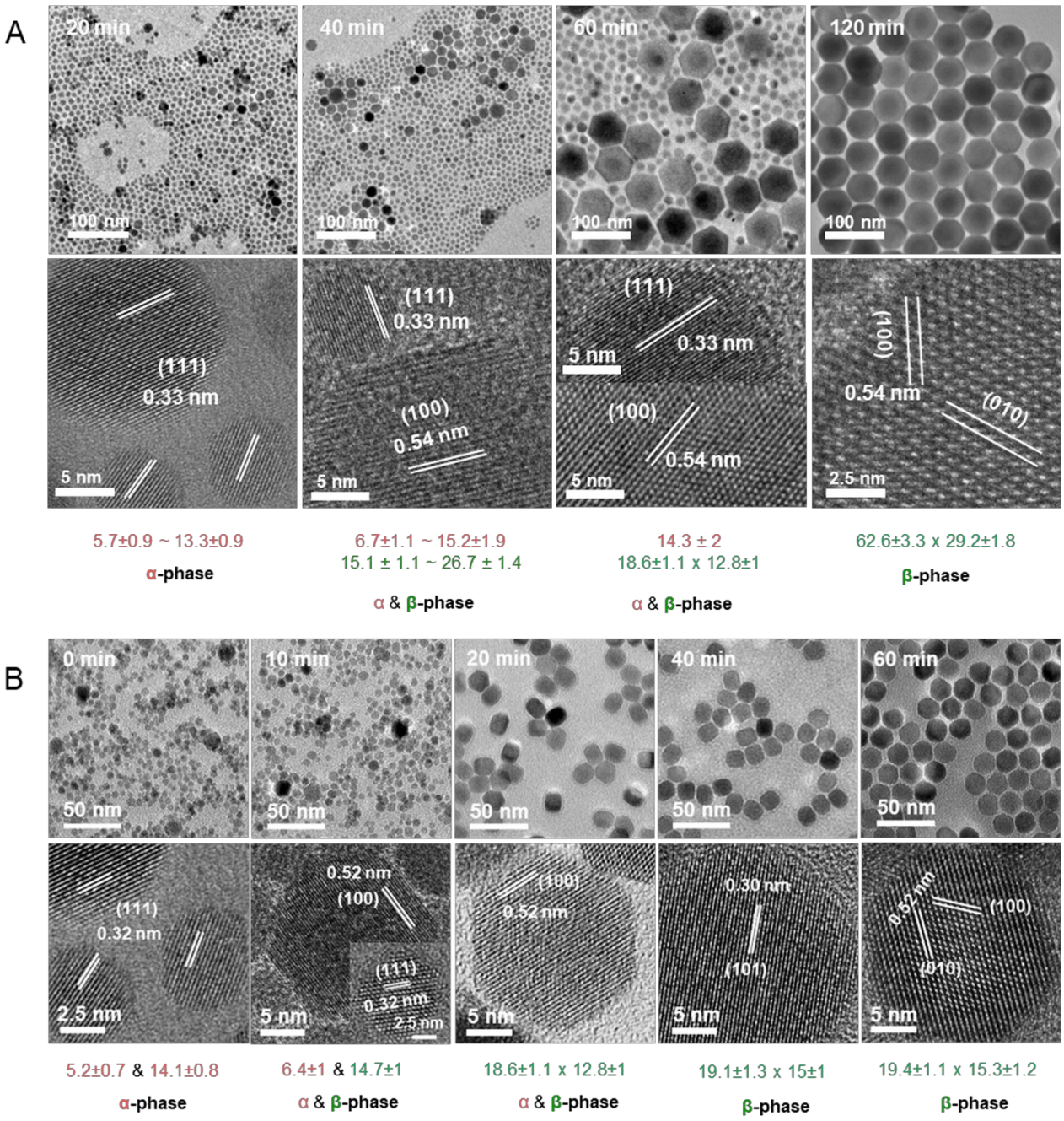

Figure S4. TEM and HRTEM images illustrating the phase transition and shape evolution during the formation of β-$NaGdF_4$:Er^{3+} (2%), Yb^{3+} (20%) large nanoplates (Plates-D63, A) and nanoprisms (Prisms-D19, B). Time displayed on each figure indicates the time of post hot-injection. The values in red and green correspond to the size of α-phase and β-phase nanocrystals, respectively.

Discotic morphology of β-$NaGdF_4$:Er^{3+} (2%), Yb^{3+} (20%) nanodisks demonstrated by TEM and HRTEM analysis

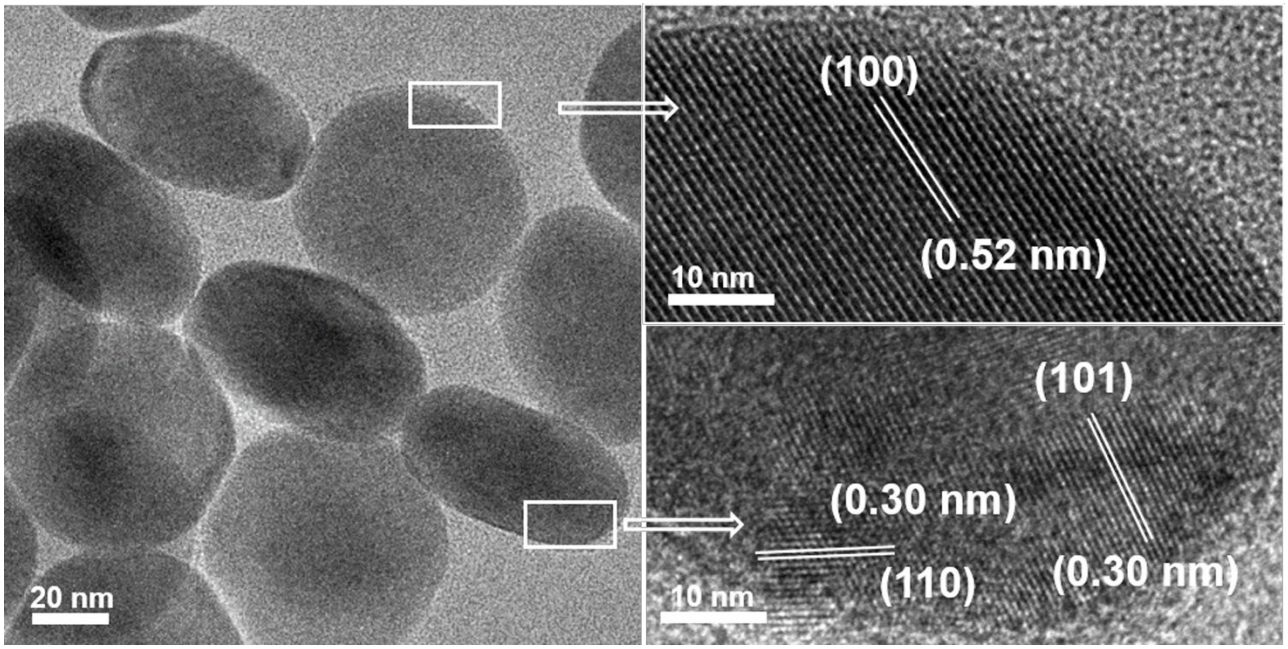

Figure S5. TEM and HRTEM images demonstrating the disk-like base and side faces of Disks-D63.

Comparison of phase transition process during formation of nanoprisms, nanorods, and nanoplates

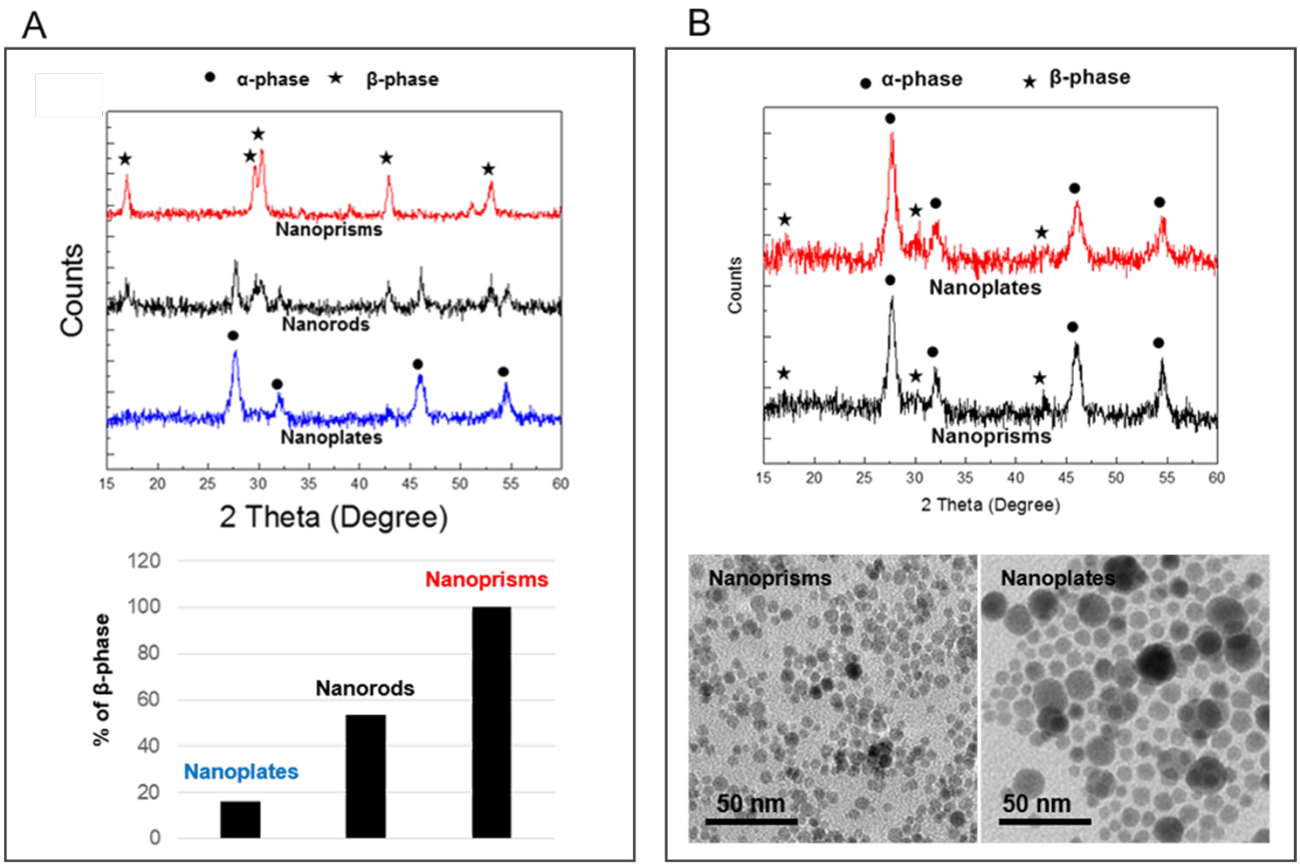

Figure S6. (A) Comparison of the α→β transition at 40 min post injection for nanocrystals with various morphologies: XRD analysis demonstrating the diffraction intensity as a function of degrees 2 theta; the percentage of β-phase nanocrystals during α→β transition at 40 min post hot-injection. (B) XRD analysis and TEM images demonstrating the formation of nanoprisms and nanoplates at the beginning of α→β phase transition.

Influence on the size of nanoplates by tuning the temperature post hot-injection

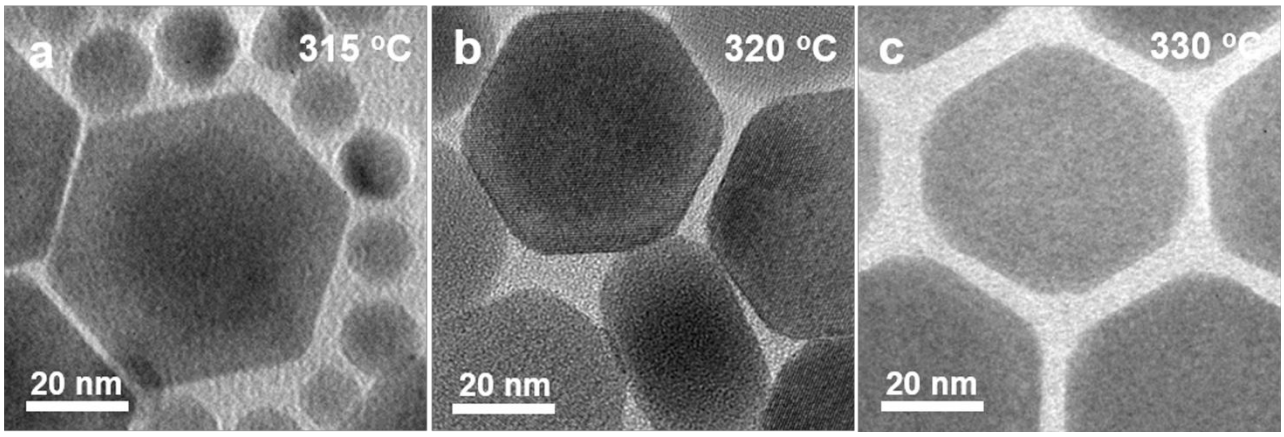

Figure S7. TEM images of nanoplates observed at 60 min post hot-injection. (a) Plates-D63 (hot-injection T: 320 °C, post hot-injection T: 315 °C). (b) Plates-D53 (hot- injection T: 320 °C, post hot-injection T: 320 °C). (c) Plates-D54 (hot- injection T: 330 °C, post hot-injection T: 330 °C. Large nanoplates were formed by lowering the temperature post hot-injection.

r_1, r_2 relaxivity of studied upconverting nanocrystals at different magnetic fields

Table S4. Comparison of r_1, r_2, and r_2/r_1 of β-$NaGdF_4$:Er^{3+} (2%), Yb^{3+} (20%) upconverting nanocrystals at different magnetic fields

Upconverting Nanocrystals	3T			7T			9.4T		
	r_2	r_1	r_2/r_1	r_2	r_1	r_2/r_1	r_2	r_1	r_2/r_1
Prisms-D19	47.81	0.93	51.41	65.41	0.64	102.20	86.13	0.43	200.30
Spheres-D21	56.03	0.86	65.15	82.53	0.79	104.47	114.31	0.31	368.74
Rods-D17	61.50	1.37	44.89	129.40	1.15	112.52	195.60	0.41	477.07
Rods-D20	79.21	1.32	60.01	145.72	0.89	163.73	182.52	0.27	676.00
Rods-D23	65.90	1.18	55.85	109.31	0.73	149.74	142.30	0.32	444.69
Plates-D40	59.70	0.89	67.08	99.64	0.7	142.34	139.41	0.34	410.03
Plates-D63	63.94	0.69	92.67	101.52	0.62	163.74	153.33	0.22	696.95
Disks-D63	57.06	0.4	142.65	82.31	0.41	200.76	111.74	0.25	446.96

Table S4 indicated that the nanorods had better r_2 relaxivity comparing to other upconverting nanoparticles.

Negative contrast enhancement in T_2-weighted images by studied upconverting nanocrystals

Table S5. Comparison of negative contrast in T_2-weighted images of β-$NaGdF_4$:Er^{3+} (2%), Yb^{3+} (20%) upconverting nanocrystals at different magnetic fields

Upconverting Nanocrystals	% of Signal density normalized to water (Gd^{3+} = 0.125 mM)		
	3T	7T	9.4T
Prisms-D19	81%	74%	67%
Spheres-D21	78%	71%	64%
Rods-D17	85%	67%	59%
Rods-D20	77%	64%	53%
Rods-D23	78%	73%	57%
Plates-D40	76%	70%	60%
Plates-D63	94%	60%	57%
Disks-D63	94%	70%	63%

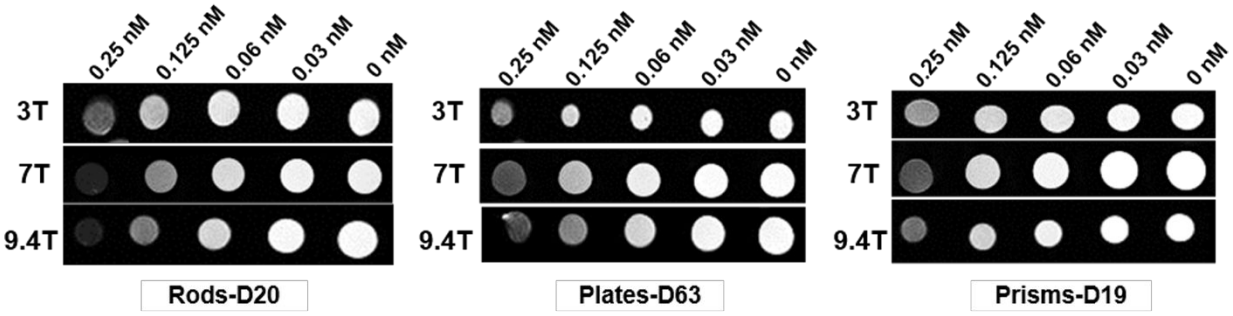

Figure S8. The T_2-weighted MR images of nanorods, nanoplates, and nanoprisms vs various Gd^{3+} concentrations in 0.5% agarose at 3T, 7T, and 9.4T magnetic fields, respectively. Rods-D20 achieved the best negative contrast in T_2-weighted images.

5 ONE-POT ENCAPSULATION

5.1 NCs with LnNPs

One-pot synthesis of theranostic nanocapsules with lanthanide doped nanoparticles

Synthèse en une étape de nanocapsules théranostiques contenant des nanoparticules dopées au lanthanide

Miao Wang[a, e], Yu Zhang[b], Michael Ng[c], Artiom Skripka[a], Ting Cheng[a], Xu Li[a, b, f], Kishore Kumar Bhakoo[c], Alex Y. Chang[d, e], Federico Rosei[a], Fiorenzo Vetrone[*a]

[a] Institut National de la Recherche Scientifique (INRS), Centre Énergie, Matériaux et Télécommunications, Université du Québec, Varennes (QC), Canada

[b] Institute of Materials Research and Engineering (IMRE), Agency for Science, Technology and Research (A*STAR), Singapore

[c]. Singapore Bioimaging Consortium (SBIC), Agency for Science, Technology and Research (A*STAR), Singapore

[d] Department of Oncology, Johns Hopkins University, Baltimore, Maryland, USA

[e] Johns Hopkins Singapore, Singapore

[f] Department of Chemistry, National University of Singapore, Singapore

*. Corresponding author, vetrone@emt.inrs.ca

Chem. Sci., 2020, 11, 6653–6661. – **Cover Article**

DOI: 10.1039/x0xx00000x

Received 20th February 2020; Accepted 30th May 2020

As introduced in Chapter 1, in conventional PDT, PS convert the excited light to ROS that are toxic to malignant cells. Most clinically available PS are excited in the VIS or UV region thereby limiting the use of this cancer therapeutic technique to diseases on or very near to the surface. UCNPs decorated with specific PS can form the core of a theranostic nanoplatform where UCNPs play the role of energy transducers that excite the attached PS under NIR stimulus. The indirect sensitization of the PS, through the UCNPs excited *via* NIR light, can extend the range of PDT as not only do UCNPs enable PDT at greater tissue depth, but also provide the added benefit of disease visualization (*e.g.* optical and/or MRI). However, high quality UCNPs are usually synthesized in an organic environment with OA and/or OM ligands used as capping ligands, which prevents them from being readily dispersible in an aqueous milieu unless further surface chemistry and functionalization is undertaken, which many times can have adverse effects on their luminescence properties. Adding to the complexity, the majority of efficient PS are also hydrophobic in nature. To provide aqueous dispersity and stability in physiological conditions, surface engineering undoubtedly becomes a crucial step to enable the use of UCNPs in PDT.

In this chapter, *we demonstrate an original one-pot synthesis strategy to co-encapsulate hydrophobic NaGdF4:Er^{3+} (2 mol%), Yb^{3+} (20 mol%) UCNPs and ZnPc into NCs via the interfacial templating condensation approach.* The encapsulation followed a microemulsion mechanism in an aqueous environment at near neutral pH, using triblock copolymers (F127), PEO-PPO-PEO, as the templating and protecting agent. It allows first to encapsulate UCNPs in PEO-PPO-PEO micelles, and then grow the silica shell within the micellar PPO core and PEO corona interface. Following this protocol, we successfully co-encapsulate UCNPs (without surface modification thereby maintaining their original optical properties) and ZnPc in one-pot, and minimize the distance between the two payloads to facilitate the energy transfer from UCNPs to ZnPc. *The integrated nanocapsule demonstrates excellent colloidal stability, biocompatibility, and reduced likelihood of ZnPc leakage, as well as enhanced negative contrast for T_2-weighted imaging and photodynamic therapy.* The latter is obtained through

indirect excitation of co-encapsulated ZnPc by UCNPs, resulting in singlet oxygen generation and *in vitro* eradication of BT474 breast cancer cells. Overall, the presented one-pot approach shined light on the co-encapsulation of OA capped inorganic UCNPs with hydrophobic PS, constituting an important step forward in the surface engineering of UCNPs and UC-PDT systems. This approach could be extended to encompass various therapeutic, diagnostic or target agents, thus bringing theranostic functionalities to cancer treatment.

Chemical Science

ROYAL SOCIETY OF CHEMISTRY

EDGE ARTICLE

View Article Online
View Journal | View Issue

Cite this: *Chem. Sci.*, 2020, **11**, 6653

All publication charges for this article have been paid for by the Royal Society of Chemistry

One-pot synthesis of theranostic nanocapsules with lanthanide doped nanoparticles†

Miao Wang, [ae] Yu Zhang,[b] Michael Ng,[c] Artiom Skripka, [a] Ting Cheng, [a] Xu Li,[abf] Kishore Kumar Bhakoo,[c] Alex Y. Chang,[de] Federico Rosei [a] and Fiorenzo Vetrone *[a]

We report a one-pot synthesis strategy for a new theranostic nanoplatform by simultaneously encapsulating Er^{3+}, Yb^{3+} doped $NaGdF_4$ upconverting nanoparticles (UCNPs) and photosensitizer zinc phthalocyanine (ZnPc) into polymeric micelle/silica nanocapsules. This approach consists of interfacial templating condensation, using triblock copolymers, namely (ethylene oxide)$_{106}$(propylene oxide)$_{70}$(ethylene oxide)$_{106}$ (PEO-PPO-PEO) as the templating and protecting agent. The encapsulation follows a straightforward microemulsion mechanism in an aqueous environment at a near-neutral pH. To prevent the interaction between the hydrophobic oleic acid (OA) ligands of UCNPs and the silanol groups of hydrated tetramethoxysilane (TMOS), we adjusted the addition sequence of TMOS. It allowed us first to encapsulate UCNPs in PEO-PPO-PEO micelles, and then grow the silica shell within the micellar PPO core and PEO corona interface. The silica shell is incorporated for its chemical and mechanical stability, while the PEO corona gives additional steric balance to the nanocapsule. Using this strategy we successfully co-encapsulated UCNPs and ZnPc in one-pot, and minimized the distance between the two payloads to facilitate the energy transfer from UCNPs to ZnPc. The integrated nanocapsule has an average hydrodynamic size of 85 nm with a low polydispersity index of 0.1, and demonstrates excellent colloidal stability, biocompatibility, enhanced negative contrast for T_2-weighted imaging and photodynamic therapy. The latter is obtained through indirect excitation of co-encapsulated ZnPc by UCNPs, resulting in singlet oxygen generation and *in vitro* eradication of BT474 breast cancer cells. Overall, the presented one-pot approach shines light on the co-encapsulation of OA-capped inorganic UCNPs with hydrophobic photosensitizers, constituting an important step forward in the surface engineering of UCNPs, as well as upconversion based photodynamic therapy systems.

Received 20th February 2020
Accepted 30th May 2020

DOI: 10.1039/d0sc01033b

rsc.li/chemical-science

1 Introduction

Photodynamic therapy (PDT) has been widely studied for cancer treatment including skin, prostate, head and neck, pancreatic, breast, and lung cancer[1–4] and utilizes photosensitizers (PS) as light-sensitive drugs to locally treat the target tissue upon irradiation with light of appropriate wavelengths. The excited PS interacts with surrounding oxygen molecules to generate reactive oxygen species (ROS), including singlet oxygen ($^1O_2$), which causes oxidative damage to biological substrates and ultimately cell death.[5] In addition to having less systemic side effects and cumulative cytotoxicity, PDT is able to overcome the multi-drug resistance caused by chemotherapy.[6] Moreover, unlike chemotherapeutic drugs and radiotherapy that tend to be immunosuppressive, PDT is capable of triggering an antitumor immune response by activation of the innate and/or adaptive immune system, subsequently prolonging survival of patients.[6,7] However, the efficacy of PS drugs is severely constrained by their inherent water-insolubility and poor pharmacokinetics.[8,9] Moreover, the typical PS excitation wavelengths in the visible spectral range have limited tissue penetration depth. For this reason, PDT is limited to the treatment of tumours on or just under the skin, the lining of internal organs or cavities, thus being less effective in treating large and deep-seated tumours.[10] In order to reach deep lying tumours, near-infrared (NIR) light with wavelengths in the optical transparency windows of biological tissues could be used.[11,12] However, most efficient PS

[a]*Institut National de la Recherche Scientifique (INRS), Centre Énergie, Matériaux et Télécommunications, Université du Québec, Varennes (QC), Canada. E-mail: vetrone@emt.inrs.ca*

[b]*Institute of Materials Research and Engineering (IMRE), Agency for Science, Technology and Research (A*STAR), Singapore*

[c]*Singapore Bioimaging Consortium (SBIC), Agency for Science, Technology and Research (A*STAR), Singapore*

[d]*Department of Oncology, Johns Hopkins University, Baltimore, Maryland, USA*

[e]*Johns Hopkins Singapore, Singapore*

[f]*Department of Chemistry, National University of Singapore, Singapore*

† Electronic supplementary information (ESI) available: All experimental details including synthesis and characterization procedures, as well as additional experimental data. See DOI: 10.1039/d0sc01033b

cannot be excited with NIR light directly (*e.g.* MC540, Ce6, ZnPc, *etc.*).[13] To overcome this crucial challenge, the synergistic combination of photon upconverting materials and PDT drugs has been proposed and explored in recent years.[14–20]

Lanthanide (Ln^{3+})-doped upconverting nanoparticles (UCNPs) have been widely studied for PDT because of their unique ability to convert NIR radiation to UV and/or visible wavelengths *via* the anti-Stokes, multiphoton process of upconversion.[21,22] UCNPs decorated with a PS form the core of a theranostic (*thera*py + diag*nostic*) nanoplatform capable of both PDT (*thera*py) and imaging (diag*nostic*). In PDT, UCNPs play the role of energy transducers that facilitate indirect excitation of the attached PS under NIR stimulus. Not only do UCNPs enable PDT at greater tissue depth, but also provide the added benefit of disease visualization (*e.g.* optical and/or magnetic resonance imaging [MRI]).[15,23–30] However, high quality UCNPs are usually synthesized in an organic environment with oleic acid (OA) and/or oleylamine (OM) as capping ligands, which prevents UCNPs from being readily dispersible in an aqueous milieu.[31] The majority of efficient PS drugs are also hydrophobic in nature.[9] To provide aqueous dispersity and stability under physiological conditions, surface engineering undoubtedly becomes a crucial step to enable the use of UCNPs in PDT (UC-PDT).

To date, several major strategies have been explored to combine PS and UCNPs, of which mesoporous silica coating is a common and well-studied method, which allows for high PS payloads.[13,15,18,32,33] A typical process of mesoporous silica coating involves the self-assembly of cationic surfactants and silica precursors around the UCNPs in a basic solution, where the surfactants are used as a template for the formation of the silica shell. The mesopores are generated after subsequent removal of the surfactant micelles by either thermal decomposition or solvent extraction.[34] The PS of interest is then loaded into the pores. However, leakage of the PS in the blood circulatory system is inevitable without capping the pores, which otherwise leads to potential whole-body phototoxicity and inadequate accumulation of the PS in the targeted tissue.[13] Cetyltrimethylammonium bromide (CTAB), a surfactant, which is commonly employed to generate mesopores, is also highly toxic.[22] Therefore, any incomplete removal of CTAB can impede the use of UCNPs in biomedicine. In addition, mesoporous silica coating requires a multi-step preparation as addressed above. Finally, additional surface modification of the silica shell is required to prevent silica coated UCNPs from aggregating.[9,23]

To enable a simpler one-pot synthesis of the UC-PDT system, another strategy known as polymer encapsulation has been proposed, in which amphiphilic polymers self-assemble into a micelle with both the UCNPs and PS based on their mutual hydrophobicity.[26,35,36] While it is a versatile and cost-effective approach, using polymeric micelles does not address the problem of leakage. The polymeric micelles spontaneously dissociate when their concentrations fall below the critical micelle concentration (CMC), a scenario which such PS carriers encounter when diluted by several orders of magnitude upon intravenous delivery *in vivo*.[37] As a result, the micelles could disintegrate and precipitate out their content.

To address the aforementioned issues, a silica–polymer hybrid system could be applied. The basic idea of this one-pot encapsulation is to confine the hydrolysis and condensation of the silica precursors to the core/corona interface of amphiphilic triblock copolymer [(ethylene oxide)$_{106}$(propylene oxide)$_{70}$(ethylene oxide)$_{106}$ (PEO-PPO-PEO)] micelles. This forms a silica shell cross-linked micelle where the polymeric micelle is stabilised by silica cross-linking to prevent its disintegration. The free dangling PEO blocks can also prevent unwanted aggregation of the silica shells. In addition, the silica cross-linking provides a more effective diffusion channel for the movement of water and oxygen in and out of the silica shell without the need for generating pores. Importantly, in UC-PDT systems cytotoxic $^1O_2$ is generated by PS which are activated *via* energy transfer (ET) from the NIR excited UCNPs. The ET can be either radiative[14,18,26,35,36] or non-radiative,[16,38–41] and its efficiency is affected by the distance between the UCNPs (energy donors) and PS (energy acceptors). To that end, co-encapsulation of UCNPs and PS in polymeric micelle/silica nanocapsules advantageously minimizes the distance between the two. The UCNP and the PS could be virtually in contact with each other, while the conventional approach of PS loading in the mesoporous silica coating results in greater separation between the two species.[15,18,20,42]

Here, we established an original one-pot synthesis strategy to co-encapsulate hydrophobic $NaGdF_4$:Er^{3+} (2 mol%), Yb^{3+} (20 mol%) UCNPs and ZnPc (zinc phthalocyanine, hydrophobic PS) *via* the interfacial templating condensation approach. The resultant theranostic nanocapsules exhibited excellent colloidal stability, biocompatibility, and a PDT effect against BT474 chemo-resistant breast cancer cells. In addition, the encapsulated $NaGdF_4$ UCNPs demonstrated promising negative contrast enhancement for T_2 weighted MRI, to be used for imaging guided UC-PDT.

2 Results and discussion

2.1. Mechanism of polymeric micelle/silica co-encapsulation of UCNPs and PS by interfacial templating condensation

Scheme 1 illustrates the co-encapsulation of UCNPs and PS drugs *via* interfacial templating condensation. It is a single step approach for the synthesis of polymeric micelle/silica nanocapsules that can deliver UC-PDT and MRI at the same time. To achieve core/shell/corona nanocapsules, amphiphilic PEO-PPO-PEO triblock copolymers (F127), hydrophobic UCNPs and ZnPc are initially mixed in tetrahydrofuran (THF), a water-miscible organic solvent (Scheme 1a). The mixture is then injected into water where F127 will spontaneously self-assemble into micelles composed of a hydrophobic PPO core and a hydrophilic PEO corona. Simultaneously, UCNPs and ZnPc are localized in the PPO core due to their hydrophobic nature (Scheme 1b). Subsequently, silica precursors tetramethoxysilane (TMOS) are injected into the aqueous solution. Upon contact with water, TMOS starts to hydrolyse and condense at the interface of micellar core/corona, forming an ultrathin silica shell adjoining the micellar core (Scheme 1c). As the reaction proceeds, the unreacted silica precursors further hydrolyse and

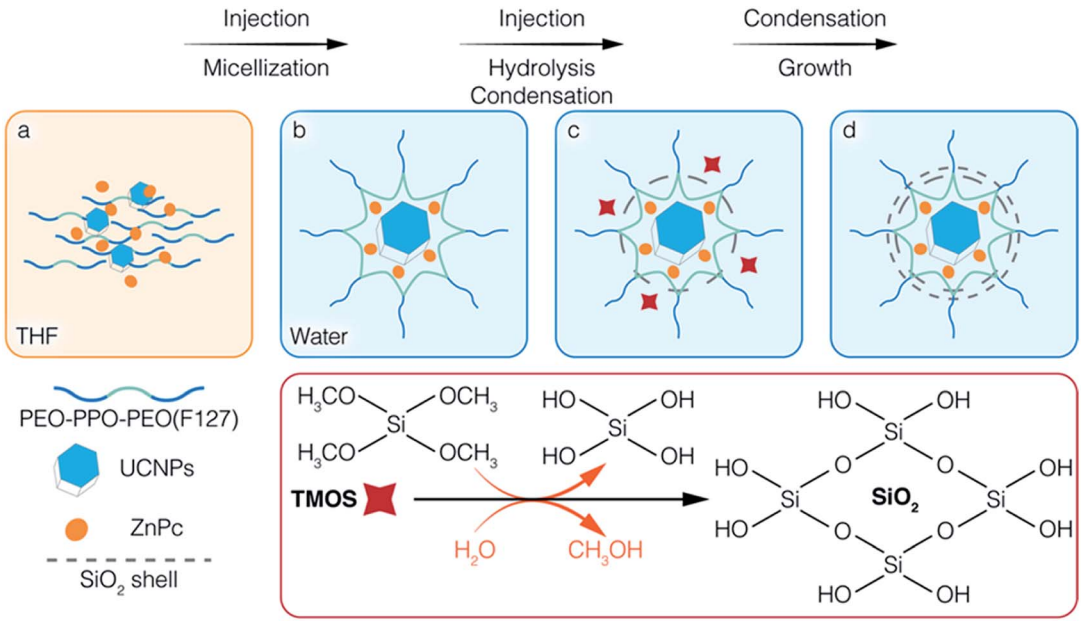

Scheme 1 The formation of polymeric micelle/silica nanocapsules co-encapsulating UCNPs and organic PS drugs (ZnPc) *via* the interfacial templating condensation approach. The chemical equation illustrates the hydrolysis and self-condensation of silica precursor TMOS in water.

condense onto the outer surface of the silica shell, thickening it. Core/shell/corona nanostructures are eventually formed. The UCNPs and ZnPc are encapsulated in the micellar core, with the silica shell confined at the micellar core/corona interface, and free PEO chains that make up the corona protruding out into the water (Scheme 1d). This approach allowed for (1) integrating the cargo and carrier in one-pot; (2) high aqueous colloidal stability, antifouling and steric stabilization provided by the free PEO chains;[43,44] (3) synthesis to be carried out in benign environments (in a near-neutral pH aqueous solution and at room temperature); (4) ZnPc to be brought closer to UCNPs, thus facilitating energy transfer from UCNPs to ZnPc; and (5) the control over the number of UCNPs encapsulated inside the nanocapsules. In addition, the silica shell surrounding the core of the polymeric micelles efficiently prevented the micelles from disintegrating even when the polymer concentration fell below its CMC,[37,43] thus reducing the likelihood of ZnPc leaking.

2.2. Influence of TMOS on the encapsulation

According to the reported encapsulation protocol,[43] F127, TMOS and payload mixture are injected simultaneously into water, where the payloads are encapsulated into the core of the F127 micelles and the silica precursors condense at the confined interface between the core and corona of the micelles. It was successful for the encapsulation of hydrophobic PS drugs, such as ZnPc; however, when we attempted to encapsulate UCNPs using the same protocol, the mixture became cloudy and precipitated. TEM images confirmed that highly aggregated UCNPs precipitated due to improper micellization (Fig. S1A–D†). Unlike organic molecules, the hydrophobicity of UCNPs originates from the OA capping ligand. The carboxylic end of OA is usually coordinated to the outermost Ln^{3+} ions by electrostatic interactions, which is also confirmed by the asymmetric stretching of O=C–OH from the FTIR results (Fig. 1C). When TMOS and OA-capped UCNPs were mixed with THF, TMOS hydrolysed to form silanol groups upon contact with the trace water in THF. The carboxylic groups (COOH) of OA are better anchoring points for the silanol groups *via* hydrogen bonding compared to the C–O groups of PEO.[45] As a result, one or two Si–OH of silanol interacted with the COOH of OA-capped UCNPs, and others linked with each other to form a bridge between silanols (–O–Si–O–Si–), leading to the aggregation and precipitation of the UCNPs. On the other hand, the silanol groups might increase the hydrophilicity of surrounding UCNPs, resulting in the deficient absorption of UCNPs in the PPO core. Consequently, once such a mixture was injected into water, the preformed and newly formed silanol linking hampered the micellar encapsulation of the UCNPs. Based on this understanding, we modified the procedure by encapsulating UCNPs into the hydrophobic core prior to growing the silica shell.

First, only F127 and UCNPs were mixed in THF, injected into water, and left to stir for 2 days to encapsulate UCNPs into the PPO core through the micellization of F127. Then, TMOS dissolved in THF was injected into the micellar solution, in which the not fully hydrolysed TMOS diffused to the micelle and bonded to PEO chains through hydrogen bonding.[46] Subsequently, the silanol groups condensed at the interface region to form a thin silica shell surrounding the core of the micelles. With the modified protocol we were successful in preventing the interaction between OA and silanol, and to achieve the formation of core/shell/corona nanocapsules loaded with OA-capped UCNPs. Moreover, we were able to control the multiplicity of UCNPs per nanocapsule by varying the concentration of the

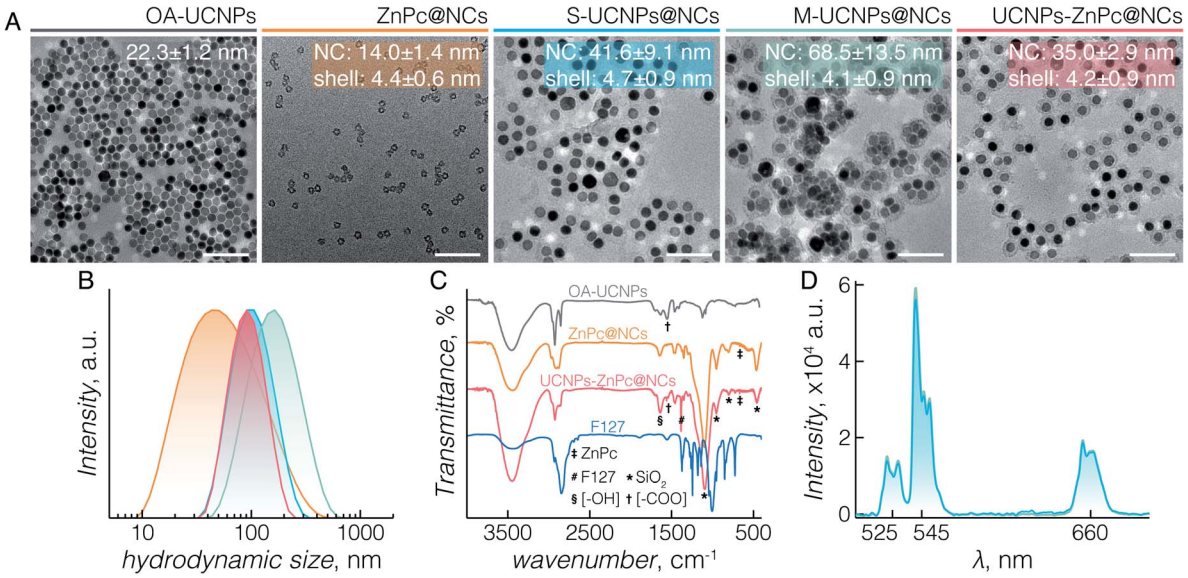

Fig. 1 (A) TEM images demonstrating the various compounds studied. "NC" indicates the longest diameter of an individual nanocapsule; "shell" indicates the thickness of the silica shell. Estimated size is expressed as mean ± standard deviation (SD). Scale bars in all images correspond to 100 nm. (B) The hydrodynamic size of ZnPc@NCs, S-UCNPs@NCs, M-UCNPs@NCs, and UCNPs-ZnPc@NCs. (C) The organic/inorganic hybrid structure of the studied compounds characterized by FTIR analysis. (D) The upconversion luminescence spectra of S-UCNPs@NCs and M-UCNPs@NCs upon 980 nm laser irradiation. Note, colour coding of different compounds in (A) is maintained in (B), (C) and (D).

reactants. By adjusting the ratio of UCNPs/F127 added during the encapsulation, nanocapsules loaded with a different number (n) of UCNPs can be obtained, namely S-UCNPs@NCs and M-UCNPs@NCs synthesized with 1.7×10^{16} and 2.5×10^{16} UCNPs per mmol of F127, respectively. A clear stock solution of UCNPs, which is characteristic of stable and well dispersed UCNPs in the solvent, is crucial for successful encapsulation. Small hydrodynamic sizes and narrow size distributions are favourable in biomedical applications, thus we synthesised UCNPs-ZnPc@NCs where ZnPc was co-encapsulated with a single UCNP as follows. At fixed concentrations of F127, TMOS, and UCNPs, various amounts of ZnPc (0.3, 0.6, and 1.2 mg) were tested for co-encapsulation with UCNPs in the PPO core. From the TEM characterization, we observed that monodisperse nanocapsules can only be obtained by loading 0.3 mg ZnPc (Fig. 1A_UCNPs-ZnPc@NCs and Fig. S1E and F†). Increasing the loading amount to 0.6 and 1.2 mg caused ZnPc to be encapsulated alone without co-encapsulation with UCNPs (see the "empty" nanocapsules shown in Fig. S1G and H†). The loading efficiency for UCNPs-ZnPc@NCs is 1.2% (w/w), which is comparable with the previous literature values, such as encapsulation of UCNPs and ZnPc in lipid micelles [1.6% (w/w)],[47] and loading of ZnPc in mesoporous silica decorated UCNPs [1.8% (w/w)].[20]

2.3. Characterization of hybrid nanocapsules

TEM images (Fig. 1A) demonstrate the morphologies of OA-capped UCNPs (grey), ZnPc@NCs (orange), S-UCNPs@NCs (blue), M-UCNPs@NCs (green), and UCNPs-ZnPc@NCs (red). OA-capped UCNPs are monodisperse in size and have a hexagon-shaped morphology with a size of 22 ± 1 nm. The XRD peaks (Fig. S2†) indicate a pure β (hexagonal)-phase (space group: $P\bar{6}$ or $P6_3/m$), in excellent agreement with the reference data (JCPDS 27-699). All the nanocapsules formed are well dispersed with an ultrathin but complete silica shell of less than 5 nm thickness. The TEM size of nanocapsules is around 14 nm (ZnPc@NCs), 42 nm (S-UCNPs@NCs), 69 nm (M-UCNPs@NCs), and 35 nm (UCNPs-ZnPc@NCs). DLS analysis (Fig. 1B and Table S1†) reveals their hydrodynamic size (nm) and polydispersity indexes (PDI): ZnPc@NCs, 43/0.4; S-UCNPs@NCs, 93/0.2; M-UCNPs@NCs, 145/0.2; and UCNPs-ZnPc@NCs, 86/0.1. The PDI is an indication of the dispersity with respect to the size distribution. A value within 0.05–0.7 is considered highly monodisperse and acceptable for nanocarriers in biomedical applications.[48] The contents of UCNPs and ZnPc in nanocapsules were analysed by ICP-AES (Table S2†). The amounts of nanocapsules used in this study were calculated based on the ICP data. TEM images (Fig. 1A_UCNPs-ZnPc@NCs, Fig. S1E and F†) clearly demonstrate that the UCNPs (dark colour) are centred in the core, and enclosed by the well-defined thin silica shell (~4 nm thickness) (grey colour). UCNPs, compared with silica, have higher electron density and scatter electrons more strongly, thus appearing darker in colour. The resultant blue coloured aqueous colloid of UCNPs-ZnPc@NCs was transparent and no precipitates were observed up to 6 months of storage at room temperature. The monodispersity of the colloid was confirmed by DLS (Table S1 and Fig. S3†).

The organic/inorganic hybrid structure of the three groups of nanocapsules studied is confirmed by FTIR analysis (Fig. 1C). Characteristic frequencies of F127 triblock copolymers (2890 cm^{-1}, C–H stretching; 1466 cm^{-1}, C–H bending; 1382 cm^{-1}, C–H wagging; and 843 cm^{-1}, C–H rocking) and

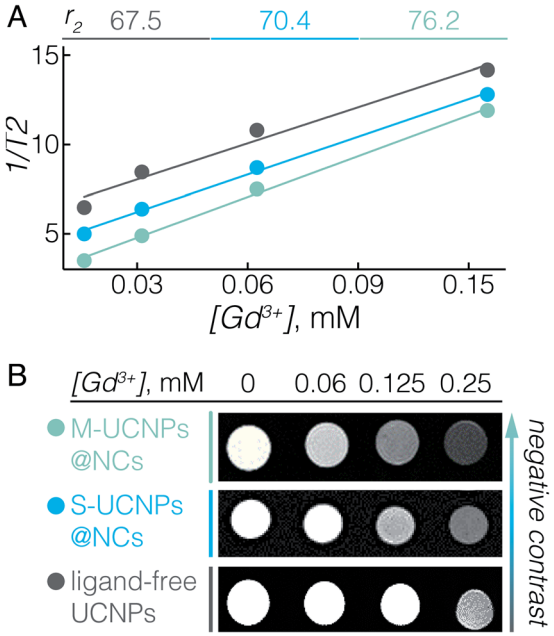

Fig. 2 MR relaxivity r_2 and T_2-weighted images of ligand-free UCNPs (grey), S-UCNPs@NCs (blue) and M-UCNPs@NCs (green). (A) Plot of $1/T_2$ *versus* Gd^{3+} concentration, the slope indicates the corresponding specific relaxivities r_2. (B) The negative contrast demonstrated on T_2-weighted images at a 7 T magnetic field.

silica (795 cm^{-1}, Si–O–Si symmetric stretching; 953 cm^{-1}, Si–OH stretching; and 1056 cm^{-1}, Si–O–Si asymmetric stretching) are present in the nanocapsules. The peak at 460 cm^{-1} is specific to Si–O–Si bending of silica. OA-capped UCNPs (1550 cm^{-1}, O=C–OH asymmetric stretching) and ZnPc (668 cm^{-1}, C–H out of plane deformation) are observed within the UCNPs-ZnPc@NCs, whereas only the transmittance for ZnPc is observed for ZnPc@NCs. The characteristic bands of hydroxyl groups (3436 cm^{-1}, O–H stretching; and 1640 cm^{-1}, H–O–H bending) are also observed for the hybrids, indicating the presence of a large number of structural hydroxyl groups and hydroxyl groups from physically adsorbed water. In addition, the absorbance spectrum of UCNPs-ZnPc@NCs and ZnPc@NCs confirmed that ZnPc was successfully encapsulated inside the nanocapsules (Fig. S4†). Fig. 1D shows the corresponding upconversion luminescence spectra of S-UCNPs@NCs and M-UCNPs@NCs following 980 nm laser excitation. In both cases, green emission centered at 525 nm ($^2H_{11/2} \rightarrow {}^4I_{15/2}$) and 545 nm ($^4S_{3/2} \rightarrow {}^4I_{15/2}$), and red emission centered at 660 nm ($^4F_{9/2} \rightarrow {}^4I_{15/2}$) were observed from the Er^{3+}. No significant difference of emission intensity was observed between S-UCNPs@NCs and M-UCNPs@NCs. It is well known that the emission intensity of UCNPs decreases upon dispersion in aqueous media compared to that in hydrophobic solvents. The decrease is attributed to the non-radiative decay of the Ln^{3+} excited states caused by surface ligands and higher energy vibrational modes of water.[49–52] Nonetheless, although decreased in absolute intensity, the upconversion spectra of encapsulated UCNPs (Fig. S5†) revealed no other significant differences compared to those of OA-UCNPs in hexane (Fig. S5†).[53]

The UCNPs used here, $NaGdF_4$:Er^{3+}, Yb^{3+}, not only serve as energy donors for UC-PDT, but can also be used as a contrast agent for MRI due to the paramagnetic properties of Gd^{3+}.[11,54] In fact, we previously reported that ligand-free $NaGdF_4$ UCNPs with sizes between 20 and 60 nm have the ability to enhance negative contrast in T_2-weighted MRI.[55] To elaborate on the potential of UCNPs@NCs for use in MRI, we investigated their T_2 relaxivity at a 7 T magnetic field. Fig. 2A displays the concentration-dependent negative contrast gradient produced by ligand-free UCNPs, S-UCNPs@NCs, and M-UCNPs@NCs, all of which have high r_2 values which attest to enhanced negative contrast in T_2-weighted images (Fig. 2B). The encapsulated UCNPs demonstrated higher r_2 values than ligand-free UCNPs. In UCNPs@NCs the hydrophilic PEO dangling chains facilitate the diffusion of a large amount of water molecules to the vicinity of the $NaGdF_4$ magnetic core, which consequently results in the large T_2 relaxation rate.[56,57] In addition, the ultrathin porous silica shell synergizes the increase of r_2 by decreasing the barrier between Gd^{3+} and water protons, when compared with a thick

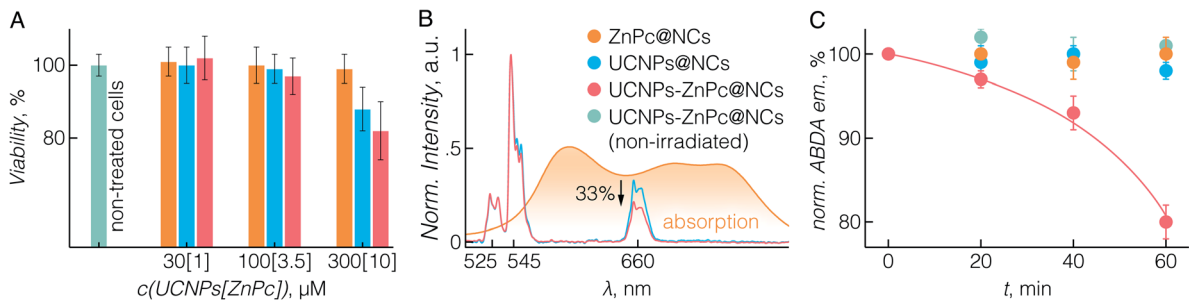

Fig. 3 (A) Viability of untreated (green) BT474 cells, and those cultured in the presence of ZnPc@NCs (orange), UCNPs@NCs (blue), and UCNPs-ZnPc@NCs (red) for 72 h. Individual % of cell viability is the mean ± SD from three independent experiments. No significant growth inhibition was observed at or below 100 μM concentration of UCNPs ($p > 0.05$). (B) Upconversion luminescence spectrum of UCNPs-ZnPc@NCs and UCNPs@NCs upon 980 nm irradiation, and the absorption spectrum of ZnPc@NCs, indicating the partial spectral overlap between the ZnPc absorbance and the UCNP emission. (C) Production of $^1O_2$ (measured using ABDA) upon irradiation for various time periods (0, 20, 40, and 60 min) with a 980 nm laser at 1.5 W cm^{-2} power density. Only UCNPs-ZnPc@NCs exposed to laser irradiation (red) produced $^1O_2$, while no change in ABDA emission was observed for non-irradiated control UCNPs-ZnPc@NCs (green), or irradiated ZnPc@NCs and UCNPs@NCs.

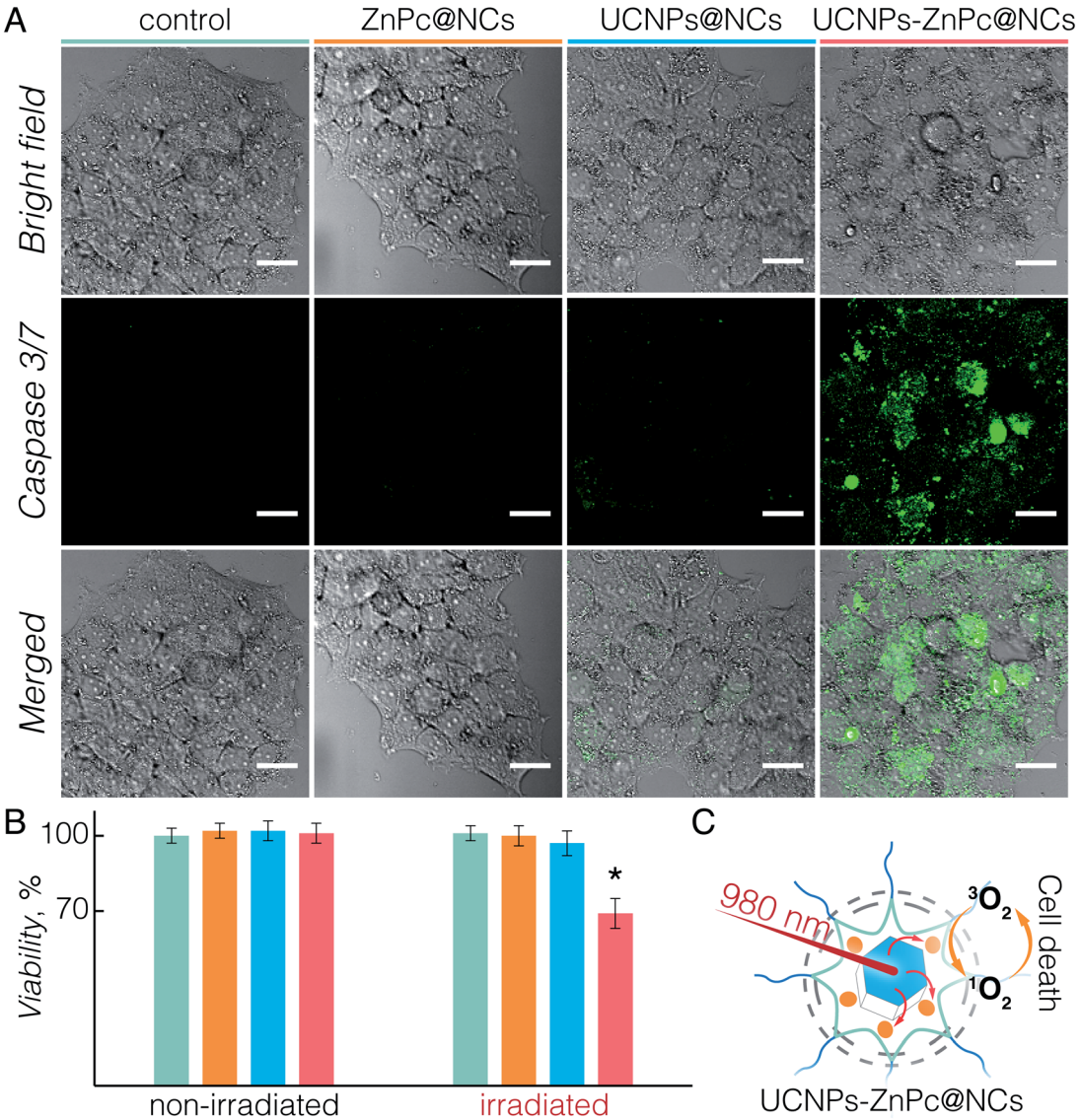

Fig. 4 (A) Confocal fluorescence microscopy images of BT474 cells: untreated (control), incubated with ZnPc@NCs (3.5 μM), UCNPs@NCs (100 μM), and UCNPs-ZnPc@NCs (100 μM UCNPs with 3.5 μM ZnPc). Cell nuclei stained with Caspase 3/7 detection reagent (green colour) (λ_{ex} = 488 nm, λ_{em} = 525 nm) indicating the apoptotic cells. Scale bars in all images correspond to 50 μm. (B) Viability of BT474 cells incubated with the studied compounds in the absence of irradiation and post 980 nm irradiation. 31% of cell growth inhibition by UCNPs-ZnPc@NCs post irradiation was observed with a $p < 0.05$ significance (indicated with an asterisk). Note, colour coding of different compounds in (A) is maintained in (B). (C) Scheme illustrating the UC-PDT mechanism of UCNPs-ZnPc@NCs.

silica shell.[58] We have also found that M-UCNPs@NCs exhibited slightly higher r_2 and a consequent darker T_2-weighted image than S-UCNPs@NCs, which could be due to the larger cluster of UCNPs in M-UCNPs@NCs. It has been reported that the r_2 values can be greatly increased by clustering T_2 contrast agents in reservoirs such as liposomes or micelles, and the increase of r_2 is attributed to the intrinsic mechanism of spin–spin relaxation, which relies on the local concentration of the contrast agents.[58–60] In this regard, the encapsulation of multiple UCNPs in nanocapsules could be an effective strategy to improve the MRI prowess of Gd^{3+}-based UCNPs. To study the potential diagnostic application of the synthesised UCNPs-ZnPc@NCs, we evaluated their magnetic contrast enhancement by MRI *in vitro*. BT474 cells were incubated with a maximal benign concentration of UCNPs-ZnPc@NCs (100 μM), while non-treated cells were used as a control. Fig. S6† clearly demonstrates the enhanced negative contrast (darker T_2-weighted images) at a 7 T magnetic field, indicating their potential for precisely locating the delivered payloads by MRI.

2.4. *In vitro* cytotoxicity and singlet oxygen production by UCNPs-ZnPc@NCs

To study the potential biomedical application of UCNPs-ZnPc@NCs, we first evaluated their cytotoxicity. The BT474 breast cancer cell line was used, which is resistant to chemotherapeutic drugs such as paclitaxel, as the cellular model for

the *in vitro* study.[61] In fact, paclitaxel resistance remains a major challenge in the treatment of breast cancer.[62] First, the cytotoxicity of UCNPs-ZnPc@NCs, UCNPs@NCs, and ZnPc@NCs was investigated by cell proliferation assay using CCK-8. Fig. 3A demonstrates that there was no significant cell growth inhibition in all three groups up to a 100 μM concentration of UCNPs, which was selected for all further cell studies.

Further we sought to evaluate the $^1O_2$ generation potential of UCNPs-ZnPc@NCs. As can be seen in Fig. 3B, the emission spectrum of UCNPs, particularly that originating from $^4F_{9/2} \rightarrow {}^4I_{15/2}$ transition at 660 nm, overlaps with the absorption Q-band of ZnPc. With the presence of ZnPc in the nanocapsules, we observed approximately 33% quenching of the red UC emission around 660 nm compared to significantly lower quenching of the green emission at *ca.* 545 nm resulting from the lower spectral overlap with the absorption of ZnPc. This indicated that ZnPc molecules were close enough to the surface of UCNPs which then could act as energy donors for ZnPc. The capacity of ($^1O_2$) production was assessed using ABDA as a probe molecule.[20] As shown in Fig. 3C, three control groups were studied: ABDA incubated with UCNPs-ZnPc@NCs without laser irradiation, ZnPc@NCs with laser irradiation, and UCNPs@NCs with laser irradiation. The emission from ABDA remained constant for these control groups over time, indicating that no $^1O_2$ was generated. However, when incubated with UCNPs-ZnPc@NCs and exposed to laser irradiation, the emission of ABDA significantly decreased demonstrating $^1O_2$ generation by indirectly excited ZnPc molecules ($p < 0.05$), which indicates that there are sufficient amounts of $^1O_2$ produced by ZnPc.[63] Cumulatively, we were able to demonstrate not only the effective and simple co-encapsulation of ZnPc with UCNPs, but also the ability of this system to show photosensitizing behaviour under deep-tissue penetrating NIR excitation.

2.5. *In vitro* UC-PDT effect of UCNPs-ZnPc@NCs

Upon establishing the biocompatibility and $^1O_2$ generation of UCNPs-ZnPc@NCs, we proceeded to investigate the UC-PDT effect in BT474 cancer cells (Fig. 4). To select the suitable power density for the irradiation, we first investigated the phototoxicity of 980 nm light on live cells considering the potential hyperthermia effect.[64] Upon irradiation at 1.5, 3, and 6 W cm^{-2} power densities for 40 min, the viability of BT474 cells was 100%, 94%, and 70%, respectively (Fig. S7†). No significant damage to cells was observed upon irradiation at 1.5 W cm^{-2}, and therefore this power density was used for subsequent irradiation experiments. Additionally, the chosen value is in the power density range reported in previous studies (usually below 2.5 W cm^{-2}).[8,15,20,36,54,65] As a control, non-treated cells and those incubated with UCNPs@NCs and ZnPc@NCs were irradiated (see the Materials and methods section in the ESI†). No significant growth inhibition was observed in these three groups (Fig. 4B). However, cells incubated with UCNPs-ZnPc@NCs and irradiated under 980 nm light had around 31% of growth inhibition at 24 h post irradiation. This indicated that the cell growth inhibition was induced by the UC-PDT effect (Fig. 4C): $^1O_2$ produced by ZnPc caused the oxidative damage of BT474 cells. To further confirm the UC-PDT induced growth inhibition, we analysed the apoptosis induction by staining the cells with a fluorescence assay using Caspase 3/7 green.[66–68] This agent is intrinsically non-fluorescent, but in the presence of activated caspase 3/7 (an indicator of apoptosis) produces a bright green-fluorescent signal ($\lambda_{ex} = 488$ nm, $\lambda_{em} = 530$ nm). Following the same irradiation treatment, cells incubated with UCNPs-ZnPc@NCs, as well as the control groups, were incubated with Caspase 3/7 green, and imaged under a fluorescence confocal microscope (Fig. 4A and S8†). Green luminescence of the apoptosis marker was observed in the cells treated with UCNPs-ZnPc@NCs upon 980 nm laser irradiation compared to the other three groups, revealing the induction of apoptosis. Some green emission was also observed in the cells incubated with UCNPs@NCs. The slight apoptosis induced by UCNPs@NCs may stem from the photothermal damage of UCNPs upon 980 nm irradiation, since there was no apoptosis induction observed in both non-treated cells and those incubated with ZnPc@NCs upon irradiation. Altogether, it proved that UC-PDT can inhibit cell growth through apoptosis, even in the paclitaxel resistant breast cancer cells.

3 Conclusions

We developed a one-pot approach to simultaneously encapsulate Er^{3+}, Yb^{3+} doped $NaGdF_4$ UCNPs and ZnPc (PS) into polymeric micelle/silica nanocapsules *via* the interfacial templating condensation approach. Using PEO-PPO-PEO block copolymers as the templating and protecting agent, the encapsulation follows a straightforward microemulsion mechanism which directly proceeds in a near-neutral pH aqueous environment. The surface hydrophobic nature of UCNPs is crucial for the success of encapsulation. To protect the hydrophobic OA ligands of UCNPs from reaction with the silanol groups of hydrated TMOS, we optimized the synthesis procedure by allowing UCNPs to be encapsulated by PEO-PPO-PEO micelles prior to the addition of TMOS. By this means, we have successfully synthesized UCNPs-ZnPc@NCs comprising a single UCNP surrounded by the co-encapsulated ZnPc, and minimized the distance between the two payloads to facilitate the energy transfer from UCNPs to ZnPc. Such an organic/inorganic hybrid nanocapsule demonstrated excellent colloidal stability, biocompatibility, and enhanced negative contrast T_2-weighted MRI, as well as a PDT effect *in vitro*, eradicating BT474 breast cancer cells under NIR excitation. The developed one-pot approach shines light on the co-encapsulation of OA-capped inorganic UCNPs with a hydrophobic PS, and constitutes an important step forward in the surface engineering of UCNPs and UC-PDT systems. The UC-PDT efficacy and the T_2 contrast enhancement of the developed NCs will be further expanded upon in future *in vivo* studies. This strategy could be extended for developing multifunctional nanocarriers to encompass various nanoparticles and therapeutic or diagnostic agents, thus bringing theranostic functionalities such as NIR, MRI or CT imaging guided therapy and controlled drug release to personalized medicine.

Conflicts of interest

There are no conflicts to declare.

Acknowledgements

F. V. acknowledges funding from the Natural Sciences and Engineering Research Council (NSERC) of Canada through the Discovery Grants program and the Discovery Accelerator Supplement (DAS) award, the Canada Foundation for Innovation for infrastructure and its operation, and the Fonds de Recherche du Québec-Nature et technologies (FRQNT). F. R. acknowledges the NSERC for a Discovery Grant and the Canada Research Chairs program for funding and partial salary support. M. W. and A. Y. C. are grateful for the Johns Hopkins Singapore Research Fund provided by a private limited company for supporting their Santa Fe research programme. A. S. is grateful to FRQNT for financial support in the form of a scholarship for doctoral studies. X. L., M. N. and K. B. acknowledge the support of A*STAR, Singapore.

References

1 T. J. Dougherty, C. J. Gomer, B. W. Henderson, G. Jori, D. Kessel, M. Korbelik, J. Moan and Q. Peng, *JNCI, J. Natl. Cancer Inst.*, 1998, **90**, 889–905.
2 D. E. Dolmans, D. Fukumura and R. K. Jain, *Nat. Rev. Cancer*, 2003, **3**, 380–387.
3 S. B. Brown, E. A. Brown and I. Walker, *Lancet Oncol.*, 2004, **5**, 497–508.
4 G. Yi, S. H. Hong, J. Son, J. Yoo, C. Park, Y. Choi and H. Koo, *Quant. Imaging Med. Surg.*, 2018, **8**, 433–443.
5 J. P. Celli, B. Q. Spring, I. Rizvi, C. L. Evans, K. S. Samkoe, S. Verma, B. W. Pogue and T. Hasan, *Chem. Rev.*, 2010, **110**, 2795–2838.
6 A. P. Castano, T. N. Demidova and M. R. Hamblin, *Photodiagn. Photodyn. Ther.*, 2005, **2**, 91–106.
7 F. Vatansever and M. R. Hamblin, in *Cancer Immunology: Bench to Bedside Immunotherapy of Cancers*, ed. N. Rezaei, Springer Berlin Heidelberg, Berlin, Heidelberg, 2015, pp. 383–399.
8 Q. Sun, F. He, H. Bi, Z. Wang, C. Sun, C. Li, J. Xu, D. Yang, X. Wang, S. Gai and P. Yang, *Chem. Eng. J.*, 2019, **362**, 679–691.
9 Ł. Lamch, A. Pucek, J. Kulbacka, M. Chudy, E. Jastrzębska, K. Tokarska, M. Bułka, Z. Brzózka and K. A. Wilk, *Adv. Colloid Interface Sci.*, 2018, **261**, 62–81.
10 S. Pervaiz and M. Olivo, *Clin. Exp. Pharmacol. Physiol.*, 2006, **33**, 551–556.
11 E. Hemmer, A. Benayas, F. Légaré and F. Vetrone, *Nanoscale Horiz.*, 2016, **1**, 168–184.
12 G. Chen, H. Qiu, P. N. Prasad and X. Chen, *Chem. Rev.*, 2014, **114**, 5161–5214.
13 D. Yang, P. a. Ma, Z. Hou, Z. Cheng, C. Li and J. Lin, *Chem. Soc. Rev.*, 2015, **44**, 1416–1448.
14 P. Zhang, W. Steelant, M. Kumar and M. Scholfield, *J. Am. Chem. Soc.*, 2007, **129**, 4526–4527.
15 N. M. Idris, M. K. Gnanasammandhan, J. Zhang, P. C. Ho, R. Mahendran and Y. Zhang, *Nat. Med.*, 2012, **18**, 1580–1585.
16 K. Liu, X. Liu, Q. Zeng, Y. Zhang, L. Tu, T. Liu, X. Kong, Y. Wang, F. Cao, S. A. G. Lambrechts, M. C. G. Aalders and H. Zhang, *ACS Nano*, 2012, **6**, 4054–4062.
17 X. Liu, M. Zheng, X. Kong, Y. Zhang, Q. Zeng, Z. Sun, W. J. Buma and H. Zhang, *Chem. Commun.*, 2013, **49**, 3224–3226.
18 H. S. Qian, H. C. Guo, P. C.-L. Ho, R. Mahendran and Y. Zhang, *Small*, 2009, **5**, 2285–2290.
19 Q. Sun, F. He, C. Sun, X. Wang, C. Li, J. Xu, D. Yang, H. Bi, S. Gai and P. Yang, *ACS Appl. Mater. Interfaces*, 2018, **10**, 33901–33912.
20 Y. Huang, A. Skripka, L. Labrador-Páez, F. Sanz-Rodríguez, P. Haro-González, D. Jaque, F. Rosei and F. Vetrone, *Nanoscale*, 2018, **10**, 791–799.
21 M. Haase and H. Schäfer, *Angew. Chem., Int. Ed.*, 2011, **50**, 5808–5829.
22 S. Gai, C. Li, P. Yang and J. Lin, *Chem. Rev.*, 2014, **114**, 2343–2389.
23 Y. Liu, X. Meng and W. Bu, *Coord. Chem. Rev.*, 2019, **379**, 82–98.
24 H. Qiu, M. Tan, T. Ohulchanskyy, J. Lovell and G. Chen, *Nanomaterials*, 2018, **8**, 344.
25 Q. Liu, Y. Sun, T. Yang, W. Feng, C. Li and F. Li, *J. Am. Chem. Soc.*, 2011, **133**, 17122–17125.
26 C. Wang, H. Tao, L. Cheng and Z. Liu, *Biomaterials*, 2011, **32**, 6145–6154.
27 G. Chen, J. Shen, T. Y. Ohulchanskyy, N. J. Patel, A. Kutikov, Z. Li, J. Song, R. K. Pandey, H. Ågren, P. N. Prasad and G. Han, *ACS Nano*, 2012, **6**, 8280–8287.
28 C. Wang, L. Cheng, Y. Liu, X. Wang, X. Ma, Z. Deng, Y. Li and Z. Liu, *Adv. Funct. Mater.*, 2013, **23**, 3077–3086.
29 G. Jalani, R. Naccache, D. H. Rosenzweig, L. Haglund, F. Vetrone and M. Cerruti, *J. Am. Chem. Soc.*, 2016, **138**, 1078–1083.
30 N. Liu, R. Marin, Y. Mazouzi, G. O. Cron, A. Shuhendler and E. Hemmer, *Nanoscale*, 2019, **11**, 6794–6801.
31 F. Wang and X. Liu, *Chem. Soc. Rev.*, 2009, **38**, 976–989.
32 X.-F. Qiao, J.-C. Zhou, J.-W. Xiao, Y.-F. Wang, L.-D. Sun and C.-H. Yan, *Nanoscale*, 2012, **4**, 4611–4623.
33 G. Yang, D. Yang, P. Yang, R. Lv, C. Li, C. Zhong, F. He, S. Gai and J. Lin, *Chem. Mater.*, 2015, **27**, 7957–7968.
34 Y. Zhang, B. Y. W. Hsu, C. Ren, X. Li and J. Wang, *Chem. Soc. Rev.*, 2015, **44**, 315–335.
35 J. Shan, S. J. Budijono, G. Hu, N. Yao, Y. Kang, Y. Ju and R. K. Prud'homme, *Adv. Funct. Mater.*, 2011, **21**, 2488–2495.
36 A. Skripka, V. Karabanovas, G. Jarockyte, R. Marin, V. Tam, M. Cerruti, R. Rotomskis and F. Vetrone, *Adv. Funct. Mater.*, 2019, **29**, 1807105.
37 E. S. Read and S. P. Armes, *Chem. Commun.*, 2007, 3021–3035.
38 S. Jiang and Y. Zhang, *Langmuir*, 2010, **26**, 6689–6694.
39 Y. Wang, K. Liu, X. Liu, K. Dohnalová, T. Gregorkiewicz, X. Kong, M. C. G. Aalders, W. J. Buma and H. Zhang, *J. Phys. Chem. Lett.*, 2011, **2**, 2083–2088.
40 M. R. Hamblin, *Dalton Trans.*, 2018, **47**, 8571–8580.

41 S. Drozdek, J. Szeremeta, L. Lamch, M. Nyk, M. Samoc and K. A. Wilk, *J. Phys. Chem. C*, 2016, **120**, 15460–15470.
42 Y. Wang, G. Yang, Y. Wang, Y. Zhao, H. Jiang, Y. Han and P. Yang, *Nanoscale*, 2017, **9**, 4759–4769.
43 H. Tan, N. S. Liu, B. He, S. Y. Wong, Z.-K. Chen, X. Li and J. Wang, *Chem. Commun.*, 2009, 6240–6242.
44 V. P. Torchilin, *J. Controlled Release*, 2001, **73**, 137–172.
45 A. A. Atia, A. M. El-Nahas, A. M. Marie and L. D. A. Mahdy, *Adsorpt. Sci. Technol.*, 2006, **24**, 797–814.
46 D. Zhao, J. Feng, Q. Huo, N. Melosh, G. H. Fredrickson, B. F. Chmelka and G. D. Stucky, *Science*, 1998, **279**, 548–552.
47 H. J. Wang, R. Shrestha and Y. Zhang, *Part. Part. Syst. Charact.*, 2014, **31**, 228–235.
48 M. Danaei, M. Dehghankhold, S. Ataei, F. Hasanzadeh Davarani, R. Javanmard, A. Dokhani, S. Khorasani and M. Mozafari, *Pharmaceutics*, 2018, **10**, 57.
49 R. Naccache, F. Vetrone, V. Mahalingam, L. A. Cuccia and J. A. Capobianco, *Chem. Mater.*, 2009, **21**, 717–723.
50 A. Skripka, R. Marin, A. Benayas, P. Canton, E. Hemmer and F. Vetrone, *Phys. Chem. Chem. Phys.*, 2017, **19**, 11825–11834.
51 M. Kraft, C. Würth, V. Muhr and T. Hirsch, *Nano Res.*, 2018, **11**, 6360–6374.
52 N. Bogdan, F. Vetrone, G. A. Ozin and J. A. Capobianco, *Nano Lett.*, 2011, **11**, 835–840.
53 J.-C. Boyer, F. Vetrone, L. A. Cuccia and J. A. Capobianco, *J. Am. Chem. Soc.*, 2006, **128**, 7444–7445.
54 Y. Dai, H. Xiao, J. Liu, Q. Yuan, P. a. Ma, D. Yang, C. Li, Z. Cheng, Z. Hou, P. Yang and J. Lin, *J. Am. Chem. Soc.*, 2013, **135**, 18920–18929.
55 M. Wang, Y. Zhang, Q. Yao, M. Ng, M. Lin, X. Li, K. K. Bhakoo, A. Y. Chang, F. Rosei and F. Vetrone, *Chem. Mater.*, 2019, **31**, 5160–5171.
56 P. A. Hardy and R. M. Henkelman, *Magn. Reson. Imaging*, 1989, **7**, 265–275.
57 J. Qin, S. Laurent, Y. S. Jo, A. Roch, M. Mikhaylova, Z. M. Bhujwalla, R. N. Muller and M. Muhammed, *Adv. Mater.*, 2007, **19**, 1874–1878.
58 X. Zhang, B. Blasiak, A. J. Marenco, S. Trudel, B. Tomanek and F. C. J. M. van Veggel, *Chem. Mater.*, 2016, **28**, 3060–3072.
59 H. Ai, C. Flask, B. Weinberg, X.-T. Shuai, M. D. Pagel, D. Farrell, J. Duerk and J. Gao, *Adv. Mater.*, 2005, **17**, 1949–1952.
60 F. Yang, A. Skripka, M. S. Tabatabaei, S. H. Hong, F. Ren, A. Benayas, J. K. Oh, S. Martel, X. Liu, F. Vetrone and D. Ma, *ACS Nano*, 2019, **13**, 408–420.
61 Z. Li, T. Tian, X. Hu, X. Zhang, F. Nan, Y. Chang, F. Lv and M. Zhang, *Biochem. Biophys. Res. Commun.*, 2013, **441**, 538–543.
62 B. T. McGrogan, B. Gilmartin, D. N. Carney and A. McCann, *Biochim. Biophys. Acta, Rev. Cancer*, 2008, **1785**, 96–132.
63 T. Entradas, S. Waldron and M. Volk, *J. Photochem. Photobiol., B*, 2020, **204**, 111787.
64 Q. Zhan, J. Qian, H. Liang, G. Somesfalean, D. Wang, S. He, Z. Zhang and S. Andersson-Engels, *ACS Nano*, 2011, **5**, 3744–3757.
65 J. Xu, R. Lv, S. Du, S. Gai, F. He, D. Yang and P. Yang, *J. Mater. Chem. B*, 2016, **4**, 4138–4146.
66 J. S. Khalili, X. Yu, J. Wang, B. C. Hayes, M. A. Davies, G. Lizee, B. Esmaeli and S. E. Woodman, *Clin. Cancer Res.*, 2012, **18**, 4345–4355.
67 M. Miyata, M. Kambe, O. Tajima, S. Moriya, H. Sawaki, H. Hotta, Y. Kondo, H. Narimatsu, T. Miyagi, K. Furukawa and K. Furukawa, *Cancer Sci.*, 2011, **102**, 2139–2149.
68 T. C. Huang, J. F. Lee and J. Y. Chen, *Mar. Drugs*, 2011, **9**, 1995–2009.

SUPPORTING INFORMATION

One-Pot Synthesis of Theranostic Nanocapsules with Lanthanide Doped Nanoparticles

Miao Wang[a, e], Yu Zhang[b], Michael Ng[c], Artiom Skripka[a], Ting Cheng[a], Xu Li[a, b, f], Kishore Kumar Bhakoo[c], Alex Y. Chang[d, e], Federico Rosei[a], Fiorenzo Vetrone[*a]

[a.] *Institut National de la Recherche Scientifique (INRS), Centre Énergie, Matériaux et Télécommunications, Université du Québec, Varennes (QC), Canada*
[b.] *Institute of Materials Research and Engineering (IMRE), Agency for Science, Technology and Research (A*STAR), Singapore*
[c.] *Singapore Bioimaging Consortium (SBIC), Agency for Science, Technology and Research (A*STAR), Singapore*
[d.] *Department of Oncology, Johns Hopkins University, Baltimore, Maryland, USA*
[e.] *Johns Hopkins Singapore, Singapore*
[f.] *Department of Chemistry, National University of Singapore, Singapore*

*. Corresponding author, vetrone@emt.inrs.ca

Table of Contents

Experimental Procedures

Synthesis of $NaGdF_4$:Er^{3+} (2%), Yb^{3+} (20%) UCNPs

Gadolinium oxide (Gd_2O_3, 99.99%), erbium oxide (Er_2O_3, 99.99%), ytterbium oxide (Yb_2O_3, 99.99%), triflouroacetic acid (CF_3COOH, 99%), sodium trifluoroacetate (CF_3COONa, 98%), oleic acid (technical grade, 90%), and 1-octadecene (technical grade, 90%) were all purchased from Sigma-Aldrich and were used without further purification.

$NaGdF_4$:Er^{3+} (2%), Yb^{3+} (20%) UCNPs were synthesized *via* the hot-injection thermolysis approach[1-3], which allows to directly decompose the metal trifluoroacetate precursors. Briefly, the obtained $(CF_3COO)_3Ln$ (Ln = Gd, Yb, Er) precursors and CF_3COONa were first dispersed in 7.5 mL each of 1-octadecene and oleic acid (OA) and degassed with stirring at 125 °C. Then, the precursor solution was injected into the degassed and preheated (315 °C) mixture of 12.5 mL each of 1-octadecene and oleic acid at a rate of 1.5 mL min^{-1} (Harvard Apparatus Pump 11 Elite). The mixed solution was then left to stir vigorously under an inert argon atmosphere for 1 h. After the reaction was completed, the solution was cooled down to room temperature and the synthesized UCNPs were precipitated using absolute ethanol and centrifuged at 6500 rpm for 15 min. The solids were then washed with a mixture of hexane/ethanol (1:4) twice and finally re-dispersed in hexane.

Polymeric micelle/silica encapsulation of UCNPs and ZnPc

Pluronic® F127 ((ethylene oxide)$_{106}$(propylene oxide)$_{70}$(ethylene oxide)$_{106}$, PEO-PPO-PEO, MW = 12,600 g mol^{-1}), tetramethoxysilane (TMOS, 98%), tetrahydrofuran (THF, ≥99.9%) and zinc phthalocyanine (ZnPc, 97%) were purchased from Sigma-Aldrich. ZnPc was dissolved in THF at a concentration of 2 mg mL^{-1} (stock solution). The synthesized $NaGdF_4$:Er^{3+} (2%), Yb^{3+} (20%) UCNPs dispersed in hexane (31.8 mg mL^{-1}) were used as stock solution.

Polymeric micelle/silica nanocapsules with various payloads were prepared by modifying the interfacial templating condensation approach.[4] We have made nanocapsules with ZnPc (ZnPc@NCs), nanocapsules with various number (n) of UCNPs, namely S-UCNPs@NCs (n < 3) and M-UCNPs@NCs (n > 3), and nanocapsules with both UCNPs and ZnPc (UCNPs-ZnPc@NCs).

To prepare ZnPc@NCs, F127 (37.5 mg) was dissolved in THF (750 µL) and mixed with ZnPc (150 µL). After stirring at room temperature for 3 h, TMOS (55 µL) was added to the solution and sonicated for 1 min. The solution was injected into stirred deionized (DI) water (10 mL) at a rate of 60-90 µL min^{-1}. Stirring was continued for another 4 days for THF evaporation as well as TMOS hydrolysis and condensation. Afterwards, the solution was dialyzed against DI water for 24 h using a dialysis membrane (MWCO of 10,000 g mol^{-1}, Spectra/Por® regenerated cellulose). Finally, the solution was centrifuged for 10 min at 10,000 rpm, the supernatant was further passed through a 0.2 µm filter to remove large aggregates.

To synthesize the nanocapsules with UCNPs (S-UCNPs@NCs, M-UCNPs@NCs, and UCNPs-ZnPc@NCs), designated amounts of UCNP stock solution was firstly air dried to remove hexane. Then, the dried UCNPs were re-dispersed in THF and mixed with F127 or F127 and ZnPc, namely solution A1 (6.4 mg UCNPs, 15 mg F127, and 900 µL THF), solution A2 (9.5 mg UCNPs, 15 mg F127, and 900 µL THF), and solution A3 (6.4 mg UCNPs, 15 mg F127, 150 µL ZnPc, and 900 µL THF), respectively. After stirring at room temperature for 3 h and sonicating for 10 min, each of the solutions A(1-3) were individually injected into DI water (10 mL) at a rate of 60-90 µL min^{-1} while being stirred, to obtain respective solutions B(1-3). Stirring was continued for 2 more days to evaporate THF. Afterwards, 30 µL of TMOS was dissolved in THF (300 µL) and injected at a rate of 60-90 µL min^{-1} into each of the solutions B(1-3). It was stirred at room temperature for another 2 days for hydrolysis and condensation of TMOS. The solution was then subjected to centrifugation (6,000 rpm for 30 min), discarding the supernatant containing empty (i.e., UCNP-free) nanocapsules and re-dispersing the precipitates in DI water. The dispersion was further passed through a 0.2 µm filter to remove large aggregates.

Characterization

The crystalline phase of OA-capped UCNPs under investigation was analysed by X-ray diffraction (XRD) using a Bruker D8 Advanced Diffractometer, Cu Kα radiation (λ=1.5406 Å, power of the generator: 40 kV and 40 mA). Scan range was 20 – 80° 2θ, with a step size of 0.04° and a count time of 1s. The morphology and size distribution of the silica nanocapsules and UCNPs were determined by transmission electron microscopy (TEM) with a JEOL JEM-2010 microscope operating at 80 kV. The sample solution was prepared on a formvar/carbon film supported on a 300 mesh copper grid (3 mm in diameter). Inductively coupled plasma - atomic emission spectroscopy (ICP-AES) was used to determine the content of Na^+, Gd^{3+}, Yb^{3+}, and Er^{3+} in the UCNPs. The samples were digested in 70% HNO_3 with sonication at 65 °C, and then diluted to below 5% HNO_3 before conducting ICP-AES measurements. Dynamic light scattering (DLS) was performed with Malvern Zetasizer Nano-S using a HeNe laser (633 nm) to measure the hydrodynamic size and size distribution of different nanocapsules. All measurements were conducted using DI water as the dispersant in a glass cuvette. A Fourier-Transform Infrared (FTIR) spectrophotometer (Varian 3100 Excalibur) was used to characterize the chemical composition of the synthesised nanocapsules. For FTIR sample preparation, the aqueous suspensions of UCNPs-ZnPc@NCs were freeze-dried and dispersed in KBr pellets. Luminescent measurements were carried out under 980 nm excitation using a laser diode (BWT, China). The laser beam was focused on the sample using a lens to obtain a spot of a Gaussian intensity distribution with a 0.4 mm diameter. The emitted light was collected by a lens in a 90° configuration, and then transferred to a spectrophotometer (Avaspec-2048L-USB2) using an optical fiber. The UV-Visible (UV-VIS) absorption spectra were obtained using a Varian Cary 5000 spectrometer.

Evaluation of singlet oxygen ($^1O_2$) generation

$^1O_2$ production was detected by 9, 10-anthracenediyl-bis(methylene) dimalonic acid (ABDA) (Sigma-Aldrich).[5] In this method, the ABDA fluorescence emission is bleached due to reaction with the $^1O_2$. Briefly, ABDA was dissolved in dimethyl sulfoxide (DMSO) (Sigma Aldrich, USA) and diluted in water to a final concentration of 20 µM. UCNPs-ZnPc@NCs, UCNPs@NCs, or ZnPc@NCs alone were mixed with ABDA

and irradiated by a 980 nm CW laser (1.5 W cm^{-2}) for 0, 20, 40, and 60 min, respectively. Magnetic stirring and constant temperature (24 °C) were kept during the irradiation experiments. The fluorescence emission of ABDA at 431 nm (excited at 380 nm) was measured using a microplate fluorescence spectrophotometer (Cytation/5 imaging reader, BioTek).

Cell culture and cytotoxicity assay

The breast cancer cells BT474 (American Type Culture Collection) were cultured in Dulbecco's modified Eagle medium (DMEM) (high glucose [4.5 g L^{-1}], with sodium pyruvate and L-glutamine), containing 10% fatal bovine serum (Invitrogen), 1% antibiotic with 100 UI ml^{-1} penicillin, and 100 mg ml^{-1} streptomycin (Invitrogen). Cell incubation was maintained at 37 °C, and 5% CO_2. The culture medium was changed two to three times a week and cells were passaged serially using 0.25% trypsin/EDTA (Invitrogen).

The cytotoxicity of S-UCNPs@NCs, ZnPc@NCs, and UCNPs-ZnPc@NCs was evaluated by determining the viability of BT474 breast cancer cells using Cell Counting Kit-8 (CCK-8) (Sigma-Aldrich),[6] of which highly water-soluble tetrazolium salt is reduced by dehydrogenases in cells to give an orange colour product (formazan). The amount of the formazan dye generated is directly proportional to the number of living cells. Briefly, BT474 cells were seeded into 96 well plates at a density of 10,000 cells per well and incubated for 24 h. Three groups of the nanocapsules with the designated concentrations, containing UCNPs (30, 100, 300 μM) or ZnPc (1, 3.5, 10 μM), were added to the cultured cells. After incubation with nanocapsules for 72 h, CCK-8 solution was added into cultured cells and incubated for another 2 h. The absorbance at 450 nm of the mixture was measured using a Benchmark Plus microplate spectrophotometer (Bio-Rad). The absorbance values obtained were recalculated as percentage values of viability,

Viability (%) = 100 x $(A_T-A_B)/(A_C-A_B)$

where A_T, is the absorption values of wells containing nanocapsules, A_C is the absorption values of control wells, and A_B is the absorption values of a blank solution. Data were expressed as mean ± standard deviation (SD). Statistical significance of differences observed between groups was calculated using a two-tail paired Student's t-Test at the 95% confidence level. Significance was represented as p-value < 0.05.

In vitro therapeutic efficacy of UC-PDT

To determine the therapeutic effect of UCNPs-ZnPc@NCs, we evaluated the growth inhibition and apoptosis of breast cancer BT474 cells after 980 nm irradiation (1.5 W cm^{-2}). The sequential irradiation was done as follows: 40 min of irradiation, 40 min rest, 40 min of irradiation. The total irradiation period was 80 min. Cell growth inhibition by UCNPs-ZnPc@NCs, UCNPs@NCs, and ZnPc@NCs was tested using CCK-8 cell proliferation assay as described in the previous section. The apoptosis induction was evaluated using Caspase-3/7 green detection reagent (Invitrogen), a fluorescence probe that presents green emission upon 488 nm excitation if reacted with the Caspase-3/7, released by the apoptotic cells. Briefly, 30,000 cells were seeded in eight-chambered cover glass plate (LAB-TEK, Chambered Cover glass System), and incubated with the above 3 groups of nanocapsules containing 100 μM UCNPs and / or 3.5 μM ZnPc for 24 h before the sequential irradiation treatment. After another 24 h of incubation, the Caspase-3/7 green detection reagent was added and incubated with the cells for 6 h to allow the accumulation of the reagent into the cells. Live cell imaging was performed using a confocal laser scanning microscope (Nikon). 20×/0.5 NA dry objective (Nikon) was selected for imaging acquisition. The fluorescence image was acquired at λ_{exc} = 488 nm and λ_{exc} = 530 nm.

T_2 relaxivity measurements and T_2-weighted images

T_2 relaxation measurements and phantom images were obtained by using a 7-Tesla Bruker Clinscan MRI system. To determine the effect of polymeric micelle/silica encapsulation on T_2 relaxivity of UCNPs, the water dispersible ligand-free UCNPs were used as a non-encapsulation group. Ligand-free UCNPs were prepared by removing the capped OA ligands using hydrochloric acid solution (pH = 4).[7] Prior to imaging, a phantom was prepared by series dilution of ligand-free UCNPs, S-UCNPs@NCs and M-UCNPs@NCs at concentrations of 0.125, 0.06, 0.03, 0.015 mM. T_2 relaxation times were determined from a multi-echo spin-echo sequence: TR = 4000 ms; TE: 6.7–250.6 ms. The transverse (r_2) relaxivities were calculated from the slope of $1/T_2$ versus molar [Gd^{3+}] concentration plots. The relevant acquisition parameters were optimized to generate T_2-weighted images, being TR/TE = 3000/61 ms.

BT474 cells were seeded in a 6-well plate (30,000 cells per well) and incubated for 24 h, UCNPs-ZnPc@NCs containing 100 μM of Gd^{3+} were then added. After 24 h incubation, the cells were detached by 0.25% tripsin-EDTA (Invitrogen), and washed with 1x PBS 3 times to remove the non-uptaken UCNPs-ZnPc@NCs. Prior to imaging, a phantom was prepared by mixing the collected cells into a 0.5% agarose solution. T_2 -weighted images were obtained using the same acquisition parameters described above.

Supplementary Experimental Data

TEM images demonstrating the influence of TMOS and ZnPc on the encapsulation

Figure S1. (A-D) TEM images of nanocapsules from the failed encapsulation when simultaneously injecting the mixture of TMOS, F127 and UCNPs in water. Nanocapsules with UCNPs are demonstrated in the suspension of the resultant solution and aggregated UCNPs are observed in the precipitate of the resultant solution. (E-H) TEM images demonstrating the co-encapsulation of UCNPs and ZnPc at various loading amounts of ZnPc: morphology of the monodispersed UCNPs-ZnPc@NCs with a single UCNP at the loading dose of 0.3 mg (E and F), failed encapsulations at the loading dose of 0.6 (G) and 1.2 mg (H), respectively.

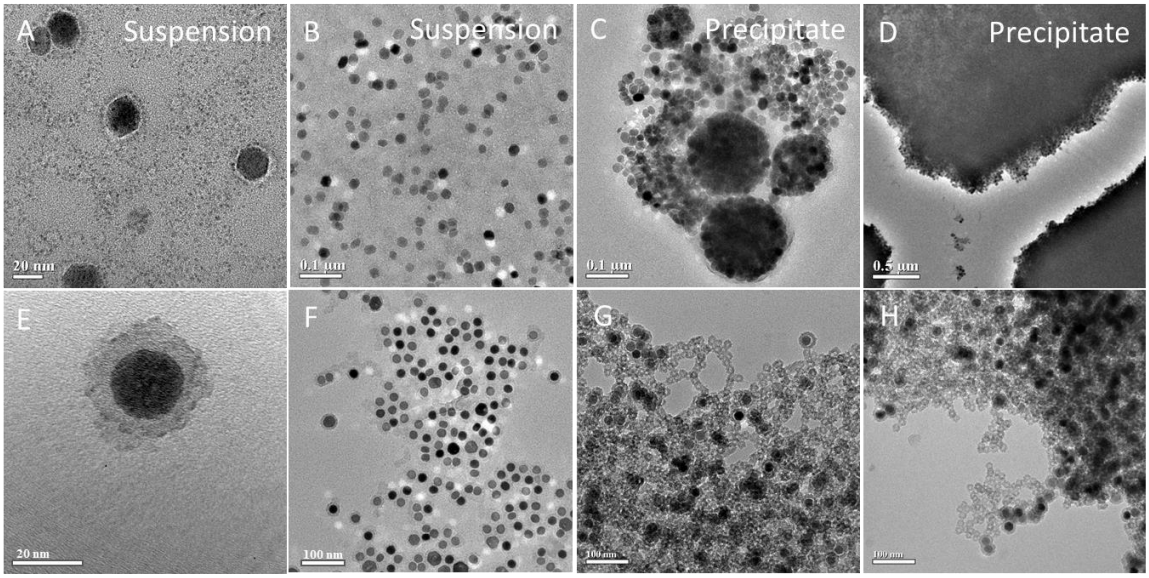

XRD analysis of OA-UCNPs

Figure S2. (A) The diffraction peaks of XRD indicated a pure β-phase, in agreement with the reference data (JCPDS 27-699).

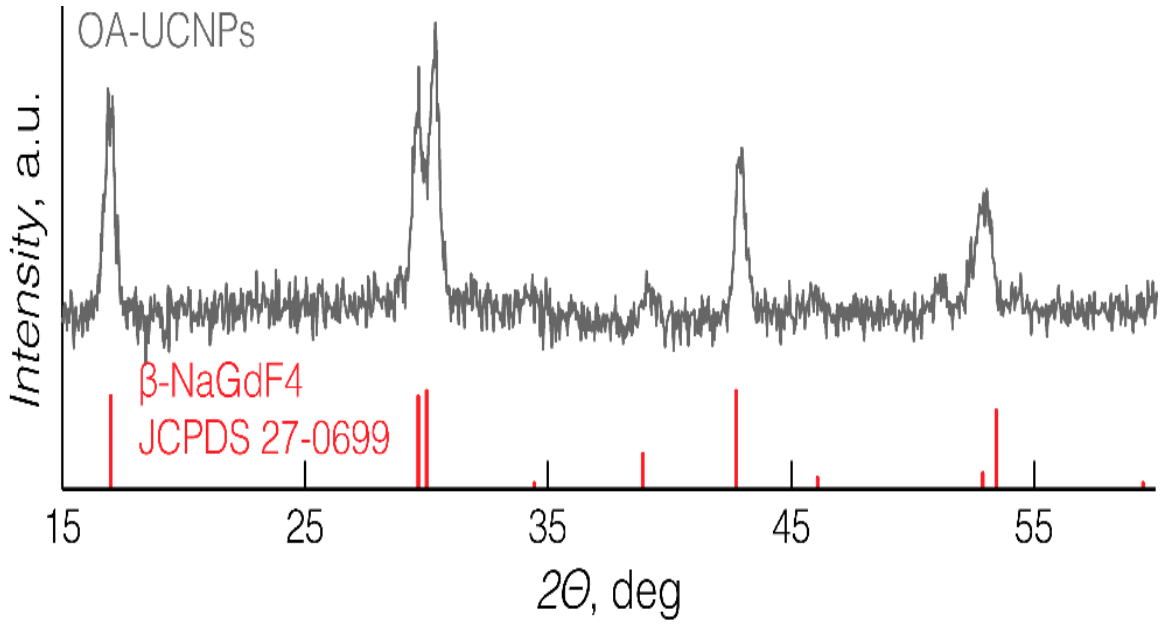

DLS analysis of the NCs studied

Table S1. The hydrodynamic sizes and polydispersity indexes (PDI) of nanocapsules analysed by DLS.

Nanocapsules (NCs)	Z-ave Size (nm)	Main Peak (nm)	PDI
S-UCNPs@NCs	92.8	110	0.199
M-UCNPs@NCs	145.3	180	0.217
ZnPc@NCs	43.04	71.92	0.392
UCNPs-ZnPc@NCs	85.6	97.2	0.113
UCNPs-ZnPc@NCs_6 Months	90.1	99.6	0.154

Figure S3. The hydrodynamic size of UCNPs-ZnPc@NCs analysed after 6 months storage at room temperature.

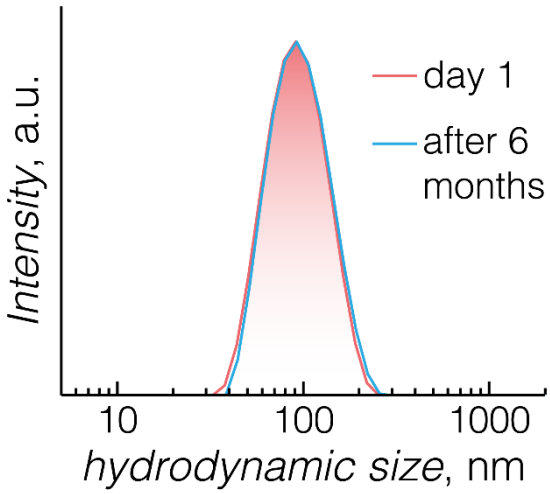

ICP data demonstrating the content of UCNPs and ZnPc encapsulated in the nanocapsules studied

Table S2. Content of $NaGdF_4:Er^{3+}$ (2%), Yb^{3+} (20%) UCNPs and ZnPc encapsulated in the synthesized polymeric micelle/silica nanocapsules analysed by ICP

Nanocapsules (NCs)	mM (mmol l^{-1})			
	$[Gd^{3+}]$	$[Yb^{3+}]$	$[Er^{3+}]$	$[Zn^{2+}]$
S-UCNPs@NCs	0.789	0.191	0.018	x
M-UCNPs@NCs	0.820	0.202	0.018	x
UCNPs-ZnPc@NCs	1.386	0.341	0.036	0.031
ZnPc@NCs	x	x	x	0.046

X: not detected

Light absorbance spectrum of ZnPc encapsulated in the nanocapsules studied

Figure S4. Absorbance spectrum of the synthesized nanocapsules demonstrating ZnPc molecules were encapsulated in UCNPs-ZnPc@NCs and ZnPc@NCs, respectively.

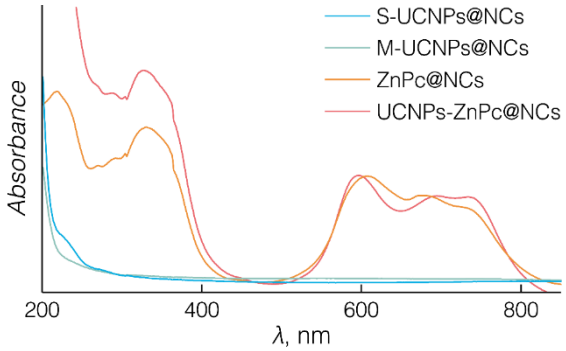

Comparison of upconversion spectrum between OA-UCNPs and encapsulated UCNPs

Figure S5. The upconversion spectra of OA-capped UCNPs in hexane and encapsulated UCNPs in water. Spectra are normalized to the maximum intensity.

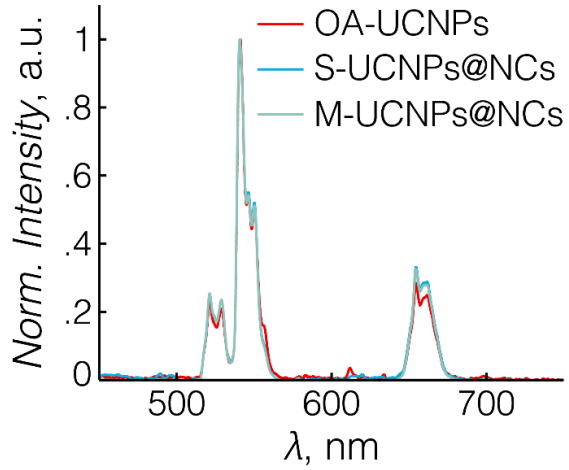

In vitro T_2 contrast enhancement of UCNPs-ZnPc@NCs by MRI

Figure S6. T_2-weighted image demonstrates the enhanced negative contrast in the BT474 cells incubated with UCNPs-ZnPc@NCs compared to the non-treated cells at 7 T magnetic field.

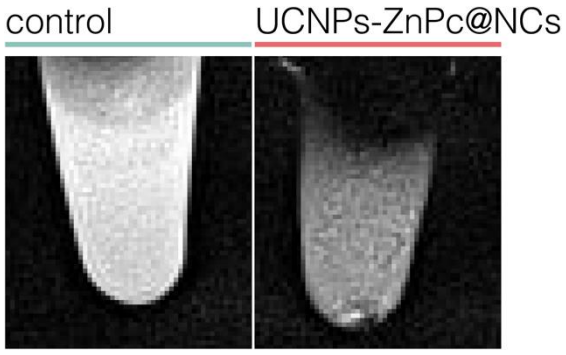

The viability of BT474 cells upon 980 nm irradiation

Figure S7. The viability (%) of BT474 cells upon 980 nm irradiation. BT474 cells were seeded into 96 well plates at a density of 10,000 cells per well and incubated for 24 h, then irradiated by 980 nm light for 40 min at various power densities (1.5, 3, and 6 W cm^{-2}). Non-irradiated wells were set as control. The cell viability was analysed by CCK-8. Data were expressed as mean ± standard deviation (SD) of triplicated experiments.

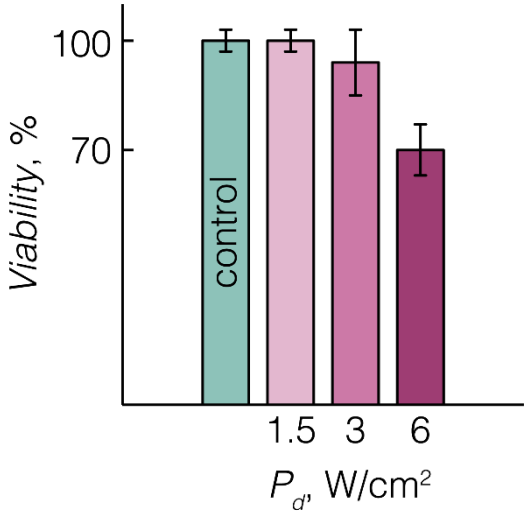

In vitro UC-PDT effect of UCNPs-ZnPc@NCs in BT474 breast cancer cells.

Figure S8. Fluorescence microscopy images of BT474 cells, incubated with the 4 groups of NCs for 24 h before 980 nm irradiation. Cell nuclei were stained with caspase 3/7 detection reagent (λ_{ex} = 488 nm, λ_{em} = 530 nm), green colour indicates the apoptotic cells. The % corresponds to the apoptosis induced by each group. The scale bars in all images stand for 200 µm.

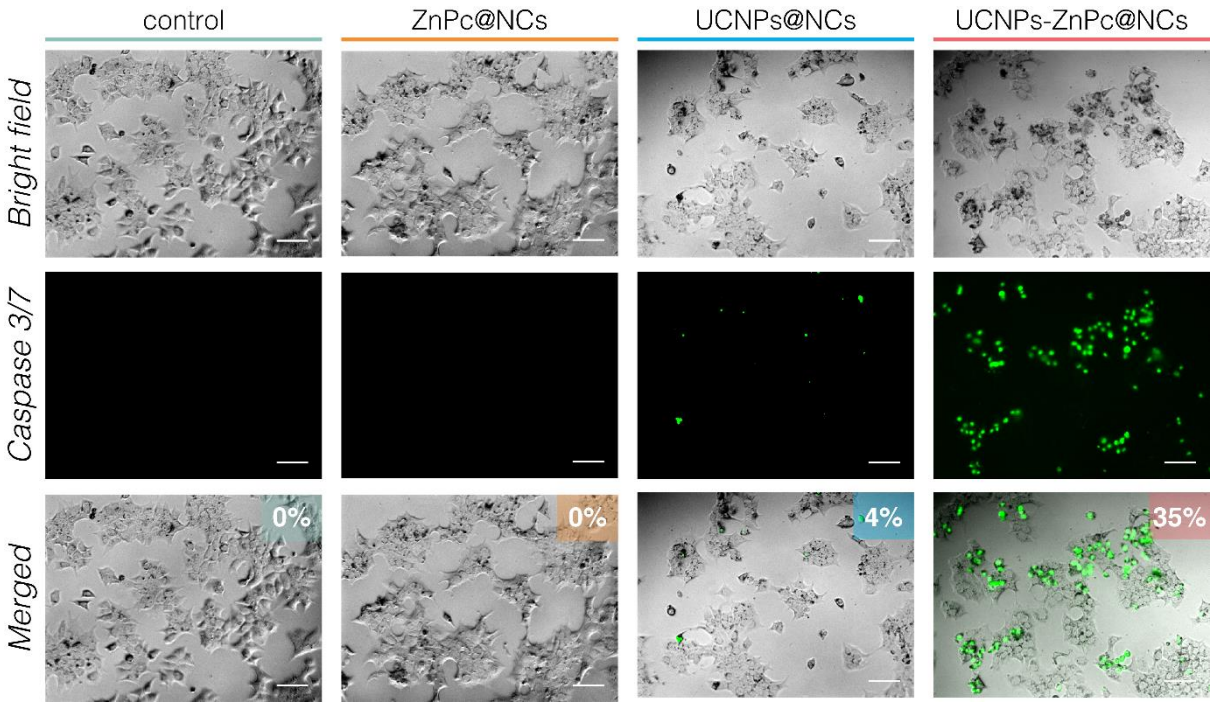

References

1. J.-C. Boyer, F. Vetrone, L. A. Cuccia and J. A. Capobianco, *Journal of the American Chemical Society*, 2006, **128**, 7444-7445.
2. F. Vetrone, R. Naccache, V. Mahalingam, C. G. Morgan and J. A. Capobianco, *Advanced Functional Materials*, 2009, **19**, 2924-2929.
3. R. Naccache, F. Vetrone, V. Mahalingam, L. A. Cuccia and J. A. Capobianco, *Chemistry of Materials*, 2009, **21**, 717-723.
4. H. Tan, N. S. Liu, B. He, S. Y. Wong, Z.-K. Chen, X. Li and J. Wang, *Chemical Communications*, 2009, 6240-6242.
5. Y. Huang, A. Skripka, L. Labrador-Páez, F. Sanz-Rodríguez, P. Haro-González, D. Jaque, F. Rosei and F. Vetrone, *Nanoscale*, 2018, **10**, 791-799.
6. B. Y. W. Hsu, M. Wang, Y. Zhang, V. Vijayaragavan, S. Y. Wong, A. Y.-C. Chang, K. K. Bhakoo, X. Li and J. Wang, *Nanoscale*, 2014, **6**, 293-299.
7. N. Bogdan, F. Vetrone, G. A. Ozin and J. A. Capobianco, *Nano Letters*, 2011, **11**, 835-840.

5.2 Silica shell stabilized NCs for improved drug delivery

Silica Shell Stabilized Nanocapsules for Fluorescence-Enhanced and Nuclear-Targeted Drug Delivery

Nanocapsules Stabilisées par Coque de Silice pour l'administration de Médicaments à Fluorescence et à Visée Nucléaire

Yu Zhang,[†,‖] **Miao Wang**,[§,‖] Grace H. B. Ng,[††,‖] Mingyan Tan,[†] Siew Yee Wong,[†] Cathleen Teh,[††] Alex Yuang-chi Chang,[‡] Federico Rosei,[§] John Wang, [‡‡] Fiorenzo Vetrone,[*,§] and Xu Li,[*,†]

[†] Institute of Materials Research and Engineering, A*STAR, 2 Fusionopolis Way, Innovis, Singapore 138634

[§] Institut National de la Recherche Scientifique (INRS), Centre Énergie, Matériaux et Télécommunications, Université du Québec, J3X 1S2 Varennes (QC), Canada

[††] Institute of Molecular and Cell Biology, A*STAR, 61 Biopolis Drive, Proteos, Singapore 138673

[‡‡] Department of Materials Science & Engineering, Faculty of Engineering, National University of Singapore, Singapore 117576

[‡] Department of Oncology, Johns Hopkins University, Baltimore, Maryland, USA

‖, the authors have the same contributions to the publication.

In preparation.

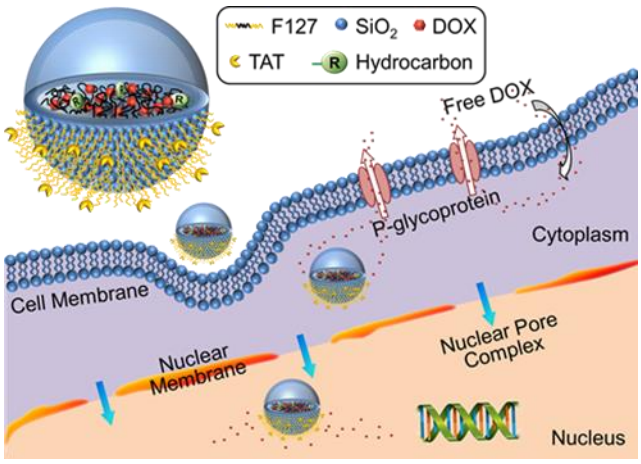

To further demonstrate the capacity of the NCs for active target drug delivery, we conjugated a nuclear-targeted agent (TAT peptide) to the PEO corona of the NCs, facilitating the nuclear penetration of the payloads. Doxorubicin (DOX), a conventional chemotherapy drug, is chosen as a model drug in this paper. DOX works in part by interfering with the function of DNA. Multidrug resistance caused by the inefficient drug delivery to cancer cells is one of the obstacles to the effective cancer treatment. Nuclear-targeted delivery systems are

allowed for improving the nuclear-distribution of DOX and reducing systemic side effects. Moreover, DOX can act as a fluorescence marker because of its inherent fluorescence property, allowing for tracing itself in the targeted cells without introducing additional fluorescence dyes. However, we noticed that the fluorescence of encapsulated DOX was quenched due to the self-aggregation of DOX molecules at high local concentrations. To this end, we established a hydrocarbon modification approach to prevent the aggregation-caused fluorescence quenching, in which organosilica such as TMPES, are introduced to the inner surface of silica shell. These hydrocarbons interact with the encapsulated DOX molecules through the hydrophobic and/or π-π stacking, and therefore inhibit the self-aggregation of DOX, even in the high loading concentrations. The hydrocarbon modification approach also shows a good generality to prevent the fluorescence quenching when extending to other planar aromatic cargoes (*e.g.* coumarin and rhodamine dyes). With the help of this delivery system, DOX is more efficiently delivered and accumulated in the nuclei, which is simultaneously demonstrated by its enhanced fluorescence imaging, and the growth inhibition of DOX against cancer cells is therefore significantly improved, especially in DOX-resistant cancer cells. This study demonstrates that the developed NCs can be modified with more functionalities for improved theranostic delivery.

Silica Shell Stabilized Nanocapsules for Fluorescence-Enhanced and Nuclear-Targeted Drug Delivery

Yu Zhang,[†,‖] Miao Wang,[§,‖] Grace H. B. Ng,[††,‖] Mingyan Tan,[†] Siew Yee Wong,[†] Cathleen Teh,[††] Alex Yuang-chi Chang,[‡] Federico Rosei,[§] John Wang, [‡‡] Fiorenzo Vetrone,[,§] and Xu Li,*[,†]*

[†] Institute of Materials Research and Engineering, A*STAR, 2 Fusionopolis Way, Innovis, Singapore 138634

[§] Institut National de la Recherche Scientifique (INRS), Centre Énergie, Matériaux et Télécommunications, Université du Québec, J3X 1S2 Varennes (QC), Canada

[††] Institute of Molecular and Cell Biology, A*STAR, 61 Biopolis Drive, Proteos, Singapore 138673

[‡‡] Department of Materials Science & Engineering, Faculty of Engineering, National University of Singapore, Singapore 117576

[‡] Department of Oncology, Johns Hopkins University, Baltimore, Maryland, USA

ABSTRACT: Multidrug resistance caused by the inefficient drug delivery to cancer cells is one of the major obstacles to the effective cancer treatment. Nuclear-targeted delivery systems are allowed for improving the nuclear-distribution of chemotherapeutic drugs and reducing systemic side effects. Here we established an original nuclear-targeted nanocapsule based on silica shell stabilized polymeric micelles by modified interfacial templating condensation approach, using a triblock co-polymer, PEO-PPO-PEO as templating agent and TMOS as silica precursors. Nuclear-targeted agents (TAT peptide) are conjungated to the PEO block of the nanocapsules facilitating nuclear penetration. Doxorubicin (DOX), a convetional chemotherapy drug is selected as a model drug to be encapsulated inside the nanocapsules. Importantly, DOX can act as a fluorescence marker because of its inherent fluorescence

property, allowing for tracing itself in the targeted cells without introducing additional fluorescence dyes. However, we noticed that the fluorescence of encapsulated DOX was quenched due to the self-aggregation of DOX molecules at high local concentrations. To prevent the aggregation-caused fluorescence quenching, we introduced hydrocarbon groups to the inner surface of silica shell. These hydrocarbons interact with the encapsulated DOX molecules through the hydrophobic and/or π-π stacking, and therefore inhibit the self-aggregation of DOX, even in the high larding cencentrations. The hydrocarbon modification approach also shows a good generality to prevent the fluorescence quenching when extending to other planar aromatic cargoes (*e.g.* coumarin and rhodamine dyes). With the help of this delivery system, DOX is more efficiently delivered and accumulated in the nuclei, which is simultaneously demonstrated by its enhanced fluorescence imaging, and the growth inhibition of DOX against cancer cells is therefore significantly improved, especially in DOX-resistant cancer cells. This study provides an effective path to encompass various diagnostic and therapeutic agents for improved targeted drug delivery.

Introduction

Multidrug resistance is one of the main problems encountered in cancer chemotherapy, especially in metastatic cancers for which chemotherapy acts as the most effective treatment.[1–3] Transporters, typically P-glycoprotein over-expressed in the membrane of cancer cells, are the main cause responsible for the development of multidrug resistance, by expelling anticancer drugs and preventing them from accessing the cells. Drug delivery systems have been reported to be able to bypass the P-glycoprotein, accumulate in the cell cytoplasm and ultimately release the drugs there.[1] However, these drugs that have entered the cytoplasm will still be constantly pumped out of the cell by the P-glycoprotein efflux pump. Therefore, subcellular-targeted systems to deliver the drugs is poised to overcome multidrug resistance since they can enter and directly release the drugs in the organelle and thus mitigate multidrug resistance.[3–5]

Nuclear-targeted drug delivery systems are important for overcoming the multidrug resistance problems associated with some typical anticancer drugs, such as doxorubicin (DOX), camptothecin and cisplatin, the therapeutic effects of which take place in cell nuclei. So far, improvement in the anticancer efficacy of nuclear-targeted drug delivery systems is much less satisfactory primarily because of insufficient nucleus uptake.[6–9] The nuclear entrance of such systems is a strong size-dependent process with high selectivity, as limited by the nuclear pore complexes that are of tens nanometer in size and embedded in the nuclear envelop. Naturally, small molecules (*e.g.* water and ions) as well as macromolecules smaller than ~9 nm are able to pass through the nuclear pore complexes and ultimately enter the nucleus. However, drug delivery systems in this size range are susceptible to renal excretion and unintentional vascular leakage into non-targeted sites. On the other hand, those larger than ~9 nm, but smaller than the channel size of the nuclear pore complexes, are only able to cross through the nuclear envelop at almost negligible rates unless they bear a nuclear localization signal, which is a sequence of amino acids that can bind and pass through the nuclear pore complexes. In the past few years, various biocompatible nanocarriers (*e.g.* polymers, liposomes and mesoporous silica) decorated with nuclear localization signal peptides (*e.g.* SV40 T antigen, TAT peptide and adenoviral) have been well studied for nuclear-targeted drug delivery.[1,3,5,6,10,11] Conjugation of nuclear localization signal peptides to nanocarriers has made a great leap for nuclear delivery of intact nanocarrier. However it does not address the problem caused by the nanocarrier itself, for example, drugs loaded in the pores of mesoporous silica leak into non-targeted tissues or most leaked drug is trapped in the cell cytoplasm of targeted tissues, therefore hamper the drugs' nuclear localization. [6–9]

Silica shell stabilized polymeric micelles (denoted as Si-PMs) represent a type of delivery system that have gained rapid development in recent years because of their promising potential in medical diagnostics and therapy.[12,13] They are typically synthesized through single micelle

templating, a versatile platform for the synthesis of ultrasmall silica-based hybrid nanocarriers with tunable sizes between 5–30 nm. Nanoparticles within this size range are favorable for passive cell uptake and endosome escape, which benefits for nuclear delivery of intact nanocarriers.[6] In addition, the silica shell grown at the interface of hydrophobic core and hydrophilic corona of micelle template will stabilize the polymeric micelles without leakage of loaded drug from the micelles. To the best of our knowledge, there have been no reports on Si-PMs for nuclear-targeted delivery. In this study, ultrasmall Si-PMs have been developed by growing silica shell at the interface of poly(propylene oxide) (PPO) hydrophobic core and the poly(ethylene oxide) (PEO) hydrophilic corona of F127 micelle template. The dense outer layer of PEO chains provide stealth protection against early recognition by the reticuloendothelial system (RES) and prolong blood circulation.[14] Chemotherapy drugs are encapsulated into the PPO core and silica shell prevents the leakage of the drug from the Si-PMs. TAT peptide is conjugated to the PEO corona, facilitating nuclear penetration.[5]

DOX is a conventional chemotherapy drug for the treatment of many types of cancer. It works in part by interfering with the function of DNA. Primary and/or developed resistance to DOX is a major obstacle to the effective cancer treatment.[15] Nuclear-targeted delivery systems are thus required for DOX providing stealth capabilities and improving its bio-distribution with reduced systemic side effects. To demonstrate the capacity of Si-PMs for nuclear delivery against multidrug resistance, DOX was chosen as a model drug in this study. More important, DOX can act as a fluorescence marker because of its inherent fluorescence property, to trace itself in the targeted cells without introducing additional fluorescence dyes. In fact, it is highly advantageous to observe the trafficking of the delivered payloads of a targeted delivery system. However, fluorescence quenching is a common problem associated with encapsulation of fluorophores and self-fluorescent drugs like DOX. This is largely due to collisional quenching (*e.g.* by aqueous dissolved oxygen or ions), complex-formation (*e.g.* formation of non-

fluorescent self-aggregates by π–π stacking at high local concentration) and energy transfer (*e.g.* energy hopping to self-aggregates or quenchers).[16,17] With this regard, we introduced various types of hydrocarbon groups to covalently bond to the silica shell of Si-PMs through co-condensation of organosilanes and silanes, for the first time, investigated their influence on the fluorescence quenching of the encapsulated DOX, in terms of chain length, bulkiness and concentration of the hydrocarbon groups. We successfully demonstrated that the enhanced fluorescence of encapsulated DOX can be achieved by inhibiting its self-aggregation through hydrophobic and/or stacking π-π interactions between the DOX molecules and hydrocarbons. Here, we established an original hybrid Si-PMs drug delivery system encapsulated with DOX. It demonstrated the ability of targeted nuclear delivery against multidrug resistance, as well as the enhanced fluorescence of DOX for imaging tracking. Such fluorescence enhancement effect is further demonstrated to be applicable to other planar aromatic dyes (*e.g.* coumarin 545T and rhodamine 101) for diagnostic applications.

Results and discussion

Synthesis and Structure Characterization of Si-PMs. Endowing nanostructured silica with organic functionalities has been an elegant method towards the development of nanohybrid structures with cooperative and synergetic functionalities from both components. The organosilane modification of silica, covalently bonding organic groups to silica typically through the co-condensation or post-synthetic grafting method,[13] has been widely employed to increase the hydrophobicity and thus the affinity of silica to hydrophobic cargoes such as drugs[18,19] and dyes.[20] It enables the nanostructured silica with higher loading capacity coupled with slower release of hydrophobic drugs or reduced leakage of fluorescent dyes due to the interaction between the introduced organic groups and hydrophobic cargoes.[18–20] In the present study, hydrocarbons including methyl (Me), propyl (Pr), octyl (Oc) and 2-phenylethyl (Ph) groups are covalently bonded to the silica shell of the Si-PMs through co-condensation of the

respective organosilanes and silanes with F127 micelle as a template. The structure of the developed Si-PMs is schematically illustrated in Figure 1a. It consists of a PPO core, an interfacial thin silica shell and a PEO corona. Hydrophobic cargoes like DOX are encapsulated in the PPO core. During the one-pot micelle template co-condensation, hydrocarbons from organosilanes are expected to grow in the silica framework but mainly located at the inner surface of silica shell protruding into the PPO core due to compatibility matching between the hydrophobic PPO core and hydrocarbons.

TEM micrographs of the Si-PMs containing DOX (DOX@Si-PMs) are shown in Figure 1b–f. Typical nanocapsule morphology was observed with a bright-colored interior cavity composed of PPO chains and DOX molecules surrounded by a dark-colored silica shell. The DOX@Si-PMs were uniform in size (10-15 nm in diameter) with ultrathin silica shells (3-5 nm in thickness). Without hydrocarbon modification, slight aggregation of DOX@Si-PMs was observed (Figure 1b). The intensity-average hydrodynamic size measured by dynamic light scattering (DLS) confirms the aggregation of the DOX@Si-PMs, with an average

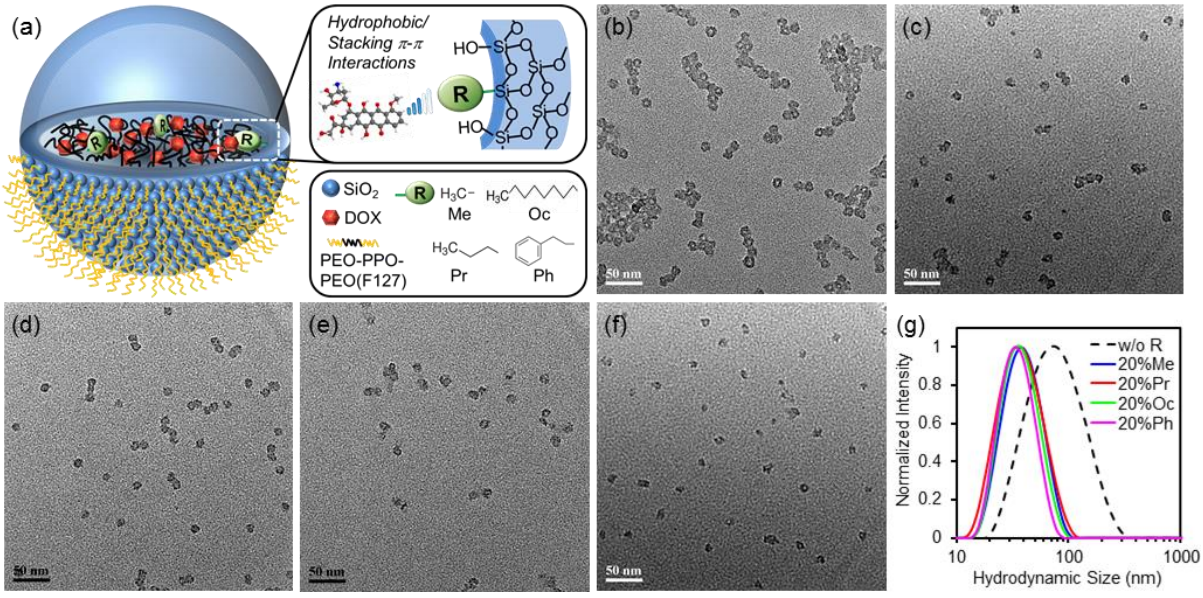

Figure 1. (a) Schematic illustration of the DOX@Si-PMs. (b)–(f) TEM micrographs of the DOX@Si-PMs modified with hydrocarbons: (b) w/o R (without hydrocarbon modification), (c) 20%Me, (d) 20%Pr, (e) 20%Oc and (f) 20%Ph. 20% represents the volume percentage of the organosilanes in the total silica precursors. (g) DLS curves of the aqueous suspensions of DOX@Si-PMs.

hydrodynamic size of ~80 nm (Figure 1g), which is much larger than that of an individual DOX@Si-PMs measured under TEM. After hydrocarbon modification, the DOX@Si-PMs were well dispersed (Figure 1c–f) and their hydrodynamic sizes decreased to ~35 nm (Figure 1g), comparable with that of pure F127 micelles (20 to 30 nm). It indicates the role of F127 micelle as a template to produce individual DOX@Si-PMs. The well dispersion of hydrocarbon modified DOX@Si-PMs with comparable hydrodynamic size as that of F127 micelle is attributed to the non-reactivity and steric hindrance of the hydrocarbons in the silica shell that reduce interparticle attraction of DOX@Si-PMs.[21,22] The size difference measured by TEM and DLS indicates the presence of free PEO chains dangled from DOX@Si-PMs, which however, cannot be observed by TEM because of the low contrast of the PEO moieties by the electron beam.

More TEM micrographs of the hydrocarbon modified DOX@Si-PMs are shown in Figure S1a–c, where the amount of hydrocarbon Ph is increased from 10 to 30% (Figure S2). The fabricated DOX@Si-PMs with 10%Ph were observed to still aggregate to a certain degree (Figure S1a) with a DLS size of ~55 nm (Figure S1d). With 20%Ph and above, the DOX@Si-PMs became well dispersed (Figure 1f and S1b–c), where the DLS sizes decreased to ~35 nm (Figure S1d).

Fluorescence Enhancement in DOX@Si-PMs. Quantum yield (QY) of DOX encapsulated in the DOX@Si-PMs with and without hydrocarbon modification was calculated based on the

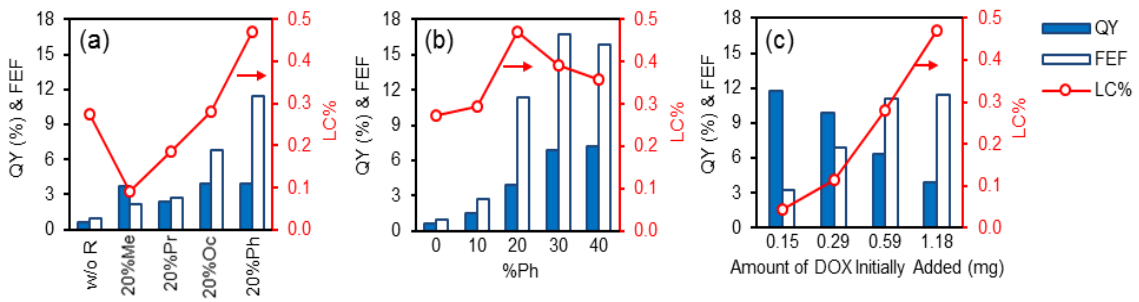

Figure 2. Variation of QY, fluorescence enhancement factor (FEF) and loading content (LC%) of DOX in DOX@Si-PMs with (a) type of hydrocarbons, (b) %Ph and (c) amount of DOX initially added. In (a) and (b), the amount of DOX initially added was fixed at 1.18 mg. In (c), the DOX@Si-PMs were modified with 20%Ph.

absorption and fluorescence (λ_{ex} = 480 nm) spectra data (Supporting information). From Figure 2 & Table S1, the QY of the DOX@Si-PMs without hydrocarbon modification is as low as 0.59%, indicating a serious fluorescence quenching that is ascribed to dimerization of the encapsulated DOX molecules when they are within close proximity to each other in a small compartment.[15,23] These dimers are non-fluorescent and also act as traps for energy transfer between DOX moleculaes.[15] With hydrocarbon modification, the QY of the DOX@Si-PMs increases to the range of 1.51–11.73%, manipulated by chemical structure and concentration of the hydrocarbon groups, as well as the amount of DOX initially added.

In order to understand the fluorescence enhancement mechanism, the visible absorption spectra were measured and are shown in Figure 3a. All three bands with the maxima located at 480, 504 and 540 nm, respectively, are assigned to DOX.[15] The introduction of hydrocarbon into silica shell does not change the band position but the shape of the spectra. As compared to the DOX@Si-PMs without hydrocarbon modification, where the 480 and 504 nm bands are of equal in intensity, the DOX@Si-PMs samples modified with hydrocarbons show that the relative intensity of 504 nm band to that of the 480 nm band increases when the content of hydrocarbon is increased. The intensity of 540 nm band follows the same trend as that of the 504 nm band. The ratio of absorption intensity at 504 nm to that at 480 nm (Abs_{504}/Abs_{480}) against hydrocarbon content is shown in Figure 3b. It reveals an increasing trend of Abs_{504}/Abs_{480} with increasing hydrocarbon content. According to previous reports[15,24] and our control test (Figure S3), a higher Abs_{504}/Abs_{480} ratio correlates with a lower dimerization degree of DOX. This indicates that the form of DOX dimers is limited in the presence of hydrocarbons. Likewise, the Abs_{504}/Abs_{480} ratio increases with increasing the chain length and bulkiness of the hydrocarbons (Figure 3c) or less content of DOX loaded initially (Figure 3d), both indicating an increasing proportion of monomers as compared to dimers. The QY enhancement was thus considered to correlate with variation of the degree of dimerization of

DOX in Si-PMs, which is supported by the proportional relationship between QY and Abs_{504}/Abs_{480} as demonstrated in Figure 3e.

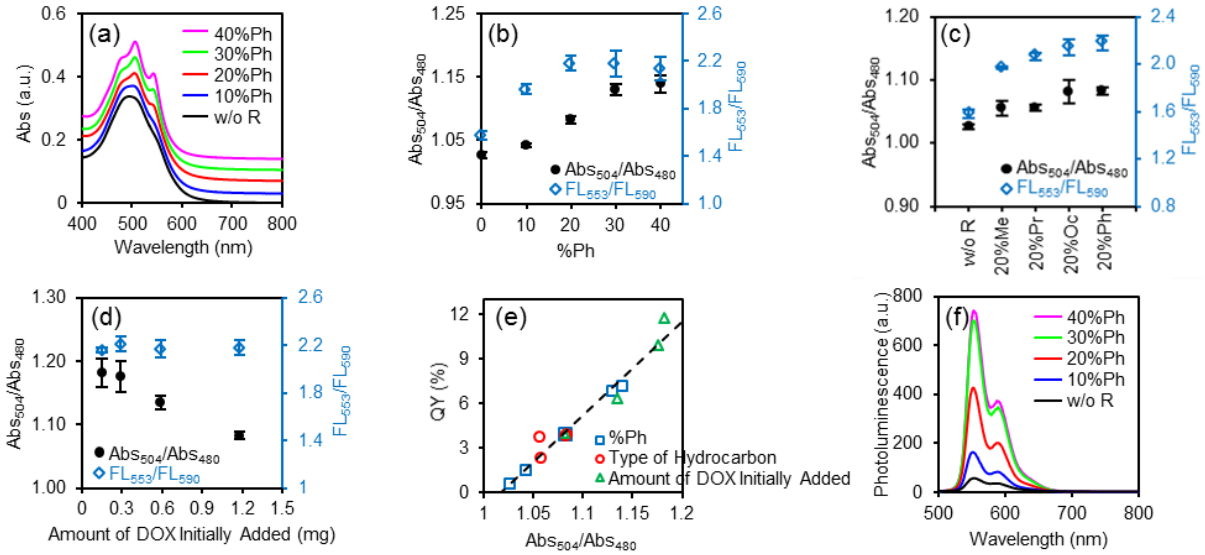

Figure 3. (a) Absorption spectra of the aqueous suspensions of DOX@Si-PMs. The curves were vertically shifted for better visualization. Variation of the ratios of Abs_{504}/Abs_{480} (black symbols) and FL_{553}/FL_{590} (blue symbols) with (b) %Ph, (c) type of hydrocarbons and (d) amount of DOX initially added. In (b) and (c), the amount of DOX initially added was fixed at 1.18 mg. In (d), the DOX@Si-PMs were modified with 20%Ph. (e) Relationship between QY and Abs_{504}/Abs_{480}. (f) Photoluminescence spectra of the aqueous suspensions of DOX@Si-PMs. In (a) and (f), the concentration of DOX in all suspensions was fixed at 26 μm.

In general, stacked dimers of DOX dissociate into monomers upon dilution.[21] When DOX was encapsulated in Si-PMs, little variation was detected in the magnitude of the Abs_{504}/Abs_{480} upon dilution of the initial aqueous solutions (Figure S4), owing to the mechanically stable Si-PMs without dissociation to change the local concentration of encapsulated DOX. It is thus more reasonable to use the loading content (LC%) of DOX in DOX@Si-PMs, instead of the averaged concentration of DOX in water, to represent the effective DOX concentration. As shown in Figure 2a, when the DOX@Si-PMs were modified with short and less hydrophobic hydrocarbons (*e.g.* Me and Pr), their DOX LC% was lower than that in the DOX@Si-PMs without hydrocarbon modification. It appears to contradict the earlier claim that the hydrocarbons are able to increase cargo loading,[18–20] This is because, during the formation of DOX@Si-PMs, the organosilanes prefer to reside and react more deeply in the micelle and

even in the PPO core due to the hydrophobic nature of hydrocarbons,[22] generating a smaller cavity inside the silica shell and thus decreasing the DOX loading capacity. Our TEM observations confirm this (Figure 1c–f). A "dilution"-like effect was thus expected in the Me and Pr-modified DOX@Si-PMs associated with a reduction in the degree of dimerization. It leads to an impressive increase in the Abs_{504}/Abs_{480} ratio and QY.

However, it cannot explain the increase in the Abs_{504}/Abs_{480} ratio and QY for the DOX@Si-PMs modified with Oc and Ph. The DOX LC% was greatly increased when the DOX@Si-PMs were modified with long, bulky and more hydrophobic hydrocarbons (*e.g.* Oc and Ph). Other mechanisms in addition to the "dilution"-like effect (*i.e.* concentration effect) that affect the degree of dimerization of the encapsulated DOX must be occurring. As reported previously, anchoring hydrocarbon functionalities to silica is able to enhance the interaction between the nanocarrier and the encapsulated cargo.[18,25] The reduced dimerization of DOX when the hydrocarbons become longer, more bulky and more hydrophobic, appears to be a consequence of the increased hydrophobic and/or stacking π-π interactions between the hydrocarbons and the anthraquinone ring of DOX as shown in Figure 1a. This can influence the electronic structure of the DOX molecules and suppress the side-by-side stacking aggregation of the planar aromatic rings of DOX.

In order to explore this, the photoluminescence spectra of the DOX@Si-PMs were measured and are shown in Figure 3f. Two principal fluorescence emission bands with maxima at 553 and 590 nm are assigned to DOX.[15] As reported previously,[26] the ratio of fluorescence intensity at these two wavelengths (FL_{553}/FL_{590}) can be used to assess the microenvironment of the encapsulated DOX and their interactions with the nanocarrier.[26] For the DOX@Si-PMs without hydrocarbon modification, the FL_{553}/FL_{590} ratio was 1.58 ± 0.04 (Figure 3c), much higher than that of free DOX in water (1.10 ± 0.02) (Figure S5). Such a remarkably large increase in the ratio of FL_{553}/FL_{590} is ascribed to the encapsulation of DOX in a much more hydrophobic PPO

domain in Si-PMs.[26] The FL_{553}/FL_{590} ratio further increased with the increasing chain length and bulkiness of the hydrocarbons (Figure 3c). It reflects increasing hydrophobic interactions between the nanocarrier and DOX.

As shown in Figure 2b, the DOX LC% in DOX@Si-PMs initially increases and reaches a maximum at 20%Ph modification, consistent with the expectation that a silica shell of higher hydrophobicity has a higher affinity to the hydrophobic DOX.[18,19] Beyond this range, a pronounced decrease in the DOX loading is observed for the DOX@Si-PMs modified with 30–40%Ph. Accordingly, the FL_{553}/FL_{590} ratio increases and plateaus at ~2.2 with increasing the hydrocarbons content (Figure 3b). The saturation level of the FL_{553}/FL_{590} ratio indicates a maximum amount of hydrocarbons capable of residing at the inner layer of silica shell and directly facing the encapsulated DOX. Excessive hydrocarbons distributed at the outer layer of the silica shell can contribute negligibly to the hydrophobic interactions. The decrease in the DOX loading for the DOX@Si-PMs modified with 30–40%Ph is thus ascribed to a decreased cavity capacity as confirmed by Figure S1b–c. As a result, for the DOX@Si-PMs modified with 10–20%Ph, the Ph substituents were effective to interact with the encapsulated DOX and suppress the self-aggregation of DOX. When the Ph content is higher than 20%, the hydrophobic and/or stacking π-π interactions become saturated, but their DOX loading declined causing further increases in QY.

In addition, the LC% of DOX in the DOX@Si-PMs followes an expected increasing trend with the amount of DOX initially added (Figure 2c), associated with decreased Abs_{504}/Abs_{480} ratios (Figure 3d). The FL_{553}/FL_{590} ratio is almost unaltered because of the identical DOX@Si-PMs nanocarriers involved.

All in all, the introduction of hydrocarbons prevent DOX from self-aggregation, resulting in the enhanced fluorescence. It either affects the DOX loading amount in DOX@Si-PMs or increases the hydrophobic and/or stacking π-π interactions with the DOX molecules. Besides,

a silica shell of higher hydrophobicity can work better for blocking oxygen and water from penetration and inhibiting the collisional quenching.[27]

Here it is worth stressing the significance of the studied hydrocarbon modification strategy in enhancing fluorescence emission. To date approaches against fluorescence quenching in conventional fluorescent silica nanoparticles include: formation of an additional silica shell to better block water and reactive species from penetration,[21,22] spatial control of dye molecules in the core area of silica by reducing the dye loading,[27] metal-enhanced fluorescence,[20,28–32] and Förster resonance energy transfer.[33] These strategies rely on controlling the concentration and spatial distribution of the fluorophore molecules in silica. However, they are not applicable to nanoparticles heavily loaded with fluorophores, where controlling the spatial distance between the incorporated fluorophores is challenging and, therefore, they suffer from the notorious problem of aggregation-caused quenching. In contrast, the hydrocarbon modification strategy has the dual benefit of simultaneously increasing both the cargo loading and QY, as what we observed for the DOX@Si-PMs modified with Oc and Ph. A fluorescence enhancement factor (FEF) was thus defined with the formula of $FEF = \frac{QY_X \times LC\%_X}{QY_{ref} \times LC\%_{ref}}$ to quantify the fluorescence brightness enhancement, where QY is the quantum yield, LC% is the loading content of DOX in DOX@Si-PMs, the subscript *X* denotes samples under investigation, and *ref* denotes the reference sample of DOX@Si-PMs without hydrocarbon modification. The FEF results shown in Figure 2 demonstrate increases up to 16.8 fold with the hydrocarbon modification. This is particularly important for DOX encapsulation to achieve both high drug loading and strong fluorescence brightness.

To further demonstrate that the hydrocarbon modification strategy can be applied to other fluorescent systems, we also investigated other aromatic dyes that are prone to self-association, for example, coumarin545T and rhodamine101. The dye loading, as indicated from the absorbance intensity shown in Figure S6a–b, increased by 6.3 times for coumarin545T and 3.2

times for rhodamine101 when the Si-PMs were modified with 20%Ph. At the same time, the QY of the Si-PMs modified with 20%Ph was also significantly increased (Figure S6c).

To demonstrate the application of hydrocarbon modified DOX@Si-PMs for tracking nuclear delivery of DOX, three samples, namely free DOX, DOX@Si-PMs and DOX@Si-PMs-20%Ph were evaluated with HeLa cervical cancer cells as fluorescence imaging markers. Free DOX is observed mostly in the nuclei (Figure 4a), demonstrating free DOX passively diffuse to the nuclei. Both DOX@Si-PMs and DOX@Si-PMs-20%Ph are located in the cytoplasm and the perinuclear region (Figure 4b–c) because the nanocarriers are too big to cross through the nuclear pore freely. It indicates less DOX is released from the nanocarriers in the cytoplasm also. Otherwise, the released DOX will diffuse to nuclei to stain them. DOX in the DOX@Si-PMs-20%Ph showed a much stronger fluorescence in the cytoplasm region than that in the DOX@Si-PMs. However, there was little difference in their cytotoxicity to HeLa cells (Figure S7). The DOX@Si-PMs-20%Ph were even slightly less cytotoxic than the DOX@Si-PMs

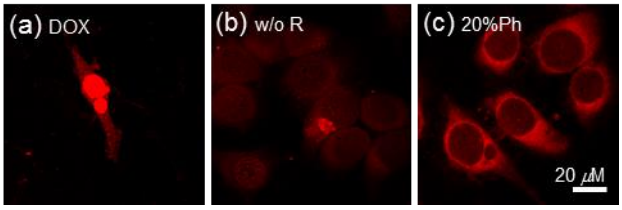

Figure 4. Confocal luminescence images of HeLa cells cultured for 24 hours in the presence of (a) free DOX, (b) DOX@Si-PMs and (c) DOX@Si-PMs-20%Ph. (b) and (c) have similar DOX LC% (0.27 and 0.28, respectively) but different QY (0.59 and 6.34%, respectively). The dosage of DOX in (a)–(c) is 10 μM.

without hydrocarbon modification. The much higher fluorescence brightness observed for the DOX@Si-PMs-20%Ph is thus more likely a consequence of the fluorescence enhancement effect from hydrocarbon modification instead of increased cellular uptake. Figure S7 also shows that both DOX@Si-PMs and DOX@Si-PMs-20%Ph were less cytotoxic than free DOX. This is because most of DOX in the DOX@Si-PMs and DOX@Si-PMs-20%Ph are still located in the nanocarriers in the cytoplasm (Figure 4b–c).

Overcoming Multidrug Resistance by TAT-Conjugated DOX@Si-PMs. TAT includes a nuclear localization signal peptide sequence that can bind to import receptors (*e.g.* importin α

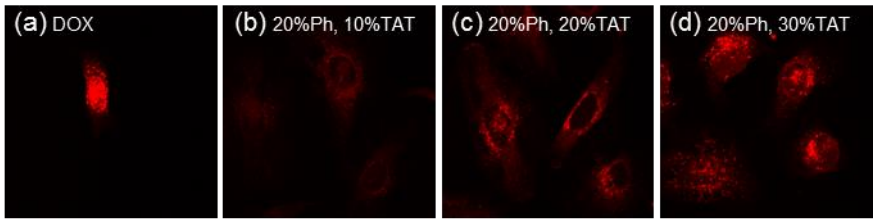

Figure 5. Confocal luminescence images of HeLa cells cultured for 24 hours in the presence of (a) free DOX and (b)–(d) TAT conjugated DOX@Si-PMs-20%Ph with (b) 10%TAT, (c) 20%TAT and (d) 30%TAT. The dosage of DOX is 5 μM.

and β) in cytoplasm and in turn bind to the nuclear pore complexes to facilitate entering nuclei.[5] In order to enhance the therapeutic efficacy of DOX@Si-PMs, DOX@Si-PMs-20%Ph, as an example, were further conjugated with varied amounts of TAT for nuclear-targeted delivery. The TAT-conjugated DOX@Si-PMs-20%Ph were then incubated with HeLa cells and their cellular uptake and subsequent localization are shown in Figure 5. Again, free DOX easily entered the nucleus by showing a strong red contrast in the entire region of the nucleus (Figure 5a). For the TAT-conjugated DOX@Si-PMs-20%Ph (Figures 5b–d), TAT facilitated the intranuclear accumulation. More scattered red spots were present in the nuclear region with increasing TAT content. When the content of TAT at the surface of DOX@Si-PMs-20%Ph increased, there was a higher chance for the nanocarriers to bind to import receptors and subsequently target the nuclear pore complexes, leading to increased nuclear uptake.[35] A z-scan study in Figure S8 further confirms the internalization of TAT conjugated DOX@Si-PMs-20%Ph nanocarriers in nuclei with the concurrence of scattered red spots in nuclei and cytoplasm through depth.

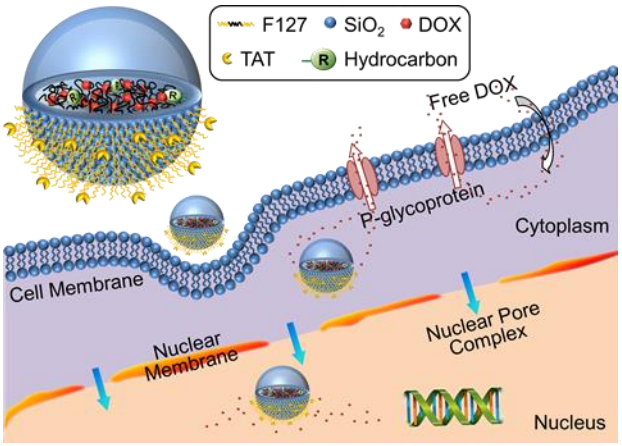

Scheme 1. Nuclear Transport of TAT-Conjugated DOX@Si-PMs to Overcome Multidrug Resistance for Nuclear Imaging and Intranuclear Anticancer Drug Delivery.

With the nuclear targeting capability, the TAT-conjugated DOX@Si-PMs-20%Ph were further assessed for their performance against drug resistance in a human ovarian cancer cell line A2780 and its DOX-resistant counterpart of A2780/ADR. P-glycoprotein transporters are over-expressed in the membrane of A2780/ADR cells (Scheme 1) therefore, they expel both free and released DOX out of the cells. As a result, a nanocarrier that can enter the nucleus and directly release the drugs in the nucleus is highly desirable.

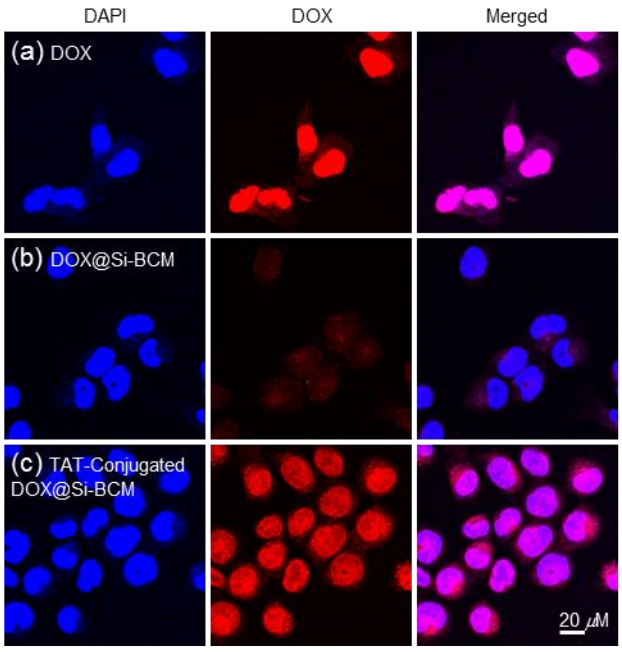

Figure 6. Confocal luminescence images of A2780 cells cultured for 24 hours in the presence of (a) free DOX, (b) DOX@Si-PMs-20%Ph and (c) TAT-conjugated DOX@Si-PMs-20%Ph (30%TAT). The red fluorescence is from DOX, and the blue fluorescence is from 4,6-diamidino-2-phenylindole (DAPI) used to stain the nuclei. The dosage of DOX is 5 μM.

The resistance of A2780 and A2780/ADR cells to free DOX was assessed by MTT assay. As shown in Figure S9, DOX showed dose-dependent cytotoxicity to A2780 cells, but little cytotoxicity to A2780/ADR cells. More than 85% of A2780/ADR cells can survive even at a relatively high DOX dosage of 8 μM, suggesting strong drug resistance to free DOX. Three samples, namely free DOX, DOX@Si-PMs-20%Ph and TAT-conjugated DOX@Si-PMs-

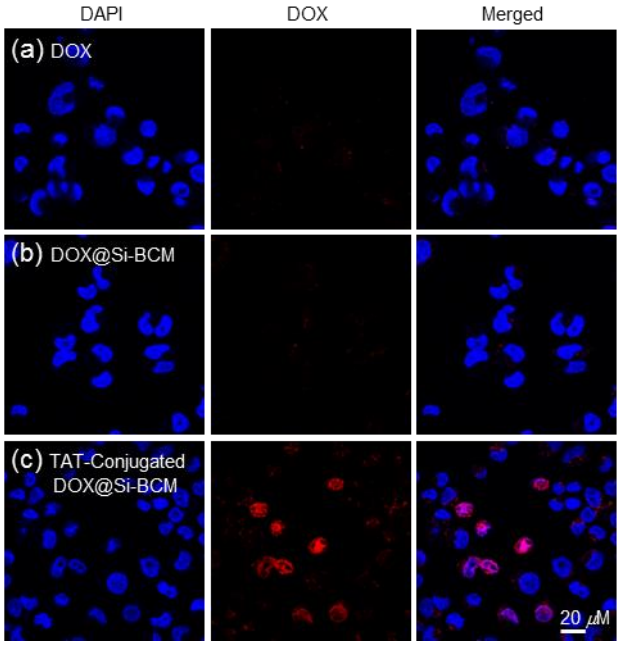

Figure 7. Confocal luminescence images of A2780/ADR cells cultured for 24 hours in the presence of (a) free DOX, (b) DOX@Si-PMs-20%Ph, and (c) TAT-conjugated DOX@Si-PMs-20%Ph (30%TAT). The red fluorescence is from DOX, and the blue fluorescence is from DAPI used to stain the nuclei. The dosage of DOX is 5 μM.

20%Ph, were incubated with A2780 and A2780/ADR cells, respectively, for 24 hours at an equivalent DOX dosage of 5 μM and were analyzed by confocal imaging (Figure 6–7). The DOX@Si-PMs-20%Ph has a low negative surface charge density of -0.84 ± 0.17 mV. The positive shift in the zeta potential of TAT-conjugated DOX@Si-PMs-20%Ph (30% TAT) (3.51 ± 0.09 mV) is consistent with the grafting of TAT peptides of cationic nature on its surface.

In the case of A2780 cells (Figure 6), DOX was mostly localized in the nuclei with a small amount in the cytoplasm. DOX@Si-PMs-20%Ph showed relatively weak red fluorescence in both the cytoplasm and the nuclei, indicating poor uptake of the nanocarriers in A2780 cells.

When TAT was conjugated to DOX@Si-PMs-20%Ph, red fluorescence was greatly increased. The red fluorescence of DOX and the blue fluorescence of DAPI overlapped well for the TAT-conjugated DOX@Si-PMs-20%Ph and an obvious purple signal was observed in the merged image of A2780 cells. It indicates an efficient TAT-mediated nuclear accumulation, after which DOX could be released within the nuclei directly and sustainably. The cytotoxicity was then investigated by MTT assay (see Figure 8). DOX, DOX@Si-PMs-20%Ph and TAT-conjugated DOX@Si-PMs-20%Ph were all potent to inhibit proliferation of A2780 cells. The DOX@Si-PMs-20%Ph had the worst anticancer activity among these three samples, which agrees well with the confocal observations. With the help of TAT, the anticancer activity was greatly increased and even better than free DOX (Figure 8).

In the case of A2780/ADR cells (Figure 7), a red signal was hardly detected in the drug resistant cancer cells treated with free DOX because of the multidrug resistance mediated by the P-glycoprotein efflux pumps. DOX@Si-PMs-20%Ph is able to bypass the drug efflux pumps with the protection of Si-PMs. However, without the help of TAT, it is difficult to pass through the nuclear pore and release DOX inside of nuclei. As a result, both free DOX and DOX@Si-PMs-20%Ph exhibit negligible cytotoxicity against A2780/ADR cells, with more than 90% of cells survived at a DOX dosage of 5 μM (Figure 8). In contrast, TAT-conjugated DOX@Si-PMs-20%Ph (30%TAT) significantly promote the nuclear accumulation of DOX in

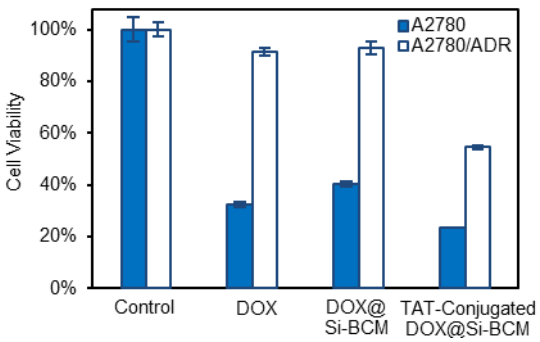

Figure 8. Viability of A2780 and A2780/ADR cells cultured in the presence of free DOX, DOX@Si-PMs-20%Ph and TAT-conjugated DOX@Si-BCMs-20%Ph (30%TAT) respectively for 1 day. The dosage of DOX is 5 μM.

A2780/ADR cells (Figure 7c), thus increase its therapeutic efficacy with cell viability reduced to 54.5% (Figure 8).

Conclusion

In summary, Si-PMs have been successfully developed for fluorescence-enhanced and nuclear-targeted drug delivery. By modifying the silica shell with organic hydrocarbons, the Si-PMs possess reinforced hydrophobic and/or stacking π-π interactions with the encapsulated DOX, which inhibits self-association and thus prevents fluorescence quenching of the DOX molecules. As demonstrated, the hydrocarbon modification strategy works well with other dyes compatible with the synthesis environment, including for example, coumarin545T and rhodamine101, and it opens a new path for the design and development of fluorescence-enhanced nanocarriers. It provides combined features of simultaneously increasing the cargo loading and fluorescence brightness, and has demonstrated the potential uses in cellular imaging. A further TAT conjugation makes Si-PMs suitable for direct intranuclear drug delivery and helps the drug (DOX) overcome multidrug resistance and improves cytotoxicity dramatically. This study provides an effective way to encompass various diagnostic and therapeutic agents for improved targeted drug delivery.

ASSOCIATED CONTENT

Supporting Information. Detailed synthesis procedures, LC%, QY and FEF values of DOX in Si-PMs, TEM micrographs, DLS curves, FTIR spectra, absorbance and photoluminescence spectra, cell viability and confocal images.

AUTHOR INFORMATION

Corresponding Author

* vetrone@emt.inrs.ca

* x-li@imre.a-star.edu.sg

Author Contributions

‖, these authors contributed equally.

REFERENCES

1. Pan, L.; Liu, J.; He, Q.; Wang, L.; Shi, J. *Biomaterials* **2013**, *34*, 2719–2730.
2. Qiu, L.; Chen, T.; Öçsoy, I.; Yasun, E.; Wu, C.; Zhu, G.; You, M.; Han, D.; Jiang, J.; Yu, R.; Tan, W. *Nano Lett.* **2015**, *15*, 457–463.
3. Pan, Z.; Wang, H.; Zhang, M.; Lin, T.; Zhang, W.; Zhao, P.; Tang, Y.; Xiong, Y.; Zeng, Y.; Huang, Y. *Acta Pharmacol. Sin.* **2016**, *37*, 1110–1120.
4. Ma, X.; Gong, N.; Zhong, L.; Sun, J.; Liang, X. *Biomaterials* **2016**, *97*, 10–21.
5. Tammam, S. N.; Azzazy, H. M. E.; Lamprecht, A. *J. Control. Release* **2016**, *229*, 140–153.
6. Pan, L.; He, Q.; Liu, J.; Chen, Y.; Ma, M.; Zhang, L.; Shi, J. *J. Am. Chem. Soc.* **2012**, *134*, 5722–5725.
7. Wu, M.; Meng, Q.; Chen, Y.; Du, Y.; Zhang, L.; Li, Y.; Zhang, L.; Shi, J. *Adv. Mater.* **2015**, *27*, 215–222.
8. Xiong, L.; Du, X.; Kleitz, F.; Qiao, S. Z. *Small* **2015**, *11*, 5919–5926.
9. Han, S.; Li, Z.; Zhu, J.; Han, K.; Zeng, Z.; Hong, W.; Li, W.; Jia, H.; Liu, Y.; Zhuo, R.; Zhang, X. *Small* **2015**, *11*, 2543–2554.
10. Yu, Z.; Pan, W.; Li, N.; Tang, B. *Chem. Sci.* **2016**, *7*, 4237–4244.
11. Peng, H.; Tang, J.; Zheng, R.; Guo, G.; Dong, A.; Wang, Y.; Yang, W. *Adv. Healthc. Mater.* **2017**, *6*, 1601289.
12. Niu, D.; Li, Y.; Shi, J. *Chem. Soc. Rev.* **2017**, *46*, 569–585.
13. Zhang, Y.; Hsu, B. Y. W.; Ren, C.; Li, X.; Wang, J. *Chem. Soc. Rev.* **2015**, *44*, 315–335.

14. Zhao, L.; Yuan, W.; Ang, C. Y.; Qu, Q.; Dai, Y.; Gao, Y.; Luo, Z.; Wang, J.; Chen, H.; Li, M.; Li, F.; Zhao, Y. *Adv. Funct. Mater.* **2016**, *26*, 3036–3047.
15. Changenet-Barret, P.; Gustavsson, T.; Markovitsi, D.; Manet, I.; Monti, S. *Phys. Chem. Chem. Phys.* **2013**, *15*, 2937–2944.
16. Sokolov, I.; Volkov, D. O. *J. Mater. Chem.* **2010**, *20*, 4247–4250.
17. Geng, J.; Goh, C. C.; Qin, W.; Liu, R.; Tomczak, N.; Ng, L. G.; Tang, B. Z.; Liu, B. *Chem. Commun.* **2015**, *51*, 13416.
18. Doadrio, J. C.; Sousa, E. M. B.; Izquierdo-Barba, I.; Doadrio, A. L.; Perez-Pariente, J.; Vallet-Regí, M. *J. Mater. Chem.* **2006**, *16*, 462–466.
19. Vallet-Regí, M.; Balas, F.; Arcos, D. *Angew. Chem. Int. Ed.* **2007**, *46*, 7548–7558.
20. Cho, E.; Volkov, D. O.; Sokolov, I. *Small* **2010**, *6*, 2314–2319.
21. Bonacchi, S.; Genovese, D.; Juris, R.; Montalti, M.; Prodi, L.; Rampazzo, E.; Zaccheroni, N. *Angew. Chem. Int. Ed.* **2011**, *50*, 4056–4066.
22. Burns, A.; Ow, H.; Wiesner, U. *Chem. Soc. Rev.* **2006**, *35*, 1028–1042.
23. Wang, T.; Chai, F.; Fu, Q.; Zhang, L.; Liu, H.; Li, L.; Liao, Y.; Su, Z.; Wang, C.; Duan, B.; Ren, D. *J. Mater. Chem.* **2011**, *21*, 5299–5306.
24. Würth, C.; Grabolle, M.; Pauli, J.; Spieles, M.; Resch-Genger, U. *Nat. Protoc.* **2013**, *8*, 1535–1550.
25. Vallet-Regí, M.; Colilla, M.; González, B. *Chem. Soc. Rev.* **2011**, *40*, 596–607.
26. Karukstis, K. K.; Thompson, E. H. Z.; Whiles, J. A.; Rosenfeld, R. J. *Biophys. Chem.* **1998**, *73*, 249–263.
27. Rampazzo, E.; Bonacchi, S.; Montalti, M.; Prodi, L.; Zaccheroni, N. *J. Am. Chem. Soc.* **2007**, *129*, 14251–14256.
28. Bardhan, R.; Grady, N. K.; Cole, J. R.; Joshi, A.; Halas, N. J. *ACS Nano* **2009**, *3*, 744–752.

29. Aslan, K.; Wu, M.; Lakowicz, J. R.; Geddes, C. D. *J. Am. Chem. Soc.* **2007**, *129*, 1524–1525.

30. Martini, M.; Perriat, P.; Montagna, M.; Pansu, R.; Julien, C.; Tillement, O.; Roux, S. *J. Phys. Chem. C.* **2009**, *113*, 17669–17677.

31. Lessard-Viger, M.; Rioux, M.; Rainville, L.; Boudreau, D. *Nano Lett.* **2009**, *9*, 3066–3071.

32. Rampazzo, E.; Bonacchi, S.; Juris, R.; Montalti, M.; Genovese, D.; Zaccheroni, N.; Prodi, L.; Rambaldi, D. C.; Zattoni, A.; Reschiglian, P. *J. Phys. Chem. B* **2010**, *114*, 14605–14613.

33. Genovese, D.; Bonacchi, S.; Juris, R.; Montalti, M.; Prodi, L.; Rampazzo, E.; Zaccheroni, N. *Angew. Chem. Int. Ed.* **2013**, *52*, 5965–5968.

34. Liu, J.; Bu, W.; Pan, L.; Zhang, S.; Chen, F.; Zhou, L.; Zhao, K.; Peng, W.; Shi, J. *Biomaterials* **2012**, *33*, 7282–7290.

35. Tsoi, K. M.; MacParland, S. A.; Ma, X.; Spetzler, V. N.; Echeverri, J.; Ouyang, B.; Fadel, S. M.; Sykes, E. A.; Goldaracena, N.; Kaths, J. M.; Conneely, J. B.; Alman, B. A.; Selzner, M.; Ostrowski, M. A.; Adeyi, O. A.; Zilman, A.; McGilvray, I. D.; Chan, W. C. W. *Nat. Mater.* **2016**, *15*, 1212–1221.

Supporting Information

Experimental section

Materials: Doxorubicin hydrochloride (DOX·HCl), dichloromethane (≥99.8%), chloroform (≥99.8%), tetrahydrofuran (THF, ≥99.9%), Pluronic F127 ((ethylene oxide)106(propylene oxide)70(ethylene oxide)106, PEO-PPO-PEO, MW = 12,600 g mol^{-1}), tetramethoxysilane (TMOS, 98%), trimethoxy(2-phenylethyl)silane (TMPES, 98%), trimethoxy(vinyl)silane (TMVS, 98%), trimethoxy(propyl)silane (TMPS, 97%), trimethoxy(octyl)silane (TMOTS, 96%), coumarin545T, rhodamine101, N,N-dimethylacetamide (DMAC, 99%), succinic anhydride (99%), diethyl ether, dimethylformamide (DMF, 99%), 1-ethyl-3-(3-dimethylaminopropyl) carbodiimide (EDC) and N-hydroxysuccinimide (NHS, 97%) were purchased from Sigma Aldrich. Sodium hydrogen carbonate (NaHCO3, ≥99%) was purchased from Ajax. Trimethoxy(methyl)silane (TMMS, 97%) was purchased from Alfa Aesar. 10× phosphate buffered saline (PBS) solution and TAT peptides were purchased from 1st Base. 1× PBS was prepared by diluting the 10× PBS with Milli-Q deionized (DI) water. Spectra/Por regenerated cellulose (RC) dialysis membrane was purchased from Spectrum Inc.

Deprotonation of DOX·HCl. DOX·HCl was deprotonated by using excess saturated NaHCO3 solution. The deprotonated DOX was extracted from the aqueous solution by dichloromethane using a separatory funnel. DOX was then collected and dried through evaporating off the dichloromethane using a rotary evaporator. The final DOX powder was dissolved in THF at a concentration of 4 mg mL^{-1} (stock solution) for later usage.

Synthesis of F127-TAT: F127 (12.5 g) was dried in a vacuum oven at 100 ^{o}C for 24 hours. It was then dissolved in anhydrous DMAC (60 mL) and heated to 70 ^{o}C under stirring. Upon complete dissolution, succinic anhydride (0.3 g) was added into the solution and stirred at 70 ^{o}C under nitrogen atmosphere. The reaction mixture was then heated to 90 ^{o}C and stirred for

another 24 hours. After cooling down to room temperature, the final dark brown reaction mixture was precipitated against excess cold diethyl ether in a drop wise manner. The precipitates were dissolved in DI water (10 mL) and dialyzed against DI water for 2 days using a dialysis membrane with molecular weight cut-off (MWCO) of 1,000 g mol^{-1}. The final aqueous solution was then freeze-dried to obtain the dicarboxylic acid modified F127 block copolymer (F127-COOH).

F127-COOH (1.26 g) was dissolved in anhydrous DMF (10 mL), to which EDC (58 mg) and NHS (35 mg) were added. The reaction solution was stirred at room temperature for 4 hours. Subsequently, TAT (0.32 g) in anhydrous DMF (1 mL) was added and the reaction was stirred for another 12 hours. Removal of DMF in vacuum gave the crude product, which was then dissolved in DI water (15 mL) and subjected to a dialysis membrane with MWCO of 3,500 g mol^{-1}. The final aqueous solution was then freeze-dried to obtain the purified TAT peptide-conjugated F127 (F127-TAT).

Preparation of DOX@Si-PMs: Silica shell cross-linked polymeric micelles (denoted as Si-PMs) loaded with DOX were prepared as follows. F127 (75 mg) was dissolved in THF and mixed with different amounts of DOX stock solution. The total volume of THF was fixed at 900 μL. After stirring at room temperature for 3 hours, TMOS and another organosilane (e.g. TMMS, TMPS, TMOTS or TMPES) were added into the solution. The total volume of the silica precursors was fixed at 65 μL. The volume percentage of the organosilane in the total silica precursors (i.e. TMOS + organosilane) ranged from 0 to 40%. After vortexing for 1 minute, the solution was injected slowly into DI water (10 g) under rapid stirring with speed of 1,000 rpm. The obtained solution was stirred at room temperature and 60 °C for 2 days, respectively, at a stirring speed of 500 rpm to evaporate off THF and ensure complete hydrolysis and condensation of the silica precursors. Afterwards, unreacted silica precursors and untrapped DOX were removed by dialysis against DI water (1.8 L; 12 hours by refreshing

DI water every 3 hours) using a dialysis membrane with MWCO of 10,000 g mol^{-1}. The solution was then subjected to centrifugation (10,000 rpm for 10 minutes) to remove any aggregates.

Preparation of TAT-Conjugated DOX@Si-PMs: F127 and F127-TAT were dissolved in THF (752.5 μL) and mixed with the DOX stock solution (147.5 μL). The total mass of F127 and F127-TAT was fixed at 75 mg, with the weight percentage of F127-TAT ranging from 10 to 30%. After stirring at room temperature for 3 hours, TMOS (52 μL) and TMPES (13 μL) were added into the solution. After vortexing for 1 minute, the solution was injected slowly into DI water (10 g) under rapid stirring with speed of 1,000 rpm. All subsequent steps were the same as described in Preparation of DOX@Si-PMs.

Preparation of Coumarin 545T@Si-PMs: F127 (75 mg), coumarin 545T THF solution (2 mg mL^{-1}, 500 μL) and THF (400 μL) were mixed together and stirred at room temperature for 3 hours. TMOS (52 μL) and TMPES (13 μL) were then added into the solution. After vortexing for 1 minute, the solution was injected slowly into DI water (10 g) under rapid stirring with speed of 1,000 rpm. The obtained solution was further stirred at room temperature for 4 days at a stirring speed of 500 rpm. Afterwards, the solution was dialyzed against DI water for 24 hours using a dialysis membrane with MWCO of 10,000 g mol^{-1}. The solution was then subjected to centrifugation at 10,000 rpm for 10 minutes to remove any aggregates.

Preparation of Rhodamine 101@Si-PMs: F127 (75 mg), rhodamine 101 THF solution (2 mg mL^{-1}, 150 μL) and THF (750 μL) were mixed together and stirred at room temperature for 3 hours. All subsequent steps were the same as described in the Preparation of Coumarin545T@Si-PMs.

Characterization: TEM (JEOL JEM-2010F, 200 kV) was employed to visualize the morphology of Si-PMs. DLS was performed with Malvern Zetasizer Nano-S using a HeNe laser (633 nm) to measure the size and size distribution of Si-PMs in water. An FTIR

spectrophotometer (Varian 3100 Excalibur) was used to characterize the chemical composition of Si-PMs. As for FTIR sample preparation, the aqueous suspensions of Si-PMs were freeze-dried completely and then dispersed ground with KBr to produce KBr pellets. UV-vis absorption spectra were recorded using a Shimadzu UV-3101 PC spectrophotometer and photoluminescence spectra were collected using a Perkin-Elmer LS 55 spectrophotometer.

Quantum Yield (QY) Measurement: QY measurements were performed by adopting a method reported by Jobin Yvon,[1] and using Rhodamine101 in ethanol as the reference fluorescent dye (QY = 100%). In detail, the aqueous suspension of DOX@Si-PMs was diluted to obtain a series of DOX concentrations of 3.3, 6.5, 13, 19.5 and 26 μM, respectively. UV-vis absorption and fluorescence (λex = 480 nm) spectra were recorded, respectively. The slope was then obtained by fitting the plot of integrated fluorescence intensity vs absorbance at 480 nm with a straight line and y-intercept at 0. QY was calculated according to the following equation:

$$\Phi_X = \Phi_{ref}\left(\frac{S_X}{S_{ref}}\right)\left(\frac{\eta_X}{\eta_{ref}}\right)^2$$

where Φ is the QY, S is the slope derived from the plot of integrated fluorescence intensity vs absorbance, η is the refractive index of the solvent, and the subscripts *X* and *ref* denote test and reference samples, respectively.

DOX Loading Content: The loading content (LC%) of DOX in the DOX@Si-PMs was measured by two different methods, allowing for a cross check. With the first method, absorbance at λmax = 480 nm of the DOX@Si-PMs aqueous suspension was measured. Quantification was performed from the calibration curve of DOX in water. With the second method, the DOX loaded in DOX@Si-PMs was first extracted from the freeze-dried samples by using THF and UV-vis was then run with the extracts. Finally, the amount of DOX loaded in DOX@Si-PMs was determined by UV-vis analysis at λmax = 480 nm based on the absorbance calibration curve of DOX in THF.2 The LC% was calculated as follows:

LC% = (Mass of DOX loaded in DOX@Si-PMs)/(Mass of DOX@Si-PMs) × 100

Confocal Fluorescence Imaging Study: HeLa cells were cultured in Dulbecco's Modified Eagle's Medium (DMEM) with high glucose (4,500 mg L^{-1}), supplemented with 4.0 mM of L-Glutamine, 10% fetal bovine serum (FBS) and 1% penicillin/streptomycin antibiotics at 37 °C in 5% CO2. A2780 and drug resistant variant, A2780/ADR cells were maintained in Roswell Park Memorial Institute (RPMI) 1640 media supplemented with 10% FBS, 2 mM of Glutamine and 1% penicillin/streptomycin antibiotics at 37 °C in 5% CO2.

Cells were seeded in a 27 mM glass bottom dish (NuncTM Glass bottom dishes, ThermoFisher Scientific) and left to grow and attach overnight. The culture media was replaced by fresh media containing DOX or DOX@Si-PMs. After 24 hours of incubation, the cells were washed with PBS and replaced with normal media for live confocal imaging. For 4,6-diamidino-2-phenylindole (DAPI) staining of the cells, the dishes were washed gently with PBS followed with fixation in 4% Paraformaldehdye (Sigma Aldrich) for 15 minutes at room temperature. They were then washed again with PBS three times to remove the fixative and finally mounted with a coverslip in mounting media (Vectashield Mounting Medium with DAPI, Vector Laboratories) for later confocal imaging. All confocal images were taken with LSM700 confocal inverted microscope, Zeiss.

Cell Viability Assay: Cells were seeded into a 96 well plate at a density of 4,000 cells per well for 1–2 days prior to drug incubation. The cells were then cultured at 37 °C in 5% CO2 in the presence of the freshly prepared culture media containing DOX or DOX@Si-PMs. After 1–7 days of incubation, the viability of cells was then measured via MTT assay (Vybrant MTT Cell Proliferation Assay Kit, ThermoFisher Scientific) according to the kit protocol. The optical density values were analyzed by a plate reader at 540 nm using Biotek SynergyTM H4 microplate reader. The data presented in this study were averaged from three experiments.

Table S1. LC%, QY and fluorescence enhancement factor (FEF) of DOX in DOX@Si-PMs

Sample code[a]		LC%	QY (%)	FEF (normalized to 'w/o R')
S1	w/o R	0.27	0.59	1
S2	20%Me	0.09	3.74	2.1
S3	20%Pr	0.19	2.37	2.8
S4	20%Oc	0.28	3.89	6.8
S5	10%Ph	0.29	1.51	2.7
S6	20%Ph	0.47	3.92	11.6
S7	30%Ph	0.39	6.87	16.8
S8	40%Ph	0.36	7.14	16.1
S9	$DOX_{0.59}$[b]	0.28	6.34	11.1
S10	$DOX_{0.29}$[b]	0.11	9.89	6.8
S11	$DOX_{0.15}$[b]	0.04	11.73	2.9

[a], S1-S8: the amount of DOX initially added was fixed at 1.18 mg; S9-S11: the DOX@Si-PMs were modified with 20%Ph. b The subscript indicates the amount of DOX initially added (mg).

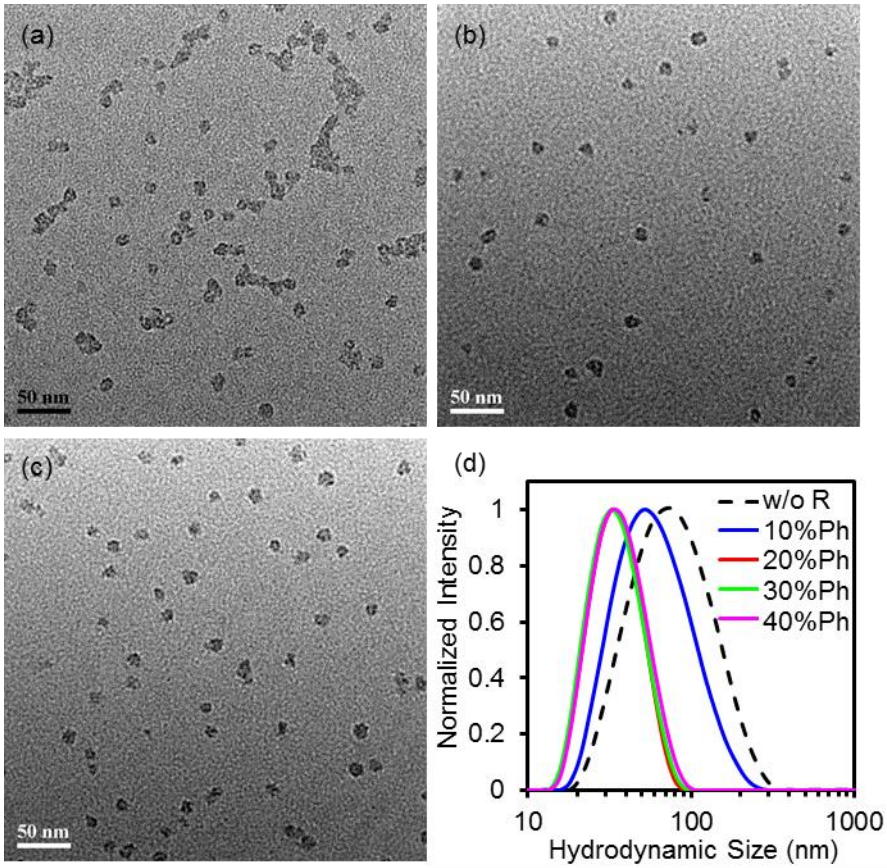

Figure S2. TEM images of DOX@Si-PMs modified with hydrocarbons: (a) 10%Ph, (b) 30%Ph and (c) 40%Ph. (d) DLS curves of the aque-ous suspensions of DOX@Si-PMs. 10–40% represent the volume percentage of the organosilanes in the total silica precursors. Those TEM images of DOX@Si-PMs without hydrocarbon modification and with 20%Ph modification are referred to Figure 1b and 1f, respectively.

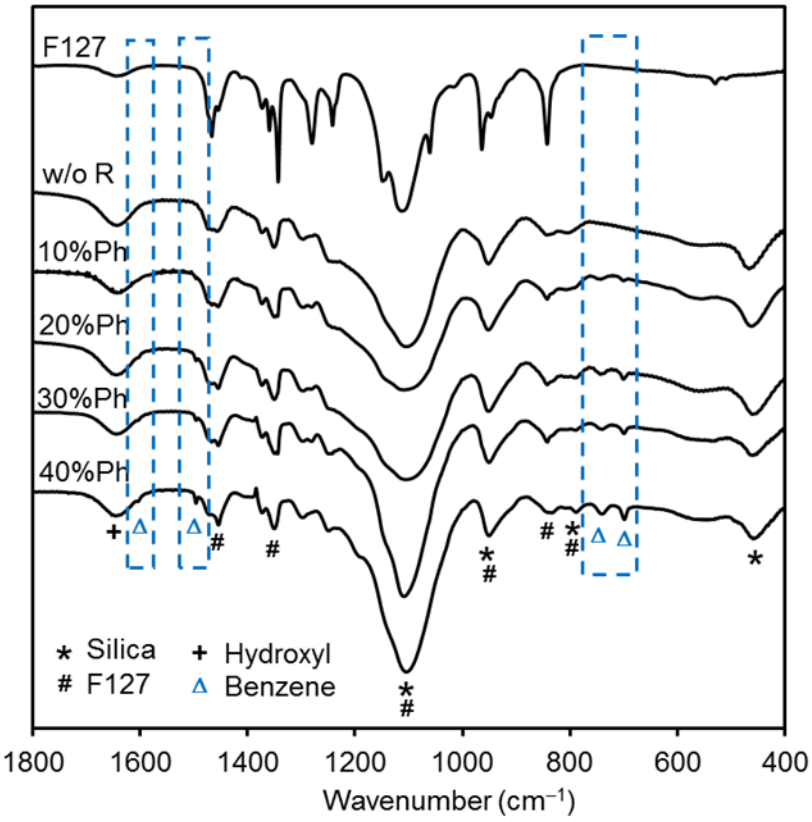

Figure S3. FTIR spectra of DOX@Si-PMs. The bands are assigned to silica (460 cm^{-1}, Si-O-Si bending), F127 block copolymers (840 cm^{-1}, C-H rocking; 1350 cm^{-1}, C-H wagging; and 1470 cm^{-1}, C-H bending) and overlaps of F127 and silica (790 cm^{-1}, Si-O-Si symmetric stretching; 950 cm^{-1}, Si-OH stretching; and 1110 cm^{-1}, Si-O-Si antisymmetric stretching). The characteristic band of hydroxyl groups (1650 cm^{-1}, H-O-H bending) indicates the presence of structure or surface hydroxyl groups. The four bands centered at 700, 740, 1495 and 1600 cm^{-1} are characteristic of the benzene ring and show that the content of phenylethyl in the DOX@Si-PMs increases with increasing %Ph.

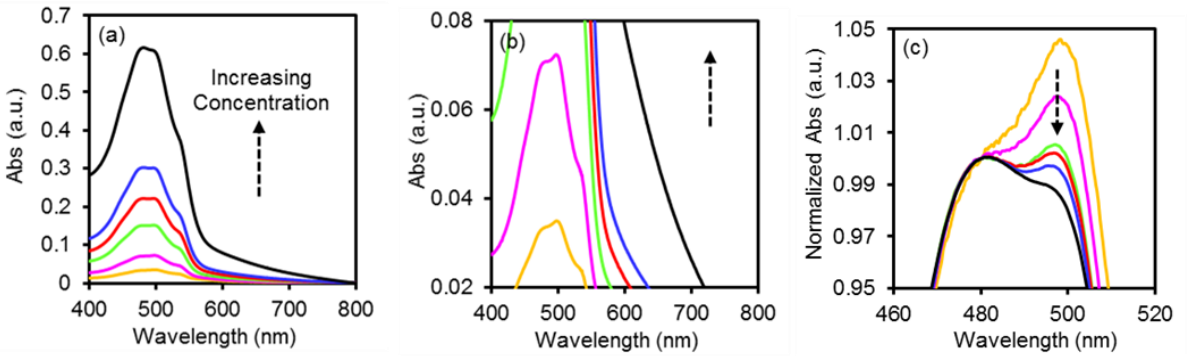

Figure S4. (a) Absorption spectra of a free DOX in water with concentrations of 3.3, 6.5, 13, 19.5, 26 and 50 μM, respectively. (b) and (c) are enlarged and normalized (to Abs_{480}) spectra of (a), respectively. The arrow indicates increasing concentration. As the concentration of DOX in water increased, which is associated with the formation of DOX dimers,[3] the ratio of absorption intensities at 498 and 480 nm (Abs_{498}/Abs_{480}) decreased.[3] The characteristic band of free DOX in water at 498 nm red-shifted to 504 nm when the DOX molecules were encapsulated in Si-PMs with increased π-π stacking interactions.[4]

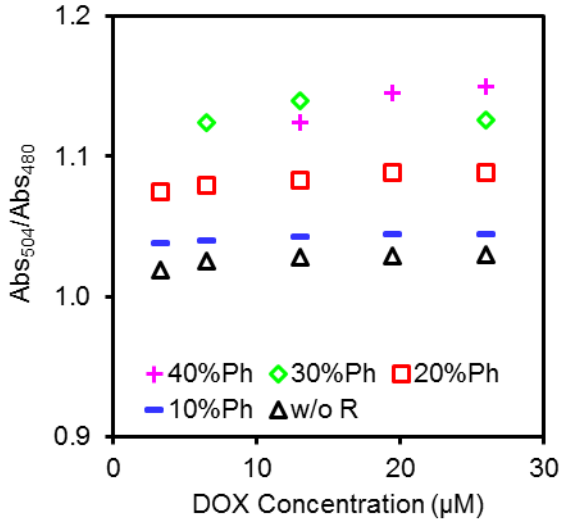

Figure S5. Variation of the Abs_{504}/Abs_{480} ratio with dilution of the aqueous suspensions of DOX@Si-PMs. A series of concentrations of DOX (3.3, 6.5, 13, 19.5 and 26 μM) were obtained by dilution of the initial aqueous suspensions of DOX@Si-PMs.

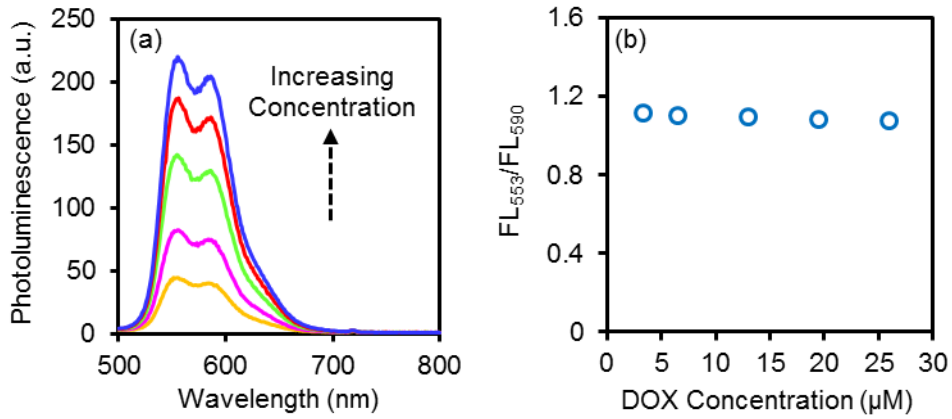

Figure S5. (a) Photoluminescence spectra of a series of free DOXs in water with concentrations of 3.3, 6.5, 13, 19.5 and 26 μM, respectively. The arrow indicates increasing concentration. (b) Variation of the FL_{553}/FL_{590} ratio with the concentration of DOX. The FL_{553}/FL_{590} ratio did not vary with the concentration of DOX in water, showing an average value of 1.10 ± 0.02.

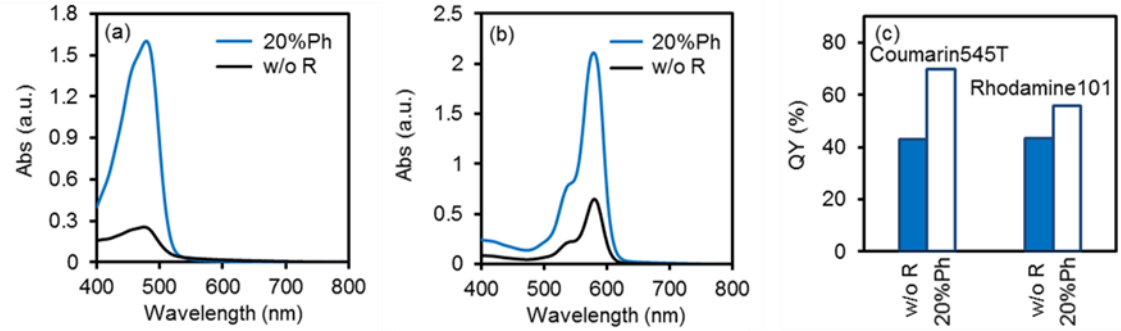

Figure S6. Absorption spectra of the aqueous suspensions of (a) coumarin 545T@Si-PMs and (b) rhodamine 101@Si-PMs. (c) QY of coumarin 545T and rhodamine 101 in Si-PMs.

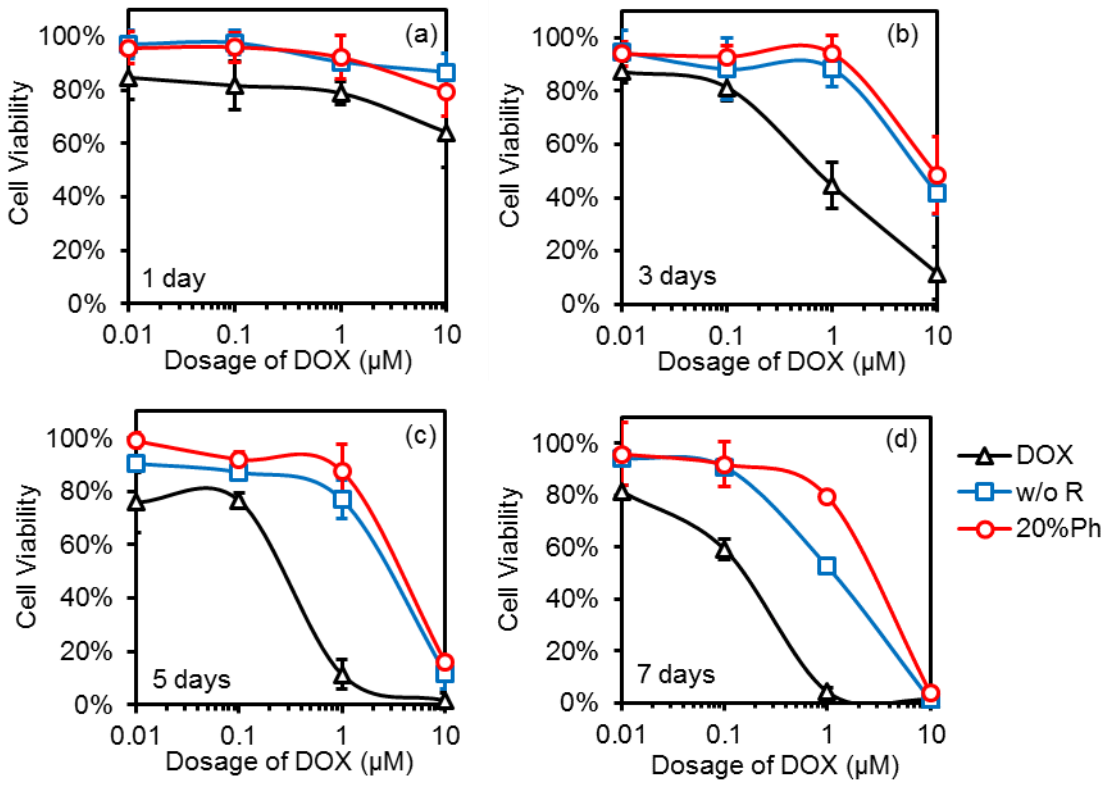

Figure S7. Viability of HeLa cells cultured in the presence of free DOX, DOX@Si-PMs without hydrocarbon modification and DOX@Si-PMs with 20%Ph modification respectively for (a) 1, (b) 3, (c) 5 and (d) 7 days.

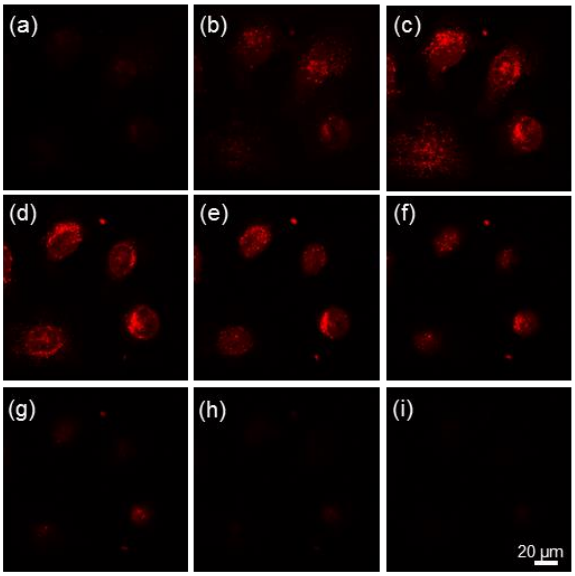

Figure S8. Z-stack recording of HeLa cells cultured with DOX@Si-PMs modified with 20%Ph and conjugated with 30%TAT. Confocal luminescence images are shown in (a)–(i). The DOX dosage was 5 μM. The images were acquired with a step size of 1.5 μm from the top to the bottom surface of the cells.

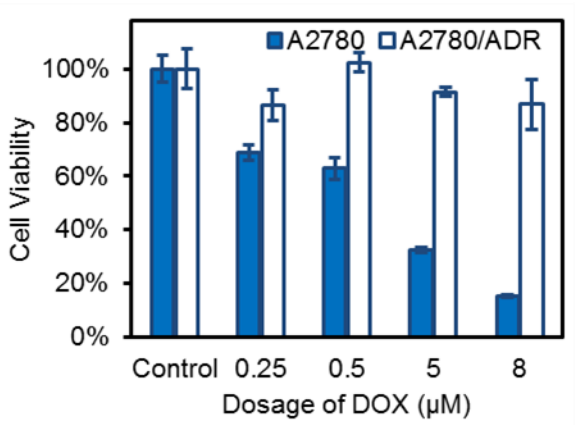

Figure S9. Viability of A2780 and A2780/ADR cells cultured in the presence of free DOX of varied dosages for 1 day.

Reference

1. Jobin Yvon Ltd. Middlesex, UK. Retrieved September 21, 2017, from http://www.horiba.com/fileadmin/uploads/Scientific/Documents/Fluorescence/quantumyieldstrad.pdf
2. Sanson, C.; Schatz, C.; Meins, J.-F. L.; Soum, A.; Thévenot, J.; Garanger, E.; Lecommandoux, S. *J. Control Release* **2010**, *147*, 428–435.
3. Changenet-Barret, P.; Gustavsson, T.; Markovitsi, D.; Manet, I.; Monti, S. *Phys. Chem. Chem. Phys.* **2013**, *15*, 2937–2944.
4. Missirlis, D.; Kawamura, R.; Tirelli, N.; Hubbell, J. A. *Eur. J. Pharm. Sci.* **2006**, *29*, 120–129.

6 THERANOSTIC NANOCAPSULES

Theranostic Nanocapsules engineered for heating, imaging and thermal sensing

Nanocapsules Théranostiques Conçues pour la Thermothérapie, l'imagerie et la Thermométrie

Miao Wang[†], Artiom Skripka[†], Yu Zhang[‡], Ting Cheng[†], Michael Ng[#], Xuan Sun[‡,ǂ], Xu Li[‡], Kishore Kumar Bhakoo[#], Alex Y. Chang[§], Federico Rose[†], Fiorenzo Vetrone[*†]

[†] Institut National de la Recherche Scientifique (INRS), Centre Énergie, Matériaux et Télécommunications, Université du Québec, Varennes (QC), Canada

[‡] Institute of Materials Research and Engineering (IMRE), Agency for Science, Technology and Research (A*STAR), Singapore

[ǂ] Department of Chemical and Biomolecular Engineering, National University of Singapore, Singapore

[#] Singapore Bioimaging Consortium (SBIC), Agency for Science, Technology and Research (A*STAR), Singapore

[§] Department of Oncology, Johns Hopkins University, Baltimore, Maryland, USA

Ready for submission to ACS NANO.

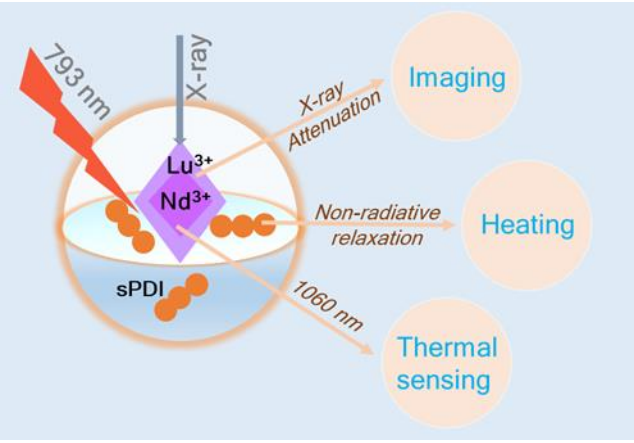

As introduced in Chapter 1, precise PTT requires selective accumulation of PTT agents in the region of interest and image-guided NIR-regulated treatment with *in situ* temperature monitoring. The combination of heating, temperature monitoring as well as imaging-based tracking using of NPs, is an ambitious goal that aims at extending and facilitating the application of PTT. Ideally, with the help of bioimaging techniques (*e.g.*, CT, MRI, US, and optical imaging), clinicians can first determine the clear boundary of tumors and ensure there are sufficient PTT agents accumulated in the targeted tumor before starting the laser irradiation. Secondly, they are able to monitor in real-time the intra tumor temperature by non-invasive, contactless nanothermometry, in order to adjust the power density and duration of irradiation. In this paper,

we extended the one-pot encapsulation approach to synthesize a theranostic NC with a hydrodynamic size less than 200 nm, working entirely in the NIR for image-guided PTT while recording temperature in real-time. We simultaneously co-encapsulated small organic molecules, bay-substituted dicyclohexylamino- perylene diimide (sPDI) as an efficient optical heater, with a rationally designed multifunctional $LiLuF_4$:10 mol% Nd^{3+}@$LiLuF_4$ core@shell DSNPs, acting as both nanothermemeters and imaging probes. The Lu^{3+} in the host matrix, acting as a CT contrast agent for tracking and locating the target of interest. Both materials can be excited at the so-called non-heating and non-damaging wavelength, 793 nm, while the nanothermometer emission (1060 nm) is located within the second biological window, allowing for a greater depth of tissue penetration and temperature readout. The sPDI molecules are self-assembled once encapsulated into the NCs, resulting in a red-shift favorable for NIR absorption. Upon irradiation the sPDI aggregates convert light to heat via non-radiative relaxation, inducing a local temperature increment and subsequently a complete eradication of MCF-7 breast cancer cells. It demonstrates high photothermal-stability, moreover, the heating rate can be tuned by adjusting the concentrations of sPDI loaded to the NCs during the synthesis. In the other hand, the temperature is accurately detected in situ by the Nd^{3+} $^4F_{3/2}$ → $^4I1_{1/2}$ transition of DSNPs. As nanothermometers, DSNPs displayed relative thermal sensitivity around 0.35% ° C^{-1} and thermal uncertainty around 0.15 °C at room temperature. A positive contrast enhancement is also exhibited in the CT images of cancer cells, showing the potential for image-guided PTT. All above, these NCs demonstrate great potential within the theranostic framework for the precise PTT as they successfully combine the requirements of heating, imaging and thermal sensing.

Theranostic Nanocapsules engineered for heating, imaging and thermal sensing

Miao Wang[†], *Artiom Skripka*[†], *Yu Zhang*[‡], *Ting Cheng*[†], *Michael Ng*[#], *Xuan Sun*[*,¦], *Xu Li*[‡], *Kishore Kumar Bhakoo*[#], *Alex Y. Chang*[§], *Federico Rose*[†], *Fiorenzo Vetrone*[*†]

[†] Institut National de la Recherche Scientifique (INRS), Centre Énergie, Matériaux et Télécommunications, Université du Québec, Varennes (QC), Canada

[‡] Institute of Materials Research and Engineering (IMRE), Agency for Science, Technology and Research (A*STAR), Singapore

[¦] Department of Chemical and Biomolecular Engineering, National University of Singapore, Singapore

[#] Singapore Bioimaging Consortium (SBIC), Agency for Science, Technology and Research (A*STAR), Singapore

[§] Department of Oncology, Johns Hopkins University, Baltimore, Maryland, USA

[*] Key Laboratory of Colloid & Interface Chemistry, Shandong University, Ministry of Education, Jinan, China

[¦] School of Chemistry and Chemical Engineering, Shandong University, Jinan, China

* Corresponding author: Fiorenzo.Vetrone@inrs.ca

Abstract: Precise photothermal therapy (PTT) requires selective accumulation of PTT agents in the region of interest and image-guided near infrared (NIR) regulated treatment with *in situ* temperature monitoring. The combination of heating, imaging, as well as thermal sensing using of nanoparticles (NPs), is an ambitious goal that aims to extend and facilitate the application of PTT. Here we reported an original theranostic nanocapsule (NC) with a hydrodynamic size less than 200 nm, working entirely in the NIR for image-guided PTT while recording temperature in real-time. These NCs are synthesized by a one-pot encapsulation approach, simultaneously co-encapsulating small organic molecules, bay-substituted dicyclohexylamino-

perylene diimide (sPDI) as an efficient optical heater, with a rationally designed multifunctional $LiLuF_4$:10 mol% Nd^{3+}@$LiLuF_4$ core@shell downshifting NPs (DSNPs), acting as both nanothermemeters and imaging probes. The Lu^{3+} in the host matrix, acting as a computer tomography (CT) contrast agent for tracking and locating the target of interest. Both materials can be excited at the so-called non-heating and non-damaging wavelength, 793 nm, while the nanothermometer emission (1060 nm) is located within the second biological window, allowing for a greater depth of tissue penetration and temperature readout. The sPDI molecules are self-assembled once encapsulated into the NCs, resulting in a red-shift favorable for NIR absorption. Upon irradiation the sPDI aggregates convert light to heat *via* non-radiative relaxation, inducing a local temperature increment and subsequently a complete eradication of MCF-7 breast cancer cells. It demonstrates high photothermal-stability, moreover, the heating rate can be tuned by adjusting the concentrations of sPDI loaded to the NCs during the synthesis. In the other hand, the temperature is accurately detected *in situ* by the Nd^{3+} $^4F_{3/2} \rightarrow {}^4I_{11/2}$ transition of DSNPs. As nanothermometers, DSNPs displayed relative thermal sensitivity around 0.35% $°C^{-1}$ and thermal uncertainty around 0.15 °C at room temperature. A positive contrast enhancement is also exhibited in the CT images of cancer cells, showing the potential for imaging-guided PTT. All above, these NCs demonstrate great potential within the theranostic framework for the precise PTT as they successfully combine the requirements of heating, imaging and thermal sensing.

Key words: Theranostic nanocapsules, nanothermometry, photothermal therapy, imaging probes

Photothermal therapy (PTT) has been widely studied for cancer treatment, and commonly utilizes photo thermal agents as heat generators to locally treat the targeted tissue upon near-infrared (NIR) radiation. The PTT agents are internalized in the tumor site, absorb NIR energy and convert it to thermal energy, resulting in local temperature increase, which subsequently

causes thermal damage to biological structures (*i.e.*, denaturation of proteins, impairment of RNA/DNA) and ultimately cell death.[1, 2] In addition to the advantages of localized treatment, minimal invasiveness, less systemic side effects and cumulative cytotoxicity, PTT is able to enhance the susceptibility of cancer cells to other treatment,[2] such as chemotherapy,[3] radiotherapy,[4] and immunotherapy.[5-9] The effectiveness of PTT is related to the temperature achieved during the treatment, the length of it, as well as to the cell and tissue characteristics.[10, 11] To ensure that the desired temperature is reached, but not exceeded, the temperature of the treated area should be monitored throughout the PTT.[12-14] Therefore it is crucial to deliver the heat to the target in a well-controlled manner. However, equipment and techniques currently available to perform PTT in this way present certain limitations and require further improvements. The breakthrough of nanotechnology and its potential application in PTT enhances the efficiency and selectivity of the treatment. Most notably, hybrid nanostructures allow: i) combination of therapies (PTT combined with chemotherapy, radiotherapy or immunotherapy), ii) imaging, and iii) real-time thermal information feedback. This reduces treatment complexity and provides better therapeutic efficacy.

Different types of nanoparticles (NPs) (inorganic and organic) have been explored for cancer PTT, including metal-based nanoparticles (*e.g.*, gold, silver, and copper), carbon-based nanoparticles, quantum dots, organic nanomaterials.[1, 15-17] For example, gold-silica nanoshells (GSN) have been approved in a clinical trial to focally ablate low-intermediate-grade tumors within the prostate.[18] This trial shows that GSN directed laser ablation is a safe and technically feasible procedure for the targeted destruction of prostate tumors. However, its therapeutic efficacy has not been fully established. Compared with the inorganic nanomaterials, small organic dyes have good biodegradability, the ease of renal clearance, and moreover their photothermal features are flexible based on the modification of their chemical structures.[19] For example, indocyanine green (ICG, cyanine-based dyes), which is approved by the US food and

drug administration (FDA) as an optical imaging agent, has also been investigated as a PTT agent for cancer treatment in the past decades. Nevertheless, the photothermal conversion efficiency of most studied cyanine dyes is overshadowed by their NIR fluorescence.[20-23] Although recently developed heptamethine indocyanine-based dyes (*e.g.*, IR825, IR780) demonstrate superior photothermal efficiencies and photo-stabilities relative to ICG,[24-27] the latter feature still requires improvement for repeated exposure to laser radiation.[23] Most recently, perylene diimide (PDI) derivatives, a class of pigments, have gained a research attention as NIR photoacoustic[28-31] and PTT[32, 33] agents, due to their exceptional chemical, thermal, and optical stabilities in air and water.[34] For example, a silica encapsulated bay-substituted dicyclohexylamino-PDI (sPDI) has been reported to have strong photothermal conversion ability and excellent structural- and photo-stability under continuous high-power laser irradiation,[32] demonstrating attractiveness for further in vivo applications.

Despite the intrinsic photothermal properties of PTT agents, actual thermal information of the treated area is required to design successful treatment that can kill the cancer cells while preserving the adjacent normal tissues healthy. Typically, temperature increase in the 41.8 ~ 45 °C range is capable of exerting a therapeutic effect over tumor cells while eliciting a minimum damage to the surrounding healthy tissues. Moreover, mild heating is favorable for induction of cell apoptosis, which is considered as a critical variable in producing a favorable tumor microenvironment for immunological responses by activation of the innate and/or adaptive immune system, subsequently prolonging survival of patients.[5-9] On the other hand, PTT at high temperatures (45 ~ 90 °C) can induce complete cell necrosis of both cancer and normal cells.[35, 36] In order to measure temperature during the PTT, remote (non-invasive) thermal sensing within the tissue, and not the surface, is preferred. In the current clinical practice of monitoring temperature in the deep-seated tumors, a thin plastic catheter with thermal probes is implanted either under computer tomography (CT) guidance percutaneously

or intraoperatively at the time of explorative surgery (*e.g.* incisional biopsy).[13] This thermometry approach is invasive to patients and leads to pain, risk of infections, and a limited number of measuring points. Based on these considerations, lack of temperature control has been quoted as the main limitation of current PTT probes.[1, 37]

Aiming for a minimally invasive PTT, contactless photoluminescence thermometry is the best choice for measuring temperatures during the treatment in the complex biological environment.[38] However, not all photoluminescence thermometry sensors, nanothermometers, effectively work within tissues. For deep-tissue imaging and temperature readout, both excitation and emission wavelengths of nanothermometers should fall within the biological optical transparency windows (BWs), where absorption and scattering of light are minimized (BW-I: 750-950 nm; BW-II: 1000-1350 nm; BW-III: 1500-1800 nm).[39, 40]

Ln^{3+} (such as Er^{3+}, Tm^{3+}, Ho^{3+} or Nd^{3+}) - based nanothermometers are promising candidates used for biomedical applications.[41-46] During the last few years, Nd^{3+}-doped downshifting NPs (DSNPs) have gained growing recognition as ratiometric nanothermometers working entirely in the NIR due to the temperature dependent population of thermally coupled Stark sub-levels of Nd^{3+} $^4F_{3/2}$ excited state.[47-50] First of all, Nd^{3+} can be efficiently excited by ~800 nm laser radiation, which has been demonstrated to be a non-heating and non-damaging wavelength in biological applications.[51] Moreover, Nd^{3+} characteristic emission bands (at around 880, 1060, and 1340 nm) all lie in the BWs. Notably, Nd^{3+} emission peaks located in the BW-II are significantly less affected by tissue auto-fluorescence, absorption, and scattering, allowing for greater imaging depth while maintaining high-spatial resolution.[51, 52]

Precise PTT requires selective accumulation of PTT agents in the region of interest and image-guided treatment with *in situ* temperature monitoring. Ideally, with the help of bio-imaging techniques (*e.g.*, CT, magnetic resonance imaging (MRI), ultrasound, and optical imaging), clinicians can first determine the clear boundary of tumors and ensure PTT agents

have sufficiently accumulated in the targeted tumor before starting the laser irradiation. Secondly, they are able to monitor the intra tumoral temperature by non-invasive contact-less nanothermometry in real-time, and adjust the power density and duration of irradiation as needed. Indeed, the combination of heating, temperature monitoring as well as imaging-based tracking of nanoparticles, is an ambitious goal that aims to extend and facilitate the application of PTT. Recently, hybrid nanostructures have been proposed, by adding a thermometric capability to the PTT probes,[53-56] including gold-based nanoparticles + Ln^{3+}-doped nanoparticles,[57-59] gold-based nanoparticles + quantum dots[60], and organic polymers + Ln^{3+}-doped nanoparticles.[61] Though these approaches constitute interesting proof-of-concept experiments, in most of the studies temperature sensing was based on the thermal coupled upconverting visible luminescence rather than NIR wavelength, and the size of hybrid nanostructures in some studies are too large (much more than 200 nm) for in vivo applications; none of them fulfils the aforementioned requisites, and thus further optimization of the synthesis is needed.

We present here theranostic nanocapsules (NCs) that have co-encapsulated small organic molecules (sPDI) as optical heaters, with a rationally designed multifunctional $LiLuF_4$: 10 mol% Nd^{3+}@$LiLuF_4$ core@shell DSNPs, acting as nanothermemeters and imaging probes. Both materials can be excited at the same wavelength, 793 nm, in the BW-I, while the nanothermometer emission is located within BW-II. Moreover, we chose $LiLuF_4$ as the host matrix because of the high x-ray attenuation by Lu^{3+}, so as to achieve an effective contrast probe for CT imaging. These theranostic NCs demonstrate excellent colloidal stability, biocompatibility, high photothermal-stability and strong PTT effects against cancer cells while recording temperature *in situ*.

Results and discussion

Design and synthesis of theranostic NCs

To design and synthesize the theranostic nanostructures for effective PTT, we focused on the key points as follows. (1) Materials used for both heaters and thermometers are working in the BWs. (2) The hybrid nanostructures can act as imaging probes. (3) Size of the developed theranostics nanostructures is within the 10 – 200 nm range, favorable for future in vivo applications.[62] We recently established a one-pot encapsulation strategy for the synthesis of theranostic NCs, co-encapsulating DSNPs and organic molecules in a near-neutral pH aqueous environment.[63] Briefly, the encapsulation follows a straight forward microemulsion mechanism, using tri-block copolymers, (ethylene oxide)$_{106}$(propylene oxide)$_{70}$(ethylene oxide)$_{106}$ (PEO-PPO-PEO), as the templating and protecting agent. Silica precursor, tetramethoxysilane (TMOS), is hydrolysed and condensed between the core/corona of the PEO-PPO-PEO micelles. This forms a silica shell cross-linked NCs with excellent colloidal and mechanic stability, and biocompatibility.

Physical confinement of PDI in a desired J-aggregation form has been reported to produce highly efficient photothermal conversion upon NIR irradiation.[32] PDI has an intrinsic and strong tendency to aggregate in high polarity solvents, due to strong electronic coupling between the neighbouring PDI molecules.[64] As reported, limited spaces such as channels and cavities of a nano- or sub-nanometer size can create physical confinement to strengthen the intermolecular interactions between the encapsulated guest molecules, thus giving rise to their aggregation.[65] J-aggregates, caused by the head to tail intermolecular interactions, increase the non-radiative relaxation of the excited states – heat production. Also the bathochromically shifted absorbance of J-aggregates compared to single molecules benefits their NIR absorption.[64] Accordingly, we selected sPDI for the photothermal conversion upon NIR irradiation because it is prone to form J-aggregates through effective intermolecule π-π stacking.[32]

To real-time monitor the temperature during PTT, we selected $LiLuF_4$: 10 mol% Nd^{3+} @$LiLuF_4$ DSNPs as thermometers, which can be excited with the same wavelength (793 nm) as that used for the sPDI. The DSNPs are synthesized following a two-step thermal decomposition approach established by our group.[66] $LiLuF_4$ host was selected due to its propensity to effectively lift the M_J degeneracy from the $^{2S+1}L_J$ terms of Nd^{3+}, allowing to observe fine Stark components of $^4F_{3/2} \rightarrow {}^4I_J$ radiative transitions even at room temperature. Thus, upon 793 nm laser irradiation, a sharp and intense emission (~1060 nm) from Nd^{3+}-doped core can be readily used for single-band temperature read-out. [42, 50, 67-69] Furthermore, the inert shell protects the emission of Nd^{3+} from surface quenching, resulting in a brighter emission favourable for the nanothermometry. [51, 70, 71] In addition, the Lu^{3+} in the host plays a role in CT imaging due to its high x-ray attenuation.

Utilizing the one-pot encapsulation approach, we synthesized 3 groups of the NCs: i) co-encapsulated with DSNPs and sPDI (DSNPs+sPDI@NCs), ii) NCs encapsulated with DSNPs only (DSNPs@NCs), and iii) NCs encapsulated with sPDI only (sPDI@NCs). The last two groups served as controls. Since both materials are excited by the same wavelength, 793 nm, the irradiation energy is shared between them. Therefore, relative amounts of DSNPs and sPDI caged in NCs is most likely to affect the photothermal conversion of PDI. To evaluate these features, we synthesized DSNPs+sPDI@NCs with various sPDI loading amount which is 0.3 mg (L), 0.6 mg (M), and 1.2 mg (H), respectively, namely DSNPs+sPDI_L@NCs, DSNPs+sPDI_M@NCs, and DSNPs+sPDI_H@NCs.

Characterization of theranostic NCs

The core/shell DSNPs have a bipyramid-shaped morphology and a size of 36 × 27 nm (major × minor axes), where the active core is 21 × 19 nm and the inert shell is 7 × 4 nm (Figure S1A and B). The XRD peaks (Figure S1C) confirm a pure tetragonal ($I4_1/a$) phase, in excellent agreement with the reference data (PDF no. 00-027-1251). TEM images (Figure 1A)

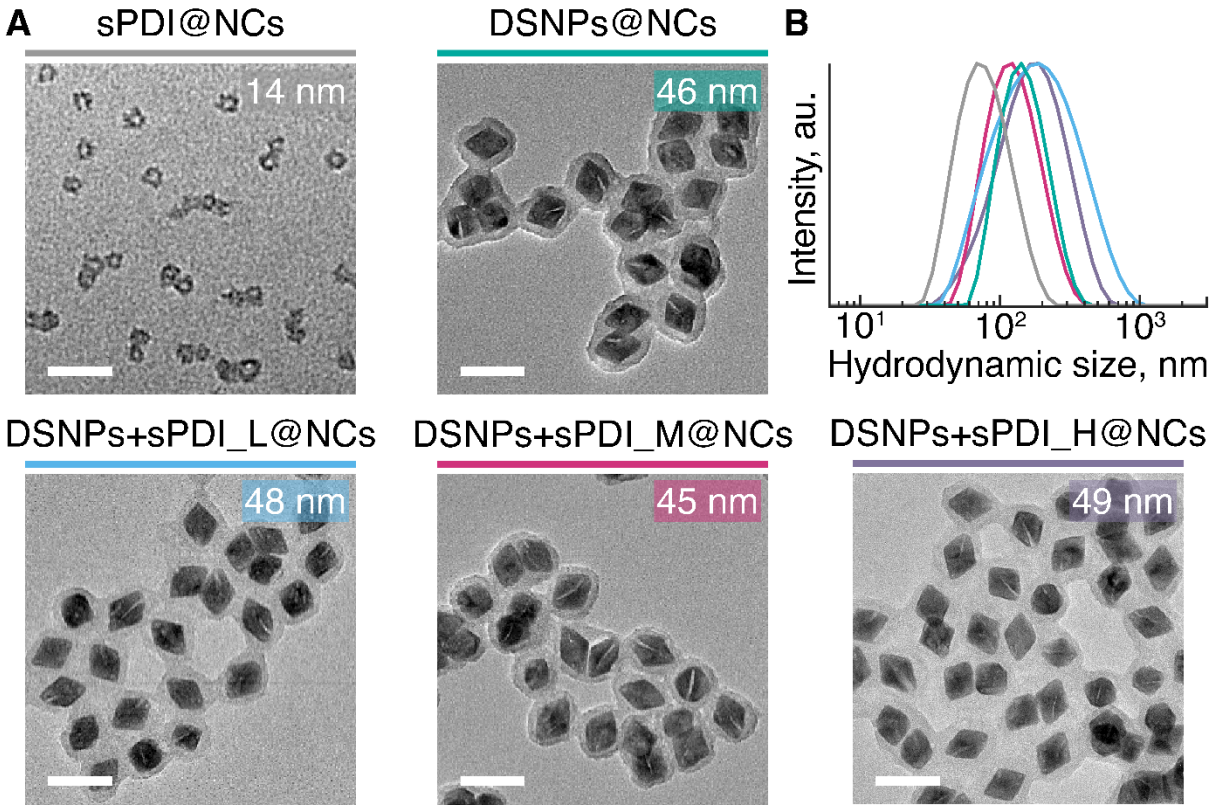

Figure 1. (A) TEM images demonstrating the morphology of the NCs studied, including sPDI@NCs,, DSNPs@NCs, DSNPs+sPDI_L@NCs, DSNPs+sPDI_M@NCs, DSNPs+sPDI_H@NCs (B). DLS analysis of the NCs studied (F). Note, color coding of different NCs in A is maintained in B. Scale bars in all images correspond to 50 nm.

demonstrate the morphologies of sPDI@NCs (grey), DSNPs@NCs (green), DSNPs+sPDI_L@NCs (light blue), DSNPs+sPDI_M@NCs (pink), and DSNPs+sPDI_H@NCs (purple). All the NCs formed have an ultrathin but complete silica shell of less than 10 nm thickness. Sizes of NCs estimated from TEM images are around 14 nm (sPDI@NCs), 46 nm (DSNPs@NCs), 48 nm (DSNPs+sPDI_L@NCs), 45 nm (DSNPs+sPDI_M@NCs), and 49 nm (DSNPs+sPDI_H@NCs). DLS analysis (Figure. 1B) reveals their excellent monodispersity based on the hydrodynamic size (nm)/polydispersity indexes sPDI@NCs 70/0.2, DSNPs@NCs 137/0.1, DSNPs+sPDI_L@NCs 158/0.3, DSNPs+sPDI_M@NCs 116/0.2, and DSNPs+sPDI_H@NCs 155/0.3. The size of the NCs and low polydispersity indexes are favourable for the in vivo applications.[62] The contents of DSNPs in NCs were analysed by ICP-AES and the sPDI content was estimated using the absorbance

at 750 nm. The amount of NCs used in this study was calculated based on the ICP data. The TEM size, DLS size, DSNPs and sPDI concentrations of the studied NCs are listed in Table S2.

The organic/inorganic hybrid structure of the three groups of NCs studied was confirmed by FTIR analysis (Figure S2). Non-encapsulated DSNPs and sPDI were dispersed in THF and used as references. The characteristic band of OA (1558 cm^{-1}, O=C−OH asymmetric stretching) indicates the presence of OA-capped DSNPs. sPDI is characterized by the absorption bands at 1593 cm^{-1} (conjugated C=C stretching), 1642 cm^{-1} and 1689 cm^{-1} (imide C=O stretching). Characteristic frequencies of F127 triblock copolymers (1344 cm^{-1}, C−H wagging and 1466 cm^{-1}, C−H bending) and silica (952 cm^{-1}, Si−OH stretching) are present in all the NCs studied. OA-capped DSNPs are observed in both DSNPs@NCs and DSNPs+sPDI@NCs, and sPDI features appeared within DSNPs+sPDI@NCs and sPDI@NCs. The spectra in Figure S3 demonstrates the absorption profile of sPDI aggregates in the NCs. Compared to the sPDI in THF (sPDI monomers), the absorption band width of the encapsulated sPDI is broadened and red-shiftted to 900 nm, their main absorption peaks shift from ~680 nm to ~720 nm, indicating the success of sPDI J-aggregations.[32] There are no changes in the band shape amongst the three groups of DSNPs+sPDI@NCs with various sPDI loading, suggesting that the different loading amounts do not affect the interactions between sPDI molecules in the NCs.

Monitoring temperature during heating upon 793 nm irradiation

Accurate temperature monitoring by nanothermometer during heating: in water dispersions of DSNPs@NCs and DSNPs+sPDI@NCs, Nd^{3+} emission from DSNPs was used to optically determine the temperature of the dispersion. Our group recently reported that the photoluminescence ratio thermometric parameter Δ (=I_1(1050.7-1055.5 nm)/I_2(1055.9-1057.2 nm)) defined for the most intense Nd^{3+} emission band around 1060 nm, shows high temperature

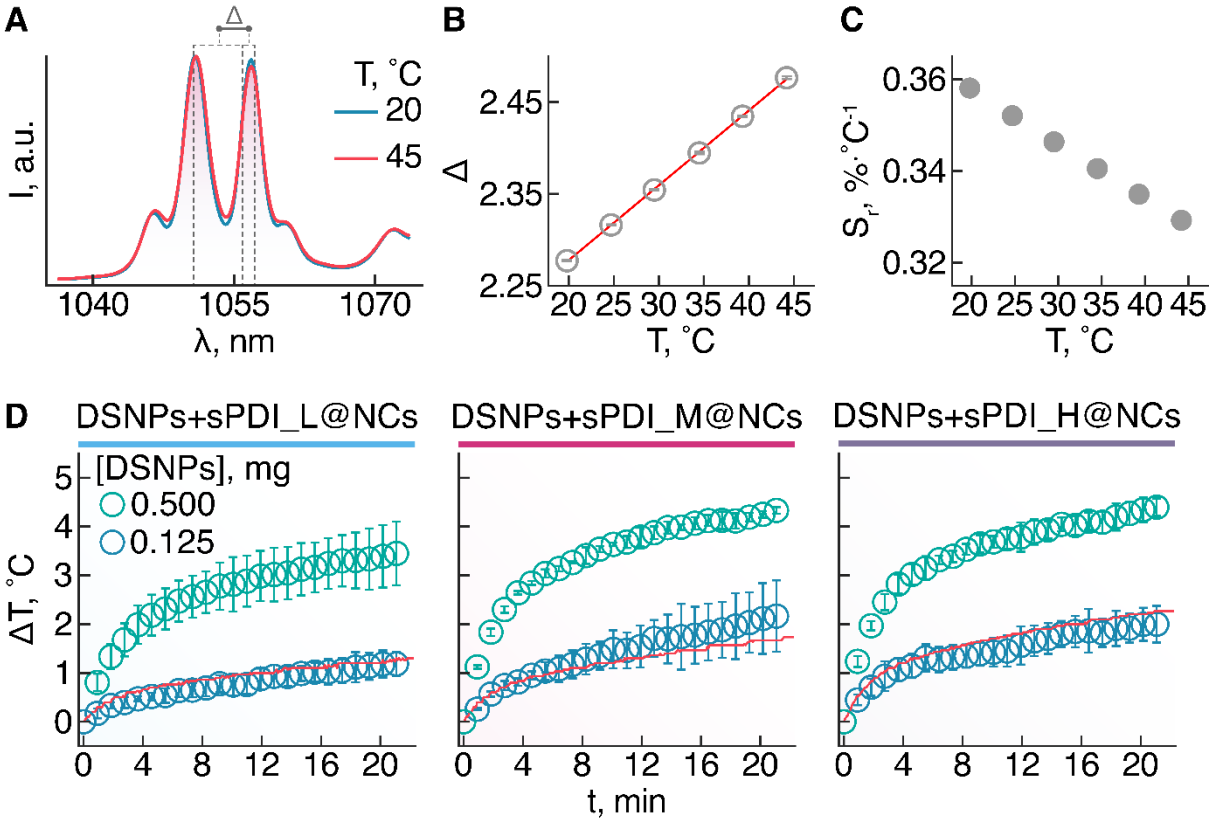

Figure 2. (A) Nd^{3+} DS emission around 1060 nm at different temperatures of the NCs dispersion. Integration ranges used to construct thermometric parameter **Δ** are also shown. (B) thermometric parameter **Δ** increases linearly with temperature increase). (C) shows a relative temperature sensitivity of 0.35% °C^{-1} at 20 °C. (D) Measuring heating of samples DSNPs+sPDI_L@NCs, DSNPs+sPDI_M@NCs, and DSNPs+sPDI_H@NCs under 10 W/cm^2 power density 793 nm laser irradiation with concentration of DSNPs set to 0.125 mg/mL (blue circle) and 0.5 mg/mL (green circle). The thermocouple readout measured for low concentration case as a reference is demonstrated by the red line.

sensitivity and relatively low temperature uncertainty, suitable for remote single-band photoluminescence thermometry.[67] Herein, the same wavelength integration ranges within the Nd^{3+} $^4F_{3/2} \rightarrow {}^4I_{11/2}$ radiative transition where used to build Δ calibration curves, which were subsequently used to determine heating generated by the co-encapsulated sPDI molecules (Figure 2A and B). The relative thermal sensitivity was around 0.35% °C^{-1} at 20 °C (Figure 2C and Figure S4), and the temperature uncertainty (δT) under the present acquisition conditions was around 0.15 °C.

Effects of the loading concentration of sPDI on photothermal conversion: the temperature of all the test samples is measured under 793 nm continuous laser irradiation (10 Wcm^{-2}) for 20 min. A thermocouple was placed inside the cuvette as a contact based reference.

Temperature increase of 1.1 °C caused by the DSNPs@NCs (0.5 mg/mL) (Figure S4A) indicated that there is minimal heat generation from the DSNPs themselves. The heating of DSNPs+sPDI@NCs with various sPDI concentrations is demonstrated in Figure 2D and S4. With concentration of DSNPs set to 0.125 mg/mL (blue circle), the content of sPDI is about 5 μg (DSNPs+sPDI_L@NCs), 10 μg (DSNPs+sPDI_M@NCs), and 17 μg (DSNPs+sPDI_H@NCs), respectively. The rapid temperature increase within first 4 min is observed in all the three samples, measured as 0.5 °C, 0.8 °C, and 1.1 °C from the thermal couple readout (red line). It then gradually increased to 1.1 °C, 1.6 °C, and 2.2 °C at the end of the irradiation, 20 min (Figure 2D). It reveals that the heating rate of DSNPs+sPDI@NCs can be directly tuned by the loading concentrations of sPDI during the synthesis. On the other hand, temperature changes measured *via* the NIR emission from DSNPs (blue circle) closely resemble the readout of the locally present thermocouple (Figure 2D). Increasing the DSNPs' concentration to 0.5 mg/mL (green circle), the content of sPDI in the three types of DSNPs+sPDI@NCs is increased by 4-fold, respectively, the heating ability is also increased (Figure 2D). For example, there is ~4 times of temperature increment observed in DSNPs+sPDI_M@NCs. However, the temperature changing is not obvious between DSNPs+sPDI_M@NCs and DSNPs+sPDI_H@NCs, suggesting a thermal saturated effect at the high concentration of sPDI.[32] However, the heat production is proportional to the sPDI content at the range of 5 to 40 μg, which can be a good reference used for subsequent in vitro and in vivo studies.

The photothermal stability is particularly important for organic PTT agents. Using DSNPs+sPDI_M@NCs (DSNPs/sPDI: 0.5 mg/40 μg) as an example, we evaluated the photothermal stability following multiple heating-cooling cycles. The temperature increment remains constant during the five laser ON/OFF cycles with 20 min for each cycle (Figure S5). Such good photothermal stability indicates the structural stability of the sPDI J-aggregates in

the NCs. This stems from the hybrid polymeric/silica structure, which confines the mobility of the intercalated sPDI molecules and thus the spatial arrangement of aggregates, resulting in their enhanced stability. More importantly, co-encapsulating DSNPs do not affect the photothermal stability of the sPDI aggregates.

In vitro evaluation of theranostic NCs

Cytotoxicity assay: to study the potential biomedical applications of the theranostic NCs, we first evaluated their cytotoxicity. Using MCF-7 breast cancer cells as a cellular model, DSNPs@NCs, sPDI@NCs, and DSNPs+sPDI_M@NCs were investigated by the cell proliferation assay. There was no significant cell growth inhibition observed up to a 0.13 mg/mL concentration of DSNPs (Figure S6A), which is selected for all further studies. To select the proper power density for the irradiation, we investigated the phototoxicity of 793 nm light to live cells. Upon irradiation at 2.5, 5, and 10 W cm^{-2} power densities for 20 min, no significant damage to cells was observed for any of the selected power densities (Figure S6B). To achieve high heating effect at lower DSNPs concentration, we used 10 Wcm^{-2} for subsequent irradiation experiments.

CT properties and in vitro CT imaging: CT imaging can provide deep anatomic structures with high spatial resolution and 3D tomography information based on differential X-ray absorption of tissue as a widely used clinical imaging tool. To study the potential diagnostic application of the synthesized NCs, the CT phantom images were acquired using DSNPs with various Lu^{3+} concentrations (0, 1, and 10 mmol/L) for CT measurement (Figure 3A). Hounsfield units (HU) [72] were measured to evaluate its X-ray attenuation ability. HU is a relative quantitative measurement of radio density used in the interpretation of CT images. The region of interest with greater x-ray beam attenuation has positive values and appears bright; in contrast, region of lesser x-ray attenuation has negative values and appears dark. With the Lu^{3+} concentration increasing, the CT images became brighter and the measured HU values

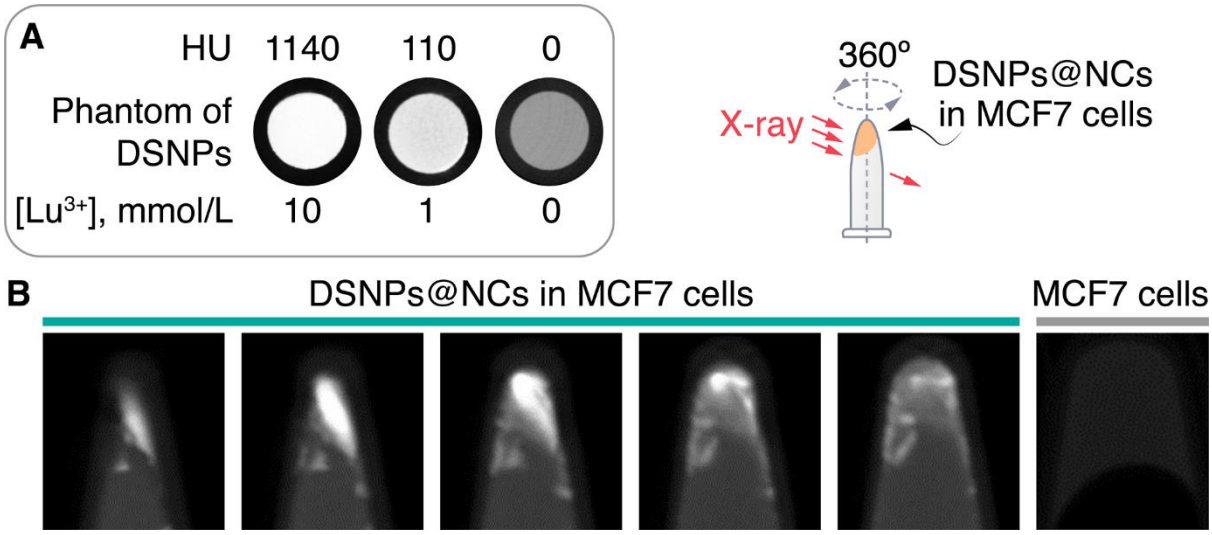

Figure 3. (A) CT images demonstrated the positive contrast enhancement of DSNPs with the designated Lu^{3+} concentrations. HU was calculated based on the mean of grey scales by CT scan. (B) MCF-7 cells were cultured with a maximal benign concentration of DSNPs@NCs with 0.5 mmol/L of Lu^{3+}, the un-treated cells were set as control. Both groups of cells were harvested in a PCR tube post 24 h incubation. The MCF-7 cell pellets, embedded with and without the DSNPs@NCs in the PCR tubes, were scanned by CT. Series of vertical cross-sectional images demonstrates the distribution of the cells in the PCR tubes. A scheme illustration of B is inserted.

also increased accordingly due to the higher attenuation coefficient of Lu^{3+}, suggesting that the DSNPs exhibited the expected CT contrast effect and could be applied in CT imaging. We further demonstrated the feasibility of our DSNPs for CT imaging in vitro. Series of vertical cross-sectional images of the cell pellets embedded with DSNPs@NCs as well as the control, are obtained by CT scan. A bright image is clearly demonstrated that the majority of cells are attached at the bottom and on one side wall of the PCR tube (Figure 3B), and the calculated HU value is 1450, significantly higher than the control one (0.06). Thus the positive contrast enhancement of DSNPs in MCF-7 cells is confirmed. It demonstrates the high potential of the DSNPs@NCs as CT contrast agents for imaging tracking and precisely locating the delivered payloads.

In vitro PTT effects: upon establishing the biocompatibility of the theranostic NCs, we proceeded to investigate the PTT on MCF-7 cells. Un-treated cells and those incubated with DSNPs@NCs were set as controls (see Materials and methods section). As shown in Figure 4A, no significant growth inhibition was observed in the control groups. For the cells incubated

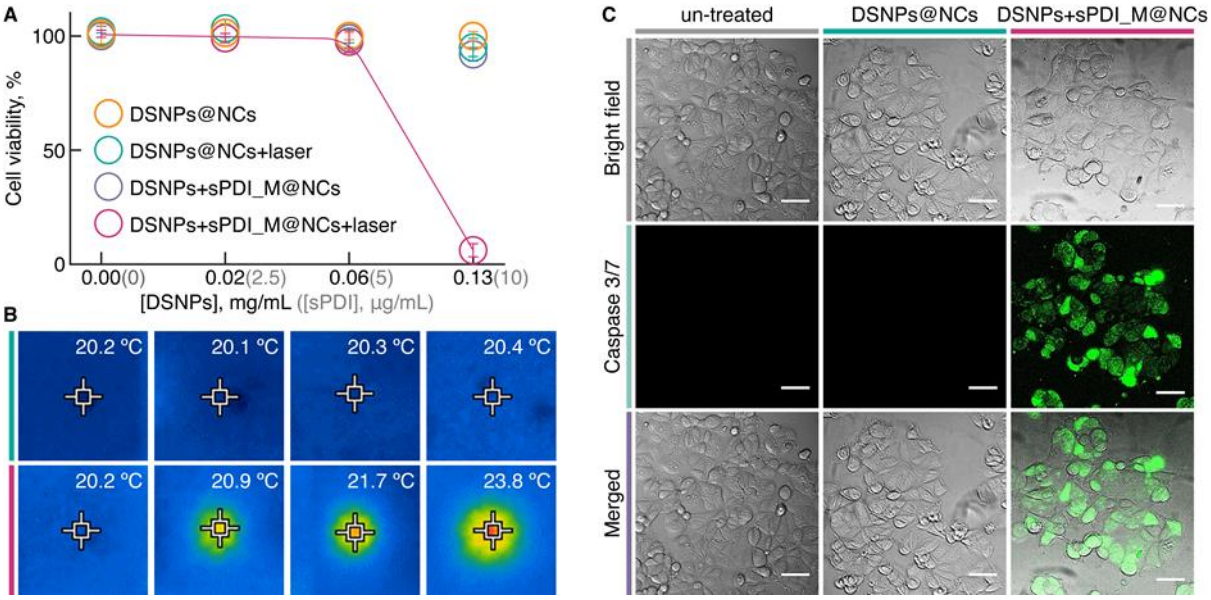

Figure 4. (A) Samples encapsulated with DSNPs only, DSNPs plus sPDI are divided into 4 groups and incubated with MCF-7 cells for 24 h, respectively. The cell growth is completely inhibited by DSNPs+sPDI_M@NCs upon 10 W/cm^2 power density 793 nm laser irradiation with concentration of DSNPs set to 0.13 mg/mL (PDI ~ 2 µg), while the other 3 groups remain unaffected. Line in A is guide for the eye. (B) The temperatures of culture medium, containing the cells incubated with DSNPs+sPDI_M@NCs are measured using an IR gun before (a) and post irradiations at various sPDI content (b) 0.5 µg, (c) 1 µg, and (d) 2 µg. (C) Confocal fluorescence microscopy images of MCF-7 cells: untreated, incubated with DSNPs@NCs (0.13 mg/mL), and DSNPs+sPDI@NCs (0.13 mg/mL of DSNPs with 10 µg/mL of sPDI). Cell nuclei stained by Caspase 3/7 detection reagent (green colour) (λ_{ex} = 488 nm, λ_{em} = 525 nm) indicating the apoptotic cells. Scale bars in all images correspond to 50 µm.

with DSNPs+sPDI_M@NCs at different concentrations and irradiated under 793 nm light (10 Wcm^{-2}) for 20 min, we observed a sudden and complete growth inhibition at 24 h post irradiation at the dose of 0.13 mg/mL (DSNPs) / 10 µg/mL (sPDI). Meanwhile we measured the temperature increment using an IR thermometer (IR gun) at the end of 20 min irradiation. It shows significant temperature increase up to 3.6 °C in the wells of cells incubated with the theranostic NCs (Figure 4B). This indicates that the cell growth inhibition is induced by the PTT effect of the sPDI aggregates. Cancer hyperthermia (or thermal therapy) requires a local temperature increment in tumors up to cytotoxic levels (43 – 45°C),[73] and the cellular homeostasis can be maintained within 37 – 41°C.[1] Thus we observed a sudden cell growth inhibition, revealing that 3.6 °C increment is enough for complete inhibition of the proliferation of in vitro cultured MCF-7 cells. To further confirm the PTT induced growth inhibition, we

analysed the apoptosis induction by staining the cells with a fluorescent assay Caspase 3/7 green.[74-76] This agent is intrinsically non-fluorescent, but in the presence of activated caspase 3/7 (an indicator of apoptosis), produces a bright green-fluorescent signal (λ_{ex} = 488 nm, λ_{em} = 530 nm). Following the same irradiation treatment, cells incubated with DSNPs+sPDI_M@NCs, as well as the control groups, were incubated with Caspase 3/7 green, and imaged under the fluorescence confocal microscope (Figure. 4C). Green luminescence of the apoptosis marker was observed in the cells treated with the DSNPs+sPDI_M@NCs upon 793 nm laser irradiation compared to the other 2 groups, revealing the induction of cell apoptosis. These results are in a good agreement with a previous report that lower elevated temperatures lead to cell apoptosis rather than necrosis.[7] Altogether, it proved that the developed DSNPs+sPDI@NCs can inhibit cell growth through apoptosis in MCF-7 cells.

Conclusion and perspectives

We synthesized theranostic nanocapsules co-encapsulating inorganic $LiLuF_4$: 10 mol% Nd^{3+}@$LiLuF_4$ DSNPs and organic sPDI for PTT. The Lu^{3+} in the host matrix, acting as a CT contrast agent, allows for tracking and locating the target of interest. Upon 793 nm irradiation the sPDI aggregates convert light to heat *via* non-radiative relaxation, resulting in a local temperature increment, which is locally detected by the Nd^{3+} $^4F_{3/2} \rightarrow {}^4I_{11/2}$ transition of the co-encapsulated DSNPs. As nanothermometers, DSNPs displayed relative thermal sensitivity around 0.35% $°C^{-1}$ and thermal uncertainty around 0.15 °C at room temperature. These theranostic nanocapsules demonstrated excellent biocompatibility, photothermal stability and a strong PTT effect against MCF-7 breast cancer cells. A positive contrast enhancement is also exhibited in the CT images of MCF-7 cells, showing the potential for imaging-guided PTT. Overall, these theranostic NCs provide a unique path to furnish NIR-controlled heating and temperature monitoring, aiming for the localized non-invasive PTT. The PTT efficacy and the CT positive contrast enhancement of the developed NCs will be further

expanded upon *in vivo* studies. This system could be extended to encompass various therapeutic, diagnostic or target agents, thus bringing theranostic functionalities to the precise nanomedicine.

Experimental section

Synthesis of $LiLuF_4$: 10 mol% Nd^{3+}@$LiLuF_4$ DSNPs

Lu_2O_3 (REacton, 99.9%), Nd_2O_3 (REacton, 99.999%), trifluoroacetic acid (99%), 1-octadecene (ODE, 90%), and oleic acid (OA, 90%) were purchased from Alfa Aesar (USA). Lithium trifluoroacetate (97%) and oleylamine (OM, 70%) were obtained from Sigma-Aldrich (USA). All chemicals were used without further purification.

Precursor preparation: 0.45 mmol Lu_2O_3 and 0.05 mmol Nd_2O_3 was mixed with 5 mL trifluoroacetic acid and 5 mL of water in 100 mL three-neck round bottom flasks to prepared 1 mmol lanthanide (Ln) trifluoroacetate precursors for the synthesis of $LiLuF_4$:Nd^{3+} (10% Nd^{3+} doping) core. The mixtures were refluxed under vigorous stirring at 80 ºC until the solutions became clear. The the temperature was decreased to 60 ºC to evaporate the residual liquid. Precursors for $LiLuF_4$ shell were prepared similarly from Lu_2O_3.

DSNP synthesis: Core/shell DSNPs were prepared by modified thermal-decomposition method.[67] First nuclei (FN) formation and stabilization were involved for core synthesis.

FN formation: Dried Ln trifluoroacetate precursors were mixed with 1.0 mmol lithium trifluoroacetate, 5 mL OA, 5mL OM and 10 mL ODE. Solution was degassed at 110 ºC under vacuum for 30 min. After degassing, the solution was back-filled with argon (Ar), the temperature was raised to 330 ºC. After 1 h reaction, the solution was then cooled to room temperature (RT). Magnetic stirring was maintained during the process.

Stabilization: Core DSNPs were formed by the stabilization of FN with excess of OA and ODE. FN (0.5 mmol, ~ 10 mL of stock solution) was mixed with 15 mL each of OA and ODE in a 100 ml three-neck round bottom flask. Similarly, the solution was degassed at 110 ºC under

vacuum for 30 min first, followed by 1 h reaction at 330 ºC in Ar environment. A small portion (0.5 mL) of core DSNPs was sampled for characterization after cooling.

Core shelling: Shelling of the core material was achieved *via* the hot-injection approach. Two solutions were prepared. Solution A was prepared by adding equal parts of OA and ODE into 0.1 mmol of stabilized DSNPs core in 100 mL three-neck round bottom flask. The total volume of solution A was 20 mL. Solution B was a mixture of 0.2 mmol Ln shelling precursors, 0.2 mmol lithium trifluoroacetate, and 10 mL each of OA and ODE. Both solutions were degassed under vacuum at 110 ºC for 30 min. After degassing, temperature of Solution A was raised to 315 ºC under Ar. Solution B was then injected into Solution A using a syringe and pump system (Harvard Apparatus Pump 11 Elite, USA). The injection rate was 1.5 mL/min. Solution cooled to RT after 1 h reaction. Resultant core/shell DSNPs were precipitated with ethanol, and washed sequentially with hexane/ethanol, toluene/acetone and hexane/ethanol (1/4 v/v in each case) *via* centrifugation (5400 RCF).

Encapsulation of DSNPs and sPDI

Pluronic® F127 ((ethylene oxide)$_{106}$(propylene oxide)$_{70}$(ethylene oxide)$_{106}$, PEO-PPO-PEO, MW = 12,600 g mol^{-1}), tetramethoxysilane (TMOS, 98%), tetrahydrofuran (THF, ≥99.9%) are purchased from Sigma-Aldrich. Bay-substituted dicyclohexylamino perylene diimide (sPDI) is obtained from our collaborators at Shandong University, China. sPDI was dissolved in THF at a concentration of 2 mg mL^{-1} (stock solution). The synthesized $LiLuF_4:Nd^{3+}$ (10%)@$LiLuF_4$ DSNPs dispersed in hexane (58.7 mg mL^{-1}) were used as stock solution.

Polymeric micelle/silica nanocapsules with various payloads were prepared by our recently established one-pot encapsulation approach.[63] Three groups of NCs are prepared. They are NCs with DCA-PDI (DCA-PDI@NCs), NCs with DSNPs (DSNPs@NCs), and NCs with both DSNPs and various amount of sPDI including DSNPs+DCA-PDI_L@NCs (lower sPDI),

DSNPs+DCA-PDI_M@NCs (medium sPDI), and DSNPs+DCA-PDI_H@NCs (higher sPDI). The synthesis parameters are listed in table S1.

sPDI@NCs: F127 (37.5 mg) was dissolved in THF (750 μL) and mixed with ZnPc (150 μL). After stirring at room temperature for 3 h, TMOS (55 μL) was added to the solution and sonicated for 1 min. The solution was injected into stirred deionized (DI) water (10 mL) at a rate of 60-90 μL min^{-1}. Stirring was continued for another 4 days for THF evaporation as well as TMOS hydrolysis and condensation. Afterwards, the solution was dialyzed against DI water for 24 h using a dialysis membrane (MWCO of 10,000 g mol^{-1}, Spectra/Por® regenerated cellulose). Finally, the solution was centrifuged for 10 min at 10,000 rpm, the supernatant was further passed through a 0.2 μm filter to remove large aggregates.

DSNPs@NCs: The designated amounts of DSNP stock solution was firstly air dried to remove hexane. Then, the dried DSNPs were re-dispersed in THF and mixed with F127. After stirring at room temperature for 3 h and sonicating for 10 min, The solution was injected into DI water (10 mL) at a rate of 60-90 μL min^{-1} while being stirred. Stirring was continued for 2 more days to evaporate THF. Afterwards, 30 μL of TMOS was dissolved in THF (300 μL) and injected at a rate of 60-90 μL min^{-1} into the solution. It was stirred at room temperature for another 2 days for hydrolysis and condensation of TMOS. The solution was then subjected to centrifugation (6,000 rpm for 30 min), discarding the supernatant containing empty (i.e., DSNP-free) NCs and re-dispersing the precipitates in DI water. The dispersion was further passed through a 0.2 μm filter to remove large aggregates.

DSNPs+sPDI@NCs: The air dried DSNPs were redispersed in THF and mixed with F127 and various amount of sPDI (0.3, 0.6, and 1.2 mg) to obtain three solutions. Each of the solutions was stirred for 3 h and sonocated for 10 min, and then injected into the 10 mL of DI water, respectively, following the protocol above discribed for the synthesis of DSNPs@NCs.

Characterization of the NCs

The crystalline phase of OA-capped DSNPs under investigation was analysed by X-ray diffraction (XRD) using a Bruker D8 Advanced Diffractometer, Cu Kα radiation (λ=1.5406 Å, power of the generator: 40 kV and 40 mA). Scan range was 20 – 80° 2θ, with a step size of 0.04° and a count time of 1s. The morphology and size distribution of the silica nanocapsules and DSNPs were determined by transmission electron microscopy (TEM) with a JEOL JEM-2010 microscope operating at 80 kV. The sample solution was prepared on a formvar/carbon film supported on a 300 mesh copper grid (3 mm in diameter). Inductively coupled plasma - atomic emission spectroscopy (ICP-AES) was used to determine the content of Li^{+}, Lu^{3+}, and Nd^{3+} in the DSNPs. The samples were digested in 70% HNO_3 with sonication at 65 ºC, and then diluted to below 5% HNO_3 before conducting ICP-AES measurements. Dynamic light scattering (DLS) was performed with Malvern Zetasizer Nano-S using a HeNe laser (633 nm) to measure the hydrodynamic size and size distribution of different nanocapsules. All measurements were conducted using DI water as the dispersant in a glass cuvette. A Fourier-Transform Infrared (FTIR) spectrophotometer (Varian 3100 Excalibur) was used to characterize the chemical composition of the synthesized NCs. For FTIR sample preparation, the aqueous suspensions of the synthesized NCs were freeze-dried and dispersed in KBr pellets. The UV-Visible (UV-VIS) absorption spectra were obtained using a Varian Cary 5000 spectrometer. The X-ray attenuation of DSNPs was measured using a preclinical micro-CT scanner (SkyScan 1176, Bruker Biospin, Germany) and their attenuation values were then calculated in Hounsfield units (HU).

Nanothermometry measurements

Temperature Sensitivity of DSNPs: The thermal response of the theranostic NCs in water was measured in the 20–45 °C temperature range at 5 °C increments. The temperature was changed using a temperature controlled cuvette holder (qpod 2e by Quantum Northwest,

Washington, USA). 10 min intervals were maintained between the measurements in order to assure the stabilization of set temperature across the sample.

Photoluminescence of different DSNPs was recorded under 793 nm laser diode excitation (CNI, China; 710 mW, ~3 mm diameter excitation spot size ≃ 10 W/cm2) with a Shamrock 500i monochromator (Andor, Ireland) equipped with an iDus InGaAs 1.7 NIR detector (Andor, Ireland). 4 s integration time per spectrum was used for calibration and heating measurements. Each heating experiment was done in a triplicate. Measurement data presented in Figure 2 was subsequently binned, with 10 data points per bin, to better appreciate the temperature readout. In order to remove any stray light from the excitation source long pass (LP) 830 nm filter (Semrock, Inc., USA) was used.

Nanothermometer characterizing parameters were calculated following the guidelines set by Brites et al.[77] PL intensity ratio (Δ) was estimated taking the ratio between the integrated intensities I_1(1050.7-1055.5 nm) and I_2(1055.9-1057.2 nm) at each temperature value:

$$\Delta = \frac{I_1}{I_2}$$

The relative thermal sensitivity (Sr) of the DSNPs was calculated as

$$S_r = \frac{1}{\Delta}\frac{\partial \Delta}{\partial T}$$

And the temperature uncertainty (δT) was given by

$$\delta T = \frac{1}{S_r}\frac{\delta \Delta}{\Delta}$$

The $\delta\Delta/\Delta$ was estimated by

$$\frac{\delta \Delta}{\Delta} = \sqrt{\left(\frac{\delta I_1}{I_1}\right)^2 + \left(\frac{\delta I_2}{I_2}\right)^2}$$

Here, δI_i and I_i were calculated by integrating, equivalent in range, baseline variation (noise, out of signal range), and the emission band (signal), respectively, thus obtaining the signal-to-noise ratio. (note, the above equations also appears in P24)

Cell culture and cytotoxicity assay

The breast cancer cells MCF-7 (American Type Culture Collection) were cultured in Dulbecco's modified Eagle medium (DMEM) (high glucose [4.5 g L^{-1}], with sodium pyruvate and L-glutamine), containing 10% fatal bovine serum (Invitrogen), 1% antibiotic with 100 UI ml^{-1} penicillin, and 100 mg ml^{-1} streptomycin (Invitrogen). Cell incubation was maintained at 37 ºC, and 5% CO_2. The culture medium was changed two to three times a week and cells were passaged serially using 0.25% trypsin/EDTA (Invitrogen).

The cytotoxicity of DSNPs@NCs, sPDI@NCs, and DSNPs+sPDI_M@NCs was evaluated by determining the viability of MCF-7 breast cancer cells using Cell Counting Kit-8 (CCK-8) (Sigma-Aldrich),[78] of which highly water-soluble tetrazolium salt is reduced by dehydrogenases in cells to give an orange colour product (formazan). The amount of the formazan dye generated is directly proportional to the number of living cells. Briefly, MCF-7 cells were seeded into 96 well plates at a density of 10,000 cells per well and incubated for 24 h. Three groups of the nanocapsules with the designated concentrations, containing DSNPs (0.03, 0.06, 0.13, 0.26 mg mL^{-1}) or sPDI (2.5, 5, 10, 20 µg mL^{-1}), were added to the cultured cells. After incubation with the NCs for 72 h, CCK-8 solution was added into cultured cells and incubated for another 2 h. The absorbance at 450 nm of the mixture was measured using a Benchmark Plus microplate spectrophotometer (Bio-Rad). The absorbance values obtained were recalculated as percentage values of viability,

$$\text{Viability (\%)} = 100 \times (A_T - A_B)/(A_C - A_B)$$

where A_T, is the absorption values of wells containing nanocapsules, A_C is the absorption values of control wells, and A_B is the absorption values of a blank solution. Data were expressed as mean ± standard deviation (SD). Statistical significance of differences observed between groups was calculated using a two-tail paired Student's t-Test at the 95% confidence level. Significance was represented as p-value < 0.05.

In vitro PTT efficacy analysis

To determine the therapeutic effect of the theranostic NCs, we evaluated the growth inhibition and apoptosis of breast cancer MCF-7 cells after 793 nm irradiation (10 W cm^{-2}). The sequential irradiation was done as follows: 20 min of irradiation, 40 min rest, 20 min of irradiation. The total irradiation period was 40 min. Cell growth inhibition by DSNPs+sPDI_M@NCs, DSNPs@NCs related to the untreated cells, was tested using CCK-8 cell proliferation assay as described in the previous section. The apoptosis induction was evaluated using Caspase-3/7 green detection reagent (Invitrogen), a fluorescence probe that presents green emission upon 488 nm excitation if reacted with the Caspase-3/7, released by the apoptotic cells. Briefly, 15,000 cells were seeded in eight-chambered cover glass plate (LAB-TEK, Chambered Cover glass System), and incubated with the above 2 groups of NCs containing 0.13 mg mL^{-1} DSNPs and / or 2 μg sPDI for 24 h before the sequential irradiation treatment. After another 24 h of incubation, the Caspase-3/7 green detection reagent was added and incubated with the cells for 6 h to allow the accumulation of the reagent into the cells. Live cell imaging was performed using a confocal laser scanning microscope (Nikon). 20×/0.5 NA dry objective (Nikon) was selected for imaging acquisition. The fluorescence image was acquired at λ_{exc} = 488 nm and λ_{exc} = 530 nm.

CT imaging

Various Lu^{3+} concentrations of DSNPs (0, 1, and 10 mmol/L) were mixed with 0.5% agarose solution in a series of 0.2 mL PCR tubes for phantom test. Their X-ray attenuation values were then calculated in Hounsfield units (HU). For in vitro CT imaging, MCF cells were seeded in a 6-well plate (15,000 cells per well) and incubated for 24 h, DSNPs@NCs containing 0.5 mmol/L of Lu^{3+} were then added. The un-treated cells were set as control. After 24 h incubation, the cells were detached by 0.25% tripsin-EDTA (Invitrogen), and washed with 1x PBS 3 times to remove the non-uptake DSNPs@NCs, and collected in a 0.2 mL PCR tube. CT

images were obtained using a preclinical micro-CT scanner (SkyScan 1176, Bruker Biospin, Germany). Imaging parameters are as follows: image pixel size, 35 μm; voltage, 40 KV; current, 600 μA; rotation steps, 0.7 degrees; exposure time 37 ms.

Supporting information

Characterizations of DSNPs (TEM and XRD analysis), Characterizations of NCs (FTIR, absorbance spectra, heat generation and nanothermometry measurements, heating and cooling cycles)

Author Contributions

The manuscript was written through contributions of all authors. All authors have given approval to the final version of the manuscript

Notes

The authors declare no competing financial interest.

ACKNOWLEDGMENT

F.V. acknowledges funding from the Natural Sciences and Engineering Research Council (NSERC) of Canada through the Discovery Grants program and the Discovery Accelerator Supplement (DAS) award, the Canada Foundation for Innovation for infrastructure and its operation, and the Fonds de Recherche du Québec-Nature et technologies (FRQNT). F.R. acknowledges NSERC for a Discovery Grant and the Canada Research Chairs program for funding and partial salary support. MW and Alex Chang are grateful to the Johns Hopkins Singapore Research Fund provided by Private limited Company for supporting their Santa Fe research programme. MW appreciates Dr. Chen, Way Cherng's (Bruker Singapore Pte. Ltd.) assistance for the experiments of CT scan. XL, MN and KB acknowledge the support of A*STAR, Singapore.

Reference

1. Jaque, D.; Martinez Maestro, L.; del Rosal, B.; Haro-Gonzalez, P.; Benayas, A.; Plaza, J. L.; Martin Rodriguez, E.; Garcia Sole, J. Nanoparticles for Photothermal Therapies. *Nanoscale* **2014,** 6, 9494-9530.

2. Zhi, D.; Yang, T.; O'Hagan, J.; Zhang, S.; Donnelly, R. F. Photothermal Therapy. *J. Controlled Release* **2020,** 325, 52-71.

3. Minchinton, A. I.; Tannock, I. F. Drug Penetration in Solid Tumors. *Nat. Rev. Cancer* **2006,** 6, 583-592.

4. Gerweck, L. E. Hyperthermia in Cancer Therapy: The Biological Basis and Unresolved Questions. *Cancer Res.* **1985,** 45, 3408-3414.

5. Chen, Q.; Xu, L.; Liang, C.; Wang, C.; Peng, R.; Liu, Z. Photothermal Therapy with Immune-Adjuvant Nanoparticles Together with Checkpoint Blockade for Effective Cancer Immunotherapy. *Nat. commun.* **2016,** 7, 13193.

6. Yang, Y.; Zhu, W.; Dong, Z.; Chao, Y.; Xu, L.; Chen, M.; Liu, Z. 1d Coordination Polymer Nanofibers for Low-Temperature Photothermal Therapy. *Adv. Mater.* **2017,** 29, 1703588.

7. Huang, L.; Li, Y.; Du, Y.; Zhang, Y.; Wang, X.; Ding, Y.; Yang, X.; Meng, F.; Tu, J.; Luo, L.; Sun, C. Mild Photothermal Therapy Potentiates Anti-Pd-L1 Treatment for Immunologically Cold Tumors *Via* an All-in-One and All-in-Control Strategy. *Nat. commun.* **2019,** 10, 4871.

8. Lugade, A. A.; Moran, J. P.; Gerber, S. A.; Rose, R. C.; Frelinger, J. G.; Lord, E. M. Local Radiation Therapy of B16 Melanoma Tumors Increases the Generation of Tumor Antigen-Specific Effector Cells That Traffic to the Tumor. *J. Immunol.* **2005,** 174, 7516-7523.

9. Lee, Y.; Auh, S. L.; Wang, Y.; Burnette, B.; Wang, Y.; Meng, Y.; Beckett, M.; Sharma, R.; Chin, R.; Tu, T.; Weichselbaum, R. R.; Fu, Y. X. Therapeutic Effects of Ablative Radiation

on Local Tumor Require Cd8+ T Cells: Changing Strategies for Cancer Treatment. *Blood* **2009,** 114, 589-595.

10. van der Zee, J. Heating the Patient: A Promising Approach? *Ann. Oncol.* **2002,** 13, 1173-1184.

11. Hildebrandt, B.; Wust, P.; Ahlers, O.; Dieing, A.; Sreenivasa, G.; Kerner, T.; Felix, R.; Riess, H. The Cellular and Molecular Basis of Hyperthermia. *Crit. Rev. Oncol. Hematol.* **2002,** 43, 33-56.

12. Wust, P.; Hildebrandt, B.; Sreenivasa, G.; Rau, B.; Gellermann, J.; Riess, H.; Felix, R.; Schlag, P. M. Hyperthermia in Combined Treatment of Cancer. *Lancet Oncol.* **2002,** 3, 487-497.

13. Falk, M. H.; Issels, R. D. Hyperthermia in Oncology. *Int. J. Hyperthermia* **2001,** 17, 1-18.

14. Kapp, D. S.; Hahn, G. M.; Carlson, R. W., Principles of Hyperthermia. In *Holland-Frei Cancer Medicine. 5th Edition*, BC Decker: 2000.

15. de Melo-Diogo, D.; Pais-Silva, C.; Dias, D. R.; Moreira, A. F.; Correia, I. J. Strategies to Improve Cancer Photothermal Therapy Mediated by Nanomaterials. *Adv. Healthcare Mater.* **2017,** 6, 1700073.

16. Doughty, A. C.; Hoover, A. R.; Layton, E.; Murray, C. K.; Howard, E. W.; Chen, W. R. Nanomaterial Applications in Photothermal Therapy for Cancer. *Materials* **2019,** 12, 779.

17. Marin, R.; Skripka, A.; Besteiro, L. V.; Benayas, A.; Wang, Z.; Govorov, A. O.; Canton, P.; Vetrone, F. Highly Efficient Copper Sulfide-Based near-Infrared Photothermal Agents: Exploring the Limits of Macroscopic Heat Conversion. *Small* **2018,** 14, 1803282.

18. Rastinehad, A. R.; Anastos, H.; Wajswol, E.; Winoker, J. S.; Sfakianos, J. P.; Doppalapudi, S. K.; Carrick, M. R.; Knauer, C. J.; Taouli, B.; Lewis, S. C.; Tewari, A. K.; Schwartz, J. A.; Canfield, S. E.; George, A. K.; West, J. L.; Halas, N. J. Gold Nanoshell-

Localized Photothermal Ablation of Prostate Tumors in a Clinical Pilot Device Study. *Proc. Natl. Acad. Sci. U. S. A.* **2019,** 116, 18590-18596.

19. Sharifi, S.; Behzadi, S.; Laurent, S.; Laird Forrest, M.; Stroeve, P.; Mahmoudi, M. Toxicity of Nanomaterials. *Chem. Soc. Rev.* **2012,** 41, 2323-2343.

20. Zheng, X.; Xing, D.; Zhou, F.; Wu, B.; Chen, W. R. Indocyanine Green-Containing Nanostructure as near Infrared Dual-Functional Targeting Probes for Optical Imaging and Photothermal Therapy. *Mol. Pharm.* **2011,** 8, 447-456.

21. Yu, J.; Javier, D.; Yaseen, M. A.; Nitin, N.; Richards-Kortum, R.; Anvari, B.; Wong, M. S. Self-Assembly Synthesis, Tumor Cell Targeting, and Photothermal Capabilities of Antibody-Coated Indocyanine Green Nanocapsules. *J. Am. Chem. Soc.* **2010,** 132, 1929-1938.

22. Cheng, L.; Wang, C.; Feng, L.; Yang, K.; Liu, Z. Functional Nanomaterials for Phototherapies of Cancer. *Chem. Rev.* **2014,** 114, 10869-10939.

23. Jung, H. S.; Verwilst, P.; Sharma, A.; Shin, J.; Sessler, J. L.; Kim, J. S. Organic Molecule-Based Photothermal Agents: An Expanding Photothermal Therapy Universe. *Chem. Soc. Rev.* **2018,** 47, 2280-2297.

24. Cheng, L.; He, W.; Gong, H.; Wang, C.; Chen, Q.; Cheng, Z.; Liu, Z. Pegylated Micelle Nanoparticles Encapsulating a Non-Fluorescent near-Infrared Organic Dye as a Safe and Highly-Effective Photothermal Agent for in Vivo Cancer Therapy. *Adv. Funct. Mater.* **2013,** 23, 5893-5902.

25. Yue, C.; Liu, P.; Zheng, M.; Zhao, P.; Wang, Y.; Ma, Y.; Cai, L. Ir-780 Dye Loaded Tumor Targeting Theranostic Nanoparticles for Nir Imaging and Photothermal Therapy. *Biomaterials* **2013,** 34, 6853-6861.

26. Luo, S.; Tan, X.; Fang, S.; Wang, Y.; Liu, T.; Wang, X.; Yuan, Y.; Sun, H.; Qi, Q.; Shi, C. Mitochondria-Targeted Small-Molecule Fluorophores for Dual Modal Cancer Phototherapy. *Adv. Funct. Mater.* **2016,** 26, 2826-2835.

27. Zhang, J.; Liu, Z.; Lian, P.; Qian, J.; Li, X.; Wang, L.; Fu, W.; Chen, L.; Wei, X.; Li, C. Selective Imaging and Cancer Cell Death *Via* Ph Switchable near-Infrared Fluorescence and Photothermal Effects. *Chem. Sci.* **2016,** 7, 5995-6005.

28. Cui, C.; Yang, Z.; Hu, X.; Wu, J.; Shou, K.; Ma, H.; Jian, C.; Zhao, Y.; Qi, B.; Hu, X. Organic Semiconducting Nanoparticles as Efficient Photoacoustic Agents for Lightening Early Thrombus and Monitoring Thrombolysis in Living Mice. *ACS nano* **2017,** 11, 3298-3310.

29. Yang, Z.; Tian, R.; Wu, J.; Fan, Q.; Yung, B. C.; Niu, G.; Jacobson, O.; Wang, Z.; Liu, G.; Yu, G. Impact of Semiconducting Perylene Diimide Nanoparticle Size on Lymph Node Mapping and Cancer Imaging. *ACS nano* **2017,** 11, 4247-4255.

30. Jiang, Y.; Pu, K. Advanced Photoacoustic Imaging Applications of near-Infrared Absorbing Organic Nanoparticles. *Small* **2017,** 13, 1700710.

31. Hu, X.; Lu, F.; Chen, L.; Tang, Y.; Hu, W.; Lu, X.; Ji, Y.; Yang, Z.; Zhang, W.; Yin, C. Perylene Diimide-Grafted Polymeric Nanoparticles Chelated with Gd3+ for Photoacoustic/T 1-Weighted Magnetic Resonance Imaging-Guided Photothermal Therapy. *ACS Appl. Mater. Interfaces* **2017,** 9, 30458-30469.

32. Li, H.; Zhang, Y.; Chen, B.; Wang, Y.; Teh, C.; Ng, G. H.; Meng, J.; Huang, Z.; Dong, W.; Tan, M. Y. J-Aggregation of Perylene Diimides in Silica Nanocapsules for Stable near-Infrared Photothermal Conversion. *ACS Appl. Bio Mater.* **2019,** 2, 1569-1577.

33. Jiao, Y.; Liu, K.; Wang, G.; Wang, Y.; Zhang, X. Supramolecular Free Radicals: Near-Infrared Organic Materials with Enhanced Photothermal Conversion. *Chem. Sci.* **2015,** 6, 3975-3980.

34. Würthner, F. Perylene Bisimide Dyes as Versatile Building Blocks for Functional Supramolecular Architectures. *Chem. Commun.* **2004**, 1564-1579.

35. Pang, C. L., *Hyperthermia in Oncology*. CRC Press: 2015.

36. Chu, K. F.; Dupuy, D. E. Thermal Ablation of Tumors: Biological Mechanisms and Advances in Therapy. *Nat. Rev. Cancer* **2014,** 14, 199-208.

37. Fratila, R. M.; De La Fuente, J. M., *Nanomaterials for Magnetic and Optical Hyperthermia Applications*. Elsevier: 2018.

38. Quintanilla, M.; Liz-Marzan, L. M. Guiding Rules for Selecting a Nanothermometer. *Nano Today* **2018,** 19, 126-145.

39. Wang, F.; Wan, H.; Ma, Z.; Zhong, Y.; Sun, Q.; Tian, Y.; Qu, L.; Du, H.; Zhang, M.; Li, L. Light-Sheet Microscopy in the near-Infrared Ii Window. *Nat. Methods* **2019,** 16, 545-552.

40. Hemmer, E.; Benayas, A.; Légaré, F.; Vetrone, F. Exploiting the Biological Windows: Current Perspectives on Fluorescent Bioprobes Emitting above 1000 Nm. *Nanoscale Horiz.* **2016,** 1, 168-184.

41. Vetrone, F.; Naccache, R.; Zamarrón, A.; Juarranz de la Fuente, A.; Sanz-Rodríguez, F.; Martinez Maestro, L.; Martín Rodriguez, E.; Jaque, D.; García Solé, J.; Capobianco, J. A. Temperature Sensing Using Fluorescent Nanothermometers. *ACS nano* **2010,** 4, 3254-3258.

42. Skripka, A.; Karabanovas, V.; Jarockyte, G.; Marin, R.; Tam, V.; Cerruti, M.; Rotomskis, R.; Vetrone, F. Decoupling Theranostics with Rare Earth Doped Nanoparticles. *Adv. Funct. Mater.* **2019,** 29, 1807105.

43. Hemmer, E.; Acosta-Mora, P.; Mendez-Ramos, J.; Fischer, S. Optical Nanoprobes for Biomedical Applications: Shining a Light on Upconverting and near-Infrared Emitting Nanoparticles for Imaging, Thermal Sensing, and Photodynamic Therapy. *J. Mater. Chem. B* **2017,** 5, 4365-4392.

44. Hemmer, E.; Vetrone, F. Nanothermometry Using Upconverting Nanoparticles. *Upconverting Nanomaterials: Perspectives, Synthesis, and Applications* **2016**, 319.

45. Skripka, A.; Benayas, A.; Marin, R.; Canton, P.; Hemmer, E.; Vetrone, F. Double Rare-Earth Nanothermometer in Aqueous Media: Opening the Third Optical Transparency Window to Temperature Sensing. *Nanoscale* **2017,** 9, 3079-3085.

46. Jaque, D.; Vetrone, F. Luminescence Nanothermometry. *Nanoscale* **2012,** 4, 4301-4326.

47. Wawrzynczyk, D.; Bednarkiewicz, A.; Nyk, M.; Strek, W.; Samoc, M. Neodymium (Iii) Doped Fluoride Nanoparticles as Non-Contact Optical Temperature Sensors. *Nanoscale* **2012,** 4, 6959-6961.

48. Benayas, A.; Del Rosal, B.; Pérez-Delgado, A.; Santacruz-Gómez, K.; Jaque, D.; Hirata, G. A.; Vetrone, F. Nd: Yag near-Infrared Luminescent Nanothermometers. *Adv. Opt. Mater.* **2015,** 3, 687-694.

49. Suta, M.; Antić, Ž.; Đorđević, V.; Kuzman, S.; Dramićanin, M. D.; Meijerink, A. Making Nd3+ a Sensitive Luminescent Thermometer for Physiological Temperatures—an Account of Pitfalls in Boltzmann Thermometry. *Nanomaterials* **2020,** 10, 543.

50. Kolesnikov, I.; Golyeva, E.; Kurochkin, M.; Lähderanta, E.; Mikhailov, M. Nd3+-Doped Yvo4 Nanoparticles for Luminescence Nanothermometry in the First and Second Biological Windows. *Sens. Actuators, B* **2016,** 235, 287-293.

51. Skripka, A.; Benayas, A.; Brites, C. D. S.; Martín, I. R.; Carlos, L. D.; Vetrone, F. Inert Shell Effect on the Quantum Yield of Neodymium-Doped near-Infrared Nanoparticles: The Necessary Shield in an Aqueous Dispersion. *Nano Lett.* **2020,** 20, 7648-7654.

52. Cerón, E. N.; Ortgies, D. H.; Del Rosal, B.; Ren, F.; Benayas, A.; Vetrone, F.; Ma, D.; Sanz-Rodríguez, F.; Solé, J. G.; Jaque, D. Hybrid Nanostructures for High-Sensitivity Luminescence Nanothermometry in the Second Biological Window. *Adv. Mater.* **2015,** 27, 4781-4787.

53. Marciniak, L.; Pilch, A.; Arabasz, S.; Jin, D.; Bednarkiewicz, A. Heterogeneously Nd 3+ Doped Single Nanoparticles for Nir-Induced Heat Conversion, Luminescence, and Thermometry. *Nanoscale* **2017,** 9, 8288-8297.

54. Rocha, U.; Upendra Kumar, K.; Jacinto, C.; Ramiro, J.; Caamano, A. J.; García Solé, J.; Jaque, D. Nd3+ Doped Laf3 Nanoparticles as Self-Monitored Photo-Thermal Agents. *Appl. Phys. Lett.* **2014,** 104, 053703.

55. Kolesnikov, I.; Golyeva, E.; Kalinichev, A.; Kurochkin, M.; Lähderanta, E.; Mikhailov, M. Nd3+ Single Doped Yvo4 Nanoparticles for Sub-Tissue Heating and Thermal Sensing in the Second Biological Window. *Sens. Actuators, B* **2017,** 243, 338-345.

56. Xu, L.; Li, J.; Lu, K.; Wen, S.; Chen, H.; Shahzad, M. K.; Zhao, E.; Li, H.; Ren, J.; Zhang, J. Sub-10 Nm Nandf4 Nanoparticles as near-Infrared Photothermal Probes with Self-Temperature Feedback. *ACS Appl. Nano Mater.* **2020,** 3, 2517-2526.

57. Quintanilla, M.; García, I.; de Lázaro, I.; García-Alvarez, R.; Henriksen-Lacey, M.; Vranic, S.; Kostarelos, K.; Liz-Marzán, L. M. Thermal Monitoring During Photothermia: Hybrid Probes for Simultaneous Plasmonic Heating and near-Infrared Optical Nanothermometry. *Theranostics* **2019,** 9, 7298.

58. Ramirez-Garcia, G.; Honorato-Colin, M. Á.; De la Rosa, E.; López-Luke, T.; Panikar, S. S.; de Jesus Ibarra-Sanchez, J.; Piazza, V. Theranostic Nanocomplex of Gold-Decorated Upconversion Nanoparticles for Optical Imaging and Temperature-Controlled Photothermal Therapy. *Journal of Photochemistry and Photobiology A: Chemistry* **2019,** 384, 112053.

59. Huang, Y.; Skripka, A.; Labrador-Páez, L.; Sanz-Rodríguez, F.; Haro-González, P.; Jaque, D.; Rosei, F.; Vetrone, F. Upconverting Nanocomposites with Combined Photothermal and Photodynamic Effects. *Nanoscale* **2018,** 10, 791-799.

60. Suo, H.; Zhao, X.; Zhang, Z.; Wu, Y.; Guo, C. Upconverting Luvo4: Nd3+/Yb3+/Er3+@ Sio2@ Cu2s Hollow Nanoplatforms for Self-Monitored Photothermal Ablation. *ACS Appl. Mater. Interfaces* **2018,** 10, 39912-39920.

61. Drobczyński, S.; Prorok, K.; Tamarov, K.; Duś-Szachniewicz, K.; Lehto, V.-P.; Bednarkiewicz, A. Toward Controlled Photothermal Treatment of Single Cell: Optically Induced Heating and Remote Temperature Monitoring in Vitro through Double Wavelength Optical Tweezers. *ACS Photonics* **2017,** 4, 1993-2002.

62. Mitchell, M. J.; Billingsley, M. M.; Haley, R. M.; Wechsler, M. E.; Peppas, N. A.; Langer, R. Engineering Precision Nanoparticles for Drug Delivery. *Nat. Rev. Drug Discovery* **2021,** 20, 101-124.

63. Wang, M.; Zhang, Y.; Ng, M.; Skripka, A.; Cheng, T.; Li, X.; Bhakoo, K. K.; Chang, A. Y.; Rosei, F.; Vetrone, F. One-Pot Synthesis of Theranostic Nanocapsules with Lanthanide Doped Nanoparticles. *Chem. Sci.* **2020,** 11, 6653-6661.

64. Clark, A. E.; Qin, C.; Li, A. D. Beyond Exciton Theory: A Time-Dependent Dft and Franck− Condon Study of Perylene Diimide and Its Chromophoric Dimer. *J. Am. Chem. Soc.* **2007,** 129, 7586-7595.

65. Alarcos, N.; Cohen, B.; Ziółek, M.; Douhal, A. Photochemistry and Photophysics in Silica-Based Materials: Ultrafast and Single Molecule Spectroscopy Observation. *Chem. Rev.* **2017,** 117, 13639-13720.

66. Cheng, T.; Marin, R.; Skripka, A.; Vetrone, F. Small and Bright Lithium-Based Upconverting Nanoparticles. *J. Am. Chem. Soc.* **2018,** 140, 12890-12899.

67. Skripka, A.; Morinvil, A.; Matulionyte, M.; Cheng, T.; Vetrone, F. Advancing Neodymium Single-Band Nanothermometry. *Nanoscale* **2019,** 11, 11322-11330.

68. Savchuk, O.; Carvajal, J.; De la Cruz, L.; Haro-Gonzalez, P.; Aguilo, M.; Diaz, F. Luminescence Thermometry and Imaging in the Second Biological Window at High

Penetration Depth with Nd: Kgd (Wo 4) 2 Nanoparticles. *J. Mater. Chem. C* **2016,** 4, 7397-7405.

69. Quintanilla, M.; Zhang, Y.; Liz-Marzán, L. M. Subtissue Plasmonic Heating Monitored with Caf2: Nd3+, Y3+ Nanothermometers in the Second Biological Window. *Chem. Mater.* **2018,** 30, 2819-2828.

70. Auzel, F.; Malta, O. A Scalar Crystal Field Strength Parameter for Rare-Earth Ions: Meaning and Usefulness. *J. Phys. France* **1983,** 44, 201-206.

71. Huang, P.; Zheng, W.; Tu, D.; Shang, X.; Zhang, M.; Li, R.; Xu, J.; Liu, Y.; Chen, X. Unraveling the Electronic Structures of Neodymium in Liluf4 Nanocrystals for Ratiometric Temperature Sensing. *Adv. Sci.* **2019,** 6, 1802282.

72. Hounsfield, G. N. Computed Medical Imaging. Nobel Lecture, Decemberr 8, 1979. *J. Comput. Assist. Tomogr.* **1980,** 4, 665-674.

73. Huff, T. B.; Tong, L.; Zhao, Y.; Hansen, M. N.; Cheng, J.-X.; Wei, A. Hyperthermic Effects of Gold Nanorods on Tumor Cells. *Nanomedicine (London, England)* **2007,** 2, 125-132.

74. Khalili, J. S.; Yu, X.; Wang, J.; Hayes, B. C.; Davies, M. A.; Lizee, G.; Esmaeli, B.; Woodman, S. E. Combination Small Molecule Mek and Pi3k Inhibition Enhances Uveal Melanoma Cell Death in a Mutant Gnaq- and Gna11-Dependent Manner. *Clin. Cancer Res.* **2012,** 18, 4345-4355.

75. Miyata, M.; Kambe, M.; Tajima, O.; Moriya, S.; Sawaki, H.; Hotta, H.; Kondo, Y.; Narimatsu, H.; Miyagi, T.; Furukawa, K.; Furukawa, K. Membrane Sialidase Neu3 Is Highly Expressed in Human Melanoma Cells Promoting Cell Growth with Minimal Changes in the Composition of Gangliosides. *Cancer Sci.* **2011,** 102, 2139-2149.

76. Huang, T. C.; Lee, J. F.; Chen, J. Y. Pardaxin, an Antimicrobial Peptide, Triggers Caspase-Dependent and Ros-Mediated Apoptosis in Ht-1080 Cells. *Mar. Drugs* **2011,** 9, 1995-2009.

77. Bünzli, J.-C. G., Lanthanide Luminescence: From a Mystery to Rationalization, Understanding, and Applications. In *Handbook on the Physics and Chemistry of Rare Earths*, Elsevier: 2016; Vol. 50, pp 141-176.

78. Hsu, B. Y. W.; Wang, M.; Zhang, Y.; Vijayaragavan, V.; Wong, S. Y.; Chang, A. Y.-C.; Bhakoo, K. K.; Li, X.; Wang, J. Silica–F127 Nanohybrid-Encapsulated Manganese Oxide Nanoparticles for Optimized T 1 Magnetic Resonance Relaxivity. *Nanoscale* **2014,** 6, 293-299.

Supporting information

Table S1. Synthesis parameters of the NCs studied

NCs	DSNPs (mg)	sPDI (mg)	THF (μL)	F127 (mg)	TMOS (μL)	DI water (mL)
sPDI@NCs	×	0.6	900 (+300)	37.5	55	10
DSNPs@NCs	6.4	×	900 (+300)	15	30	10
DSNPs+sPDI_L@NCs	6.4	0.3	900 (+300)	15	30	10
DSNPs+sPDI_M@NCs	6.4	0.6	900 (+300)	15	30	10
DSNPs+sPDI_H@NCs	6.4	1.2	901 (+300)	15	30	10

Table S2. Characteristic parameters of the compounds studied

Samples	DSNPs (mg/mL)	sPDI (μg/mL)	TEM size (nm)	Z-ave Size (nm)	Main Peak (nm)	Polydispersity index
DSNPs@NCs	2.0	×	46.2 ± 5.3	137.4	155.9	0.1
DSNPs+sPDI_L@NCs	1.8	72.4	48.1 ± 7.5	158.4	220.1	0.3
DSNPs+sPDI_M@NCs	1.7	132.2	45.2 ± 8.4	116.2	133.5	0.2
DSNPs+sPDI_H@NCs	0.74	99.8	49.8 ± 8.6	154.8	188.4	0.3
sPDI@NCs	×	34.0	14.3 ± 2.1	70.4	82.2	0.2
DSNPs in hexane	58.7	×	(36 ± 2) × (27 ±2)	×	×	×

Note, the TEM size is mean ± SD (standard deviation).

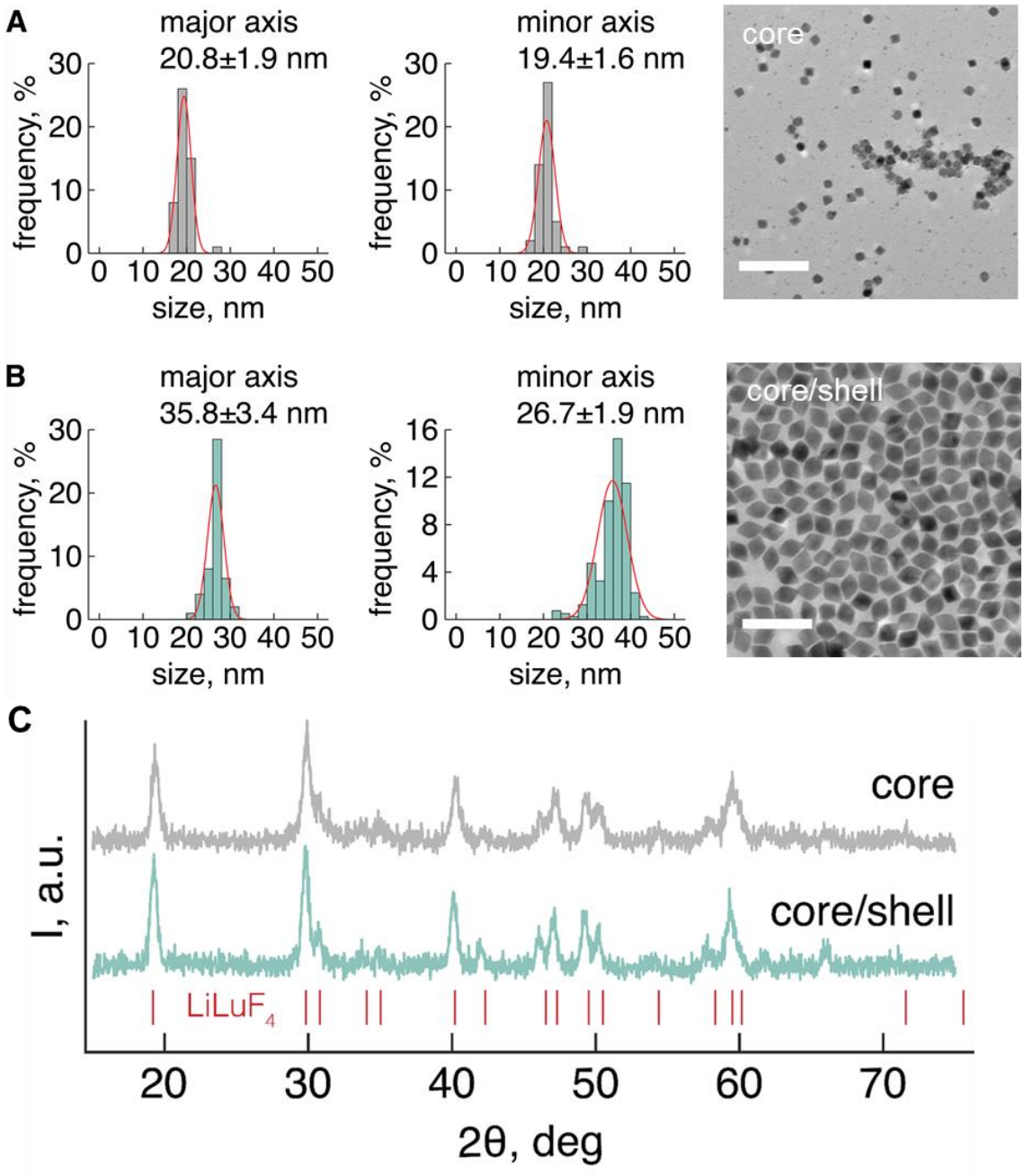

Figure S1. TEM images demonstrating the morphology of DSNPs, $LiLuF_4:Nd^{3+}$ (10%) core (A) and $LiLuF_4$: 10 mol% Nd^{3+}@$LiLuF_4$ core/shell (B). (C) XRD analysis of the core/shell DSNPs.

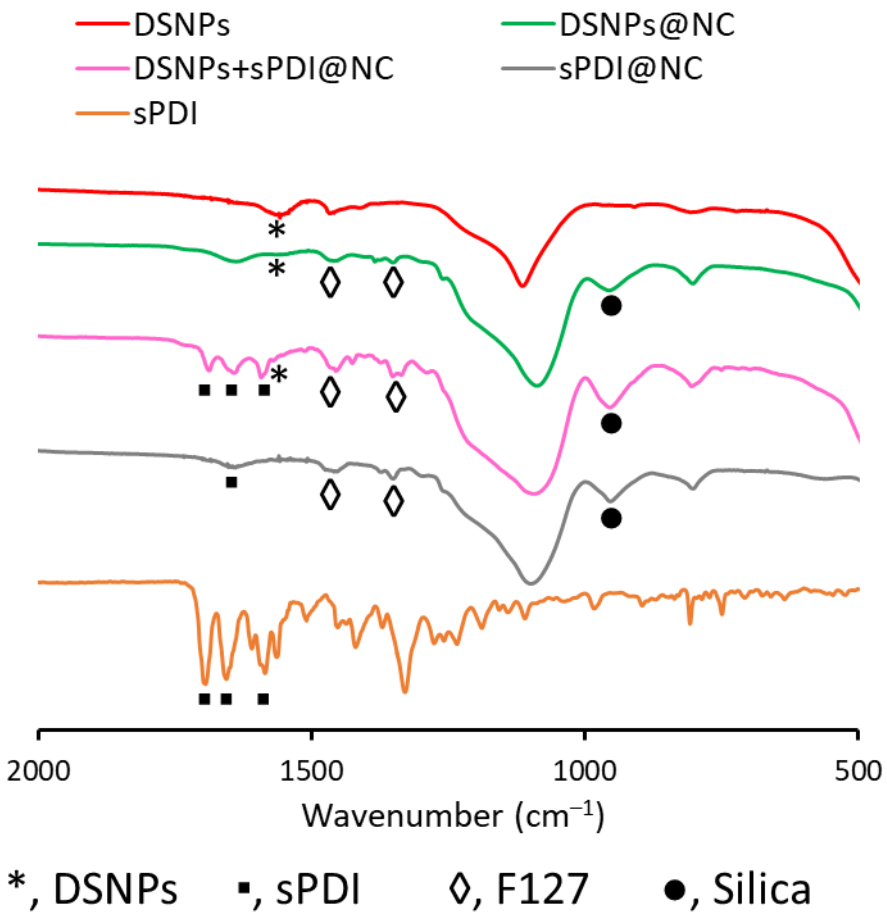

Figure S2. FTIR analysis of the NCs studied.

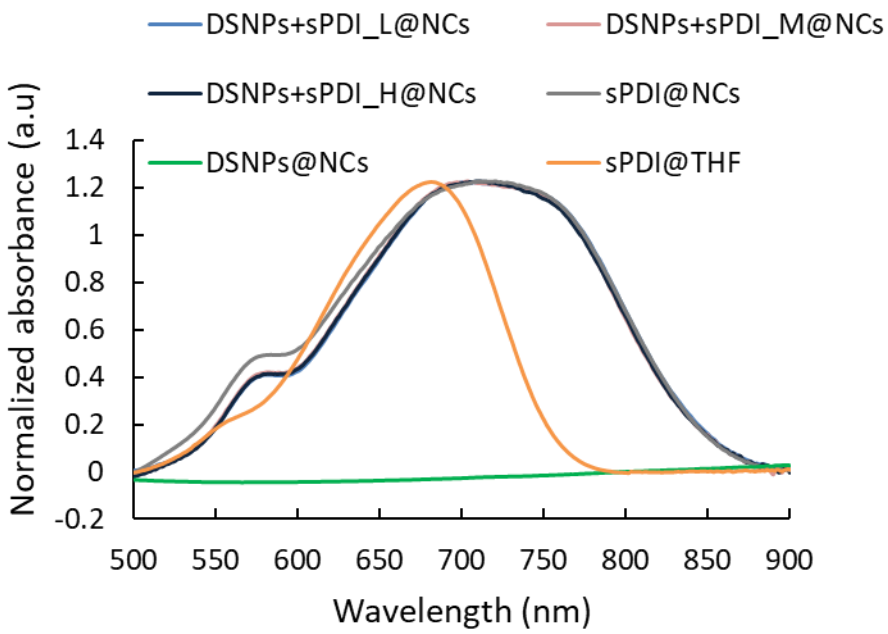

Figure S3. Absorbance spectra of the NCs studied.

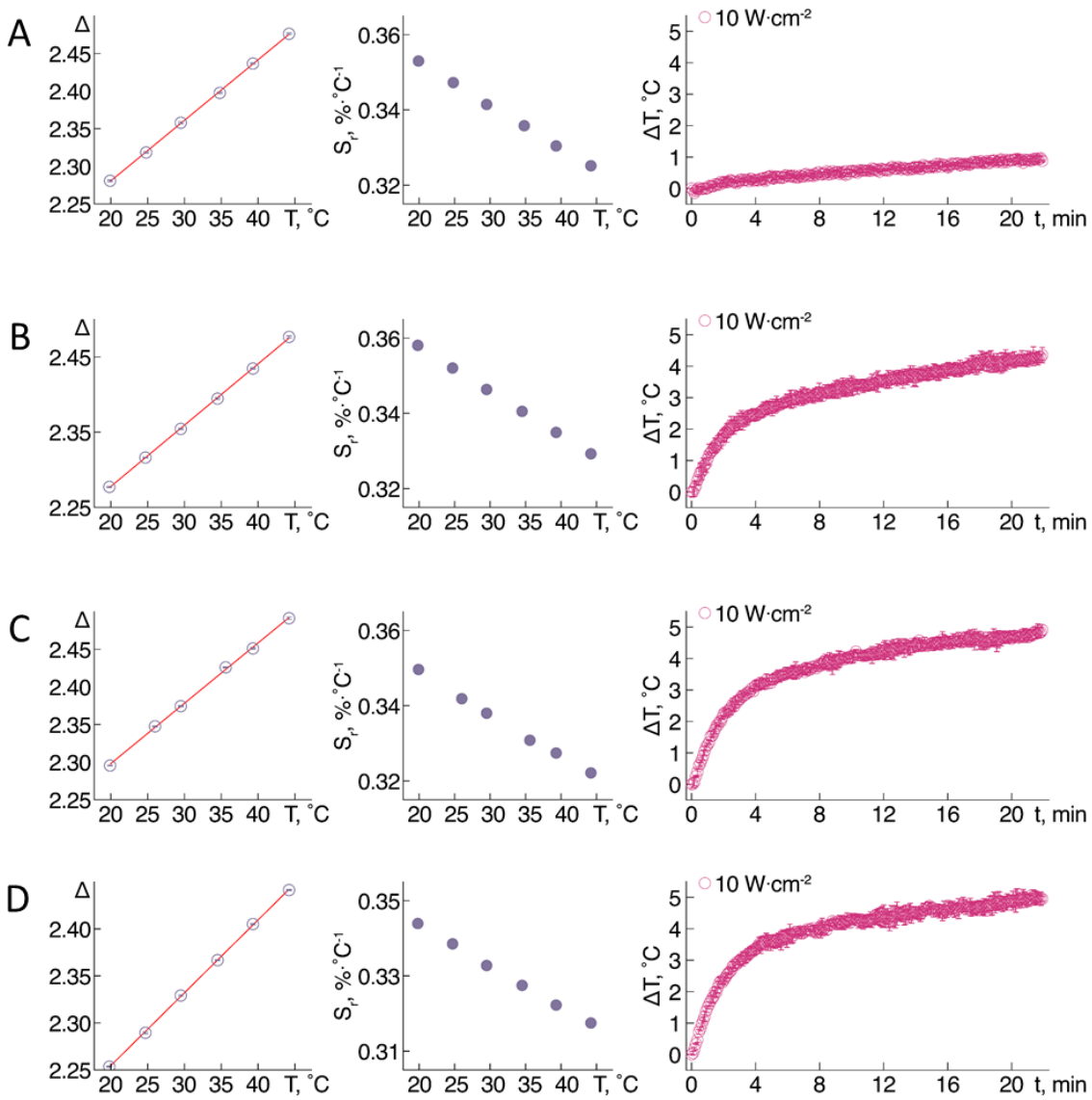

Figure 4S. Heating of samples with different combination ratios of sPDI/DSNPs determined via luminescence nanothermometry (NT), when exciting samples with 10 Wcm^{-2} power density of 793 nm laser. Calibration curve and relative sensitivity of NCs is also shown. (A) DSNPs@NCs (0/0.5 mg), (B) DSNPs+sPDI_L@NCs (20 ug/0.5 mg), (C) DSNPs+sPDI_M@NCs (40 ug/0.5 mg), (D) DSNPs+sPDI_H@NCs (67 ug/0.5 mg).

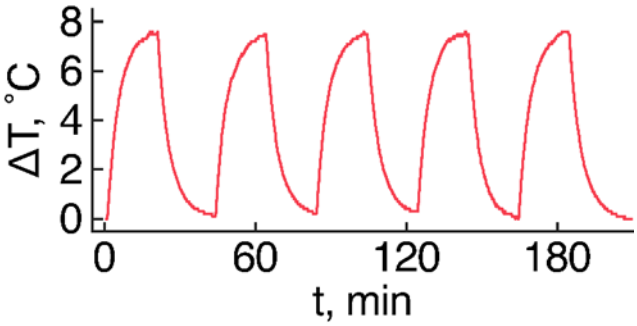

Figure S5. Heating and cooling cycles for DSNPs+sPDI_M@NCs (DSNPs ~0.5 mg/mL, sPDI ~40 µg/mL).

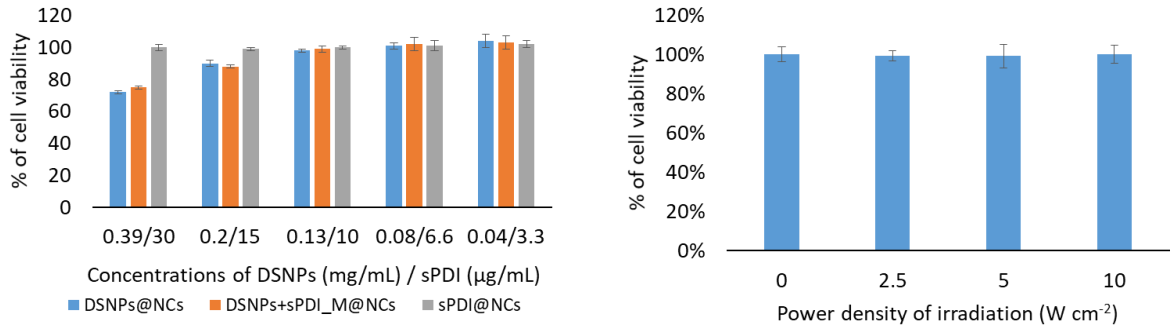

Figure S6. (A) Viability (%) of MCF-7 cells cultured in the presence of DSNPs@NCs (blue), DSNPs+sPDI@NCs (orange), and sPDI@NCs (gray) for 72 h. Individual % of cell viability is the mean ± SD from three independent experiments. No significant growth inhibition was observed at or below 0.13 mg/mL concentration of DSNPs ($p > 0.05$). (B) Viability (%) of MCF-7 cells upon 793 nm irradiation. MCF-7 cells were seeded into 96 well plates at a density of 10,000 cells per well and incubated for 24 h, then irradiated by 793 nm light for 20 min at various power densities (2.5, 5, and 10 W cm^{-2}). Non-irradiated wells were set as control. The cell viability was analysed by CCK-8. Data were expressed as mean ± standard deviation (SD) of triplicated experiments.

7 CONCLUSION AND PERSPECTIVES

7.1 General conclusion

Nanomedicine has addressed several challenges associated with conventional therapy and provided much needed solutions. Nanotheranostics plays an essential role in generating personized medicine to various diseases including cancer, however, the research in this area is still at an early stage. LnNPs have attracted significant attention at the forefront of materials science and within the biomedical field due to their unique optical properties. They have been investigated as imaging probes, nanothermometers, and energy mediators for light-controlled release of therapeutic moieties. In this thesis, we focused mainly on the development of theranostic nanocapsules, combining LnNPs and other therapeutic modalities for image-guided NIR-regulated PDT and PTT.

In Part I, we report a one-step thermolysis approach for the synthesis of β-$NaGdF_4$ UCNPs with diverse morphologies. While sphere or plate shaped β-$NaGdF_4$ UCNPs can be synthesized *via* hot-injection thermolysis, the direct synthesis of nanorods has not been previously reported in the literature. We found that the modulation of temperature during the hot-injection step was an effective approach to control the size and shape of β-$NaGdF_4$ UCNPs formed, and used it to achieve the direct synthesis of β-$NaGdF_4$ nanorods. Further investigation into the mechanism revealed that different temperatures resulted in a different supersaturation concentration that changes the nucleation and growth of α-phase nanoparticles, subsequently affecting the Ostwald ripening mode during the α → β phase transition.

Careful control of the morphology was important because it affects both the upconversion luminescence intensity, as well as the contrast enhancement of β-$NaGdF_4$ UCNPs in MRI. The upconversion luminescence intensity upon 980 nm NIR irradiation, decreases with increasing surface to volume ratio of the UCNPs and a higher ratio of green to red emission was observed when the aspect ratio was close to 1. The β-$NaGdF_4$ UCNPs with the sizes ranging from 20 to 60 nm, can be used for negative contrast agents in MRI, which contrast enhancement on T_2–weighted magnetic resonance images increases with increasing size. Except that nanorods performed the best as T_2 contrast agents despite being smaller compared to the nanoplates.

In fact, surface modification is a critical step to convert hydrophobic UCNPs and therapeutic agents to water dispersible formulations that favorable for in vivo applications. In Part II, we established an original one-pot encapsulation approach, to simultaneously encapsulate the above synthesized β-$NaGdF_4$ UCNPs and a photodynamic drug, ZnPc, into a single theranostic nanocapsule that carry both MRI and NIR-regulated photodynamic therapy

functionalities. This approach consists of interfacial condensation, using PEO-PPO-PEO block copolymers as the templating and protecting agent, the encapsulation follows a straightforward microemulsion mechanism which directly proceeds in a near-neutral pH aqueous environment. Silica precursor, TMOS, is hydrolysed and condensed between the core/corona of the PEO-PPO-PEO micelles. This forms a silica shell cross-linked micelle where the polymeric micelle is stabilised by silica cross-linking to prevent its disintegration. To protect the hydrophobic OA ligands of UCNPs from reaction with the silanol groups of hydrated TMOS, both UCNPs and ZnPc are first co-encapsulated in PEO-PPO-PEO micelles, and thereafter, TMOS is added to grow the silica shell between the PPO and PEO interface to increase its chemical and mechanical stability. The resultant polymeric micelle/silica nanocapsules have an average hydrodynamic size of 85 nm, low polydispersity index of 0.1 and excellent colloidal stability. In addition, the close distance between the two co-encapsulated payloads allows for efficient energy transfer. Evaluating it *in vitro* using BT474 breast cancer cells, it demonstrates good biocompatibility, T_2 contrast enhancement and the eradication of BT474 breast cancer cells following NIR irradiation. This one-pot approach constitutes an important step forward in the surface engineering of UCNPs and UC-PDT systems. It could be extended for developing multifunctional nanocarriers to encompass various NPs and therapeutic or diagnostic agents, thus bringing theranostic functionalities such as NIR, MRI or CT image-guided therapy and controlled drug release to personalized medicine.

In Section 2 of the same part, we employed the same strategy developed above to encapsulate the chemotherapy drug, DOX, and modified the surface of the NCs by conjugating it with nuclear targeted agents (TAT peptides) for active drug delivery into cancer cells. With the help of this TAT-conjugated NCs, more DOX is delivered and accumulated in the nucleus and a significant growth inhibition against cancer cells is demonstrated, especially in DOX resistant cells. In addition, we established a hydrocarbon modified encapsulation approach to prevent the fluorescence quenching of organic compounds (*e.g.* DOX, coumarin and rhodamine dyes) from their self-aggregation inside of the NCs. With the addition of organosilica such as TMPES to the inner surface of silica shells, the hydrocarbon groups of TMPES interact with the encapsulated DOX by the hydrophobic and/or π-π stacking to inhibit its self-aggregations. This method is expected to extend encapsulating other planar aromatic compounds for the improved functionalities. This study proved that the NCs can be modified for more functionalities in theranostic applications.

In Part III, we extended the one-pot encapsulation strategy to co-encapsulate $LiLuF_4$:Nd^{3+} (10%)@$LiLuF_4$ DSNPs and an optical heater sPDI for NIR-regulated PTT. The Nd^{3+}-doped DSNPs, serve as a ratiometric nanothermometer for contactless detection of temperature, so that the heating caused by the PDI is monitored in real time and controlled

during the therapy. Moreover, the Lu^{3+} in the host matrix, acting as a CT contrast agent, allows for tracking and localization of the NCs inside the biological tissue. A promising contrast enhancement in CT images is demonstrated in MCF-7 cells, showing the potential for imaging-guided PTT. Both DSNPs and sPDI are excited at the same heating-free wavelength, 793 nm, while the nanothermometer emission (~1060 nm) is located within the second biological window. The thermal sensitivity is 0.35 at 20 °C. This theranostic NCs demonstrate excellent photothermal-stability and a strong PTT effect against MCF-7 breast cancer cells while measuring its temperature *in situ*.

7.2 Perspectives

We have established a theranostic nanoplatform based on the LnNPs and other therapeutic modalities for imaging-guided PDT and PTT. However, research in the biological applications of LnNPs is still at the infancy stage; more research is required to optimize the efficiency of these nanotheranostic platforms. Therefore, there are several interesting directions for future work relative to this thesis.

7.2.1 Optimization of UCNPs and materials

In Chapter 5, we mainly focus on developing the one-pot encapsulation approach to optimize the surface modification of LnNPs and establish the theranostic platform for UC-PDT, where we select Yb^{3+}/Er^{3+}co-doped $NaGdF_4$ UCNPs as an energy mediator and a MRI contrast agent, and equipped with a PDT drug, ZnPc. To further improve the therapeutic effects of this system, there are several options that can be considered in future studies. (1) With regard to the design of UCNPs, the core/shell architecture can be used to improve the upconversion efficiency. Nd^{3+} can also be co-doped with Yb^{3+} into the shell to facilitate the energy transfer of $Nd^{3+}\rightarrow Yb^{3+}\rightarrow Er^{3+}$, as Nd^{3+} can be excited by the so-called heating-free wavelength around 800 nm, achieving a much deeper tissue penetration than that of 980 nm. To avoid surface deactivations, growing one more inert shell outside the first shell can be considered. (2) PDT drugs (whose absorption band overlaps with the green emission of Er^{3+}) such as Rose Bengal (RB), can be co-encapsulated together with ZnPc (absorbing the red emission of Er^{3+}) in the NCs. By this means, the visible emissions are absorbed by both RB (~540 nm) and ZnPc (~680 nm) for the $^1O_2$ production, subsequently leading an improved photo oxidative damages against cancer cells. Moreover, the slight cell apoptosis induced by the photothermal damages of the visible emission of Er^{3+} also can be limited.

7.2.2 Development of theranostic nanocapsules for combination therapy

In Chapter 6, we have demonstrated an effective theranostic NCs for PTT, where Nd^{3+} doped $LiLuF_4$ core@shell DSNPs act as a nanothermometer and a CT imaging probe, and small

organic molecules, sPDI, as a thermal generator. The *in vitro* evaluation of this NCs shows promising results on PTT efficacy, CT contrast enhancement, and real-time temperature monitoring, respectively. In fact, the thermal sensitivity of the thermometers can be further improved by adjusting the doping concentration of Nd^{3+}, as our group recently explored that doping 5% Nd^{3+} in $LiLuF_4$ host achieves the highest thermal sensitivity and lowest uncertainty.[208] To target future *in vivo* applications, we have ideas to extend this system for more functionalities. (1) Conjugating specific antibodies to the NCs for active drug delivery. Trastuzumab, a monoclonal antibody targeted to the HER2 receptor, is widely utilized for the treatment of patients with HER2-positive early stage, locally advanced and metastatic breast cancer.[211] Therefore, Trastuzumab can be used for both therapy and delivery in HER2 positive breast cancer when it conjugates on the PEO chains of the NCs, using EDC and NHS as catalysts (This conjugation approach is described in *section 5.2*). (2) Paclitaxel, a chemotherapy drug, can be co-encapsulated in the NCs. The combination of trastuzumab and paclitaxel is expected to achieve synergistic therapeutic effect and overcome the limitations of conventional chemotherapy. Moreover, the release of paclitaxel may increase with the local temperature increasing caused by the encapsulated sPDI. (3) The performance of the developed NCs combined with molecular target therapy, chemotherapy, and PTT, can be first evaluated *in vitro* in breast cancer cell lines with various HER2 expression levels (BT-474, MDA-MB-468 and MCF-7) and normal breast cells (HMEC). The *in vivo* performance can be evaluated using the HER2 positive xenograft mouse model.

7.2.3 In vivo evaluation

In this thesis, we focus on the preparation and characterization of theranostic NCs. Their performance also has been evaluated at the cellular level. However, the *in vivo* assay is indispensable for stepping forward in the field of nanomedicine. Specifically, 1) The toxicity studies including cytotoxicity to normal tissues, LnNP distribution, metabolism, pharmacokinetics and pharmacodynamics in animal models are required; 2) PDT, PTT, and multifunctional bioimaging based on the LnNPs mentioned in the thesis will be evaluated in animal models.

8 REFERENCE

1. Sung, H.; Ferlay, J.; Siegel, R. L.; Laversanne, M.; Soerjomataram, I.; Jemal, A.; Bray, F. Global Cancer Statistics 2020: Globocan Estimates of Incidence and Mortality Worldwide for 36 Cancers in 185 Countries. *CA Cancer J. Clin.* **2021,** 71, 209-249.

2. De, M.; Ghosh, P. S.; Rotello, V. M. Applications of Nanoparticles in Biology. *Adv. Mater.* **2008,** 20, 4225-4241.

3. Mitchell, M. J.; Billingsley, M. M.; Haley, R. M.; Wechsler, M. E.; Peppas, N. A.; Langer, R. Engineering Precision Nanoparticles for Drug Delivery. *Nat. Rev. Drug Discovery* **2021,** 20, 101-124.

4. Salvioni, L.; Rizzuto, M. A.; Bertolini, J. A.; Pandolfi, L.; Colombo, M.; Prosperi, D. Thirty Years of Cancer Nanomedicine: Success, Frustration, and Hope. *Cancers (Basel)* **2019,** 11, 1855.

5. Prasad, P. N., *Introduction to Nanomedicine and Nanobioengineering*. John Wiley & Sons: 2012; Vol. 7.

6. Cheng, Z.; Al Zaki, A.; Hui, J. Z.; Muzykantov, V. R.; Tsourkas, A. Multifunctional Nanoparticles: Cost Versus Benefit of Adding Targeting and Imaging Capabilities. *Science* **2012,** 338, 903-910.

7. Danhier, F.; Feron, O.; Préat, V. To Exploit the Tumor Microenvironment: Passive and Active Tumor Targeting of Nanocarriers for Anti-Cancer Drug Delivery. *J. Controlled Release* **2010,** 148, 135-146.

8. Rosenblum, D.; Joshi, N.; Tao, W.; Karp, J. M.; Peer, D. Progress and Challenges Towards Targeted Delivery of Cancer Therapeutics. *Nat. Commun.* **2018,** 9, 1410.

9. Attia, M. F.; Anton, N.; Wallyn, J.; Omran, Z.; Vandamme, T. F. An Overview of Active and Passive Targeting Strategies to Improve the Nanocarriers Efficiency to Tumour Sites. *J. Pharm. Pharmacol.* **2019,** 71, 1185-1198.

10. Tran, S.; DeGiovanni, P. J.; Piel, B.; Rai, P. Cancer Nanomedicine: A Review of Recent Success in Drug Delivery. *Clin. Transl. Med.* **2017,** 6, 44.

11. Rastinehad, A. R.; Anastos, H.; Wajswol, E.; Winoker, J. S.; Sfakianos, J. P.; Doppalapudi, S. K.; Carrick, M. R.; Knauer, C. J.; Taouli, B.; Lewis, S. C.; Tewari, A. K.; Schwartz, J. A.; Canfield, S. E.; George, A. K.; West, J. L.; Halas, N. J. Gold Nanoshell-Localized Photothermal Ablation of Prostate Tumors in a Clinical Pilot Device Study. *Proc. Natl. Acad. Sci. U. S. A.* **2019,** 116, 18590-18596.

12. Thakor, A. S.; Jokerst, J. V.; Ghanouni, P.; Campbell, J. L.; Mittra, E.; Gambhir, S. S. Clinically Approved Nanoparticle Imaging Agents. *J. Nucl. Med.* **2016,** 57, 1833-1837.

13. Chow, E. K.-H.; Ho, D. Cancer Nanomedicine: From Drug Delivery to Imaging. *Sci. Transl. Med.* **2013,** 5, 216rv214.

14. Wolfram, J.; Ferrari, M. Clinical Cancer Nanomedicine. *Nano Today* **2019,** 25, 85-98.

15. Lammers, T.; Aime, S.; Hennink, W. E.; Storm, G.; Kiessling, F. Theranostic Nanomedicine. *Acc. Chem. Res.* **2011,** 44, 1029-1038.

16. Lammers, T.; Storm, G. Setting Standards to Promote Progress in Bio–Nano Science. *Nat. Nanotechnol.* **2019,** 14, 626-626.

17. Wong, X. Y.; Sena-Torralba, A.; Alvarez-Diduk, R.; Muthoosamy, K.; Merkoci, A. Nanomaterials for Nanotheranostics: Tuning Their Properties According to Disease Needs. *ACS nano* **2020,** 14, 2585-2627.

18. Vankayala, R.; Hwang, K. C. Near‐Infrared‐Light‐Activatable Nanomaterial‐Mediated Phototheranostic Nanomedicines: An Emerging Paradigm for Cancer Treatment. *Adv. Mater.* **2018,** 30, 1706320.

19. Gray, T., *Elements: A Visual Exploration of Every Known Atom in the Universe*. Black Dog & Leventhal: 2012.

20. Holden, N.; Coplen, T. The Periodic Table of the Elements. *Chem. Int.* **2004,** 26, 8-9.

21. Connelly, N. G.; Hartshorn, R. M.; Damhus, T.; Hutton, A. T., *Nomenclature of Inorganic Chemistry: Iupac Recommendations 2005*. Royal Society of Chemistry: 2005.

22. Haxel, G. B.; Hedrick, J. B.; Orris, G. J.; Stauffer, P. H.; Hendley II, J. W. *Rare Earth Elements: Critical Resources for High Technology*; 2327-6932; 2002.

23. Holden, N. E. History of the Origin of the Chemical Elements and Their Discoverers. *Prepared for the 41st IUPAC General Assembly* **2001,** 29.

24. Gschneidner, K. A.; Capellen, J., *1787-1987, Two Hundred Years of Rare Earths*. Rare-earth Information Center: 1987.

25. Bethencourt, M.; Botana, F. J.; Calvino, J. J.; Marcos, M.; RodrÍguez-Chacón, M. A. Lanthanide Compounds as Environmentally-Friendly Corrosion Inhibitors of Aluminium Alloys: A Review. *Corros. Sci.* **1998,** 40, 1803-1819.

26. Gonzalez, V.; Vignati, D. A. L.; Leyval, C.; Giamberini, L. Environmental Fate and Ecotoxicity of Lanthanides: Are They a Uniform Group Beyond Chemistry? *Environ. Int.* **2014,** 71, 148-157.

27. Eliseeva, S. V.; Bünzli, J.-C. G. Rare Earths: Jewels for Functional Materials of the Future. *New J. Chem.* **2011,** 35, 1165-1176.

28. Cotton, S., *Lanthanide and Actinide Chemistry*. John Wiley & Sons: 2013.

29. Du, Y. P.; Zhang, Y. W.; Sun, L. D.; Yan, C. H. Optically Active Uniform Potassium and Lithium Rare Earth Fluoride Nanocrystals Derived from Metal Trifluroacetate Precursors. *Dalton Trans.* **2009**, 8574-8581.

30. Haase, M.; Schäfer, H. Upconverting Nanoparticles. *Angew. Chem. Int. Ed.* **2011,** 50, 5808-5829.

31. Auzel, F. Upconversion and Anti-Stokes Processes with F and D Ions in Solids. *Chem. Rev.* **2004,** 104, 139-174.

32. Wang, F.; Liu, X. Recent Advances in the Chemistry of Lanthanide-Doped Upconversion Nanocrystals. *Chem. Soc. Rev.* **2009,** 38, 976-989.

33. Chen, G.; Qiu, H.; Prasad, P. N.; Chen, X. Upconversion Nanoparticles: Design, Nanochemistry, and Applications in Theranostics. *Chem. Rev.* **2014,** 114, 5161-5214.

34. Chen, G.; Ohulchanskyy, T. Y.; Liu, S.; Law, W. C.; Wu, F.; Swihart, M. T.; Ågren, H.; Prasad, P. N. Core/Shell $NaGdF_4$: Nd^{3+}/$NaGdF_4$ Nanocrystals with Efficient Near-Infrared to Near-Infrared Downconversion Photoluminescence for Bioimaging Applications. *ACS nano* **2012,** 6, 2969-2977.

35. Chivian, J. S.; Case, W. E.; Eden, D. D. The Photon Avalanche: A New Phenomenon in Pr^{3+} - Based Infrared Quantum Counters. *Appl. Phys. Lett.* **1979,** 35, 124-125.

36. Joubert, M.-F. Photon Avalanche Upconversion in Rare Earth Laser Materials. *Opt. Mater.* **1999,** 11, 181-203.

37. Lee, C.; Xu, E. Z.; Liu, Y.; Teitelboim, A.; Yao, K.; Fernandez-Bravo, A.; Kotulska, A. M.; Nam, S. H.; Suh, Y. D.; Bednarkiewicz, A. Giant Nonlinear Optical Responses from Photon-Avalanching Nanoparticles. *Nature* **2021,** 589, 230-235.

38. Chen, G.; Yang, C.; Prasad, P. N. Nanophotonics and Nanochemistry: Controlling the Excitation Dynamics for Frequency Up-and Down-Conversion in Lanthanide-Doped Nanoparticles. *Acc. Chem. Res.* **2013,** 46, 1474-1486.

39. Blasse, G.; Grabmaier, B., In *Luminescent Materials*, Springer: 1994; pp 33-70.

40. Krämer, K. W.; Biner, D.; Frei, G.; Güdel, H. U.; Hehlen, M. P.; Lüthi, S. R. Hexagonal Sodium Yttrium Fluoride Based Green and Blue Emitting Upconversion Phosphors. *Chem. Mater.* **2004,** 16, 1244-1251.

41. Mahalingam, V.; Vetrone, F.; Naccache, R.; Speghini, A.; Capobianco, J. A. Colloidal Tm^{3+}/Yb^{3+} - Doped $LiYF_4$ Nanocrystals: Multiple Luminescence Spanning the UV to NIR Regions via Low - Energy Excitation. *Adv. Mater.* **2009,** 21, 4025-4028.

42. Li, Z.; Wang, B.; Xing, L.; Liu, S.; Tan, N.; Xiao, S.; Ding, J. Enhancement of Upconversion Luminescence of $YAlO_3$: Er^{3+} by Gd^{3+} Doping. *Chinese Optics Letters* **2012,** 10, 081602.

43. Hemmer, E.; Benayas, A.; Légaré, F.; Vetrone, F. Exploiting the Biological Windows: Current Perspectives on Fluorescent Bioprobes Emitting above 1000 nm. *Nanoscale Horiz.* **2016,** 1, 168-184.

44. Weber, M. J. Optical Properties of Yb^{3+} and Nd^{3+}-Yb^{3+} Energy Transfer in $YAlO_3$. *Physical Review B* **1971,** 4, 3153.

45. Bashkatov, A. N.; Genina, E. A.; Kochubey, V. I.; Tuchin, V. V. Optical Properties of Human Skin, Subcutaneous and Mucous Tissues in the Wavelength Range from 400 to 2000 nm. *J. Phys. D: Appl. Phys.* **2005,** 38, 2543-2555.

46. Jacques, S. L. Optical Properties of Biological Tissues: A Review. *Phys. Med. Biol.* **2013,** 58, R37-R61.

47. Wang, R.; Li, X.; Zhou, L.; Zhang, F. Epitaxial Seeded Growth of Rare‐Earth Nanocrystals with Efficient 800 nm near‐Infrared to 1525 nm Short‐Wavelength Infrared Downconversion Photoluminescence for in Vivo Bioimaging. *Angew. Chem. Int. Ed.* **2014,** 53, 12086-12090.

48. Wang, Y.-F.; Liu, G.-Y.; Sun, L.-D.; Xiao, J.-W.; Zhou, J.-C.; Yan, C.-H. Nd^{3+}-Sensitized Upconversion Nanophosphors: Efficient In Vivo Bioimaging Probes with Minimized Heating Effect. *ACS Nano* **2013,** 7, 7200-7206.

49. van Dijk, J. M. F.; Schuurmans, M. F. H. On the Nonradiative and Radiative Decay Rates and a Modified Exponential Energy Gap Law for 4f–4f Transitions in Rare‐Earth Ions. *J. Chem. Phys.* **1983,** 78, 5317-5323.

50. Zhang, Y.-W.; Sun, X.; Si, R.; You, L.-P.; Yan, C.-H. Single-Crystalline and Monodisperse LaF_3 Triangular Nanoplates from a Single-Source Precursor. *J. Am. Chem. Soc.* **2005,** 127, 3260-3261.

51. Mai, H.-X.; Zhang, Y.-W.; Si, R.; Yan, Z.-G.; Sun, L.-d.; You, L.-P.; Yan, C.-H. High-Quality Sodium Rare-Earth Fluoride Nanocrystals: Controlled Synthesis and Optical Properties. *J. Am. Chem. Soc.* **2006,** 128, 6426-6436.

52. Boyer, J.-C.; Vetrone, F.; Cuccia, L. A.; Capobianco, J. A. Synthesis of Colloidal Upconverting $NaYF_4$ Nanocrystals Doped with Er^{3+}, Yb^{3+} and Tm^{3+}, Yb^{3+} via Thermal Decomposition of Lanthanide Trifluoroacetate Precursors. *J. Am. Chem. Soc.* **2006,** 128, 7444-7445.

53. Boyer, J.-C.; Cuccia, L. A.; Capobianco, J. A. Synthesis of Colloidal Upconverting $NaYF_4$: Er^{3+}/Yb^{3+} and Tm^{3+}/Yb^{3+} Monodisperse Nanocrystals. *Nano Lett.* **2007,** 7, 847-852.

54. Wang, F.; Deng, R.; Wang, J.; Wang, Q.; Han, Y.; Zhu, H.; Chen, X.; Liu, X. Tuning Upconversion through Energy Migration in Core–Shell Nanoparticles. *Nature Materials* **2011,** 10, 968-973.

55. Vetrone, F.; Naccache, R.; Mahalingam, V.; Morgan, C. G.; Capobianco, J. A. The Active-Core/Active-Shell Approach: A Strategy to Enhance the Upconversion Luminescence in Lanthanide-Doped Nanoparticles. *Adv. Funct. Mater.* **2009,** 19, 2924-2929.

56. Cheng, T.; Marin, R.; Skripka, A.; Vetrone, F. Small and Bright Lithium-Based Upconverting Nanoparticles. *J. Am. Chem. Soc.* **2018,** 140, 12890-12899.

57. Read, E. S.; Armes, S. P. Recent Advances in Shell Cross-Linked Micelles. *Chemical Communications* **2007**, 3021-3035.

58. Jalil, R. A.; Zhang, Y. Biocompatibility of Silica Coated $NaYF_4$ Upconversion Fluorescent Nanocrystals. *Biomaterials* **2008,** 29, 4122-4128.

59. Wang, L.; Zhao, W.; Tan, W. Bioconjugated Silica Nanoparticles: Development and Applications. *Nano Research* **2008,** 1, 99-115.

60. Roy, I.; Ohulchanskyy, T. Y.; Bharali, D. J.; Pudavar, H. E.; Mistretta, R. A.; Kaur, N.; Prasad, P. N. Optical Tracking of Organically Modified Silica Nanoparticles as DNA Carriers: A Nonviral, Nanomedicine Approach for Gene Delivery. *Proc. Natl. Acad. Sci. U. S. A.* **2005,** 102, 279-284.

61. Yang, J.; Deng, Y.; Wu, Q.; Zhou, J.; Bao, H.; Li, Q.; Zhang, F.; Li, F.; Tu, B.; Zhao, D. Mesoporous Silica Encapsulating Upconversion Luminescence Rare-Earth Fluoride Nanorods for Secondary Excitation. *Langmuir* **2010,** 26, 8850-8856.

62. Lamch, Ł.; Pucek, A.; Kulbacka, J.; Chudy, M.; Jastrzębska, E.; Tokarska, K.; Bułka, M.; Brzózka, Z.; Wilk, K. A. Recent Progress in the Engineering of Multifunctional Colloidal Nanoparticles for Enhanced Photodynamic Therapy and Bioimaging. *Adv. Colloid Interface Sci.* **2018**.

63. Liu, Y.; Meng, X.; Bu, W. Upconversion-Based Photodynamic Cancer Therapy. *Coord. Chem. Rev.* **2019,** 379, 82-98.

64. Gai, S.; Li, C.; Yang, P.; Lin, J. Recent Progress in Rare Earth Micro/Nanocrystals: Soft Chemical Synthesis, Luminescent Properties, and Biomedical Applications. *Chem. Rev.* **2014,** 114, 2343-2389.

65. Yang, D.; Ma, P. a.; Hou, Z.; Cheng, Z.; Li, C.; Lin, J. Current Advances in Lanthanide Ion (Ln^{3+})-Based Upconversion Nanomaterials for Drug Delivery. *Chem. Soc. Rev.* **2015,** 44, 1416-1448.

66. Chen, F.; Hableel, G.; Zhao, E. R.; Jokerst, J. V. Multifunctional Nanomedicine with Silica: Role of Silica in Nanoparticles for Theranostic, Imaging, and Drug Monitoring. *J. Colloid Interface Sci.* **2018,** 521, 261-279.

67. McDonald, D. M.; Choyke, P. L. Imaging of Angiogenesis: From Microscope to Clinic. *Nat. Med.* **2003,** 9, 713-725.

68. Bünzli, J.-C. G. Lanthanide Luminescence for Biomedical Analyses and Imaging. *Chem. Rev.* **2010,** 110, 2729-2755.

69. Bünzli, J.-C. G.; Eliseeva, S. V. Intriguing Aspects of Lanthanide Luminescence. *Chem. Sci.* **2013,** 4, 1939-1949.

70. Wu, S.; Han, G.; Milliron, D. J.; Aloni, S.; Altoe, V.; Talapin, D. V.; Cohen, B. E.; Schuck, P. J. Non-Blinking and Photostable Upconverted Luminescence from Single Lanthanide-Doped Nanocrystals. *Proc. Natl. Acad. Sci. U. S. A.* **2009,** 106, 10917-10921.

71. Park, Y. I.; Kim, J. H.; Lee, K. T.; Jeon, K.-S.; Na, H. B.; Yu, J. H.; Kim, H. M.; Lee, N.; Choi, S. H.; Baik, S.-I.; Kim, H.; Park, S. P.; Park, B.-J.; Kim, Y. W.; Lee, S. H.; Yoon, S.-Y.; Song, I. C.; Moon, W. K.; Suh, Y. D.; Hyeon, T. Nonblinking and Nonbleaching Upconverting Nanoparticles as an Optical Imaging Nanoprobe and T1 Magnetic Resonance Imaging Contrast Agent. *Adv. Mater.* **2009,** 21, 4467-4471.

72. Yan, C.; Zhao, H.; Perepichka, D. F.; Rosei, F. Lanthanide Ion Doped Upconverting Nanoparticles: Synthesis, Structure and Properties. *Small (Weinheim an der Bergstrasse, Germany)* **2016,** 12, 3888-3907.

73. König, K. Multiphoton Microscopy in Life Sciences. *J. Microsc.* **2000,** 200, 83-104.

74. Zeng, S.; Xiao, J.; Yang, Q.; Hao, J. Bi-Functional $NaLuF_4$: $Gd^{3+}/Yb^{3+}/Tm^{3+}$ Nanocrystals: Structure Controlled Synthesis, Near-Infrared Upconversion Emission and Tunable Magnetic Properties. *J. Mater. Chem.* **2012,** 22, 9870-9874.

75. Zhou, B.; Shi, B.; Jin, D.; Liu, X. Controlling Upconversion Nanocrystals for Emerging Applications. *Nat. Nanotechnol.* **2015,** 10, 924.

76. Lim, S. F.; Riehn, R.; Ryu, W. S.; Khanarian, N.; Tung, C.-k.; Tank, D.; Austin, R. H. In Vivo and Scanning Electron Microscopy Imaging of Upconverting Nanophosphors in Caenorhabditis Elegans. *Nano Lett.* **2006,** 6, 169-174.

77. Jalani, G.; Naccache, R.; Rosenzweig, D. H.; Haglund, L.; Vetrone, F.; Cerruti, M. Photocleavable Hydrogel-Coated Upconverting Nanoparticles: A Multifunctional Theranostic Platform for NIR Imaging and on-Demand Macromolecular Delivery. *J. Am. Chem. Soc.* **2016,** 138, 1078-1083.

78. van de Rijke, F.; Zijlmans, H.; Li, S.; Vail, T.; Raap, A. K.; Niedbala, R. S.; Tanke, H. J. Up-Converting Phosphor Reporters for Nucleic Acid Microarrays. *Nat. Biotechnol.* **2001,** 19, 273-276.

79. Dai, Y.; Xiao, H.; Liu, J.; Yuan, Q.; Ma, P. a.; Yang, D.; Li, C.; Cheng, Z.; Hou, Z.; Yang, P. In Vivo Multimodality Imaging and Cancer Therapy by Near-Infrared Light-Triggered Trans-Platinum Pro-Drug-Conjugated Upconverison Nanoparticles. *J. Am. Chem. Soc.* **2013,** 135, 18920-18929.

80. Idris, N. M.; Gnanasammandhan, M. K.; Zhang, J.; Ho, P. C.; Mahendran, R.; Zhang, Y. In Vivo Photodynamic Therapy Using Upconversion Nanoparticles as Remote-Controlled Nanotransducers. *Nat. Med.* **2012,** 18, 1580.

81. Cheng, L.; Yang, K.; Li, Y.; Zeng, X.; Shao, M.; Lee, S.-T.; Liu, Z. Multifunctional Nanoparticles for Upconversion Luminescence/MR Multimodal Imaging and Magnetically Targeted Photothermal Therapy. *Biomaterials* **2012,** 33, 2215-2222.

82. Skripka, A.; Karabanovas, V.; Jarockyte, G.; Marin, R.; Tam, V.; Cerruti, M.; Rotomskis, R.; Vetrone, F. Decoupling Theranostics with Rare Earth Doped Nanoparticles. *Adv. Funct. Mater.* **2019,** 29, 1807105.

83. Fan, W.; Shen, B.; Bu, W.; Chen, F.; He, Q.; Zhao, K.; Zhang, S.; Zhou, L.; Peng, W.; Xiao, Q. A Smart Upconversion-Based Mesoporous Silica Nanotheranostic System for Synergetic Chemo-/Radio-/Photodynamic Therapy and Simultaneous MR/UCL Imaging. *Biomaterials* **2014,** 35, 8992-9002.

84. Lv, R.; Yang, P.; He, F.; Gai, S.; Li, C.; Dai, Y.; Yang, G.; Lin, J. A Yolk-Like Multifunctional Platform for Multimodal Imaging and Synergistic Therapy Triggered by a Single Near-Infrared Light. *Acs Nano* **2015,** 9, 1630-1647.

85. He, F.; Yang, G.; Yang, P.; Yu, Y.; Lv, R.; Li, C.; Dai, Y.; Gai, S.; Lin, J. A New Single 808 nm NIR Light‐Induced Imaging‐Guided Multifunctional Cancer Therapy Platform. *Adv. Funct. Mater.* **2015,** 25, 3966-3976.

86. Lv, R.; Zhong, C.; Li, R.; Yang, P.; He, F.; Gai, S.; Hou, Z.; Yang, G.; Lin, J. Multifunctional Anticancer Platform for Multimodal Imaging and Visible Light Driven Photodynamic/Photothermal Therapy. *Chem. Mater.* **2015,** 27, 1751-1763.

87. Liu, J.; Bu, J.; Bu, W.; Zhang, S.; Pan, L.; Fan, W.; Chen, F.; Zhou, L.; Peng, W.; Zhao, K. Real‐Time In Vivo Quantitative Monitoring of Drug Release by Dual‐Mode Magnetic Resonance and Upconverted Luminescence Imaging. *Angew. Chem.* **2014,** 126, 4639-4643.

88. Kasban, H.; El-Bendary, M.; Salama, D. A Comparative Study of Medical Imaging Techniques. *Int. J. Intell. Syst.* **2015,** 4, 37-58.

89. Lee, D.-E.; Koo, H.; Sun, I.-C.; Ryu, J. H.; Kim, K.; Kwon, I. C. Multifunctional Nanoparticles for Multimodal Imaging and Theragnosis. *Chem. Soc. Rev.* **2012,** 41, 2656-2672.

90. Zijlmans, H. J. M. A. A.; Bonnet, J.; Burton, J.; Kardos, K.; Vail, T.; Niedbala, R. S.; Tanke, H. J. Detection of Cell and Tissue Surface Antigens Using Up-Converting Phosphors: A New Reporter Technology. *Anal. Biochem.* **1999,** 267, 30-36.

91. Han, X.; Xu, K.; Taratula, O.; Farsad, K. Applications of Nanoparticles in Biomedical Imaging. *Nanoscale* **2019,** 11, 799-819.

92. Chatterjee, D. K.; Rufaihah, A. J.; Zhang, Y. Upconversion Fluorescence Imaging of Cells and Small Animals Using Lanthanide Doped Nanocrystals. *Biomaterials* **2008,** 29, 937-943.

93. Vetrone, F.; Naccache, R.; Juarranz de la Fuente, A.; Sanz-Rodríguez, F.; Blazquez-Castro, A.; Rodriguez, E. M.; Jaque, D.; Solé, J. G.; Capobianco, J. A. Intracellular Imaging of Hela Cells by Non-Functionalized $NaYF_4:Er^{3+}$, Yb^{3+} Upconverting Nanoparticles. *Nanoscale* **2010,** 2, 495-498.

94. Nyk, M.; Kumar, R.; Ohulchanskyy, T. Y.; Bergey, E. J.; Prasad, P. N. High Contrast In Vitro and In Vivo Photoluminescence Bioimaging Using Near Infrared to Near Infrared Up-Conversion in Tm^{3+} and Yb^{3+} Doped Fluoride Nanophosphors. *Nano Lett.* **2008,** 8, 3834-3838.

95. Shen, J.; Chen, G.; Vu, A.-M.; Fan, W.; Bilsel, O. S.; Chang, C.-C.; Han, G. Engineering the Upconversion Nanoparticle Excitation Wavelength: Cascade Sensitization of Tri-Doped Upconversion Colloidal Nanoparticles at 800 Nm. *Adv. Opt. Mater.* **2013,** 1, 644-650.

96. Xie, X.; Gao, N.; Deng, R.; Sun, Q.; Xu, Q.-H.; Liu, X. Mechanistic Investigation of Photon Upconversion in Nd^{3+}-Sensitized Core–Shell Nanoparticles. *J. Am. Chem. Soc.* **2013,** 135, 12608-12611.

97. Zhong, Y.; Tian, G.; Gu, Z.; Yang, Y.; Gu, L.; Zhao, Y.; Ma, Y.; Yao, J. Elimination of Photon Quenching by a Transition Layer to Fabricate a Quenching-Shield Sandwich Structure for 800 nm Excited Upconversion Luminescence of Nd^{3+}-Sensitized Nanoparticles. *Adv. Mater.* **2014,** 26, 2831-2837.

98. Prodi, L.; Rampazzo, E.; Rastrelli, F.; Speghini, A.; Zaccheroni, N. Imaging Agents Based on Lanthanide Doped Nanoparticles. *Chem. Soc. Rev.* **2015,** 44, 4922-4952.

99. Na, H. B.; Song, I. C.; Hyeon, T. Inorganic Nanoparticles for MRI Contrast Agents. *Adv. Mater.* **2009,** 21, 2133-2148.

100. Naccache, R.; Chevallier, P.; Lagueux, J.; Gossuin, Y.; Laurent, S.; Vander Elst, L.; Chilian, C.; Capobianco, J. A.; Fortin, M.-A. High Relaxivities and Strong Vascular Signal Enhancement for $NaGdF_4$ Nanoparticles Designed for Dual MR/Optical Imaging. *Adv. Healthcare Mater.* **2013,** 2, 1478-1488.

101. Johnson, N. J. J.; Oakden, W.; Stanisz, G. J.; Scott Prosser, R.; van Veggel, F. C. J. M. Size-Tunable, Ultrasmall $NaGdF_4$ Nanoparticles: Insights into Their T1 MRI Contrast Enhancement. *Chem. Mater.* **2011,** 23, 3714-3722.

102. Park, J.; Lee, E.; Hwang, N.-M.; Kang, M.; Kim, S. C.; Hwang, Y.; Park, J.-G.; Noh, H.-J.; Kim, J.-Y.; Park, J.-H.; Hyeon, T. One-Nanometer-Scale Size-Controlled Synthesis of Monodisperse Magnetic Iron Oxide Nanoparticles. *Angew. Chem. Int. Ed.* **2005,** 44, 2872-2877.

103. Jun, Y.-w.; Huh, Y.-M.; Choi, J.-s.; Lee, J.-H.; Song, H.-T.; KimKim; Yoon, S.; Kim, K.-S.; Shin, J.-S.; Suh, J.-S.; Cheon, J. Nanoscale Size Effect of Magnetic Nanocrystals and Their Utilization for Cancer Diagnosis via Magnetic Resonance Imaging. *J. Am. Chem. Soc.* **2005,** 127, 5732-5733.

104. Chen, F.; Bu, W.; Zhang, S.; Liu, X.; Liu, J.; Xing, H.; Xiao, Q.; Zhou, L.; Peng, W.; Wang, L.; Shi, J. Positive and Negative Lattice Shielding Effects Co-Existing in Gd (Iii) Ion Doped Bifunctional Upconversion Nanoprobes. *Adv. Funct. Mater.* **2011,** 21, 4285-4294.

105. Xia, A.; Chen, M.; Gao, Y.; Wu, D.; Feng, W.; Li, F. Gd^{3+} Complex-Modified $NaLuF_4$-Based Upconversion Nanophosphors for Trimodality Imaging of NIR-to-NIR Upconversion

Luminescence, X-Ray Computed Tomography and Magnetic Resonance. *Biomaterials* **2012,** 33, 5394-5405.

106. Osseni, S. A.; Lechevallier, S.; Verelst, M.; Perriat, P.; Dexpert-Ghys, J.; Neumeyer, D.; Garcia, R.; Mayer, F.; Djanashvili, K.; Peters, J. A.; Magdeleine, E.; Gros-Dagnac, H.; Celsis, P.; Mauricot, R. Gadolinium Oxysulfide Nanoparticles as Multimodal Imaging Agents for T2-Weighted Mr, X-Ray Tomography and Photoluminescence. *Nanoscale* **2014,** 6, 555-564.

107. Das, G. K.; Johnson, N. J.; Cramen, J.; Blasiak, B.; Latta, P.; Tomanek, B.; van Veggel, F. C. $NaDyF_4$ Nanoparticles as T2 Contrast Agents for Ultrahigh Field Magnetic Resonance Imaging. *J. Phys. Chem. Lett.* **2012,** 3, 524-529.

108. Wang, M.; Zhang, Y.; Yao, Q.; Ng, M.; Lin, M.; Li, X.; Bhakoo, K. K.; Chang, A. Y.; Rosei, F.; Vetrone, F. Morphology Control of Lanthanide Doped $NaGdF_4$ Nanocrystals via One-Step Thermolysis. *Chem. Mater.* **2019,** 31, 5160-5171.

109. Dougherty, T. J.; Gomer, C. J.; Henderson, B. W.; Jori, G.; Kessel, D.; Korbelik, M.; Moan, J.; Peng, Q. Photodynamic Therapy. *J. Natl. Cancer Inst.* **1998,** 90, 889-905.

110. Dolmans, D. E.; Fukumura, D.; Jain, R. K. Photodynamic Therapy for Cancer. *Nat. Rev. Cancer* **2003,** 3, 380.

111. Brown, S. B.; Brown, E. A.; Walker, I. The Present and Future Role of Photodynamic Therapy in Cancer Treatment. *Lancet Oncol.* **2004,** 5, 497-508.

112. Yi, G.; Hong, S. H.; Son, J.; Yoo, J.; Park, C.; Choi, Y.; Koo, H. Recent Advances in Nanoparticle Carriers for Photodynamic Therapy. *Quant. Imaging Med. Surg.* **2018,** 8, 433-443.

113. Celli, J. P.; Spring, B. Q.; Rizvi, I.; Evans, C. L.; Samkoe, K. S.; Verma, S.; Pogue, B. W.; Hasan, T. Imaging and Photodynamic Therapy: Mechanisms, Monitoring, and Optimization. *Chem. Rev.* **2010,** 110, 2795-2838.

114. Castano, A. P.; Demidova, T. N.; Hamblin, M. R. Mechanisms in Photodynamic Therapy: Part Three—Photosensitizer Pharmacokinetics, Biodistribution, Tumor Localization and Modes of Tumor Destruction. *Photodiagnosis Photodyn. Ther.* **2005,** 2, 91-106.

115. Vatansever, F.; Hamblin, M. R., Photodynamic Therapy and Antitumor Immune Response. In *Cancer Immunology: Bench to Bedside Immunotherapy of Cancers*, Rezaei, N., Ed. Springer Berlin Heidelberg: Berlin, Heidelberg, 2015; pp 383-399.

116. Pervaiz, S.; Olivo, M. Art and Science of Photodynamic Therapy. *Clin. Exp. Pharmacol. Physiol.* **2006,** 33, 551-556.

117. Zhang, P.; Steelant, W.; Kumar, M.; Scholfield, M. Versatile Photosensitizers for Photodynamic Therapy at Infrared Excitation. *J. Am. Chem. Soc.* **2007,** 129, 4526-4527.

118. Liu, K.; Liu, X.; Zeng, Q.; Zhang, Y.; Tu, L.; Liu, T.; Kong, X.; Wang, Y.; Cao, F.; Lambrechts, S. A. G.; Aalders, M. C. G.; Zhang, H. Covalently Assembled NIR Nanoplatform

for Simultaneous Fluorescence Imaging and Photodynamic Therapy of Cancer Cells. *ACS Nano* **2012,** 6, 4054-4062.

119. Liu, X.; Zheng, M.; Kong, X.; Zhang, Y.; Zeng, Q.; Sun, Z.; Buma, W. J.; Zhang, H. Separately Doped Upconversion-C60 Nanoplatform for NIR Imaging-Guided Photodynamic Therapy of Cancer Cells. *Chem. Commun.* **2013,** 49, 3224-3226.

120. Qian, H. S.; Guo, H. C.; Ho, P. C.-L.; Mahendran, R.; Zhang, Y. Mesoporous-Silica-Coated up-Conversion Fluorescent Nanoparticles for Photodynamic Therapy. *Small* **2009,** 5, 2285-2290.

121. Qiu, H.; Tan, M.; Ohulchanskyy, T.; Lovell, J.; Chen, G. Recent Progress in Upconversion Photodynamic Therapy. *Nanomaterials* **2018,** 8, 344.

122. Yang, G.; Yang, D.; Yang, P.; Lv, R.; Li, C.; Zhong, C.; He, F.; Gai, S.; Lin, J. A Single 808 nm Near-Infrared Light-Mediated Multiple Imaging and Photodynamic Therapy Based on Titania Coupled Upconversion Nanoparticles. *Chem. Mater.* **2015,** 27, 7957-7968.

123. Qiao, X.-F.; Zhou, J.-C.; Xiao, J.-W.; Wang, Y.-F.; Sun, L.-D.; Yan, C.-H. Triple-Functional Core–Shell Structured Upconversion Luminescent Nanoparticles Covalently Grafted with Photosensitizer for Luminescent, Magnetic Resonance Imaging and Photodynamic Therapy In Vitro. *Nanoscale* **2012,** 4, 4611-4623.

124. Shan, J.; Budijono, S. J.; Hu, G.; Yao, N.; Kang, Y.; Ju, Y.; Prud'homme, R. K. PEGylated Composite Nanoparticles Containing Upconverting Phosphors and Meso-Tetraphenyl Porphine (Tpp) for Photodynamic Therapy. *Adv. Funct. Mater.* **2011,** 21, 2488-2495.

125. Wang, C.; Tao, H.; Cheng, L.; Liu, Z. Near-Infrared Light Induced In vivo Photodynamic Therapy of Cancer Based on Upconversion Nanoparticles. *Biomaterials* **2011,** 32, 6145-6154.

126. Jiang, S.; Zhang, Y. Upconversion Nanoparticle-Based FRET System for Study of Sirna in Live Cells. *Langmuir* **2010,** 26, 6689-6694.

127. Wang, Y.; Liu, K.; Liu, X.; Dohnalová, K.; Gregorkiewicz, T.; Kong, X.; Aalders, M. C. G.; Buma, W. J.; Zhang, H. Critical Shell Thickness of Core/Shell Upconversion Luminescence Nanoplatform for FRET Application. *J. Phys. Chem. Lett.* **2011,** 2, 2083-2088.

128. Hamblin, M. R. Upconversion in Photodynamic Therapy: Plumbing the Depths. *Dalton Trans.* **2018,** 47, 8571-8580.

129. Drozdek, S.; Szeremeta, J.; Lamch, L.; Nyk, M.; Samoc, M.; Wilk, K. A. Two-Photon Induced Fluorescence Energy Transfer in Polymeric Nanocapsules Containing $CdSe_xS_{1-x}$/ZnS Core/Shell Quantum Dots and Zinc (II) Phthalocyanine. *J. Phys. Chem. C* **2016,** 120, 15460-15470.

130. Wang, M.; Zhang, Y.; Ng, M.; Skripka, A.; Cheng, T.; Xu, L.; Bhakoo, K. K.; Chang, A. Y.; Rosei, F.; Vetrone, F. One-Pot Synthesis of Theranostic Nanocapsules with Lanthanide Doped Nanoparticles. *Chem. Sci.* **2020**.

131. Zhi, D.; Yang, T.; O'Hagan, J.; Zhang, S.; Donnelly, R. F. Photothermal Therapy. *J. Controlled Release* **2020,** 325, 52-71.

132. Jaque, D.; Martinez Maestro, L.; del Rosal, B.; Haro-Gonzalez, P.; Benayas, A.; Plaza, J. L.; Martin Rodriguez, E.; Garcia Sole, J. Nanoparticles for Photothermal Therapies. *Nanoscale* **2014,** 6, 9494-9530.

133. Roti Roti, J. L. Cellular Responses to Hyperthermia (40–46 °C): Cell Killing and Molecular Events. *Int. J. Hyperthermia* **2008,** 24, 3-15.

134. Hildebrandt, B.; Wust, P.; Ahlers, O.; Dieing, A.; Sreenivasa, G.; Kerner, T.; Felix, R.; Riess, H. The Cellular and Molecular Basis of Hyperthermia. *Crit. Rev. Oncol. Hematol.* **2002,** 43, 33-56.

135. Wust, P.; Hildebrandt, B.; Sreenivasa, G.; Rau, B.; Gellermann, J.; Riess, H.; Felix, R.; Schlag, P. M. Hyperthermia in Combined Treatment of Cancer. *Lancet Oncol.* **2002,** 3, 487-497.

136. Huff, T. B.; Tong, L.; Zhao, Y.; Hansen, M. N.; Cheng, J.-X.; Wei, A. Hyperthermic Effects of Gold Nanorods on Tumor Cells. *Nanomedicine (London, England)* **2007,** 2, 125-132.

137. Jain, P. K.; Huang, X.; El-Sayed, I. H.; El-Sayed, M. A. Noble Metals on the Nanoscale: Optical and Photothermal Properties and Some Applications in Imaging, Sensing, Biology, and Medicine. *Acc. Chem. Res.* **2008,** 41, 1578-1586.

138. Weissleder, R. A Clearer Vision for In Vivo Imaging. *Nat. Biotechnol.* **2001,** 19, 316-317.

139. Smith, A. M.; Mancini, M. C.; Nie, S. Second Window for In Vivo Imaging. *Nat. Nanotechnol.* **2009,** 4, 710-711.

140. Jaque, D.; Maestro, L. M.; Del Rosal, B.; Haro-Gonzalez, P.; Benayas, A.; Plaza, J.; Rodriguez, E. M.; Sole, J. G. Nanoparticles for Photothermal Therapies. *Nanoscale* **2014,** 6, 9494-9530.

141. Minchinton, A. I.; Tannock, I. F. Drug Penetration in Solid Tumours. *Nat. Rev. Cancer* **2006,** 6, 583-592.

142. Gerweck, L. E. Hyperthermia in Cancer Therapy: The Biological Basis and Unresolved Questions. *Cancer Res.* **1985,** 45, 3408-3414.

143. Lee, Y.; Auh, S. L.; Wang, Y.; Burnette, B.; Wang, Y.; Meng, Y.; Beckett, M.; Sharma, R.; Chin, R.; Tu, T.; Weichselbaum, R. R.; Fu, Y. X. Therapeutic Effects of Ablative Radiation on Local Tumor Require CD8+ T Cells: Changing Strategies for Cancer Treatment. *Blood* **2009,** 114, 589-595.

144. Lugade, A. A.; Moran, J. P.; Gerber, S. A.; Rose, R. C.; Frelinger, J. G.; Lord, E. M. Local Radiation Therapy of B16 Melanoma Tumors Increases the Generation of Tumor Antigen-Specific Effector Cells That Traffic to the Tumor. *J. Immunol.* **2005,** 174, 7516-7523.

145. Chen, Q.; Xu, L.; Liang, C.; Wang, C.; Peng, R.; Liu, Z. Photothermal Therapy with Immune-Adjuvant Nanoparticles Together with Checkpoint Blockade for Effective Cancer Immunotherapy. *Nat. Commun.* **2016,** 7, 13193.

146. Yang, Y.; Zhu, W.; Dong, Z.; Chao, Y.; Xu, L.; Chen, M.; Liu, Z. 1D Coordination Polymer Nanofibers for Low‐Temperature Photothermal Therapy. *Adv. Mater.* **2017,** 29, 1703588.

147. Huang, L.; Li, Y.; Du, Y.; Zhang, Y.; Wang, X.; Ding, Y.; Yang, X.; Meng, F.; Tu, J.; Luo, L.; Sun, C. Mild Photothermal Therapy Potentiates Anti-PD-L1 Treatment for Immunologically Cold Tumors via an All-in-One and All-in-Control Strategy. *Nat. Commun.* **2019,** 10, 4871.

148. de Melo‐Diogo, D.; Pais‐Silva, C.; Dias, D. R.; Moreira, A. F.; Correia, I. J. Strategies to Improve Cancer Photothermal Therapy Mediated by Nanomaterials. *Adv. Healthcare Mater.* **2017,** 6, 1700073.

149. Doughty, A. C.; Hoover, A. R.; Layton, E.; Murray, C. K.; Howard, E. W.; Chen, W. R. Nanomaterial Applications in Photothermal Therapy for Cancer. *Materials* **2019,** 12, 779.

150. Sharifi, S.; Behzadi, S.; Laurent, S.; Forrest, M. L.; Stroeve, P.; Mahmoudi, M. Toxicity of Nanomaterials. *Chem. Soc. Rev.* **2012,** 41, 2323-2343.

151. Marin, R.; Skripka, A.; Besteiro, L. V.; Benayas, A.; Wang, Z.; Govorov, A. O.; Canton, P.; Vetrone, F. Highly Efficient Copper Sulfide-Based Near-Infrared Photothermal Agents: Exploring the Limits of Macroscopic Heat Conversion. *Small* **2018,** 14, 1803282.

152. Rastinehad, A. R.; Anastos, H.; Wajswol, E.; Winoker, J. S.; Sfakianos, J. P.; Doppalapudi, S. K.; Carrick, M. R.; Knauer, C. J.; Taouli, B.; Lewis, S. C.; Tewari, A. K.; Schwartz, J. A.; Canfield, S. E.; George, A. K.; West, J. L.; Halas, N. J. Gold Nanoshell-Localized Photothermal Ablation of Prostate Tumors in a Clinical Pilot Device Study. *Proc. Natl. Acad. Sci. U. S. A.* **2019,** 116, 18590-18596.

153. Zheng, X.; Xing, D.; Zhou, F.; Wu, B.; Chen, W. R. Indocyanine Green-Containing Nanostructure as Near Infrared Dual-Functional Targeting Probes for Optical Imaging and Photothermal Therapy. *Mol. Pharm.* **2011,** 8, 447-456.

154. Yu, J.; Javier, D.; Yaseen, M. A.; Nitin, N.; Richards-Kortum, R.; Anvari, B.; Wong, M. S. Self-Assembly Synthesis, Tumor Cell Targeting, and Photothermal Capabilities of Antibody-Coated Indocyanine Green Nanocapsules. *J. Am. Chem. Soc.* **2010,** 132, 1929-1938.

155. Cheng, L.; Wang, C.; Feng, L.; Yang, K.; Liu, Z. Functional Nanomaterials for Phototherapies of Cancer. *Chem. Rev.* **2014,** 114, 10869-10939.

156. Jung, H. S.; Verwilst, P.; Sharma, A.; Shin, J.; Sessler, J. L.; Kim, J. S. Organic Molecule-Based Photothermal Agents: An Expanding Photothermal Therapy Universe. *Chem. Soc. Rev.* **2018,** 47, 2280-2297.

157. Cheng, L.; He, W.; Gong, H.; Wang, C.; Chen, Q.; Cheng, Z.; Liu, Z. Pegylated Micelle Nanoparticles Encapsulating a Non‐Fluorescent Near‐Infrared Organic Dye as a Safe and Highly‐Effective Photothermal Agent for In Vivo Cancer Therapy. *Adv. Funct. Mater.* **2013,** 23, 5893-5902.

158. Yue, C.; Liu, P.; Zheng, M.; Zhao, P.; Wang, Y.; Ma, Y.; Cai, L. Ir-780 Dye Loaded Tumor Targeting Theranostic Nanoparticles for NIR Imaging and Photothermal Therapy. *Biomaterials* **2013,** 34, 6853-6861.

159. Luo, S.; Tan, X.; Fang, S.; Wang, Y.; Liu, T.; Wang, X.; Yuan, Y.; Sun, H.; Qi, Q.; Shi, C. Mitochondria‐Targeted Small‐Molecule Fluorophores for Dual Modal Cancer Phototherapy. *Adv. Funct. Mater.* **2016,** 26, 2826-2835.

160. Zhang, J.; Liu, Z.; Lian, P.; Qian, J.; Li, X.; Wang, L.; Fu, W.; Chen, L.; Wei, X.; Li, C. Selective Imaging and Cancer Cell Death via pH Switchable Near-Infrared Fluorescence and Photothermal Effects. *Chem. Sci.* **2016,** 7, 5995-6005.

161. Jiang, Y.; Pu, K. Advanced Photoacoustic Imaging Applications of Near‐Infrared Absorbing Organic Nanoparticles. *Small* **2017,** 13, 1700710.

162. Cui, C.; Yang, Z.; Hu, X.; Wu, J.; Shou, K.; Ma, H.; Jian, C.; Zhao, Y.; Qi, B.; Hu, X. Organic Semiconducting Nanoparticles as Efficient Photoacoustic Agents for Lightening Early Thrombus and Monitoring Thrombolysis in Living Mice. *ACS nano* **2017,** 11, 3298-3310.

163. Yang, Z.; Tian, R.; Wu, J.; Fan, Q.; Yung, B. C.; Niu, G.; Jacobson, O.; Wang, Z.; Liu, G.; Yu, G. Impact of Semiconducting Perylene Diimide Nanoparticle Size on Lymph Node Mapping and Cancer Imaging. *ACS nano* **2017,** 11, 4247-4255.

164. Hu, X.; Lu, F.; Chen, L.; Tang, Y.; Hu, W.; Lu, X.; Ji, Y.; Yang, Z.; Zhang, W.; Yin, C. Perylene Diimide-Grafted Polymeric Nanoparticles Chelated with Gd^{3+} for Photoacoustic/T1-Weighted Magnetic Resonance Imaging-Guided Photothermal Therapy. *ACS Appl. Mater. Interfaces* **2017,** 9, 30458-30469.

165. Jiao, Y.; Liu, K.; Wang, G.; Wang, Y.; Zhang, X. Supramolecular Free Radicals: Near-Infrared Organic Materials with Enhanced Photothermal Conversion. *Chem. Sci.* **2015,** 6, 3975-3980.

166. Li, H.; Zhang, Y.; Chen, B.; Wang, Y.; Teh, C.; Ng, G. H.; Meng, J.; Huang, Z.; Dong, W.; Tan, M. Y. J-Aggregation of Perylene Diimides in Silica Nanocapsules for Stable Near-Infrared Photothermal Conversion. *ACS Appl. Bio Mater.* **2019,** 2, 1569-1577.

167. Würthner, F. Perylene Bisimide Dyes as Versatile Building Blocks for Functional Supramolecular Architectures. *Chem. Commun.* **2004**, 1564-1579.

168. van der Zee, J. Heating the Patient: A Promising Approach? *Ann. Oncol.* **2002,** 13, 1173-1184.

169. Hildebrandt, B.; Wust, P.; Ahlers, O.; Dieing, A.; Sreenivasa, G.; Kerner, T.; Felix, R.; Riess, H. The Cellular and Molecular Basis of Hyperthermia. *Crit. Rev. Oncol. Hematol.* **2002,** 43, 33-56.

170. Falk, M. H.; Issels, R. D. Hyperthermia in Oncology. *Int. J. Hyperthermia* **2001,** 17, 1-18.

171. Kapp, D. S.; Hahn, G. M.; Carlson, R. W., Principles of Hyperthermia. In *Holland-Frei Cancer Medicine. 5th Edition*, BC Decker: 2000.

172. Marciniak, L.; Pilch, A.; Arabasz, S.; Jin, D.; Bednarkiewicz, A. Heterogeneously Nd^{3+} Doped Single Nanoparticles for NIR-Induced Heat Conversion, Luminescence, and Thermometry. *Nanoscale* **2017,** 9, 8288-8297.

173. Rocha, U.; Upendra Kumar, K.; Jacinto, C.; Ramiro, J.; Caamano, A. J.; García Solé, J.; Jaque, D. Nd^{3+} Doped LaF_3 Nanoparticles as Self-Monitored Photo-Thermal Agents. *Appl. Phys. Lett.* **2014,** 104, 053703.

174. Kolesnikov, I.; Golyeva, E.; Kalinichev, A.; Kurochkin, M.; Lähderanta, E.; Mikhailov, M. Nd^{3+} Single Doped YVO_4 Nanoparticles for Sub-Tissue Heating and Thermal Sensing in the Second Biological Window. *Sens. Actuators, B*
2017, 243, 338-345.

175. Xu, L.; Li, J.; Lu, K.; Wen, S.; Chen, H.; Shahzad, M. K.; Zhao, E.; Li, H.; Ren, J.; Zhang, J. Sub-10 nm $NaNdF_4$ Nanoparticles as Near-Infrared Photothermal Probes with Self-Temperature Feedback. *ACS Appl. Nano Mater.* **2020,** 3, 2517-2526.

176. Fan, N. C.; Cheng, F. Y.; Ho, J. a. A.; Yeh, C. S. Photocontrolled Targeted Drug Delivery: Photocaged Biologically Active Folic Acid as a Light‐Responsive Tumor‐Targeting Molecule. *Angew. Chem. Int. Ed.* **2012,** 51, 8806-8810.

177. Yang, Y.; Velmurugan, B.; Liu, X.; Xing, B. NIR Photoresponsive Crosslinked Upconverting Nanocarriers toward Selective Intracellular Drug Release. *Small* **2013,** 9, 2937-2944.

178. Zhao, L.; Peng, J.; Huang, Q.; Li, C.; Chen, M.; Sun, Y.; Lin, Q.; Zhu, L.; Li, F. Near‐Infrared Photoregulated Drug Release in Living Tumor Tissue via Yolk‐Shell Upconversion Nanocages. *Adv. Funct. Mater.* **2014,** 24, 363-371.

179. Liu, J.; Bu, W.; Pan, L.; Shi, J. Nir‐Triggered Anticancer Drug Delivery by Upconverting Nanoparticles with Integrated Azobenzene‐Modified Mesoporous Silica. *Angew. Chem. Int. Ed.* **2013,** 52, 4375-4379.

180. Zhou, L.; Chen, Z.; Dong, K.; Yin, M.; Ren, J.; Qu, X. DNA‐Mediated Construction of Hollow Upconversion Nanoparticles for Protein Harvesting and Near‐Infrared Light Triggered Release. *Adv. Mater.* **2014,** 26, 2424-2430.

181. Min, Y.; Li, J.; Liu, F.; Yeow, E. K.; Xing, B. Near‐Infrared Light‐Mediated Photoactivation of a Platinum Antitumor Prodrug and Simultaneous Cellular Apoptosis Imaging by Upconversion‐Luminescent Nanoparticles. *Angew. Chem. Int. Ed.* **2014,** 53, 1012-1016.

182. Zhao, Y.; Shi, C.; Yang, X.; Shen, B.; Sun, Y.; Chen, Y.; Xu, X.; Sun, H.; Yu, K.; Yang, B. pH-and Temperature-Sensitive Hydrogel Nanoparticles with Dual Photoluminescence for Bioprobes. *ACS nano* **2016,** 10, 5856-5863.

183. Quintanilla, M.; Liz-Marzán, L. M. Guiding Rules for Selecting a Nanothermometer. *Nano Today* **2018,** 19, 126-145.

184. Jaque, D.; Vetrone, F. Luminescence Nanothermometry. *Nanoscale* **2012,** 4, 4301-4326.

185. Khalid, A.; Kontis, K. 2d Surface Thermal Imaging Using Rise-Time Analysis from Laser-Induced Luminescence Phosphor Thermometry. *Meas. Sci. Technol.* **2009,** 20, 025305.

186. Quintanilla, M.; Cantelar, E.; Cusso, F.; Villegas, M.; Caballero, A. C. Temperature Sensing with Up-Converting Submicron-Sized $LiNbO_3$: Er^{3+}/Yb^{3+} Particles. *Appl. Phys. Express* **2011,** 4, 022601.

187. Vetrone, F.; Naccache, R.; Zamarrón, A.; Juarranz de la Fuente, A.; Sanz-Rodríguez, F.; Martinez Maestro, L.; Martín Rodriguez, E.; Jaque, D.; García Solé, J.; Capobianco, J. A. Temperature Sensing Using Fluorescent Nanothermometers. *ACS nano* **2010,** 4, 3254-3258.

188. Hemmer, E.; Acosta-Mora, P.; Mendez-Ramos, J.; Fischer, S. Optical Nanoprobes for Biomedical Applications: Shining a Light on Upconverting and Near-Infrared Emitting Nanoparticles for Imaging, Thermal Sensing, and Photodynamic Therapy. *J. Mater. Chem. B* **2017,** 5, 4365-4392.

189. Hemmer, E.; Vetrone, F. Nanothermometry Using Upconverting Nanoparticles. *Upconverting Nanomaterials: Perspectives, Synthesis, and Applications* **2016**, 319.

190. Cao, B. S.; He, Y. Y.; Feng, Z. Q.; Li, Y. S.; Dong, B. Optical Temperature Sensing Behavior of Enhanced Green Upconversion Emissions from Er–Mo:$Yb_2Ti_2O_7$ Nanophosphor. *Sens. Actuators, B* **2011,** 159, 8-11.

191. Petit, J.; Viana, B.; Goldner, P. Internal Temperature Measurement of an Ytterbium Doped Material under Laser Operation. *Opt. Express* **2011,** 19, 1138.

192. Cai, Z. P.; Xu, H. Y. Point Temperature Sensor Based on Green Upconversion Emission in an Er:ZBLALiP Microsphere. *Sens. Actuator, A* **2003,** 108, 187-192.

193. Haro-González, P.; Martín, I. R.; Martín, L. L.; León-Luis, S. F.; Pérez-Rodríguez, C.; Lavín, V. Characterization of Er^{3+} and Nd^{3+} Doped Strontium Barium Niobate Glass Ceramic as Temperature Sensors. *Opt. Mater.* **2011,** 33, 742-745.

194. Alencar, M. A.; Maciel, G. S.; de Araújo, C. B.; Patra, A. Er^{3+}-Doped $BaTiO_3$ Nanocrystals for Thermometry: Influence of Nanoenvironment on the Sensitivity of a Fluorescence Based Temperature Sensor. *Appl. Phys. Lett.* **2004,** 84, 4753-4755.

195. Cantelar, E.; Cusso, F. Dynamics of the Yb^{3+} to Er^{3+} Energy Transfer in $LiNbO_3$. *Appl. Phys. B* **1999,** 69, 29-33.

196. Altavilla, C., *Upconverting Nanomaterials: Perspectives, Synthesis, and Applications*. CRC Press: 2016.

197. Savchuk, O. A.; Haro-Gonzalez, P.; Carvajal, J.; Jaque, D.; Massons, J.; Aguilo, M.; Diaz, F. Er: Yb:NaY_2F_5O Up-Converting Nanoparticles for Sub-Tissue Fluorescence Lifetime Thermal Sensing. *Nanoscale* **2014,** 6, 9727-9733.

198. Schartner, E. P.; Monro, T. M. Fibre Tip Sensors for Localised Temperature Sensing Based on Rare Earth-Doped Glass Coatings. *Sensors* **2014,** 14, 21693-21701.

199. Mahata, M. K.; Kumar, K.; Rai, D. V. Er^{3+}–Yb^{3+} Doped Vanadate Nanocrystals: A Highly Sensitive Thermographic Phosphor and Its Optical Nanoheater Behavior. *Sens. Actuators, B* **2015,** 209, 775-780.

200. Xu, W.; Zhao, H.; Zhang, Z.; Cao, W. Highly Sensitive Optical Thermometry through Thermally Enhanced Near Infrared Emissions from Nd3+/Yb3+ Codoped Oxyfluoride Glass Ceramic. *Sens. Actuators, B* **2013,** 178, 520-524.

201. Xu, W.; Song, Q.; Zheng, L.; Zhang, Z.; Cao, W. Optical Temperature Sensing Based on the near-Infrared Emissions from Nd 3+/Yb 3+ Codoped Cawo 4. *Opt. Lett.* **2014,** 39, 4635-4638.

202. Wawrzynczyk, D.; Bednarkiewicz, A.; Nyk, M.; Strek, W.; Samoc, M. Neodymium (Iii) Doped Fluoride Nanoparticles as Non-Contact Optical Temperature Sensors. *Nanoscale* **2012,** 4, 6959-6961.

203. Rocha, U.; Jacinto da Silva, C.; Ferreira Silva, W.; Guedes, I.; Benayas, A.; Martínez Maestro, L.; Acosta Elias, M.; Bovero, E.; van Veggel, F. C. J. M.; García Solé, J. A.; Jaque, D. Subtissue Thermal Sensing Based on Neodymium-Doped Laf3 Nanoparticles. *ACS Nano* **2013,** 7, 1188-1199.

204. Benayas, A.; del Rosal, B.; Pérez-Delgado, A.; Santacruz-Gómez, K.; Jaque, D.; Hirata, G. A.; Vetrone, F. Nd:Yag near-Infrared Luminescent Nanothermometers. *Adv. Opt. Mater.* **2015,** 3, 687-694.

205. Huang, P.; Zheng, W.; Tu, D.; Shang, X.; Zhang, M.; Li, R.; Xu, J.; Liu, Y.; Chen, X. Unraveling the Electronic Structures of Neodymium in Liluf4 Nanocrystals for Ratiometric Temperature Sensing. *Adv. Sci.* **2019,** 6, 1802282.

206. Savchuk, O.; Carvajal, J. J.; De la Cruz, L. G.; Haro-González, P.; Aguiló, M.; Díaz, F. Luminescence Thermometry and Imaging in the Second Biological Window at High Penetration Depth with Nd:Kgd(Wo4)2 Nanoparticles. *J. Mater. Chem. C* **2016,** 4, 7397-7405.

207. Quintanilla, M.; Zhang, Y.; Liz-Marzán, L. M. Subtissue Plasmonic Heating Monitored with Caf2:Nd3+,Y3+ Nanothermometers in the Second Biological Window. *Chem. Mater.* **2018,** 30, 2819-2828.

208. Skripka, A.; Morinvil, A.; Matulionyte, M.; Cheng, T.; Vetrone, F. Advancing Neodymium Single-Band Nanothermometry. *Nanoscale* **2019,** 11, 11322-11330.

209. Wang, S.; Westcott, S.; Chen, W. Nanoparticle Luminescence Thermometry. *J. Phys. Chem. B* **2002,** 106, 11203-11209.

210. Bünzli, J.-C. G., Lanthanide Luminescence: From a Mystery to Rationalization, Understanding, and Applications. In *Handbook on the Physics and Chemistry of Rare Earths*, Elsevier: 2016; Vol. 50, pp 141-176.

211. Baron, J. M.; Boster, B. L.; Barnett, C. M. Ado-Trastuzumab Emtansine (T-Dm1): A Novel Antibody-Drug Conjugate for the Treatment of Her2-Positive Metastatic Breast Cancer. *J. Oncol. Pharm. Pract.* **2014**.